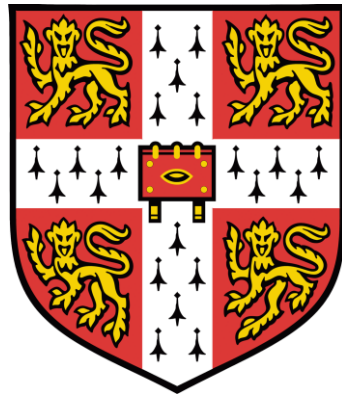


**Transmission Capacity Improvement for  
High Speed Multimode Waveguide Links  
Using Advanced Optical Launch and  
Multilevel Modulation Schemes**



Liang GENG

Jesus College

University of Cambridge

This dissertation is submitted for the degree of

Doctor of Philosophy

June, 2013

# Declaration

This dissertation is the result of my own work and includes nothing which is the outcome of work done in collaboration except where specifically indicated in the text.

# Statement of Length

This dissertation contains 53,024 words and 127 figures including appendices, bibliography, footnotes, tables and equations. The numbers of words and figures do not exceed the limits required by the Engineering Degree Committee.

# Acknowledgement

First and foremost, I would like to thank my supervisor Professor Richard Penty for providing me with invaluable guidance and exceptional research environment throughout the period of my PhD study. Without the consistent help, support and great patience from Professor Richard Penty, this thesis would not be possible.

I also thank my academic adviser Professor Ian White for sharing his wealth of knowledge on optical communication and enlightening me with forward-looking ideas. His devotion to details has benefited me with patience and precision in research.

My special thanks go to my industrial adviser Dr. David Cunningham who leads me to explore the optical world from scratch. I have particularly enjoyed the weekly discussions with Dr. David Cunningham from which I learnt not only comprehensive technical details concerning almost every aspect of optical communications but also the most up-to-date industry and market trends. Dr. David Cunningham's devotion to his research has always encouraged me to work harder.

My appreciation should also be given to Professor Richard Penty, Professor Ian White, Dr. David Cunningham and Avago Technologies for the generous grant of the scholarship to sponsor my PhD.

I wish to thank Dr. Jonathan Ingham for his stimulating discussions regarding the mode theory of multimode fibre. I also thank Professor Kevin Williams for his assistance regarding the optical mask fabrication. I thank Adrian Wonfor for providing technical support regarding computer and lab equipment related matters. My appreciation goes to Dr. Tongyun Li for sharing his knowledge on FPGA. I also thank Dr. Jinlong Wei for interesting discussions regarding simulation works and I also appreciate my roommate and colleague Yunxi Li for countless inspiring discussions.

I thank all members of Centre of Photonic Systems for their kindness, support and hard work to keep this group with an energetic and active environment.

Faithfully, I would like to thank my wife for her love and support, without which my doctoral study would not be possible. Finally my deepest appreciation goes to my parents and my parents-in-law for their trust and consistent encouragement.

To Yuan, my parents and my parents-in-law

# List of Publications

Published Journal and Conference Papers:

J. Wei, **L. Geng**, D. G. Cunningham, R. V. Penty, and I. White, "100 Gigabit Ethernet transmission enabled by carrierless amplitude and phase modulation using QAM receivers," in Optical Fiber Communication Conference/National Fiber Optic Engineers Conference (OFC/NFOEC), Anaheim, Mar 2013, p. OW4A.5.

**L. Geng**, J. Wei, R. V. Penty, I. White, and D. G. Cunningham, "3 Gbit/s LED-based step index plastic optical fiber link using multilevel pulse amplitude modulation," in Optical Fiber Communication Conference/National Fiber Optic Engineers Conference (OFC/NFOEC), Anaheim, Mar 2013, p. OTh4A.1.

J. L. Wei, **L. Geng**, D. G. Cunningham, R. V. Penty, and I. H. White, "Comparisons between gigabit NRZ, CAP and optical OFDM systems over FEC enhanced POF links using LEDs," in 14th International Conference on Transparent Optical Networks (ICTON), Jul 2012, p. Tu.P.17.

J. L. Wei, **L. Geng**, D. G. Cunningham, R. V. Penty, and I. H. White, "Gigabit NRZ, CAP and optical OFDM systems over POF links using LEDs," Optics Express, vol. 20, pp. 22284-22289, Sep 2012.

**L. Geng**, R. V. Penty, I. H. White, and D. G. Cunningham, "FEC-free 50 m 1.5 Gb/s plastic optical fibre link using CAP modulation for home networks," in 38th European Conference and Exhibition on Optical Communication (ECOC), Amsterdam, Sep 2012, p. Th.1.B.4.

**L. Geng**, S. H. Lee, K. A. Williams, R. V. Penty, I. H. White, and D. G. Cunningham, "Symmetrical 2-D Hermite-Gaussian square launch for high bit rate transmission in multimode fiber links," in Optical Fiber Communication Conference/National Fiber Optic Engineers Conference (OFC/NFOEC), Los Angeles, Mar 2011, p. OWJ5.

**L. Geng**, C. H. Kwok, S. H. Lee, J. D. Ingham, R. V. Penty, I. H. White, and D. G. Cunningham, "Efficient line launch for bandwidth improvement of 10 Gbit/s multimode fibre links using elliptical Gaussian beam," in 36th European Conference and Exhibition on Optical Communication (ECOC), Torino, Sep 2010, p. We.6.B.5.

Publications in Preparation:

**L. Geng**, R. V. Penty, I. H. White, and D. G. Cunningham, "Hermite-Gaussian Square Launch Scheme for Bandwidth Improvement over 10 Gbit/s Multimode Fiber Links," prepared for submission to Journal of Lightwave Technology

**L. Geng**, R. V. Penty, I. H. White, and D. G. Cunningham, "Multi-gigabit/s Transmissions Using Multilevel Modulation Schemes for LED-based Step Index Plastic Optical Fibre Links," prepared for submission to Journal of Lightwave Technology

# Abstract

This dissertation investigates the potential technologies in both optical and electrical domains for transmission capacity improvement in multimode waveguide links.

The first half of the dissertation focuses on the multimode waveguide made from glass, the multimode glass fibre. A new optical launch scheme is developed, namely low-loss Hermite-Gaussian launch, to achieve single mode group excitation in the multimode glass fibre. Novel implementations using elliptical Gaussian beam and square-shaped launching profiles are developed, achieving a coupling loss at least 2.5 dB lower than the previously reported line launch scheme. Theoretical calculations show that these launches provide 50% bandwidth-distance product improvement over the dual launch scheme for a 99% yield of the entire OM1 fibre installed base. It is also found experimentally that the low-loss Hermite-Gaussian launches outperform dual launch for fibres favouring either centre launch or offset launch. Misalignment tolerance measurements reveal that the bandwidth improvements over a perfectly aligned centre launch using these launches are maintained within a radial offset range of  $\leq 8 \mu\text{m}$ . Error free transmissions at 10 Gbit/s are demonstrated for different orders of low-loss Hermite-Gaussian launches over 250 m worst case OM1 fibre without the use of equalisation.

The second half of the dissertation concentrates on another type of multimode waveguide which is made from plastic, namely step-index plastic optical fibre (SI-POF). Both baseband and passband multilevel modulation schemes are investigated to provide over gigabit/s transmissions using LEDs. For the first time, fractionally-spaced equalisers are thoroughly examined in multilevel modulation systems for LED-based SI-POF links. Based on the link budget analysis, it is found that PAM-8 and CAP-64 are the best baseband and passband solutions respectively. For 25 m links, calculations show that PAM-8 and CAP-64 can achieve data rate up to 3 Gbit/s with system margins of 2.2 dB and 1.3 dB. Meanwhile for 50 m links, they achieve data rate up to 1.5 Gbit/s with system margins of 1.9 dB and 1.2 dB respectively. A new FPGA system is developed to experimentally evaluate the PAM-8 and CAP-64 schemes. Error free transmissions are achieved at 3 Gbit/s using PAM-8 for 25 m SI-POF and 1.5 Gbit/s using CAP-64 for 50 m SI-POF. These results record the highest bit-rate-distance-product achieved in LED-based SI-POF links without the use of forward error correction.

# Table of Contents

## Chapter 1 Introduction

|        |  |    |
|--------|--|----|
| 1.1.   | THE DEVELOPMENT OF OPTICAL COMMUNICATION.....  | 2  |
| 1.2.   | DATA COMMUNICATIONS OVER MULTIMODE OPTICAL WAVEGUIDES.....   | 6  |
| 1.2.1. | Multimode Glass Fibre Links.....   | 6  |
| 1.2.2. | Plastic Optical Fibre Links .....  | 8  |
| 1.3.   | EXISTING TECHNOLOGIES FOR TRANSMISSION CAPACITY IMPROVEMENT<br>OVER MULTIMODE OPTICAL WAVEGUIDES ..... | 12 |
| 1.3.1. | Mode Selective Launch .....  | 12 |
| 1.3.2. | Wavelength Division Multiplexing.....  | 13 |
| 1.3.3. | Advanced Modulation Schemes .....  | 14 |
| 1.3.4. | Parallel Optics .....  | 14 |
| 1.4.   | ORGANISATION AND CONTRIBUTIONS OF THE DISSERTATION.....  | 15 |
| 1.4.1. | Organisation of the Chapters.....  | 15 |
| 1.4.2. | Contributions of the Dissertation .....  | 16 |

## Chapter 2 Principles of Multimode Optical Waveguides

|          |  |    |
|----------|--|----|
| 2.1.     | INTRODUCTION OF MULTIMODE OPTICAL WAVEGUIDES.....        | 19 |
| 2.2.     | GRADED-INDEX MULTIMODE GLASS FIBRE.....                  | 23 |
| 2.2.1.   | Refractive Index Defects .....                           | 24 |
| 2.2.2.   | Chromatic Dispersion .....                               | 26 |
| 2.2.3.   | Attenuation in Multimode Glass Fibre.....                | 26 |
| 2.2.4.   | Mode Field Theory for Multimode Glass Fibre.....         | 27 |
| 2.2.4.1. | Mode Groups in Multimode Glass Fibre.....                | 29 |
| 2.2.4.2. | Intermodal Dispersion and Differential Modal Delay ..... | 31 |
| 2.2.5.   | Multimode Glass Fibre Standards .....                    | 32 |
| 2.3.     | PMMA-BASED STEP-INDEX PLASTIC OPTICAL FIBRE.....         | 34 |
| 2.3.1.   | Structure of SI-POF .....                                | 34 |
| 2.3.2.   | Attenuation in Plastic Optical Fibre.....                | 35 |
| 2.3.3.   | Bandwidth Limitation of Plastic Optical Fibre .....      | 36 |
| 2.3.4.   | Plastic Optical Fibre Standards.....                     | 36 |
| 2.4.     | CONCLUSIONS .....  | 38 |

## Chapter 3 Low-loss Hermite-Gaussian Launch for Bandwidth Improvement of Multimode Glass Fibre

|          |   |    |
|----------|---|----|
| 3.1.     | INTRODUCTION TO LAUNCH SCHEMES FOR MULTIMODE GLASS FIBRE .....    | 40 |
| 3.1.1.   | Overfilled Launch .....   | 42 |
| 3.1.2.   | Centre Launch .....   | 43 |
| 3.1.3.   | Offset Launch .....   | 45 |
| 3.1.4.   | Dual Launch .....   | 46 |
| 3.1.5.   | Twin-spot Launch.....   | 47 |
| 3.1.6.   | Line Launch .....   | 48 |
| 3.2.     | THEORETICAL MODELLING OF LOW-LOSS HERMITE-GAUSSIAN LAUNCH.....    | 49 |
| 3.2.1.   | Principles of the Low-loss Hermite-Gaussian Launch.....           | 50 |
| 3.2.2.   | Ideal Hermite-Gaussian Launch.....                                | 57 |
| 3.2.3.   | Low-loss Hermite-Gaussian Launch Beam Generation .....            | 63 |
| 3.2.3.1. | Coupling Efficiency of Hermite-Gaussian Launch .....              | 64 |
| 3.2.3.2. | Non-ideal Hermite-Gaussian Beam .....                             | 66 |
| 3.2.4.   | Limitations of the Low-loss Hermite-Gaussian Launch.....          | 68 |
| 3.2.4.1. | Launch with Radial Misalignment .....                             | 68 |
| 3.2.4.2. | Phase Profile Tolerance .....                                     | 71 |
| 3.2.4.3. | Rotational Misalignment.....                                      | 73 |
| 3.3.     | EXPERIMENTAL EVALUATION OF LOW-LOSS HERMITE-GAUSSIAN LAUNCH..     | 74 |
| 3.3.1.   | Fabrication of the Beam Shaping Mask.....                         | 75 |
| 3.3.2.   | Experimental Demonstrations of the Low-loss Line Launch.....      | 77 |
| 3.3.2.1. | Bandwidth Measurements .....                                      | 77 |
| 3.3.2.2. | Misalignment Tolerance.....                                       | 78 |
| 3.3.2.3. | Data Transmission Measurements at 10 Gbit/s .....                 | 79 |
| 3.3.3.   | Experimental Demonstrations of the Low-loss Square Launches ..... | 81 |
| 3.3.3.1. | Bandwidth Measurements .....                                      | 81 |
| 3.3.3.2. | Misalignment Tolerance.....                                       | 82 |
| 3.3.3.3. | Data Transmission Measurements at 10 Gbit/s .....                 | 83 |
| 3.4.     | CONCLUSIONS .....   | 85 |

## Chapter 4 Theoretical Study of Multilevel Modulation Schemes for LED-based Plastic Optical Fibre Links

|          |  |     |
|----------|--|-----|
| 4.1.     | MULTILEVEL MODULATION SCHEMES IN OPTICAL COMMUNICATIONS .....          | 89  |
| 4.2.     | PULSE AMPLITUDE MODULATION .....                                       | 92  |
| 4.2.1.   | The Nyquist Criterion .....  | 94  |
| 4.2.2.   | PAM Receiver Pulse Shape .....   | 95  |
| 4.3.     | CARRIER-LESS AMPLITUDE AND PHASE MODULATION.....                       | 100 |
| 4.3.1.   | Passband Nyquist Pulse .....   | 102 |
| 4.3.2.   | Orthogonal CAP Pulses.....   | 104 |
| 4.4.     | SYSTEM MODEL FOR MULTILEVEL MODULATIONS OVER POF.....                  | 106 |
| 4.4.1.   | Light Emitting Diode .....   | 106 |
| 4.4.1.1. | Resonant Cavity LEDs .....   | 107 |
| 4.4.1.2. | Modulation Bandwidth and Response Model .....                          | 108 |
| 4.4.2.   | Step-Index Plastic Optical Fibre .....                                 | 109 |
| 4.4.3.   | Receiver .....   | 110 |
| 4.4.4.   | Overall Response of SI-POF Links .....                                 | 111 |
| 4.4.5.   | Equalisation .....   | 112 |
| 4.4.5.1. | Feed Forward Equaliser.....  | 113 |
| 4.4.5.2. | Decision Feedback Equaliser .....                                      | 114 |
| 4.4.5.3. | Fractionally Spaced Equaliser .....                                    | 115 |
| 4.4.6.   | Link Power Budget.....   | 116 |
| 4.5.     | SIMULATION RESULTS.....  | 118 |
| 4.5.1.   | Evaluation of the Pulse Amplitude Modulation System.....               | 119 |
| 4.5.1.1. | Signal Generation and Transmission .....                               | 119 |
| 4.5.1.2. | Signal Equalisation and Recovery.....                                  | 123 |
| 4.5.1.3. | Power Penalty Analysis .....   | 127 |
| 4.5.2.   | Evaluation of the Carrier-less Amplitude and Phase Modulation System . | 128 |
| 4.5.2.1. | Signal Generation and Transmission .....                               | 128 |
| 4.5.2.2. | Demodulation and Equalisation .....                                    | 130 |
| 4.5.2.3. | Power Penalty Analysis .....   | 133 |
| 4.6.     | CONCLUSIONS .....  | 135 |

|            |   |     |
|------------|---|-----|
| Chapter 5  | FPGA-based System for Pulse Amplitude Modulation and Carrier-less Amplitude/Phase Modulation in Plastic Optical Fibre Links |     |
| 5.1.       | SYSTEM ARCHITECTURE .....   | 138 |
| 5.2.       | FPGA-BASED MODULATION SYSTEM .....  | 140 |
| 5.2.1.     | Design Overview and Clock Distribution.....   | 141 |
| 5.2.2.     | PRBS and PRS Generator .....  | 142 |
| 5.2.3.     | Look-up Table for CAP System .....  | 143 |
| 5.2.4.     | CAP Sequence Buffer Block .....   | 144 |
| 5.2.5.     | PAM Sequence Buffer Block .....   | 145 |
| 5.2.6.     | Serializer Buffer Block .....   | 145 |
| 5.2.7.     | Output Switch Block .....   | 147 |
| 5.2.8.     | The Overall FPGA System.....  | 147 |
| 5.3.       | DIGITAL TO ANALOGUE CONVERTER .....   | 149 |
| 5.4.       | TRANSCIEIVER.....   | 150 |
| 5.5.       | EXPERIMENTAL RESULTS .....  | 151 |
| 5.5.1.     | Modulation Signal Generation.....   | 151 |
| 5.5.2.     | Signal Amplification .....  | 154 |
| 5.5.3.     | Offline Processing Approach.....  | 154 |
| 5.5.4.     | Noise Measurements .....  | 155 |
| 5.5.5.     | Data Transmission Evaluations .....   | 156 |
| 5.5.5.1.   | 3 Gbit/s PAM-8 Transmission over 25 m SI-POF.....   | 156 |
| 5.5.5.2.   | 1.5 Gbit/s CAP-64 Transmission over 50 m SI-POF .....   | 159 |
| 5.6.       | CONCLUSIONS .....   | 163 |
| Chapter 6  | Conclusions and Future Work   |     |
| 6.1.       | CONCLUSIONS .....   | 165 |
| 6.2.       | FUTURE WORK.....  | 171 |
| 6.2.1.     | Mode Division Multiplexing using Hermite-Gaussian Launches.....   | 171 |
| 6.2.2.     | Multi-channel Transmission over POF .....   | 173 |
| REFERENCES | .....   | 176 |

# List of Figures

|  |    |
|--|----|
| Figure 1.1 Global internet traffic forecast of various services predicted by Cisco [13] .....  | 4  |
| Figure 1.2 Annual installation volume of different types of fibres [29] .....  | 7  |
| Figure 1.3 x86 server annual installation volume forecast in terms of port numbers of various Ethernet systems [31] .....  | 8  |
| Figure 1.4 Proposals of Fast Ethernet over plastic optical fibres.....   | 9  |
| Figure 1.5 Typical subsystems of a modern in-car communication network.....  | 10 |
| Figure 1.6 Next generation optical home network based on plastic optical fibre .....   | 11 |
| Figure 1.7 DIY cutting tool and OptoLock connector for POF from Firecomms [42] ..  | 11 |
| Figure 1.8 A duplex multimode glass fibre link using a mode selective launch technology .....  | 12 |
| Figure 1.9 Schematic diagram of a CWDM transmission system with four wavelengths   | 13 |
| Figure 2.1 Schematic diagrams of the single mode and multimode waveguides under ray optics assumption.....   | 20 |
| Figure 2.2 Refractive index profiles of (a) step-index and (b) graded-index multimode glass fibres.....  | 21 |
| Figure 2.3 Comparison between the SI-POF, GI-POF and multimode glass fibre .....   | 22 |
| Figure 2.4 Refractive index profiles for different values of profile parameter $\alpha$ .....  | 23 |
| Figure 2.5 Schematic diagram of light propagation characteristics in a graded-index multimode glass fibre.....   | 24 |
| Figure 2.6 Typical refractive index profiles with defects (red and blue). The optimal profile is shown in solid black line. Three different defective regions are shown in the shadow areas, which represent the centre defects, multiple profile parameters defects and core-cladding boundary defects respectively ..... | 26 |

|   |    |
|---|----|
| Figure 2.7 Mode field distributions for modes in mode group 3 to 8 for a 62.5 $\mu\text{m}$ core multimode glass fibre. The circular areas represent the core areas of the fibres .....                                       | 30 |
| Figure 2.8 The structure of a 1 mm SI-POF .....   | 35 |
| Figure 2.9 Comparison of the attenuation rates between the PMMA SI-POF and glass fibre against wavelength [86].....   | 36 |
| Figure 3.1 Multimode glass fibre illuminated by an LED under the OFL condition.....   | 43 |
| Figure 3.2 Multimode glass fibre illuminated by a laser under the centre launch condition .....   | 44 |
| Figure 3.3 Schematic impulse responses and frequency responses of a multimode glass fibre with centre defects under the overfilled launch and centre launch conditions.....   | 45 |
| Figure 3.4 Schematic diagram of the offset launch implementations over OM1 (left) and OM2 (right) multimode glass fibres .....  | 46 |
| Figure 3.5 The offset launch transceiver patchcord cable for Gigabit Ethernet.....  | 46 |
| Figure 3.6 Schematic diagram of the twin-spot launch.....   | 47 |
| Figure 3.7 Schematic diagram of the line launch scheme with a (5, 0) order Hermite-Gaussian profile .....   | 48 |
| Figure 3.8 Hermite-Gaussian beam profiles with zero vertical order ( $n = 0$ ) for a wavelength of 1310 nm.....   | 55 |
| Figure 3.9 Hermite-Gaussian beam profiles with equal order on horizontal and vertical directions for a wavelength of 1310 nm.....   | 56 |
| Figure 3.10 Intensity profiles of the selected Hermite-Gaussian beams. (a) (5, 0) order line launch and (b) (1, 1), (2, 2) and (3, 3) order square launches .....   | 57 |
| Figure 3.11 Calculated mode power distributions for the centre launch, offset launch, and Hermite-Gaussian launches based on the Cambridge-108MMF model. The colour of the bars indicate different fibres from the model..... | 59 |
| Figure 3.12 Definition of the mode group power extinction ratio .....   | 60 |

---

|   |    |
|---|----|
| Figure 3.13 Mode group power extinction ratios based on the Cambridge-108MMF model for the centre launch, offset launch and proposed Hermite-Gaussian launches...   | 61 |
| Figure 3.14 Calculated bandwidth-distance products based on the Cambridge-108MMF model for the centre launch, offset launch, dual launch and proposed Hermite-Gaussian launches.....  | 62 |
| Figure 3.15 Schematic diagram of the near field Hermite-Gaussian beam generation.....   | 63 |
| Figure 3.16 Schematic diagrams of incident beams coupling at the phase/intensity shaping masks for the (a) conventional line launch, (b) (5, 0) order low-loss line launch and (c) (2, 2) order low-loss square launch.....   | 64 |
| Figure 3.17 Mode group power extinction ratio against different incoming Gaussian beam waists for the (1, 1) order low-loss Hermite-Gaussian square launch.....   | 65 |
| Figure 3.18 Non-ideal Hermite-Gaussian beams generated using the beam shaping mask approach. $17\ \mu\text{m} \times 8.5\ \mu\text{m}$ FWHM elliptical Gaussian beam and $17\ \mu\text{m}$ FWHM circular Gaussian beam are used for the low-loss line launch and square launches respectively...  | 66 |
| Figure 3.19 (a) Extinction ratio calculations for the centre launch, offset launch, and proposed low-loss Hermite-Gaussian launches. (b) Bandwidth-distance product calculations for the centre launch, offset launch, dual launch and proposed low-loss Hermite-Gaussian launches. Both calculations are based on approximate Hermite-Gaussian profiles and the Cambridge-108MMF model at a wavelength of 1310 nm..... | 67 |
| Figure 3.20 Illustration of the area of interest for launching misalignment investigation   | 68 |
| Figure 3.21 Contour plots of the bandwidth-distance products achieved for the proposed low-loss Hermite-Gaussian launches for a misalignment region of $3\ \mu\text{m} \times 3\ \mu\text{m}$ . The contour levels indicate bandwidth-distance products in the unit of GHz·km.....  | 69 |
| Figure 3.22 Bandwidth-distance products based on the Cambridge-108MMF model for the centre launch, offset launch, dual launch and proposed low-loss Hermite-Gaussian launches with $3\ \mu\text{m}$ radial misalignment .....   | 70 |
| Figure 3.23 Worst case link yields with $3\ \mu\text{m}$ radial misalignment for the centre launch, offset launch, dual launch and (3, 3) order square launch.....  | 71 |

|  |    |
|--|----|
| Figure 3.24 Phase shift tolerance for different orders of low-loss Hermite-Gaussian launches. The Cambridge-108MMF model is used for all calculations.....   | 72 |
| Figure 3.25 Schematic illustrations of the rotational misalignment of the proposed low-loss Hermite-Gaussian launches.....   | 73 |
| Figure 3.26 Transparent areas on the beam shaping mask for (3, 3) order square launch at a wavelength of 1310 nm. The colour difference indicates a 180° phase change. The outline of the spot indicates the 5% intensity amplitude of an ideal profile..... | 75 |
| Figure 3.27 Fabrication steps of the beam shaping mask for the (3, 3) order square launch. Dimension is not to be scaled.....  | 76 |
| Figure 3.28 SEM images of the masks for the (5, 0) order line launch and (1, 1), (2, 2) and (3, 3) order square launches at a wavelength of 1310 nm and the schematic diagram of the cross section of the etched SiO <sub>2</sub> glass substrate.....       | 76 |
| Figure 3.29 Schematic diagram of the elliptical Gaussian beam and (5, 0) order low-loss Hermite-Gaussian line launch beam generation .....   | 77 |
| Figure 3.30 Effective modal bandwidth measurements for the centre launch, offset launch and (5, 0) order low-loss line launch over (a) Fibre A and (b) Fibre B.....  | 78 |
| Figure 3.31 Normalized bandwidths of the (5, 0) order low-loss line launch and centre launch with radial offsets from 0 μm to 10 μm.....   | 79 |
| Figure 3.32 Eye diagrams of the (a) back-to-back link, (b) centre launch, (c) offset launch and (d) (5, 0) order low-loss line launch at the received power of -6 dBm.....   | 80 |
| Figure 3.33 Corresponding BER measurements for the back-to-back link, centre launch and (5, 0) order low-loss line launch.....   | 80 |
| Figure 3.34 Schematic diagram of the (2, 2) order low-loss Hermite-Gaussian square launch beam generation and experimental setup.....  | 81 |
| Figure 3.35 Effective modal bandwidth measurements for the (1, 1), (2, 2) and (3, 3) order low-loss square launches over (a) Fibre A and (b) Fibre B.....  | 82 |
| Figure 3.36 Normalized bandwidths referring to perfectly aligned launch for the low-loss square launches and centre launch with radial offset from 0 μm to 10 μm.....  | 83 |

|   |     |
|---|-----|
| Figure 3.37 Eye diagrams of the (a) back-to-back link, (b) centre launch, (c) offset launch and (d)-(f) (1, 1), (2, 2) and (3, 3) order low-loss square launches at the received power of -6 dBm..... | 84  |
| Figure 3.38 Corresponding BER measurements for the back-to-back, centre launch and proposed low-loss square launches.....   | 84  |
| Figure 4.1 Constellation maps of the CAP-4, CAP-16, PAM-4 and PAM-8 modulation schemes (symbols are labelled with corresponding binary sequences).....  | 89  |
| Figure 4.2 Published data rates and reaches of LED-based POF links using different modulation schemes in recent years .....   | 91  |
| Figure 4.3 Schematic diagram of a pulse amplitude modulation transmission system .....  | 92  |
| Figure 4.4 A binary sequence is converted to PAM-8 symbols and modulated using a rectangular transmitter filter. $T$ is the symbol period of the PAM-8 system .....                                   | 93  |
| Figure 4.5 The spectra $Q(f)$ and $Z(f)$ corresponding to the pulse that does not satisfy the Nyquist criterion .....   | 96  |
| Figure 4.6 The spectra $Q(f)$ and $Z(f)$ corresponding to an ideal band-limited pulse that satisfies the Nyquist criterion.....   | 96  |
| Figure 4.7 Time domain waveform of a sinc function pulse truncated at $\pm 6T$ .....  | 97  |
| Figure 4.8 ISI free transmission of a sinc pulse sequence with a symbol period of $T$ ..  | 97  |
| Figure 4.9 Waveforms (top) and spectra (bottom) of a series of raised-cosine pulses with different excess bandwidths .....  | 99  |
| Figure 4.10 Schematic diagram of a carrier-less amplitude and phase modulation system .....   | 101 |
| Figure 4.11 Typical transmitter for a CAP-64 system. A binary data sequence is converted to CAP symbols and modulated to the I and Q channels respectively. The symbol period is $T$ .....            | 101 |
| Figure 4.12 The spectra of the baseband and passband Nyquist pulses. Raise-cosine pulse shaping filters with excess bandwidth of 0.5 are used in both cases .....                                     | 103 |

|   |     |
|---|-----|
| Figure 4.13 The in-phase and quadrature pulse shapes based on (a) the raised-cosine and (b) the square root raised-cosine shaping filters. The excess bandwidth is 50% and the waveforms are truncated at $\pm 2T$ .....                        | 105 |
| Figure 4.14 The structure of a RC-LED .....   | 107 |
| Figure 4.15 Frequency responses of LEDs with different bandwidths and corresponding transmitted eye diagrams for a 100 Mbit/s PAM-2 system.....   | 109 |
| Figure 4.16 Frequency responses of Eska SI-POFs for a length of 50 m .....  | 110 |
| Figure 4.17 Schematic circuit diagram of a PIN photodiode with an applied reverse bias .....  | 110 |
| Figure 4.18 Typical overall system frequency responses for SI-POF links.....  | 111 |
| Figure 4.19 Pre-cursor ISI and post-cursor ISI of a symbol after a dispersive channel .   | 112 |
| Figure 4.20 Schematic diagram of an FIR $T$ -spaced $N$ -tap FFE.....   | 113 |
| Figure 4.21 Schematic diagram of an IIR $M$ -tap DFE .....  | 114 |
| Figure 4.22 Schematic diagram of the equaliser with an $N$ -tap FFE and an $M$ -tap DFE .....   | 115 |
| Figure 4.23 Comparison between the $T$ , $T/2$ and $T/4$ spaced equalisers representing a square root raised-cosine CAP in-phase (I channel) filter.....  | 116 |
| Figure 4.24 Link power budget model for multilevel modulation schemes in SI-POF transmission systems .....  | 117 |
| Figure 4.25 Block diagram of the simulation model for PAM system evaluations.....   | 119 |
| Figure 4.26 Original modulation signals for the PAM-2, PAM-4 and PAM-8 systems. Left: With ideal rectangular pulse shaping. Right: Practical modulation signals after a Gaussian filter with the same bandwidth as the system symbol rate ..... | 120 |
| Figure 4.27 Eye diagrams of the transmitted signals after the LED for the PAM-2, PAM-4 and PAM-8 systems at various data rates .....  | 121 |
| Figure 4.28 Eye diagrams of the signal after 25 m (top) and 50 m (bottom) SI-POFs for the PAM-2, PAM-4 and PAM-8 systems at various data rates.....   | 122 |

|  |     |
|--|-----|
| Figure 4.29 Comparison between the non-equalised and equalised eye diagrams for the PAM-2, PAM-4 and PAM-8 systems at 500 Mbit/s over 50 m SI-POF .....  | 123 |
| Figure 4.30 Equalised eye diagrams for the PAM-2, PAM-4 and PAM-8 systems after 25 m (top) and 50 m (bottom) SI-POFs at various data rates. The dashed boxes indicate the non-feasible systems.....  | 124 |
| Figure 4.31 Optimisations of the numbers of taps in equalisers for 3 Gbit/s transmissions over 25 m SI-POF using PAM-4 and PAM-8. The contour levels indicate the power penalties in the unit of dBo .....   | 125 |
| Figure 4.32 Optimisations of the numbers of taps in equalisers for 1.5 Gbit/s transmissions over 50 m SI-POF using PAM-4 and PAM-8. The contour levels indicate the power penalties in the unit of dBo .....   | 126 |
| Figure 4.33 Link power budgets comparisons between the PAM-2, PAM-4 and PAM-8 modulation schemes over 25 m (top) and 50 m(bottom) SI-POFs .....  | 127 |
| Figure 4.34 Block diagram of the simulation model for CAP system evaluations .....   | 128 |
| Figure 4.35 The eye diagrams of the original modulation signals using the raised-cosine (top) and square root raised-cosine (bottom) shaping filters .....   | 129 |
| Figure 4.36 500 Mbit/s transmissions over 50 m SI-POF using CAP-4, CAP-16 and CAP-64. From left to right: received eye diagrams, received constellation maps, demodulated constellation maps .....   | 130 |
| Figure 4.37 Constellation diagrams for the CAP-4, CAP-16 and CAP-64 systems at various data rates over 25 m (top) and 50 m (bottom) SI-POFs .....  | 132 |
| Figure 4.38 Optimisations of the numbers of taps in equalisers for 3 Gbit/s transmission over 25 m SI-POF (left) and 1.5 Gbit/s transmission over 50 m SI-POF (right) using CAP-64. The contour levels indicate the power penalties in the unit of dBo ..... | 133 |
| Figure 4.39 Link power budgets comparisons between the CAP-4, CAP-16 and CAP-64 modulation schemes over 25 m (top) and 50 m(bottom) SI-POFs .....  | 134 |
| Figure 5.1 Schematic diagram of the system for multilevel modulation scheme evaluations for LED-based SI-POF links.....  | 139 |

|   |     |
|---|-----|
| Figure 5.2 Top view of the Altera Stratix III development board .....   | 140 |
| Figure 5.3 Clock distribution of the FPGA based evaluation system.....  | 141 |
| Figure 5.4 A 4-bit Fibonacci linear feedback shift register for the MLS generation .....  | 142 |
| Figure 5.5 The 40-sample look-up table for the CAP I (top) and Q (bottom) channels in the CAP-64 system. Raised-cosine shaping filters are used for both pulse shapes .....       | 143 |
| Figure 5.6 Block diagram of the CAP look-up table in the FPGA system.....   | 144 |
| Figure 5.7 Block diagram of the CAP sequence buffer .....   | 144 |
| Figure 5.8 Block diagram of the PAM sequence buffer .....   | 145 |
| Figure 5.9 Block diagram of the serializer buffer.....  | 146 |
| Figure 5.10 Block diagram of the dedicated serializer.....  | 146 |
| Figure 5.11 Output switch implemented between the serializer buffers and dedicated serializers in the FPGA system providing channel selectivity.....                              | 147 |
| Figure 5.12 Complete schematic block diagram of the FPGA-based evaluation system  | 148 |
| Figure 5.13 (a) Top view of the DAC5682z EVM board and (b) block diagram of the DAC5682z chip .....   | 149 |
| Figure 5.14 Top view of the FC1000T transceiver evaluation board .....  | 150 |
| Figure 5.15 PAM system electrical eye diagrams generated by the DAC in comparison with the calculations.....  | 151 |
| Figure 5.16 CAP I channel (left) and Q channel (right) pulses generated by the DAC. The sampling rate is 200 MHz. Pulses are truncated at $\pm 2.5$ symbol period .....           | 152 |
| Figure 5.17 Comparisons of the eye diagrams between the DAC outputs and calculations for the (a) CAP-4, (b) CAP-16 and (c) CAP-64 systems at a symbol rate of 250 Msymbol/s ..... | 153 |
| Figure 5.18 The amplified and non-amplified PAM-8 waveforms at 1 Gsymbol/s. The amplitude of the waveforms is not to be scaled.....   | 154 |

|   |     |
|---|-----|
| Figure 5.19 Measured noise standard deviations with (left) and without (right) the photodiode.....  | 155 |
| Figure 5.20 Comparison between the modulation and the received signals for the 3 Gbit/s PAM-8 system over 25 m SI-POF.....  | 156 |
| Figure 5.21 Corresponding received eye diagram for the 3 Gbit/s PAM-8 system over 25 m SI-POF .....   | 157 |
| Figure 5.22 Equalisation adaption iterations for the 3 Gbit/s PAM-8 transmission over 25 SI-POF with (a) 60-tap FFE and 20-tap DFE and (b) 80-tap FFE and 30-tap DFE          | 158 |
| Figure 5.23 (a) Equalised eye diagrams of the 3 Gbit/s PAM-8 system at -12 dBm and (b) corresponding BER curves in comparison with back-to-back .....                         | 159 |
| Figure 5.24 Comparison between the modulation and received signals for the 1.5 Gbit/s CAP-64 system over 50 m SI-POF.....   | 160 |
| Figure 5.25 Received eye diagram and constellation map for the 1.5 Gbit/s CAP-64 system over 50 m SI-POF .....  | 160 |
| Figure 5.26 Equalisation adaption iterations for the 1.5 Gbit/s CAP-64 transmission over 50 m SI-POF (a) Q channel, (b) I channel .....                                       | 161 |
| Figure 5.27 (a) Equalised constellation map of the 1.5 Gbit/s CAP-64 transmission over 50 m SI-POF (b) Corresponding BER curve in comparison with the back-to-back case ..... | 162 |
| Figure 6.1 Mode division multiplexing system using two different orders of the low-loss Hermite-Gaussian square launches .....  | 171 |
| Figure 6.2 Link budget analysis of a two-channel mode division multiplexing system using the low-loss Hermite-Gaussian square launches .....                                  | 172 |
| Figure 6.3 Mode division multiplexing system using the optically combined CAP modulation scheme .....   | 173 |
| Figure 6.4 Hexagonal SI-POF bundle for parallel transmission using an MicroLED array .....  | 174 |

Figure 6.5 Schematic diagram of an MicroLED pair for the optically combined CAP modulation system for a SI-POF in a hexagonal arranged bundle ..... 175

# List of Tables

|   |     |
|---|-----|
| Table 2-1 Comparison between RG-6, SI-POF, MMF and SMF [40] .....                               | 34  |
| Table 2-2 List of SI-POF standards specified in IEC 60793-2-40 .....                            | 37  |
| Table 3-1 Minimum modal bandwidths of OM1 and OM2 fibres .....                                  | 43  |
| Table 3-2 List of the parameters used in numerical calculations.....                            | 58  |
| Table 3-3 List of the optimised Gaussian beam waists and corresponding coupling losses<br>..... | 65  |
| Table 4-1 List of parameters used in simulations .....  | 118 |

# CHAPTER

# 1

## INTRODUCTION

*This chapter gives a general overview of the development of optical communication. As the worldwide data traffic rapidly increases, existing data communication systems have to be continuously upgraded to higher operating data rate to provide extra transmission capacity. On one hand, multimode glass fibre plays a significant role in these networks since it provides cost-effective solution to short-range applications and has mature installed base resulted from decades of implementation. Therefore, research on improving the capacity of the existing multimode glass fibre systems has always been an attractive topic. On the other hand, plastic optical fibre becomes more and more interesting for its potential applications in next generation optical home networks and automotive networks. Its large core size enables easy DIY installation and its bandwidth performance is comparable to copper cable. In the meantime, it is lighter, cheaper and more robust in challenging environments. In this chapter, following a brief introduction of various multimode waveguide systems, some existing technologies enabling high speed transmissions over both glass fibres and plastic fibres are introduced. Finally, the organisation of this dissertation is outlined.*

## 1.1. The Development of Optical Communication

Exchanging information is an indispensable element for human life since it connects people and creates an interactive society. The use of light for communication can be dated back to thousands of years ago when most of the ancient civilisations had pioneers who made use of signal fire and smoke to broadcast a piece of information, mostly as a way of drawing attention. These ideas were evolved further to more complicated signalling system using lamps and flags in the more modern history. Not until in the year of 1880, just four years after one of the most important interactive devices in human history, the Telephone, was invented, did Alexander Graham Bell demonstrate his optical version of this invention, the Photophone, which was believed to be the first time that human speech had been successfully transmitted through an optical signal [1]. The Photophone modulated the speech signal to a light beam which was projected to a selenium cell, whose resistance varied inversely with the incident illumination [2]. The receiver then demodulated the resistance variation to a current signal and drove a speaker for speech regeneration. The modulation signal in a Photophone system was directly created by the vibration of the sound wave. Hence the signal transmitted by the optical carrier was analogue, which was similar to the optical signal in a modern radio-over-fibre system except that Photophone transmission was in free-space. However, in the late nineteenth century, the electrical wire was a much more robust transmission medium. Telephone was a more practical solution for speech transmission at that time. Bell was not able to make the Photophone sufficiently practical for commercialisation and the idea was only further developed in various research institutes mainly for military uses [3].

In Bell's Photophone system, the main limitation was the beam divergence and the line of sight requirement in free-space transmission. An alternative way for optical transmission to be achieved is if the light beam is confined and guided in certain transmission media just like the electrical signal carried by copper wires. In this way, the signal power can be much better maintained and the optical path is more flexible. This concept, referred to the optical guiding phenomenon, was firstly demonstrated in 1841 by Swiss physicist Daniel Colladon when he tried to show the breaking-up of water jets by letting the fluid flow through holes at different heights on a water tank [4]. He came up with an idea of focusing the sunlight on the water tank to illuminate the water jets so that the audience at the back of the lecture hall could have a better view. Dr. Colladon found this effect fascinating and sent his idea to his friend, Francois Arago, who later invited an optics specialist in France, Dr Jacques Babinet to repeat this experiment.

Unfortunately, Dr. Babinet did not see the importance of this work and it was not further explored [5]. In the following years, an Irish-born physicist, John Tyndall, popularized the light guiding effect by doing a similar demonstration in London and described it in his book '*Notes about Light*'. The light guiding effect is known as total internal reflection, where the light can be completely reflected at a material boundary when the incident material has a lower refractive index and the angle of incidence is sufficiently large.

The development of light guiding technology experienced a dramatic progress during the late 20<sup>th</sup> century. With the 'fibre optics' concept been proposed for the first time by Indian scientist Narinder Singh in 1957 [6], the invention of the fibrescope initiated the development of all glass optical fibres. Together with the invention of the semiconductor LED and laser in the early 1960s [7], the industry of guided optical transmission had made a significant step forward for its establishment. In the early period, glass fibres had attenuation rates of  $\sim 1000$  dB/km [8], which were too high for a practical optical communication link. A remarkable paper published by Charles Kao in 1966 investigated the material loss of dielectric waveguides and proposed that 20 dB/km was a feasible target for making optical communication a viable technology and it would be achievable using glass material if the iron-impurity could be reduced [9]. Kao's proposal attracted worldwide interest. In 1970, Corning manufactured the first optical fibre with loss less than 20 dB/km at a wavelength of 633 nm [10]. In the following years, the fibre attenuation dropped dramatically thanks to the advanced glass purification technologies and the exploration of the lasers with longer wavelengths [11, 12]. Since then, optical fibre communication has become an indispensable component in modern communication systems. The ultra-high capacity enabled by optical carrier and low attenuation achieved by advanced optical fibres made high speed and long distance communications possible and established the foundation of the worldwide communication network.

As new technologies emerge, the requirement for more convenient communication approaches becomes extremely demanding. Exchanging and sharing information more efficiently has become an important element to improve people's daily lives. More and more information is sent digitally thanks to the well-established optical communication networks. The development of computing and Internet technology significantly improves the efficiency of communication whilst consuming a massive amount of

bandwidth resources. New services like file sharing, video streaming and cloud computing give a big challenge of fulfilling the increasing capacity demands of the communication industry. Figure 1.1 illustrates the forecast of global consumer Internet traffic proposed by Cisco in 2011 in terms of different internet services [13]. The compound annual growth rate (CAGR) from 2011 to 2016 was predicted as 32%. By the year of 2016, over 80,000 Petabytes<sup>1</sup> will be generated and distributed over the Internet per month. Among the listed consumption, Internet video stays as the most traffic-driven service, whose contribution to the total traffic will increase from 51% to 55% in 5 years by the end of 2016. It's worth mentioning that substantial file sharing traffic is consisted of exchanging video files. A broader definition of Internet video traffic including file sharing and other services providing video contents will contribute more than 86% of the total consumer Internet traffic [14].

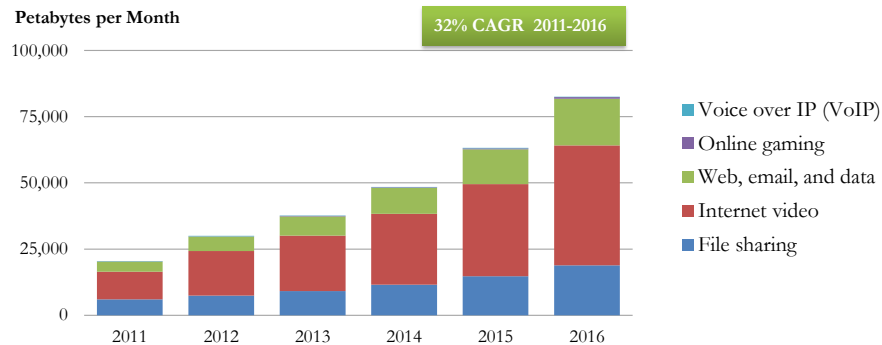


**Figure 1.1 Global internet traffic forecast of various services predicted by Cisco [13]**

The growth shown in Figure 1.1 implies that the bandwidth requirement for providing reliable future Internet service to end users will continue to increase. Before video service has become the main contributor to the capacity consumption, networks with line rates of few Mbit/s seemed sufficient for web browsing, email and some basic VoIP applications. However, to accommodate the growing video traffic demand, data rate requirement for high speed in-building backbone networks nowadays has risen to 10 Gbit/s or even to 40 Gbit/s and 100 Gbit/s in some newly established systems. In these short distance systems (less than 500 m), optical fibres are the dominant transmission media due to their high capacities compared with other media like copper cables. Among all fibre types, single mode fibre gives the highest bandwidth. However, implementing single mode fibre in short distance network environments seems unpractical and not cost-effective. One of the main reasons is the high cost of the connectivity due to the

<sup>1</sup> 1 Petabyte is equivalent to  $2^{20}$  or  $\sim 10^6$  Gbytes (a million Gbytes).

sensitive alignment requirement which is not preferred in the access-point-intensive environment of such networks [15, 16]. The other reason comes from the fact that multimode fibres have been continuously implemented for decades in various networks [17]. Although the existing multimode fibres are possibly not the most suitable media for today's bandwidth requirement, replacing the 'legacy' fibres with the more expensive single mode or multimode fibres will face significant cost concerns and marketing difficulties. Therefore, the research topic of seeking for solutions to improving the capacity of existing multimode fibres to meet the growing traffic demand is getting increasingly attractive in recent years.

As the upgrades emerge from the backbone network to the access network, technologies for the last 50 m connections to end users, such as in a home network environment, are also facing the challenge of meeting higher bandwidth requirements. It is believed that data rates over 1 gigabit/s are required for the next generation home networks [18]. Using optical transmission in home networks seems a definite trend in the coming decades since it provides sufficient bandwidth and the technologies are readily available. However, given the wiring complexity and unprofessional maintenance conditions in home networks, multimode fibres made from glass can be too fragile and also too sensitive to dust with frequent connections/disconnections. Recently, large core plastic optical fibre (POF) has drawn substantial interest from researchers for its potential applications in such networks since it is more mechanically durable, tolerant to connection misalignment, and has a reasonable bandwidth performance. Low cost LED transmitters in the visible range can be used in such links, which provides further maintenance convenience. The POF link potentially provides a user-friendly and low cost solution as an alternative to the conventional copper-based home networks. In addition to this, the mechanical durability and immunity to electromagnetic interference also makes POF a robust transmission medium for systems in challenging environments such as in-car networks.

Multimode optical waveguides play an important role in short distance network at present and will continue to dominant in the coming years due to both mass existing installed base and current technology preferences. Challenges and opportunities co-exist for researchers working on advanced technologies for transmission capacity improvement of these systems.

## 1.2. Data Communications over Multimode Optical Waveguides

Multimode optical waveguides are popular in various applications. Although they generally have lower bandwidth-distance products performance than single mode fibres, the benefits of easier installation and lower cost make them a preferred choice in short reach systems. In existing systems, both LEDs and lasers are suitable for different link scenarios as optical transmitters. In this section, the multimode waveguide systems based on both glass fibre and plastic fibre are introduced. Current technology trend and standardisation progress are also discussed.

### 1.2.1. Multimode Glass Fibre Links

Multimode glass fibres have been mainly implemented in short distance optical transmission systems, especially for in-building applications, for decades. The multimode glass fibre was introduced in the fibre distributed data interface (FDDI) standard as an alternative solution to conventional copper-based high speed local area network [19]. LEDs and 62.5  $\mu\text{m}$  multimode glass fibres were used in this technology, providing a data rate of 100 Mbit/s. FDDI had been popular for several years until the more cost-effective solution Fast Ethernet was proposed based on FDDI in late 1995 [20].

The bandwidth-distance products performance of the early generations of multimode glass fibres (OM1 and OM2) are typically limited to  $\sim 500 \text{ MHz}\cdot\text{km}^2$ . This is due to the large number of supported modes of the multimode glass fibre. Different modes propagate through the fibre with slightly different velocities. Therefore, if a large number of the supported modes are excited, the power of the input signal tends to disperse. This limits the multimode glass fibre only to be used in short distance with a link length typically less than 500 m [21]. The large core size (compared with single mode glass fibre) of the multimode glass fibre allows low cost LEDs to be used as the transmitter. However, the large beam divergence and limited modulation bandwidth of the LED reduce the overall capacity of a multimode glass fibre link and cannot meet the high bandwidth requirement at current time.

The invention of semiconductor lasers started a new phase for optical communication since the lasers provided much higher modulation bandwidth than traditional LEDs [22]. The narrower optical spectrum also reduced the chromatic dispersion due to the varying

---

<sup>2</sup> This is based on a LED transmitter using overfilled launch. Details regarding overfilled launch condition are given in Section 3.1.1.

propagation velocity for different wavelengths [23, 24]. The laser typically generates a much smaller spot than that of an LED. Therefore, the multimode glass fibre launched using a laser has fewer modes excited [25]. It was further found that by applying a radial offset at launch, the bandwidth performance of a multimode glass fibre can be improved [26]. This launch is normally referred as offset launch and it was adopted in the Gigabit Ethernet standard [27].

New multimode glass fibres have also been continuously developed to meet the increasing bandwidth demand. Besides the first generation OM1 multimode glass fibres which have been implemented for over 20 years, several other standard multimode glass fibres have also been widely implemented in the past decade as seen in Figure 1.2. Clearly, the OM1 multimode glass fibre still has the largest annual installation volume although OM2 and OM3 fibres are catching up. These ‘legacy’ fibres (OM1) are popular due to their low cost and sufficient bandwidth for most in-building applications in the Gigabit Ethernet age. However for 10 Gbit/s links, OM1 fibres tend to struggle with inadequate bandwidth for the required link length of in-building networks. They have to be boosted by using electrical dispersion compensation (EDC) technology to achieve a feasible link according to the IEEE 10GBASE-LRM standard [28].

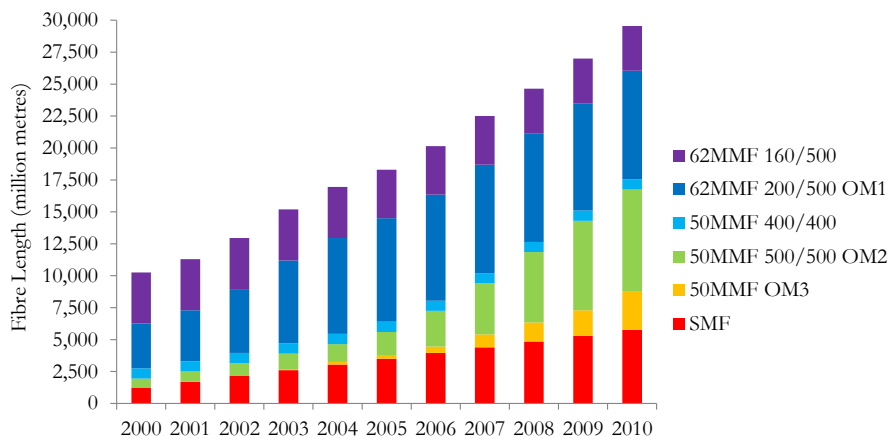


**Figure 1.2 Annual installation volume of different types of fibres [29]**

As the 40G/100G Ethernet standard was published in 2010 by IEEE802.3ba committee, it is predicted that the upgrades from 10 Gbit/s to 40 Gbit/s will take place rapidly in the following decade [30]. As seen in Figure 1.3, it is believed that the majority of servers connected by Ethernet will be operating at a data rate of 40 Gbit/s or higher by the end of 2018. In the coming 5 years of transition period from 10 Gbit/s to 40 Gbit/s or 100 Gbit/s systems, one of the most challenging issues is the cost-effective upgrades for the

existing ‘legacy’ fibre bases. Since OM1 and OM2 fibres were not considered in IEEE802.3ba standard for their limited bandwidths, replacement seems inevitable for the ‘legacy’ systems if upgrades are needed. However, as the ‘legacy’ fibres are still being actively implemented in some new systems and the costs for the 40G/100G technologies are still high, it is preferred that the installed fibres can be kept useful longer with some low cost transition upgrades. Therefore, the research of improving the capacity of ‘legacy’ multimode glass fibre systems in different domains without replacing the installed fibres becomes very attractive.

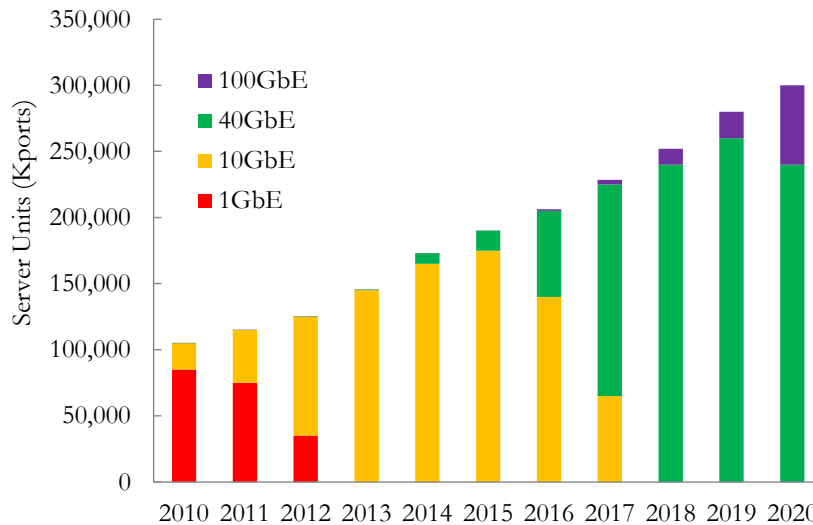


**Figure 1.3 x86 server annual installation volume forecast in terms of port numbers of various Ethernet systems [31]**

### 1.2.2. Plastic Optical Fibre Links

The first POF link was described in literature in 1988 where a 20 Mbit/s transmission over 80 m PMMA-based step-index POF was demonstrated [32]. Later in 1992 Hewlett Packard invented the first commercial POF transceiver [33] with a proposed POF link system of 50 Mbit/s for 15 m. Hewlett Packard had since become one of the most important pioneers in the field of POF communications, with the technology been succeeded by its spin-out company Avago Technologies.

The standard PMMA-based POF normally has a core size of 500  $\mu\text{m}$  to 1000  $\mu\text{m}$  [34]. The large core size makes the fibre strongly multimode which introduces significant modal dispersion [35]. A normal POF only has a bandwidth-distance product of less than 2 MHz·km [36]. In addition, POF also exhibits very high fibre loss of  $\sim 0.2$  dB/m. However, compared with the multimode glass fibre, POF is much easier to handle and tends to be more tolerant against challenging environments. The large core size also

provides low cost connectivity and installation. These factors make POF a popular transmission medium for short distance communications such as home networks and in-car networks, where either the multimode glass fibre is too fragile or the copper cable is incapable to survive in the challenging environments (damp etc.).

One of the most important applications of POF is the industrial Ethernet. As more sophisticated and flexible automation control is required in industrial plants, a standard was proposed by a group of researchers in Germany to address the problem of providing a robust and reliable solution to industrial links using Fast Ethernet over POF [37]. Figure 1.4 illustrates the three different versions of the links specified in this proposal. The 50 m link is achieved using both 650 nm and 510 nm LEDs (with connectors) whilst the 100 m link is only available using a 510 nm LED. For the 50 m links, the standard step index POF is used which provides sufficient bandwidth. This type of fibre does not support the 100 m link due to the low bandwidth performance and the double step index POF has to be used. Industry plants normally have challenging requirement for the network infrastructure against environment such as heavy electromagnetic interference, highly corrosive environment and long exposure to damp air. Conventional copper cables are normally vulnerable to these conditions. Therefore, the POF solutions are very popular and have been widely implemented in industrial links.

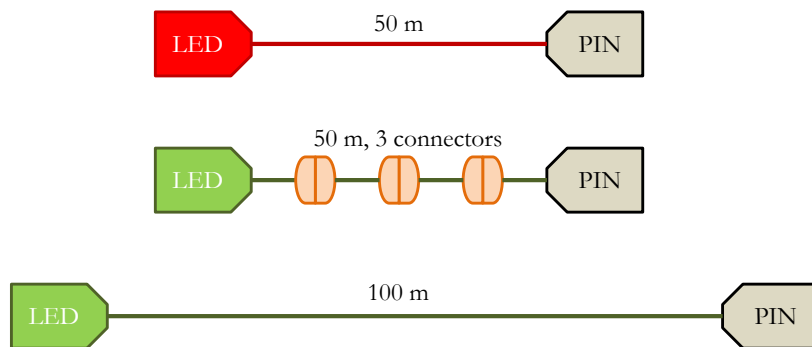


**Figure 1.4 Proposals of Fast Ethernet over plastic optical fibres**

Another popular application for POF is in-car communications. Conventionally, the media transmissions inside a vehicle are almost exclusively limited to radio, cassette and possibly CD players. As more and more advanced technologies are introduced to car systems, a variety of sophisticated entertainment and information systems can be seen in cars manufactured today. These systems normally consist of real-time audio and video transmissions which require relatively large bandwidth. The media oriented systems transport (MOST) standard was developed to meet these requirements [38]. An example

of subsystems in a typical in-car network which can be supported by MOST is illustrated in Figure 1.5. MOST was firstly introduced to support 25 Mbit/s transmission (MOST25) and has been recently upgraded to 150 Mbit/s (MOST150). MOST150 for the first time integrates the Ethernet channel and provides full support for IP applications [39]. Given the fact that services like HD video transmission and driving assistant system are going to be widely implemented in vehicles in the future, it is believed that the next generation in-car network will require a data rate of  $\sim 3$  Gbit/s.

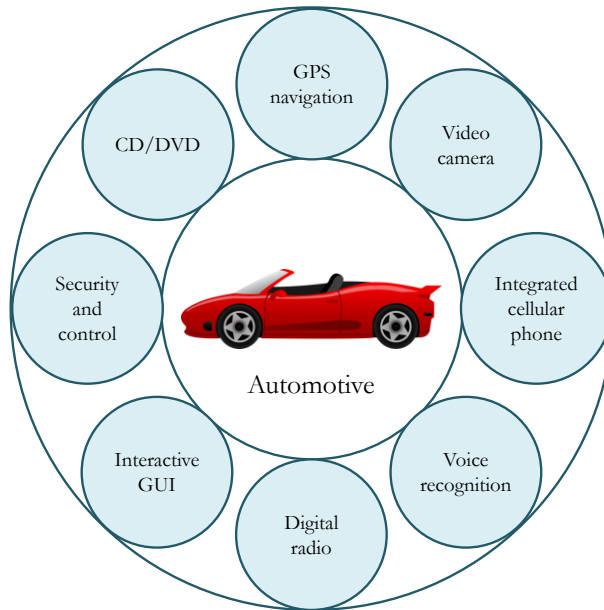


**Figure 1.5 Typical subsystems of a modern in-car communication network**

In recent years, POF is actively being investigated for another application field with huge market potential, the home networks. With even more advanced fibre fabrication technologies, the low cost standard POF has managed a bandwidth performance comparable to the copper cable which is usually used in home networks at present. Figure 1.6 shows a schematic diagram of a multi-service home network based on POF connections. The access point to this home network is provided using single mode fibre or coaxial cable. POFs are wired around the building/apartment to give various connections for different services. Compared with CAT-5 cables which are widely used in home network connections, POFs have smaller bending radius and are at least 4x lighter [40]. POFs also provide easier connectivity where DIY is possible for untrained persons [41]. An example of DIY tools developed by Firecomms Ltd. for POF interconnect is shown in Figure 1.7.

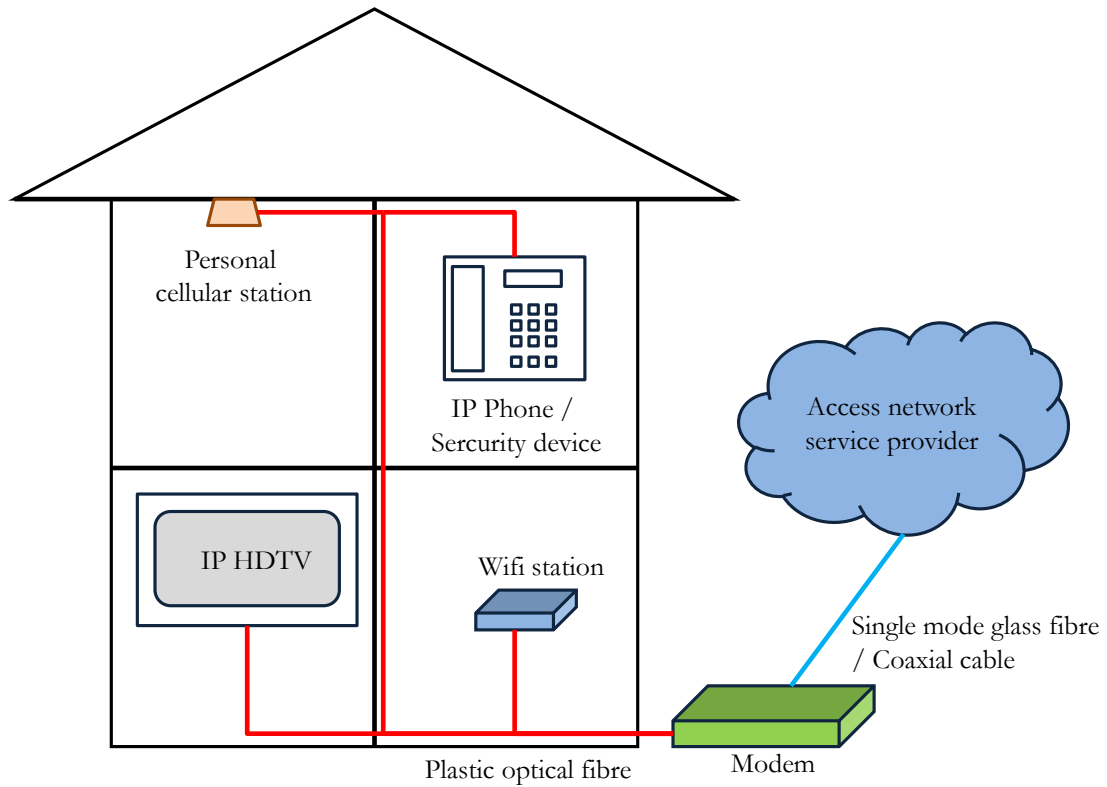
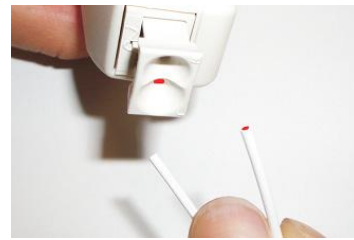


Figure 1.6 Next generation optical home network based on plastic optical fibre



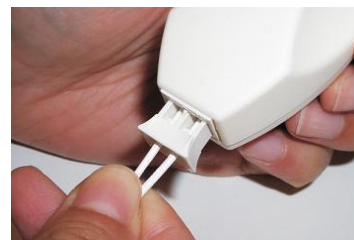
1. Slice the POF cable



2. Split the POF strands



3. Insert POF into OptoLock



4. Press OptoLock to hold POF into place

Figure 1.7 DIY cutting tool and OptoLock connector for POF from Firecomms [42]

### 1.3. Existing Technologies for Transmission Capacity Improvement over Multimode Optical Waveguides

To satisfy the capacity requirements in the evolving communication networks, various technologies have been developed in recent years. These technologies either improve the overall bandwidth or extend the reach of an optical link. In this section, four different approaches are introduced and reviewed. In particular, mode selective launch and wavelength division multiplexing are reviewed for multimode glass fibre links, whilst advanced modulation schemes and parallel optics are discussed for POF links.

#### 1.3.1. Mode Selective Launch

In the LED era of multimode glass fibre communication, light was launched into the fibre with a relatively large spot compared with the core size. This launching condition is referred as overfilled launch since all supported modes of the multimode glass fibre are excited. In a laser-based multimode glass fibre link where a launching spot with smaller size is realized, mode selective launch can be achieved by changing the launching beam profile or position on the targeted fibre to control the number and orders of the excited modes. This approach, sometimes called restricted launch or mode selective launch, is usually done by firstly launching the laser beam into a single mode fibre, and then coupling the output from the single mode fibre to an aligned multimode glass fibre [43]. A schematic diagram shown in Figure 1.8 can visualise the configuration of a duplex mode selective launch system (offset launch) using packaged patchcords configuration.

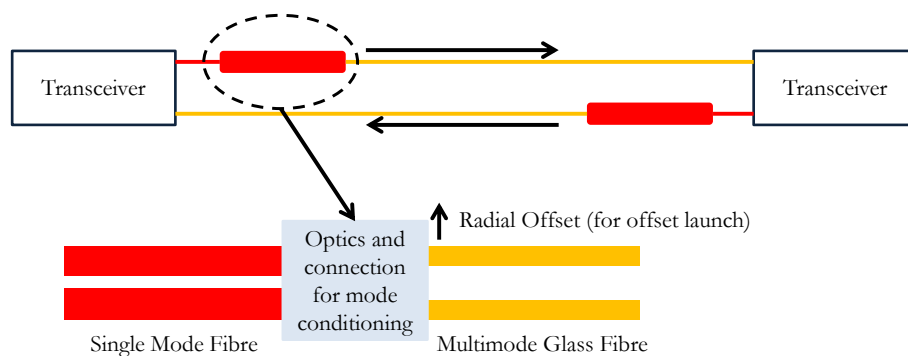


**Figure 1.8 A duplex multimode glass fibre link using a mode selective launch technology**

For an ideal graded index multimode glass fibre, only the fundamental mode will be excited if a spot with the right size is launched at the core centre. This is referred as centre launch [44]. However, this launch is vulnerable to subtle launch misalignments and refractive index defects of the multimode glass fibre, hence is not able to provide a reliable performance. During the discussion of Gigabit Ethernet standard, the offset

launch scheme was developed to provide reliable bandwidth performance with increased link yield, which overcomes the problem of profile-dependent bandwidth and directly contributes to the later published specifications [27]. In the offset launch, a radial misalignment is applied between the launching beam and the multimode glass fibre. In this way, a set of mid-order modes are excited. These modes tend to be less affected by the refractive index defects and result in guaranteeing an improved link yield for the installed fibre base. To achieve the optimal bandwidth performance, further development of dual launch requires manual testing between centre launch and offset launch to decide the preferred configuration for an installed Gigabit Ethernet multimode glass fibre link. More recently, a novel single mode group excitation launch scheme is developed to provide substantial bandwidth improvement to address the problem of extending the reach of multimode glass fibre in 10 Gbit/s Ethernet systems [45]. In this launch, a designed beam profile which only excites one mode group of the multimode glass fibre is used. Only one mid-order mode group is exclusively excited which virtually eliminates the intermodal dispersion.

### 1.3.2. Wavelength Division Multiplexing

Wavelength division multiplexing (WDM) is a well-established technology for long haul optical communication using single mode fibre. This technology can also be naturally migrated to multimode glass fibre systems. From the cost perspective, coarse wavelength division multiplexing (CWDM) is attractive because it is compatible uncooled lasers. With a  $\sim 25$  nm channel spacing in the CWDM system, the wavelength of the laser transmitter in each channel does not need to be precisely stabilised [46]. As an example, Figure 1.9 illustrates the CWDM system specified in IEEE 10GBASE-LX4 standard. In this system, four wavelengths are used to carry four independent data streams using transceiver pairs. With a lower single channel data rate of 2.5 Gbit/s, IEEE 10GBASE-LX4 manages a 10 Gbit/s multimode glass fibre link with 300 m reach [47].



Figure 1.9 Schematic diagram of a CWDM transmission system with four wavelengths

### 1.3.3. Advanced Modulation Schemes

Advanced modulation schemes have been intensively studied in the field of radio frequency (RF) communication [48]. However, due to the sufficient bandwidth, NRZ has been popular for conventional optical communication systems since the beginning. Though researchers have continuously put effort into increasing the bandwidth efficiency by using more advanced modulation schemes in the optical domain [49-53], the commercialisation process of these technologies are slow. Nevertheless, as the optical transceivers reach the physical limit at  $\sim 40$  GHz, more and more proposals regarding advanced modulation schemes have been made to the high speed standard committees for 40G/100G technologies, for example the IEEE802.3bm task force [54-56].

Undoubtedly, there has been a clear trend of evolution in the optical world to higher bandwidth efficiency. Due to the high cost, limitation of electronic devices beyond 10 Gbit/s, and the limited bandwidth of POF itself, the exploration of advanced modulation schemes has been particularly active in POF-based networks. It has been shown that discrete multi-tone (DMT) modulation can be used to increase the bandwidth efficiency of a POF system to 4.6 bit/s/Hz [57]. Given the very limited bandwidth of both LED transmitters and POF cables, advanced modulation schemes are considered as robust solutions to next generation high speed POF systems.

### 1.3.4. Parallel Optics

One of the simplest multiplexing technologies to increase channel capacity is to use parallel optics. This is very useful in connection-intensive network environment such as optical interconnects. Since optical interconnects normally require a large number of links in a limited space, it is preferred that a transmission medium with smaller radius of curvature be used. Compared with glass fibre cables which have a bending radius of 10 mm, POF can be made to have less than 1 mm [58]. This makes it very attractive for high speed optical interconnect applications. The first commercialised parallel POF product was introduced by Honda Cable in 2005 [59]. In this link, four POF cables were bundled to a ribbon terminated using a RJ45 connector. An aggregate data rate of 500 Mbit/s was achieved using this POF ribbon and multiple LED transmitters. As high bandwidth Micro-LED arrays are developed [60], parallel optics for POF can be extended to 2-D. More compact parallel links can be achieved, which potentially enables high speed and low cost optical interconnect applications.

## 1.4. Organisation and Contributions of the Dissertation

In general, multimode waveguide communication is mainly implemented for short range, terminal-intensive applications. Low cost is an inevitable factor in this field because of the frequent upgrades and large number of individual users. Though WDM is a great technology which enhances the single fibre capacity, the complexity of the multiplexing devices design significantly increases the system cost. Similarly, parallel transmission also provides a simple solution for more bandwidth, while this approach uses more components and is only feasible if the costs of the related devices are low.

Because of its early implementation and low cost, the 'legacy' OM1 multimode glass fibres have the largest volume of installed base and are still being implemented in some cost-sensitive systems. Currently, these systems are in a transition period for upgrading to 10 Gbit/s or even more advanced 40 Gbit/s and 100 Gbit/s technologies. At the same time, the higher bandwidth requirement also accelerates the implementation of optical network in consumer networks such as in home and for cars, where POFs are considered as a potential low cost and robust solution.

This dissertation contributes to the area of transmission capacity improvement of multimode waveguides. Both the optical and electrical domains are investigated to explore potential cost-effective technologies for this purpose. Specifically, this problem is considered for two main types of low cost multimode waveguides made from glass and plastic respectively. For the multimode glass fibre links, a passive optical launch scheme is reported to greatly enhance the bandwidth. The novel designs of the optics systems and launching beam profiles enable improved coupling efficiency compared with the previous line launch scheme. For the POF links, both baseband and passband multilevel modulation schemes are evaluated to enable multi-gigabit/s transmissions over LED-based step index POF (SI-POF) systems. Record high data rates of 3 Gbit/s over 25 m and 1.5 Gbit/s over 50 m SI-POF are achieved using proposed 8-level schemes.

### 1.4.1. Organisation of the Chapters

Chapter 1 outlines a general overview of the historical development of optical communication and the fast growing worldwide data traffic demands over the optical networks today. The application fields of multimode waveguide based links are introduced with a brief discussion of various industrial standards. Several existing approaches for bandwidth enhancement for multimode waveguides are also reviewed.

Chapter 2 discusses the principles of the multimode waveguides with respect to both glass fibre and plastic fibre. The mode theory of multimode glass fibre is introduced to reveal the modal dispersion effect. Various specifications of multimode glass fibres and POFs are also introduced.

Chapter 3 reports a novel low-loss optical launch scheme for bandwidth improvement in multimode glass fibre links. The first half of the chapter reviews the theoretical principles of the proposed launches, and gives the modelling results of different implementations of these launches. Based on the modelling comparisons, the second half of this chapter describes corresponding experimental works, where the effective modal bandwidths and data transmission measurements of different launches are evaluated using worst case fibre samples. The experimental results are also compared with conventional centre and offset launches.

Chapter 4 proposes the multilevel modulation schemes for high data rate transmissions over SI-POF. The principles of multilevel modulations are carefully derived, followed by the theoretical modelling and comparison between proposed schemes. Equalisation technology is investigated as one of the important elements in the proposed systems. The link power budget approach is introduced for the theoretical performance analysis of the overall systems.

Chapter 5 presents the experimental works of the multilevel modulation schemes introduced in Chapter 4. It starts with the detailed FPGA design in terms of various functional blocks. After this, experimental results measured using the FPGA system for the proposed multilevel modulation schemes are discussed.

Chapter 6 concludes and summarizes the achievements of the proposed optical and electrical approaches for bandwidth improvement and high speed data transmissions over multimode glass fibre and plastic fibre respectively. The outlook for future work related to the proposed approaches for further improvements are also discussed.

### **1.4.2. Contributions of the Dissertation**

The main contributions of this dissertation are listed with respect to the systems based on two different types of multimode waveguides.

For multimode glass fibre links:

- For the first time, elliptical Gaussian beam is used in an optical launch scheme for multimode glass fibres for the purpose of improving effective modal bandwidth and launch coupling efficiency.
- Novel square-shaped Hermite-Gaussian profiles are proposed for bandwidth improvement of multimode glass fibres. These launches, namely square launches, provide at least 2.5 dB coupling loss improvement compared with the conventional Hermite-Gaussian line launch and avoid the rotational alignment issue due to its central symmetry.
- It is experimentally demonstrated that the proposed low-loss Hermite-Gaussian launches outperform dual launch<sup>3</sup> for fibre favouring either centre or offset launch in terms of effective modal bandwidth. This guarantees a 99% yield with 50% bandwidth improvement over dual launch scheme based on OM1 fibres.
- Extended reach (250 m) is achieved using the proposed launch scheme without the use of equalisation at 10 Gbit/s.

For plastic optical fibre links:

- Thorough theoretical studies and comparisons of both baseband and passband multilevel modulation schemes for LED-based SI-POF links are demonstrated.
- For the first time, fractionally-spaced equalisers are carefully examined and optimised for the proposed links using multilevel modulation schemes.
- An FPGA platform is developed to provide both the PAM and CAP modulation signals with maximum 8 levels.
- A record 3 Gbit/s transmission over 25 m SI-POF is experimentally demonstrated using the PAM-8 modulation. This is the first successful LED-based SI-POF link that reaches the data rate goal of the next generation in-car networks without the use of any error correction code.
- A record 1.5 Gbit/s transmission is experimentally demonstrated using the CAP-64 modulation over 50 m SI-POF. This marks the highest data rate achieved in a LED-based SI-POF link fulfilling the reach requirement of home networks without the use of any error correction code.

---

<sup>3</sup> Dual launch selects between the centre launch and offset launch with a better bandwidth performance.

# CHAPTER

# 2

## PRINCIPLES OF MULTIMODE OPTICAL WAVEGUIDES

*This chapter introduces the key principles of multimode optical waveguides. Multimode glass fibre and PMMA-based SI-POF are reviewed as they are the two major transmission media implemented in existing multimode waveguide based links. To better understand the optical propagation characteristics within the multimode glass fibre, the mode theory for graded-index fibre is discussed. In addition, the mode group representation of modes in multimode glass fibre is introduced. Further to this, the differential modal delay is derived based on the propagation constant and mode power distribution concepts. Meanwhile, the large-core structure of the PMMA-based SI-POF provides much easier handling and installation, which makes it preferable for connection-intensive network environments. The fibre loss and bandwidth limitation in a POF link are discussed. Finally, the industrial standards of both multimode glass fibre and plastic fibre are outlined to show the commercialisation status of such fibres.*

## 2.1. Introduction of Multimode Optical Waveguides

The investigation of optical waveguides started in the form of a transparent rod which was proposed in 1910 by Hondros and Debye [61], followed by an experimental work demonstrated by Schriever in 1920 [62]. However, these transparent dielectric rods were proved to be impractical due to the unsupported structure and excessive losses at the rod-air boundary. Not until 1966, was a serious proposal published by Kao [9], which described the structure of a clad waveguide and predicted the utilisation of optical fibres as practical communication media, even though the loss was as high as  $1000 \text{ dBkm}^{-1}$ . Kao had for the first time proved that the loss of the fibre was due to waveguide material (silica glass in his case) impurities, resulting in tremendous efforts to improve conventional glass refining techniques. As the techniques developed, the fibres made from glass can achieve a loss as low as  $0.2 \text{ dBkm}^{-1}$  for the wavelength of  $1550 \text{ nm}$  [63]. This technology evolution made the era of light wave communication possible.

A multimode optical waveguide is dielectric and normally cylindrical, which confines electromagnetic energy and guides the light beam in the direction parallel to its optical axis [64]. Based on the mode theory of optical waveguides, the multimode waveguides support more than one mode to be propagated within the dielectric material. In general, this type of waveguide consists of a core layer in the centre, which is surrounded by another cladding layer. There is a difference in refractive indices between the core and the cladding layers. Light is mostly confined within the core area for propagation along the waveguide due to total internal reflection at the cladding incidence. Besides providing light confinement, the presence of the cladding has many other advantages. It reduces scattering loss that results from the dielectric discontinuities at the core surface and also protects the core from absorbing contaminants from the outside environment [65]. Most waveguide cables are also encapsulated in an elastic plastic material, mechanically buffering it from distortions or roughness of the adjacent surfaces [66].

Figure 2.1 illustrates the difference between a multimode optical waveguide and a single mode optical waveguide based on ray optics. It can be seen that the multimode waveguide normally has a core size larger than that of a single mode waveguide, which allows the light beams with different reflecting angles (or modes in waveguide electromagnetic mode theory) travelling through due to the total internal reflection.

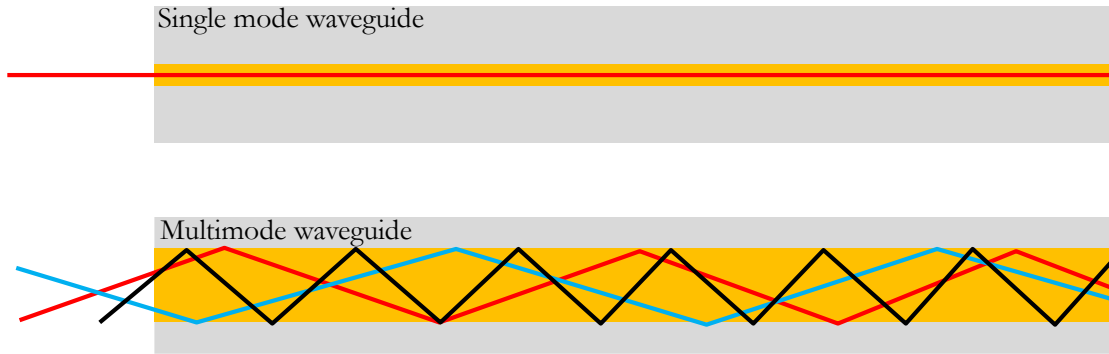


**Figure 2.1 Schematic diagrams of the single mode and multimode waveguides under ray optics assumption**

In data-communication applications for short distances, multimode glass fibres have been mainly implemented. The propagation property of a multimode glass fibre is dependent on its refractive index profile. Two commonly seen multimode glass fibre types are distinguished by the variations of the material index profile in the core area as illustrated in Figure 2.2. On the left side of this figure, the typical step-index multimode glass fibre is shown with a central core area with a refractive index  $n_1$ . Around the core is a layer of another glass cladding with refractive index  $n_2$ , where  $n_2$  is smaller than  $n_1$ . On the right side, Figure 2.2 (b) shows the more advanced type of fibre, graded-index fibre, whose core index  $n_1(r)$  varies as a function of the radial distance from the centre. It has the highest refractive index at the core centre, which gradually decreases along the fibre radius to the boundary between the core and cladding, reaching a constant cladding index. This graded-index profile equalises the group velocities of different excited modes and hence minimizes the intermodal dispersion<sup>4</sup>. Although in principle the graded-index multimode glass fibre exhibits very high effective modal bandwidth given an ideal refractive index profile, practical fabrication inevitably introduces refractive index defects, which makes the effective modal bandwidth of a multimode graded-index fibre usually not exceeding few GHz·km<sup>5</sup> [67].

<sup>4</sup> Details are introduced in Section 2.2.

<sup>5</sup> This effective modal bandwidth of the multimode fibre refers to overfilled launch bandwidth.

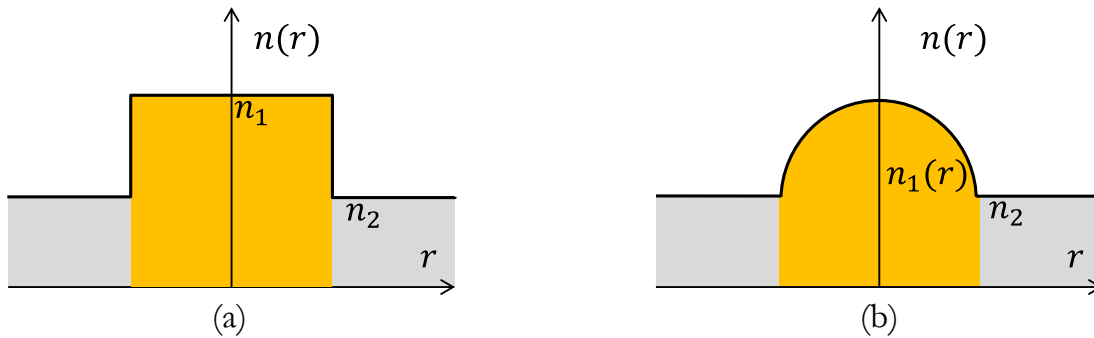


**Figure 2.2 Refractive index profiles of (a) step-index and (b) graded-index multimode glass fibres**

In recent years, another type of multimode optical waveguide made from polymer material has been of growing interest for researchers because of its potential application in next generation of low cost and high speed networks in home and vehicles. This type of multimode optical waveguide is called polymer/plastic optical fibre, or POF.

The first POF was developed in the late 1960s by DuPont with an attenuation exceeding 1000 dB/km due to the incomplete purification of the material used [68]. This was further improved in the following decade, where the rate was reduced to 125 dB/km [69]. However, glass fibres with attenuation below 1 dB/km were widely available in large quantity at that time and dominated the high data rate systems for short distance applications. Consequently, POF was in a difficult position to compete with glass fibre. In the meantime, in the short reach applications like local area networks (LANs), copper cables were found good enough to facilitate data rate of tens of megabit/s, which was considered sufficient. The development of POF was slowed down for many years as a result. Not until the 1990s, when the new technologies such as Internet started to be popularized, did the requirement of higher data rate for short distance links become dramatically demanding. In the past decades, services like dedicated personal LANs, voice over IP, file sharing and video streaming have built up huge consumption of bandwidth. Meanwhile, as the fabrication technologies were improved, POF regained its reputation as a potential optical transmission medium for short distance links since it exhibited comparable bandwidth to copper cable and provided easy installation [42]. Furthermore, the polymer material made the POF cheaper than copper cable and much less fragile than glass fibre [40].

POF is commonly strongly multimode as it is designed with a much larger core size than that of a glass fibre. Various polymer materials can be used for POF production. As the research on polymer material goes on, PMMA (Polymethylmethacrylate) becomes the

one of the most well-known materials used for POF. Other materials like polystyrene polymers [70, 71], deuterated polymers [72] and fluorinated polymers [73] are also used for POF production for specific purposes. Among these fibres, PMMA-based POF provides the most popular solution for high speed data communication networks given its low cost and mature technology.

Similarly to multimode glass fibre, the index profile of the core of the POF can either be step-index or graded-index as well. Figure 2.3 illustrates the standardised PMMA-POFs in IEC 60793-2-40 Class A4d and Class A4e [74] in comparison with the 62.5  $\mu\text{m}$  core multimode glass fibre. It can be seen that the SI-POF has a core of 980  $\mu\text{m}$  in diameter, which is covered by a cladding layer of 10  $\mu\text{m}$ . The graded-index POF (GI-POF) has a core diameter of 500  $\mu\text{m}$  covered by a cladding layer of 125  $\mu\text{m}$ . Compared with the multimode glass fibre, the core size of the POF is much larger. This guarantees good coupling at the input of the fibre with relatively relaxed alignment requirement, which reduces the connectivity cost in an optical link and also provides easy installation process not requiring trained professionals. Although the GI-POF provides a higher bandwidth performance, the price is relatively high due to the more complicated fabrication process and low market volume. The SI-POF on the other hand, though limited to a bandwidth-distance product of  $\sim 10$  MHz $\cdot$ km [75], is much cheaper. In this dissertation, SI-POFs are chosen for further discussions to provide low cost solution to high data rate links in both home and vehicle networks.



**Figure 2.3 Comparison between the SI-POF, GI-POF and multimode glass fibre**

## 2.2. Graded-index Multimode Glass Fibre

Graded-index multimode glass fibre has a maximum refractive index at the core centre, which decreases gradually to its minimum refractive index along the fibre radius until the cladding layer. This minimum refractive index is kept constant for the cladding layer. In general, the graded-index profile is given by

$$n(r) = \begin{cases} n_{core} \left(1 - \Delta \left(\frac{r}{a}\right)^\alpha\right)^{\frac{1}{2}} & r < a \\ n_{core} \left(1 - \Delta\right)^{\frac{1}{2}} = n_{cladding} & r \geq a \end{cases}, \quad 2-1$$

where  $n_{core}$  is the refractive index at the core centre,  $r$  is the radial distance from the core centre,  $a$  is the radius of the fibre core, and  $\alpha$  is the profile parameter which determines shape of the profile.  $\Delta$  is the relative difference of the refractive indices between the core and the cladding given by

$$\Delta = \frac{n_{core}^2 - n_{cladding}^2}{n_{core}^2}. \quad 2-2$$

The step-index profile can be expressed using Equation 2-1 taking the limit of  $\alpha \rightarrow \infty$  and the most common square-law graded-index profile is given for  $\alpha = 2$ . Figure 2.4 illustrates several refractive index profiles for different values of  $\alpha$ .

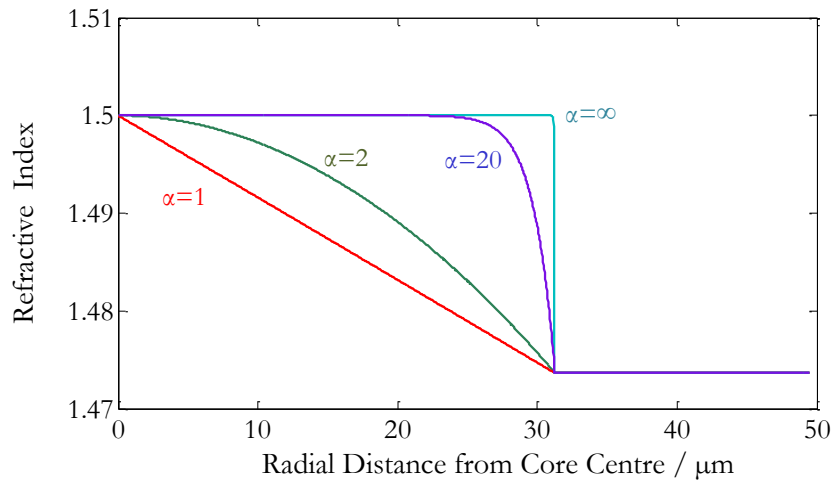


**Figure 2.4 Refractive index profiles for different values of profile parameter  $\alpha$**

The light propagation characteristic in a multimode fibre with a parabolic graded-index profile is shown in Figure 2.5. The paths of beam transmission follow curves that always intersect at the same points along the optical axis. The curved paths can be understood by regarding the graded-index profile as multiple levels of gradually decreasing step

indices along the fibre radius. Consistent refractions between these sections bend the light beam, giving an increasing angle of incidence to the next step boundary. Eventually, an incident angle that satisfies the total internal reflection is reached and the light beam is reflected back towards the other side of the core. In this way, the propagated light beam is continuously refracted and reflected.

The light travelling through the multimode glass fibre with graded-index profile in different paths tends to arrive at the fibre output nearly simultaneously. Hence the signal is less dispersed and high effective modal bandwidth is enabled. As seen in Figure 2.5, the longer paths tend to travel through the area with smaller refractive index where shorter paths mostly travel through around the core where the index is comparatively large. Since the velocity of light in a certain material follows the relationship as

$$v = \frac{c}{n}, \quad 2-3$$

the beams travelling through the longer paths have higher velocities than those travelling through shorter paths. Hence the arrival times of the beams at the output of the fibre are equalised given a suitable choice of profile parameter  $\alpha$ . In practice, a parabolic graded-index profile is commonly used for various standard multimode glass fibres with  $\alpha \approx 2$ .

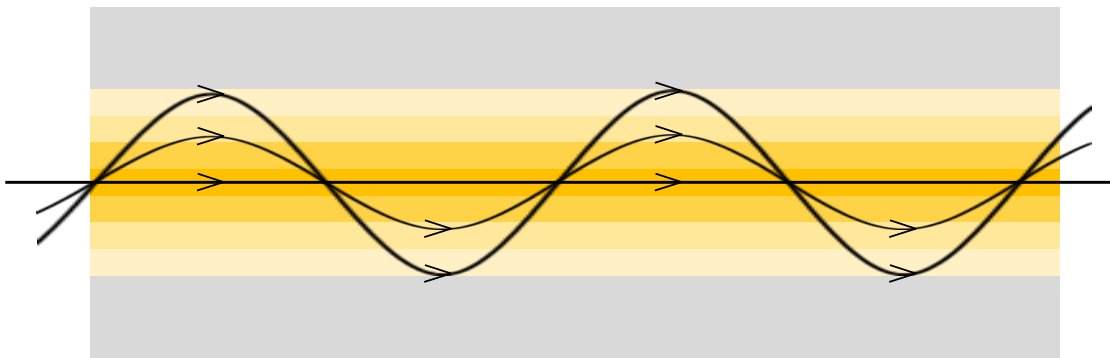


Figure 2.5 Schematic diagram of light propagation characteristics in a graded-index multimode glass fibre

### 2.2.1. Refractive Index Defects

The ideal refractive index profile for a graded-index multimode glass fibre can be determined by mode field theory, where all the excited modes of the multimode glass fibre have the same group velocity along the longitudinal direction. Or in other words, the differential modal delay<sup>6</sup> is virtually eliminated. However, the ideal refractive index

---

<sup>6</sup> Differential modal delay describes the weighted arrival time differences of supported modes. Details are given in Section 2.2.4.2.

profile is found to be strongly dependant on the launching beam wavelength and fibre material properties [76]. Profile optimisation has to be carried out for specific fibre types and operating wavelengths, where the resulting profile is very sensitive to any subtle inaccuracies. However, refractive index defects are inevitably introduced during the fibre fabrication process. These defects significantly affect the optimised refractive index and consequently alter the supported mode field distribution. These supported modes no longer share an equalised group velocity and hence the modal delays disperse. Statistically, the defects are most likely to be physically induced during manufacturing close to the core centre and the transition region between the core and cladding. Perturbation on the optimised profile parameter  $\alpha$  also commonly exists in the middle region of the fibre core radius. These irregular alterations of the ideal refractive index profile break the optimised modal delay equalisation. As a result, the launched power travelling through different modes has different propagation speeds, causing the dispersion of the transmission power at the fibre output. If the modal delay is comparable to the bit period of the system, the pulse distortion will be obvious [77]. Since the modal delay gets worse as the fibre length increases, the link reach of a multimode glass fibre is therefore significantly limited. For a typical 62.5  $\mu\text{m}$  multimode glass fibre, the overfilled launch bandwidth can be as low as 500 MHz·km for 1310 nm.

Figure 2.6 illustrates several typical refractive index profiles with manufacturing defects. Region I in the core centre represents a dip or a peak of the defective refractive index. This indicates either a weakened or enhanced profile at the centre area of the core compared with the ideal case. The defect in the middle region of the fibre core radius is recognised as multiple profile parameter  $\alpha$  shown in region II. As the modal delay equalisation property of the profile closely relates to the optimised grading shape, which is defined by the profile parameter  $\alpha$ , defects in this region significantly worsen the differential modal delay performance of the fibre. Region III illustrates the boundary refractive index profile defect as a curved transition from the fibre core to the cladding.

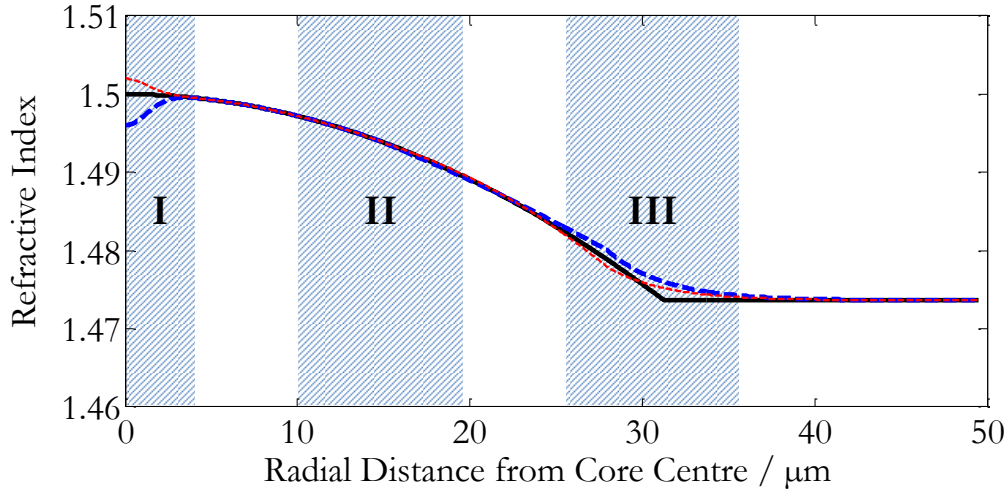


**Figure 2.6 Typical refractive index profiles with defects (red and blue). The optimal profile is shown in solid black line. Three different defective regions are shown in the shadow areas, which represent the centre defects, multiple profile parameters defects and core-cladding boundary defects respectively**

### 2.2.2. Chromatic Dispersion

Dispersion of the transmission power can also be caused by the existence of different components in the transmission light beam in terms of wavelengths. This type of dispersion is called chromatic dispersion. There are two types of chromatic dispersion in optical fibres, namely material dispersion and waveguide dispersion. The material dispersion is caused by the variation of effective refractive index with respect to different wavelengths. It has been observed that the material dispersion parameter ( $\text{ps}\cdot\text{nm}^{-1}\text{km}^{-1}$ ) reaches zero at an optimal wavelength of 1310 nm for  $\text{SiO}_2$  [78]. This is also the reason why OM1 fibres are designed to be used at this wavelength. The waveguide dispersion is caused by the variation in group velocity with respect to different wavelengths. In multimode waveguides, the waveguide dispersion is normally small and negligible in terms of the contribution to the overall dispersion characteristic [79]. Hence, given the fact that 1310 nm is the operating wavelength used for the glass fibre related work discussed in Chapter 3 in this dissertation, chromatic dispersion is assumed very small and is neglected in the numerical evaluations.

### 2.2.3. Attenuation in Multimode Glass Fibre

Attenuation or fibre loss is one of the most important factors that limit the link reach of a multimode glass fibre system. In fact, optical communication only became possible in the 1970s when the fibre loss was improved by advanced silica purification technology for fibre fabrication [12, 63]. Since the optical receiver normally requires a certain

minimum received power (i. e. sensitivity) to achieve an acceptable signal-to-noise ratio, fibre attenuation directly decides the feasibility of an optical link to meet a specific bit-error-rate requirement. Therefore, a fibre with smaller attenuation is always preferred.

Fibre attenuation is normally represented in decibels. It is defined as the power ratio between the launched beam at the input end and the received beam at the output end of the fibre, which can be written as

$$loss = 10 \log_{10} \left( \frac{P_{in}}{P_{out}} \right). \quad 2-4$$

If the fibre length is taking into account, the relationship between the powers at input and output can be expressed as

$$P_{out} = P_{in} e^{-\alpha L}, \quad 2-5$$

where  $\alpha$  is the attenuation coefficient and  $L$  is the fibre length.

In practice, dB/km is normally used to describe the attenuation of a fibre. This dB/km loss parameter can be derived from Equation 2-4 and 2-5 as

$$loss/L \text{ (dB/km)} = \frac{10}{L} \log_{10} \left( \frac{P_{in}}{P_{out}} \right) = \frac{10}{L} \log_{10} (e^{\alpha L}) = \frac{10}{\ln(10)} \alpha \approx 4.34\alpha. \quad 2-6$$

The major mechanisms contributing to fibre losses are material absorption, Rayleigh scattering and waveguide imperfections. Except for waveguide imperfections, the first two causes for fibre loss are all wavelength-dependant. The lowest attenuation window occurs in the region around 1.55  $\mu\text{m}$  for  $\text{SiO}_2$  with an attenuation parameter as low as 0.2 dB/km [80]. Another low attenuation window is at around 1.31  $\mu\text{m}$  with a worst case attenuation parameter of 1.0 dB/km [66]. Consequently, these two wavelengths have been chosen to be used for conventional optical systems and are still the most popular choices nowadays.

#### 2.2.4. Mode Field Theory for Multimode Glass Fibre

Propagation characteristics of light in a multimode glass fibre are strictly governed by the famous Maxwell's equations. The boundary condition defined by the fibre refractive index profile leads to the solutions to Maxwell's equations, which represents individual modes allowed in a multimode glass fibre. For an optical fibre, the electromagnetic fields can be expressed in cylindrical coordinates as [81]

$$\tilde{E}(r, \theta, z, t) = [E_t(r, \theta) + E_z(r, \theta)\hat{z}]e^{j(\omega t - \beta z)}, \quad 2-7$$

$$\tilde{H}(r, \theta, z, t) = [H_t(r, \theta) + H_z(r, \theta)\hat{z}]e^{j(\omega t - \beta z)}, \quad 2-8$$

where  $z$  is the longitudinal axis of the fibre and  $\hat{z}$  is the unit vector on this axis.  $E_t$  and  $H_t$  represent the transverse electric and magnetic components respectively.

The wave equations derived from Maxwell's equations can then be written as [76]

$$[\nabla^2 + k_0^2 n^2(r, \theta)][E_t(r, \theta) + E_z(r, \theta)\hat{z}] = \beta^2[E_t(r, \theta) + E_z(r, \theta)\hat{z}], \quad 2-9$$

$$[\nabla^2 + k_0^2 n^2(r, \theta)][H_t(r, \theta) + H_z(r, \theta)\hat{z}] = \beta^2[H_t(r, \theta) + H_z(r, \theta)\hat{z}], \quad 2-10$$

where  $k_0$  is the free-space wave number,  $\beta$  is the propagation constant and  $\nabla^2$  is the Laplacian operator. This set of wave equations express the electric and magnetic components separately. It can be observed that they share the equations in the exact same form. Let  $\Phi(r, \theta)$  be the scalar representation of any electric or magnetic Cartesian components. The wave equations given in Equation 2-9 and 2-10 can be re-written using one equation as

$$[\nabla^2 + k_0^2 n^2(r, \theta)]\Phi(r, \theta) = \beta^2\Phi(r, \theta). \quad 2-11$$

The fibre refractive index of a graded index multimode glass fibre is assumed longitudinally invariant in Equation 2-11. This can be further simplified since it is also axially symmetric where it is independent of  $\theta$ . Therefore, the expanded scalar wave equation can be written as

$$\frac{\partial^2 \Phi(r, \theta)}{\partial r^2} + \frac{1}{r} \frac{\partial \Phi(r, \theta)}{\partial r} + \frac{1}{r^2} \frac{\partial^2 \Phi(r, \theta)}{\partial \theta^2} + k_0^2 n^2(r) \Phi(r, \theta) = \beta^2 \Phi(r, \theta). \quad 2-12$$

Similarly, the axial symmetry can separate  $\Phi(r, \theta)$  to a product of two independent functions of radial and azimuthal variable as  $R(r)\Psi(\theta)$ . Equation 2-12 is therefore split into two separate equations as

$$\frac{d^2 R_v(r)}{dr^2} + \frac{1}{r} \frac{dR_v(r)}{dr} + \left[ k_0^2 n^2(r) - \beta^2 - \frac{\nu^2}{r^2} \right] R_v(r) = 0, \quad 2-13$$

$$\frac{d^2 \Psi_\nu(\theta)}{d\theta^2} + \nu^2 \Psi_\nu(\theta) = 0, \quad 2-14$$

where  $\nu$  is the separation constant.

With a positive integer value of  $\nu$ , Equation 2-14 gives the solution of

$$\Psi_\nu(\theta) = A \exp(-j\nu\theta), \quad 2-15$$

where  $A$  is the normalized amplitude and integer  $\nu$  is the azimuthal mode order in mode theory. To give the complete solution for Equation 2-12,  $R_\nu(r)$  has to be found. In a weakly guided scenario where the normalized refractive index difference satisfies  $\Delta \ll 1$ , analytical solutions can be found given an integer number of the profile parameter  $\alpha$  [64, 82, 83]. In practice, the profile parameter of a square-law graded-index fibre can range from 1.8 to 2.2 and defects are inevitable during the fabrication process as introduced in Section 2.2.1. No analytical solution can be found for Equation 2-13. In this case, ray optics can be used to give an asymptotical solution as [82, 83]

$$R_{\mu\nu}(r) = \exp(-jk_0 f_\mu(r)), \quad \text{2-16}$$

where  $f_\mu(r)$  is a power series function approximation of an asymptotical solution to  $R_{\mu\nu}(r)$  and  $\mu$  is the radial mode order. Together with the analytical solution to  $\Psi_\nu(\theta)$ , the final solution to the wave equation is

$$\Phi_{\mu\nu}(r, \theta) = A \exp[-jk_0 f_\mu(r) - j\nu\theta]. \quad \text{2-17}$$

$\Phi_{\mu\nu}(r, \theta)$  is the transverse mode distribution profile for any given radial and azimuthal mode order  $\mu$  and  $\nu$  respectively.

#### 2.2.4.1. Mode Groups in Multimode Glass Fibre

Solving the radial wave equation in 2-13 gives the phase constant  $\beta_{\mu\nu}$  for a particular mode of the multimode glass fibre, which is also called the propagation constant. The transmission characteristic of a fibre mode is determined by this propagation constant. Given a fibre geometry (i. e. graded-index profile), it has been shown that a group of modes sharing the same mode group number  $M$  have the same propagation constant  $\beta_M$  [84], which is defined as

$$\beta_M = n_{core} k_0 \sqrt{1 - \Delta \left(\frac{M}{M_\alpha}\right)^{\frac{\alpha}{\alpha+2}}}, \quad \text{2-18}$$

where  $M_\alpha$  is the total number of modes supported in a graded-index multimode glass fibre with profile parameter  $\alpha$ . It can be expressed as [85]

$$\begin{aligned}
 M_\alpha &= \frac{\alpha}{2(\alpha + 2)} \left( \frac{2\pi a}{\lambda_0} \right)^2 (n_{core}^2 - n_{clad}^2) \\
 &= \frac{\Delta\alpha}{2(\alpha + 2)} a^2 k_0^2 n_{core}^2
 \end{aligned}
 \tag{2-19}$$

The mode group number  $M$  in Equation 2-18 is defined as [77]

$$M = 2\mu + \nu + 1. \tag{2-20}$$

It can be understood from Equation 2-20 that for a given mode group number  $M$ , any mode in a graded-index fibre of order  $\mu$  and  $\nu$  satisfying this relationship belongs to the same group and shares the same propagation constant. Consequently, the modes belonging to this group travel with the same group velocity, which gives negligible differential modal delay. Therefore, the modal dispersion can be considered solely dependent on the differential modal delay between different mode groups. Figure 2.7 illustrates the mode profiles for mode group 3 to 8 (the first 6 mode groups with the lowest orders). The mode group number is labelled below each profile. The circular area of each profile represents a 62.5  $\mu\text{m}$  multimode glass fibre core size. It can be seen that the azimuthal order  $\nu$  decides the number of separations ‘cut’ by the diameter axes of the fibre cross section and the radial order  $\mu$  indicates the number of radial layers in the profile. Therefore, given a specific azimuthal and radial order combination, the mode profile distribution can be roughly visualised.

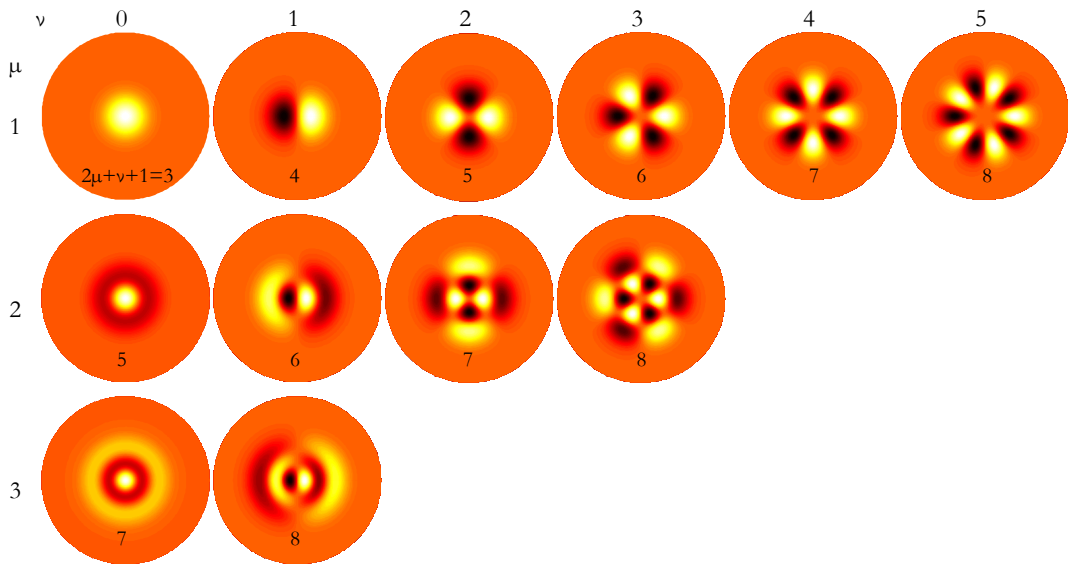


**Figure 2.7** Mode field distributions for modes in mode group 3 to 8 for a 62.5  $\mu\text{m}$  core multimode glass fibre. The circular areas represent the core areas of the fibres

### 2.2.4.2. Intermodal Dispersion and Differential Modal Delay

Intermodal dispersion is the main cause of the bandwidth limitation of a multimode glass fibre. Although an ideal graded-index fibre theoretically equalises the arrival times at the fibre output for different mode groups, differences in mode group delays exist in practical fibres since refractive index defects are inevitable. These delays cause dispersed arrival times of the energy propagating through different mode groups. Due to this effect, the initial launched optical pulse will be spread in time. This effect is called the pulse broadening effect and is a major cause of the signal distortion in a multimode glass fibre link. The group delay is defined as the propagation time per unit length and is given as the first order derivative of the propagation constant given in Equation 2-18 with respect to the angular frequency  $\omega$  as [76]

$$\tau_{group,M} = \frac{d\beta_M(\omega)}{d\omega}, \quad 2-21$$

where  $M$  is the mode group number. This group delay represents the time needed for the light in mode group  $M$  to travel through a unit length of the fibre. Imagining that an optical impulse (i.e. Dirac pulse) is propagating through a particular mode group, the received pulse at the fibre position  $z$  along the fibre can be expressed as

$$h_M(z, t, \omega) = \delta[t - z\tau_{group,M}(\omega)], \quad 2-22$$

where  $\delta(t)$  is the launched impulse. In practice, the launched optical impulse will excite different mode groups in the multimode glass fibre depending on the injecting beam profile. The launched beam power distribution over the excited modes can be decided by calculating the overlap integral between the launched beam profile and the supported modes. The power coefficients of each mode and mode group can be written as

$$\sum_{M=3}^{M_{\max}} C_M = \sum_{\mu=1}^{\mu_{\max}} \sum_{\nu=0}^{\nu_{\max}} C_{\mu\nu} = 1, \quad 2-23$$

where  $C_M$  and  $C_{\mu\nu}$  are the normalized power percentages of mode groups and individual modes respectively. Therefore, assuming the power combination of different modes are linear, the overall impulse response of the multimode glass fibre can be described using the following equation

$$h_{fibre}(z, t, \omega) = \sum_{M=3}^{M_{\max}} C_M \delta[t - z\tau_{group,M}(\omega)]. \quad 2-24$$

The mode group number  $M$  starts from 3 because the minimum radial order  $\mu$  and azimuthal order  $\nu$  are 1 and 0 respectively, which gives the lowest mode group number as  $2\mu + \nu + 1 = 3$ .

Another important parameter to quantize the mode group delay characteristic is the differential modal delay (DMD) factor. In order to define the differential modal delay, an average group delay needs to be found using

$$\tau_{average}(\omega) = \sum_{M=3}^{M_{max}} C_M \tau_{group,M}(\omega). \quad 2-25$$

This average group delay indicates the weighted mean group delay under specific mode group power distribution condition. Similarly to the definition of standard deviation in statistics, the differential modal delay is defined as

$$DMD = \sqrt{\sum_{M=3}^{M_{max}} C_M [\tau_{group,M} - \tau_{average}]^2}. \quad 2-26$$

In other words, differential modal delay is the standard deviation of the mode group delay time constants (ns/km). A large differential modal delay implies that group velocities of the excited mode groups are widely spread. Meanwhile, a small differential modal delay indicates that the excited mode groups all have similar propagation constants. Consequently, according to Equation 2-22, the launched optical impulse will be dispersed widely over time if the differential modal delay is large. Meanwhile, the pulse broadening effect is severe and the fibre bandwidth is significantly limited.

### 2.2.5. Multimode Glass Fibre Standards

The graded-index multimode glass fibre has four generations of industrial standards, namely OM1, OM2, OM3 and OM4 fibres with increasing targeted bandwidth-distance products. Except for the 62.5/125  $\mu\text{m}$  core/cladding diameter OM1 fibres, all of the other three standards characterize the fibres with 50 / 125  $\mu\text{m}$  core/cladding diameter.

OM2 fibres are widely implemented in today's local area network and data centre environments in combination with VCSELs operating at a wavelength of 850 nm for 10 Gbit/s applications. The reach at this speed is 150 m for OM2 fibre and can be extended to 300 m and 550 m using OM3 and OM4 fibres respectively. The in-building applications mostly fall in these link ranges and OM2 fibre is most popular for its low implementation cost.

For the newly published 40 GbE and 100 GbE standards, OM3 and OM4 can support link reaches up to 100 m and 150 m respectively. OM1 and OM2 are no longer supported for these data rates due to insufficient link budget. Since the 10 GbE devices will be gradually replaced by 40 GbE and 100 GbE devices. It has been recommended to industrial ventures that OM3 and OM4 should be used for all new installations.

Nevertheless, due to decades of popular implementation, the total volume of the installed OM1 fibres is still very large. This number is expected to be caught up by the more advanced 50  $\mu\text{m}$  fibres but only gradually due to the high cost for replacement. The so called 'legacy fibres', which refer to the installed OM1 fibres are the main bandwidth/reach bottleneck for most of the existing multimode glass fibre systems. Consequently, approaches for bandwidth improvement of these fibres are becoming increasingly attractive for researchers.

### 2.3. PMMA-based Step-Index Plastic Optical Fibre

Nowadays, the PMMA (Polymethylmethacrylate) based SI-POF has been improved to have a bandwidth of 200 MHz for a reach of 50 m whilst keeping a simple structure and fabrication process [75]. Thus, for the first time, the SI-POF becomes an attractive and reliable transmission medium for high speed and short distance applications. Table 2-1 illustrates the comparison between the copper cable (RG-6), SI-POF, multimode glass fibre and single mode fibre.

**Table 2-1 Comparison between RG-6, SI-POF, MMF and SMF [40]**

|                     | <b>RG-6</b> | <b>SI-POF</b> | <b>MMF</b>       | <b>SMF</b>      |
|---------------------|-------------|---------------|------------------|-----------------|
| Core material       | Copper      | PMMA          | Glass            | Glass           |
| Core diameter       | 1 mm        | 0.98 mm       | 50 $\mu\text{m}$ | 9 $\mu\text{m}$ |
| Jacket diameter     | 8.4 mm      | 2.2 mm        | 2.5 mm           | 2.5 mm          |
| Weight              | 40 g/m      | 4 g/m         | 5.1 g/m          | 5.1 g/m         |
| Min bending radius  | >20 cm      | 2.5 cm        | 5 cm             | 5 cm            |
| Bandwidth           | 7 MHz·km    | 10 MHz·km     | 1 GHz·km         | >5 GHz·km       |
| Jacketed cable cost | 60 p/m      | 30 p/m        | 18 p/m           | 24 p/m          |

The SI-POF comes with a core size of 1 mm and a cable diameter of 2.2 mm, which is the smallest among all the listed transmission media. This provides relaxed alignment requirement and easy installation compared with either multimode or single mode glass fibres. Unlike the glass fibres, no polishing is needed for cutting and connecting SI-POFs in optical links. This enables potential DIY installations which dramatically reduce the implementation cost. The smaller cable diameter and the comparative elastic material also enable a smaller banding radius which makes the SI-POF preferable for wiring in environments when large number of bends are expected such as home and vehicle networks. In addition, the resistance to water, acid and oil makes SI-POF a robust transmission medium under challenging environments.

#### 2.3.1. Structure of SI-POF

The most commonly seen SI-POF has a core size of 980  $\mu\text{m}$  in diameter covered with a cladding layer with a thickness of 10  $\mu\text{m}$ . This gives the total fibre diameter of 1 mm. The core size is  $\sim 100\text{x}$  larger (in radius) than the single mode glass fibre and  $\sim 15\text{x}$  larger than

the OM1 multimode glass fibre. The structure and refractive index profile of a 1 mm SI-POF are shown in Figure 2.8.

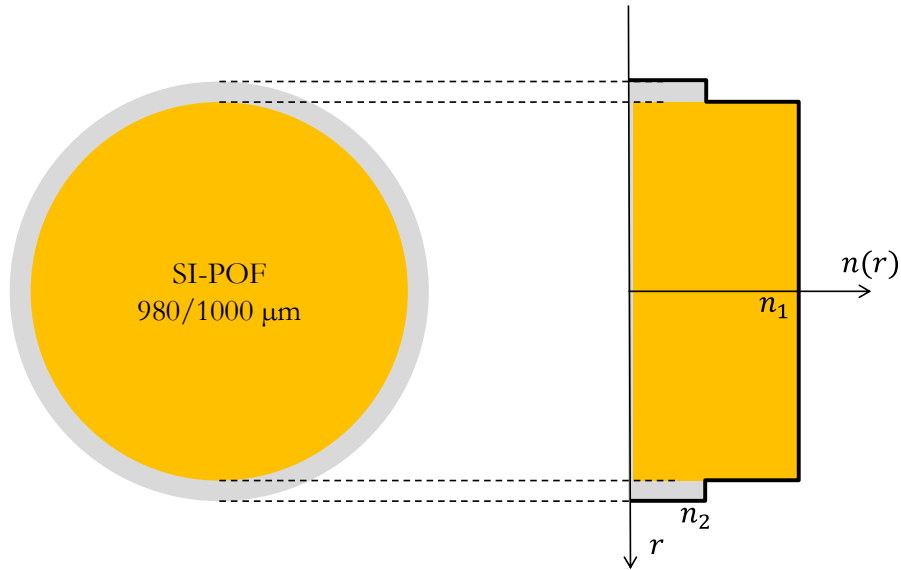


**Figure 2.8** The structure of a 1 mm SI-POF

The step-index profile can be expressed with the profile parameter  $\alpha$  approaching infinity in Equation 2-1 as

$$n(r) = \begin{cases} n_{core} & r < a \\ n_{cladding} & r \geq a \end{cases} \quad 2-27$$

The large core size of SI-POF enables easy handling and connection. Meanwhile, the launching beam is allowed to have a larger angle of incidence. The numerical aperture of a standard SI-POF is  $\sim 0.5$ , which indicates an acceptance angle of  $60^\circ$ .

### 2.3.2. Attenuation in Plastic Optical Fibre

Figure 2.9 illustrates the attenuation rates of the SI-POF against operating wavelength in comparison with glass fibre. The attenuation curve of SI-POF is caused by the absorption spectrum of the PMMA material. It can be seen that the windows for transmission with least attenuation are around 520 nm (blue), 570 nm (green) and 650 nm (red). This implies that the visible light range can be used in SI-POF links. It is obviously seen in Figure 2.9 that even in the best scenario, SI-POF has an attenuation rate of  $\sim 90$  dB/km. This is several hundreds of times higher than that of a glass fibre. Therefore, SI-POF is limited for applications in very short range links typically less than 100 m.

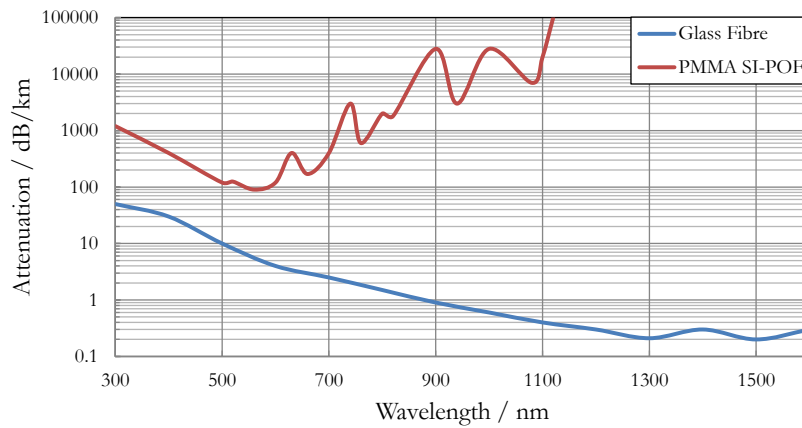


**Figure 2.9 Comparison of the attenuation rates between the PMMA SI-POF and glass fibre against wavelength [86]**

### 2.3.3. Bandwidth Limitation of Plastic Optical Fibre

It is not hard to imagine that such a large core size will allow an immense number of modes supported in a SI-POF. In Section 2.2.4.2, it has been seen that the differential modal delay is a significant factor to measure the bandwidth performance of a multimode waveguide. Typically, SI-POF supports thousands of different optical modes, which leads to a large differential modal delay. The -3 dBo (the optical intensity is degraded to half) bandwidth-distance product for a SI-POF can be as low as 2 MHz·km [87]. Consequently, consistent with the low cost concept, an LED transmitter is normally used for SI-POF links because of its matched bandwidth performance and capability of mass production with reasonable cost. However, with the more advanced fibre developed with a bandwidth-distance product beyond 10 MHz·km [75], SI-POF has shown great potential for the next generation short distance high speed applications over 1 Gbit/s.

### 2.3.4. Plastic Optical Fibre Standards

SI-POF has been standardised in IEC 60793-2-40 as listed in Table 2-2. The core diameter is not specified for the reason of providing more flexibility for the manufacturers. However the most common SI-POF is with 980  $\mu\text{m}$  core diameter. The bandwidths shown in Table 2-2 are very pessimistic as SI-POFs with bandwidths much higher than 1 MHz·km are readily available with reasonable cost [75]. It can be seen that the Class A4a fibre gives the largest total diameter which allows the maximum alignment tolerance. This is also the most widely used SI-POFs in various applications such as the MOST for in-car multimedia network. Therefore, the Class A4a SI-POF is chosen for this dissertation to provide the most cost-effective high speed POF network solutions.

Table 2-2 List of SI-POF standards specified in IEC 60793-2-40

|                       | Unit                 | Class A4a     | Class A4b     | Class A4c     |
|-----------------------|----------------------|---------------|---------------|---------------|
| Core diameter         | $\mu\text{m}$        | N/A           | N/A           | N/A           |
| Total diameter        | $\mu\text{m}$        | $1000\pm60$   | $750\pm45$    | $500\pm30$    |
| Jacket diameter       | mm                   | $2.2\pm1.0$   | $2.2\pm1.0$   | $1.5\pm1.0$   |
| Attenuation at 650 nm | dB <sub>o</sub> / km | $\leq 400$    | $\leq 400$    | $\leq 400$    |
| Bandwidth             | MHz·km               | $\geq 1$      | $\geq 1$      | $\geq 1$      |
| Numerical aperture    | N/A                  | $0.50\pm0.15$ | $0.50\pm0.15$ | $0.50\pm0.15$ |

## 2.4. Conclusions

This Chapter introduces the most commonly used multimode waveguides, namely multimode glass fibre and PMMA-based SI-POF. The basic optical transmission concept in multimode waveguide is reviewed based on ray optics. It has been seen that the propagation characteristic is closely related to the fibre refractive index profile. Two popular index profiles, namely step index and graded index profiles are discussed.

Due to the fabrication imperfections, refractive index defects are inevitable introduced to graded-index multimode glass fibres in practice. It has been shown that three major defects that most likely to exist in a multimode glass fibre are centre defects, multiple profile parameters and core-cladding boundary defects. These defects are believed to be the main causes of the bandwidth degradation of the multimode glass fibre. To understand the electromagnetic transmission properties in multimode glass fibre, mode theory is introduced for graded index multimode glass fibre. Numerical solutions based on scalar wave equation are given for individual modes supported in a square-law graded-index multimode glass fibre. These modes can be grouped into mode groups with negligible propagation constant differences. The differential modal delay is introduced based on the mode power distribution concept and the theoretical model for impulse response of a multimode glass fibre is given.

The large core size structure of the PMMA-based SI-POF enables easy handling and connection, which makes it a strong transmission medium candidate for mass-user network environments. Attenuation of the SI-POF is the major contributor to the power penalty in a successful link and the preferred low loss operating windows fall in the visible light range. The bandwidth of the SI-POF is very limited due to the large number of allowed modes which lead to large differential modal delay. However, this bandwidth is sufficient for next generation high speed applications in consumer networks such as in home and vehicle. Several industry standards for SI-POFs are listed and the Class A4a fibre is chosen for this dissertation due to its relaxed alignment requirement and mature commercialisation.

# CHAPTER

# 3

## LOW-LOSS HERMITE-GAUSSIAN LAUNCH FOR BANDWIDTH IMPROVEMENT OF MULTIMODE GLASS FIBRE

*This chapter reports a novel optical launch scheme, namely low-loss Hermite-Gaussian launch, for multimode glass fibre links, which enables significant effective modal bandwidth improvement with improved coupling efficiency compared with the conventional line launch scheme. In this launch scheme, a beam with specific field distribution is launched at the core of a multimode glass fibre, and exclusively excites a particular mode group, hence virtually eliminating intermodal dispersion. Detailed numerical studies of various versions of the proposed launch are carried out using a worst case fibre model, which represents the most challenging 5% fibres in the OM1 installed base. Theoretical studies show that the proposed low-loss launch schemes achieve selective single mode group excitation. Significant effective modal bandwidth improvement is shown in comparison with conventional centre and offset launches. Low-loss launch implementation is discussed based on a matched-profile intensity and phase beam shaping mask. Optimisation of the launching beam generation using such masks guarantees high quality of single mode group excitation whilst maintaining a low coupling loss at least 2.5 dB better than the conventional line launch scheme. Discussions concerning the limitations of the proposed launch schemes reveal that the single mode group excitation is relatively stable even with fibres with index defects or with launching misalignment. Experimental studies based on the optimised launching beam generation approach are also carried out confirming the robustness of the proposed low-loss Hermite-Gaussian launch scheme.*

### 3.1. Introduction to Launch Schemes for Multimode Glass Fibre

Multimode glass fibre, or simply multimode fibre (MMF), has been widely installed within buildings since it was originally for optical communication systems over short ranges. In the early 1990s, LEDs were the main optical sources for these systems when the operating data rates were in the range from few Mbit/s to a maximum of few hundreds of Mbit/s. Overfilled launch (OFL), where a comparatively large LED emitted light spot exciting all allowed modes in a multimode glass fibre, was the traditional launch scheme used in multimode systems. Meanwhile, OFL was also regarded as the conventional method to characterize the modal bandwidth of multimode glass fibres. Multimode glass fibres have since continued to be used in short reach communication systems, for example in-building networks and local area networks (LANs), owing to the low installation cost. It was reported in late 1990s that 90-95% installed data communication networks were over multimode glass fibres and these links were dominantly based on LED transmitters [88]. The more expensive high speed links based on laser transmitters and single mode fibres were only implemented for relatively dedicated long haul networks.

As the requirement for higher speed by end users continued to rapidly increase, researchers were looking for solutions to low cost laser-based systems for gigabit/s Ethernet in the late 1990s. These systems were proposed as an upgrade of the 100 Mbit/s Fast Ethernet optical links. Therefore, it was ideal that such solutions could be directly implemented over installed fibre cables, which were predominantly multimode glass fibres. The Gigabit Ethernet standard [27] targeted 1 gigabit/s transmissions over a distance of 500 m. Unfortunately, a significant reduction of specified bandwidth of the multimode glass fibre was found in laboratory trial using laser transmitter and 62.5  $\mu\text{m}$  fibre [88]. This reduction occurred when the fibres with relatively severe refractive index defects were used. The rather small laser output spot tended to couple the majority of the launched power to lower order mode groups which were more dispersive due to the defective centre area. The previous accepted OFL bandwidths of multimode glass fibres were no longer convincing indicators of the performances of laser-based links. Therefore, the Gigabit Ethernet study group identified differential modal delay as the parameter to predict the bandwidth performance of a multimode glass fibre. During the discussion of the Gigabit Ethernet proposals, it was found that some of the tested multimode glass fibres had effective modal bandwidths (EMB) lower than the OFL bandwidth specification with the laser beam launched at the centre [89]. Although efforts had been

made to enable high data rate transmission over multimode glass fibre using the centre launch technique [44], it was not feasible to provide sufficient bandwidth for the worst case installed fibres, mainly due to the critical alignment requirement and the refractive index defects introduced in Section 2.2.1. Considering the cost and feasibility of upgrading existing multimode glass fibre systems, it was commonly agreed that introducing novel launch scheme had the greatest potential to reduce the differential modal delay and extend the reach or improve the fibre effective modal bandwidth. To address this problem, a mode conditioning launch scheme was developed, targeted at achieving the OFL bandwidth for 99% of the installed fibres as required by the Gigabit Ethernet standard [90]. This mode conditioning launch, namely offset launch, specified a radial offset of 17-23  $\mu\text{m}$  and 10-16  $\mu\text{m}$  for OM1 and OM2 fibres between the launching beam and fibre core respectively. It excited a range of mid-order mode groups of the multimode glass fibre, which tended to be less affected by the index defects and had a relatively uniformly distributed propagation velocities. Therefore, the differential modal delay was controlled within a reasonable range and a minimum bandwidth better than the OFL was guaranteed even for the worst case fibres. The development of offset launch directly contributed to the publication of IEEE802.3z Gigabit Ethernet standard in 1998.

The demands for even higher data rate in optical systems dramatically increase in the 21<sup>st</sup> century as the multi-media industry over Internet becomes more and more mature. Services like video streaming and file sharing make the upgrades of existing networks even more demanding than the era of gigabit Ethernet. Although advanced multimode glass fibres have been developed to provide higher bandwidth, the installation cost continued to set the greatest barrier for the industry to replacing the existing 'legacy' fibres. Therefore, seeking for a cost-effective solution to improve the bandwidth of the existing multimode glass fibres, yet again, drew intensive attention of researchers. Thanks to the development of electrical dispersion compensation (EDC) technology, the overall system bandwidth of a multimode glass fibre link has been greatly improved. 10 Gbit/s transmission was enabled and standardised in the 10GBASE-LRM task force for a reach of 220 m at 1310 nm for OM1 fibres. This standard also specified dual launch, which required manual testing between direct launch (centre launch) and mode conditioning launch (offset launch) to find the preferred configuration.

In the last decade, besides the development of successive generations of multimode glass fibres with higher bandwidths (i.e. OM3 and OM4), more advanced solutions related to

mode conditioning launch including adaptive launch [91, 92] and twin-spot launch [93] have also been studied to provide alternative solutions. However, none of these schemes fully recovered the multimode glass fibre bandwidth degradation as a result of the fundamental limitation of intermodal dispersion. Not until 2010, was the line launch proposed to provide significant improvement of multimode glass fibre bandwidth [45] by enabling near single mode group operation of the fibre. However, the proposed line launch had low coupling efficiency which introduces 6.8 dB insertion loss [94].

This chapter proposes improved solutions to the problem of enhancing the multimode fibre bandwidth with a simple low cost and low loss launch scheme. The overall coupling loss of the proposed schemes is significantly lower than the proposed line launch approach whilst the multimode glass fibre bandwidth improvement is kept comparable. Similarly to the line launch approach, these solutions are based on a phase and intensity modified Hermite-Gaussian optical beam launched at the transmitter end with a specific transverse electric field profile. Each of these profiles selectively excites a single matching mode group of the multimode glass fibre, where the rest of the mode groups have modal distributions orthogonal to the launching beam profile. As a result, the differential modal dispersion is kept small since the majority of the launched power is injected into the targeted mode group, within which modes tend to propagate through the fibre with negligible velocity differences [95]. Hence, the multimode glass fibre achieves an improved bandwidth. On the launch scheme coupling efficiency side, one solution makes use of the optics design to generate an elliptical-shaped Gaussian beam to match with line launch profile. The other solution extends the Hermite-Gaussian beam profile order to the vertical direction, where the launching beam profiles with rounded-square shapes are used. Both approaches significantly increase the percentage of the area that overlaps with the outline of the launching profiles. Hence the coupling losses of these launches are improved. At the same time, both launches achieve 10 Gbit/s transmissions over a worst case fibre without the use of equalisers.

### **3.1.1. Overfilled Launch**

OFL is typically regarded as the standard approach for the multimode glass fibre bandwidth measurement [96]. In practice, the overfilled launch is approximately equivalent to a LED-based optical launch, where a comparatively large and incoherent LED spot is launched to a multimode glass fibre. Since the launching spot is large enough to cover the area of the fibre core, the fibre is naturally ‘filled’ with propagating

light. With the OFL, the power of all excited modes of the multimode glass fibre are approximately the same [97]. Figure 3.1 illustrates a multimode glass fibre under the OFL condition with an LED illuminating the entire core. Since the launched power is evenly distributed between a large number of supported modes, the differential modal delay under OFL, though large, is rather stable with respect to index defects. Nevertheless, the effective modal bandwidth of the multimode glass fibre under OFL is significantly limited by the intermodal dispersion caused by the large differential modal delay. Table 3-1 shows the worst case modal bandwidths of OM1 and OM2 fibres referred by the IEEE gigabit Ethernet standard committee under OFL condition [43]. It can be seen that the modal bandwidth of an OM1 fibre can be as low as  $160 \text{ MHz}\cdot\text{km}$  at 850 nm.

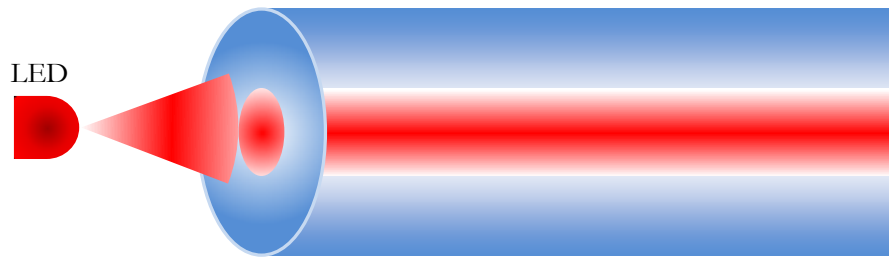


Figure 3.1 Multimode glass fibre illuminated by an LED under the OFL condition

Table 3-1 Minimum modal bandwidths of OM1 and OM2 fibres

|  | OM1 (62.5 $\mu\text{m}$ /125 $\mu\text{m}$ ,<br>core/cladding diameter) |      | OM2 (50 $\mu\text{m}$ /125 $\mu\text{m}$<br>core/cladding diameter) |      |
|--|---|------|---|------|
| Wavelength (nm)                                | 850   | 1310 | 850   | 1310 |
| Bandwidth<br>Distance Product<br>(MHz·km, OFL) | 160   | 500  | 400   | 400  |

### 3.1.2. Centre Launch

As lasers started to be widely implemented in multimode glass fibre systems, it was seen that the effective modal bandwidth of a fibre under direct laser launch condition can be either higher or lower than the minimum bandwidth characterized by OFL [88]. In contrast with the LED, the laser provides a much smaller and coherent launching beam. If the laser spot is launched to the multimode glass fibre at the core centre (i.e. centre launch), the fibre will only be filled in the centre area as seen in Figure 3.2. In other words, only a few supported mode groups will be excited. For most of the fibres which have nearly ideal index profiles, this results in very small differential modal delays, which provides high effective modal bandwidths. However, refractive index profile defects

inevitably exist in the multimode glass fibre as introduced in Section 2.2.1. Since the launched power is substantially distributed in the centre area, the centre launch is particularly vulnerable to centre defects, which introduces very high differential modal delay among low order modes. The effective modal bandwidths under centre launch condition are found even lower than the specified OFL bandwidth for fibres with defective centre areas.

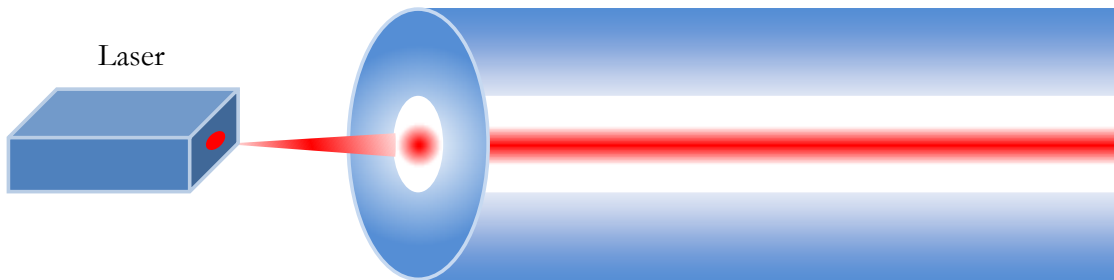


**Figure 3.2 Multimode glass fibre illuminated by a laser under the centre launch condition**

Figure 3.3 illustrates the typical impulse responses and corresponding frequency responses of a multimode glass fibre with centre defects under the OFL and centre launch conditions. It can be seen that the OFL launch achieves smooth impulse and frequency responses whilst the centre launch introduces dips in both responses. These dips imply that the launched power is distributed to two major propagating mode groups which have a large difference in modal delays. This results in the separation of arrival times at the fibre output end. Compared with OFL, this effect dramatically decreases the effective modal bandwidth of the multimode glass fibre under centre launch. Though efforts have been made to increase the effective modal bandwidth of multimode glass fibre under centre launch condition [44], the fact that its performance is strongly dependant on individual fibre profiles makes it not feasible as a single solution to high speed multimode glass fibre links. Although centre launch works fine for most of the OM1 fibres, the bandwidths are lower than the OFL bandwidth for those with severe index defects ( $\sim 20\%$  of the installed base) [98]. Therefore, in the 10GBASE-LRM standard, a dual launch scheme requiring manual testing between the centre and offset launches is suggested to guarantee the necessary effective modal bandwidth of the multimode glass fibre to achieve a successful link [28].

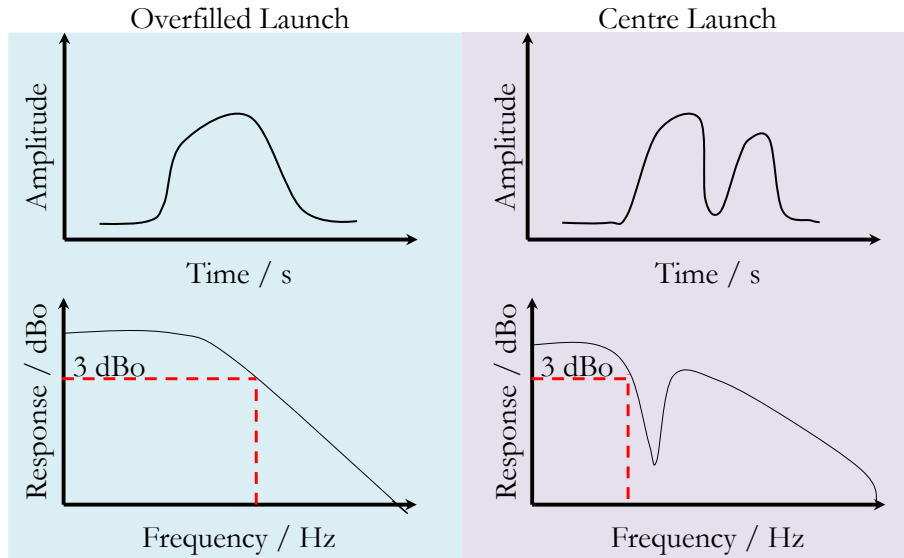


**Figure 3.3** Schematic impulse responses and frequency responses of a multimode glass fibre with centre defects under the overfilled launch and centre launch conditions

### 3.1.3. Offset Launch

Offset launch specifies a radial offset at launch between the fibre core centre and the injecting beam. It has been shown that such a radial offset excites a subset of all the mode groups supported by multimode glass fibres [26, 99]. Since only a selective range of mode groups are excited, the deviation of modal delays among these mode groups is reduced. Therefore in general the differential modal delay of the offset launch is smaller compared with that of the OFL, which enables higher bandwidth. Simulation results show that the excited mode groups are in the mid-order range for an offset launch implementation [99]. These mode groups tend to have more sub-modes than the lower order mode groups. Therefore, a large number of modes are still excited under offset launch condition, which provides good immunity to modal noise despite decreased dispersion [43].

Figure 3.4 shows the schematic diagram of an offset launching spot applied to OM1 and OM2 fibres. The specified radial offsets for OM1 and OM2 fibres are 17-23  $\mu\text{m}$  and 10-16  $\mu\text{m}$  respectively [89]. Theoretical results have shown that these offsets ensure that at least 99% of the installed fibres can achieve the minimum OFL bandwidth [99]. The benefit of the offset launch over the OFL is insignificant for fibres with nearly ideal index profiles since the modal delays are well equalised. However, fibres with non-ideal profiles are guaranteed with improvement from using the offset launch. This is more essential than improving the bandwidths of the fibres which are already considered good, as the worst case fibres are the bottleneck of any proposed systems.

The development of the offset launch guarantees the bandwidth performance of the worst case fibres and directly enables the gigabit Ethernet standard with an extended reach [90]. A practical implementation of the offset launch is shown in Figure 3.5 as a transceiver link patchcord for 1000BASE and 10GBASE Ethernet. Single mode fibre is used to generate the launching spot and a radial offset is realized by using an offset fusion splice. This implementation minimizes the misalignment problem at the offset launching point compared with other approaches like an offset connector [76]. For a full duplex link, two of these patchcords should be used at both transceiver ends.

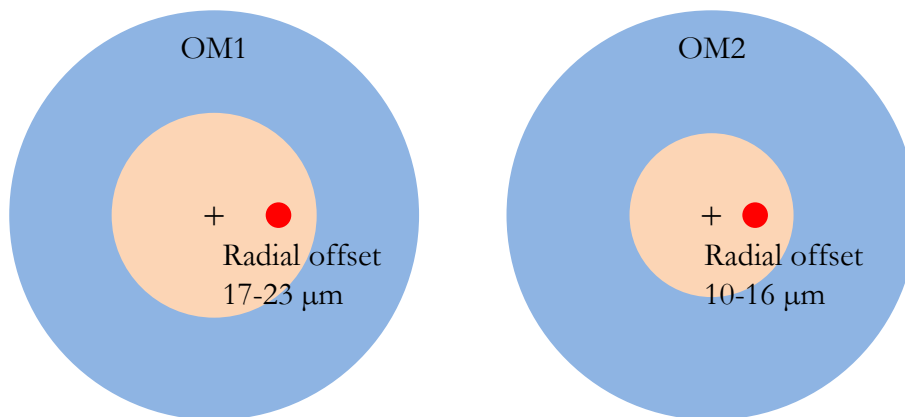


Figure 3.4 Schematic diagram of the offset launch implementations over OM1 (left) and OM2 (right) multimode glass fibres

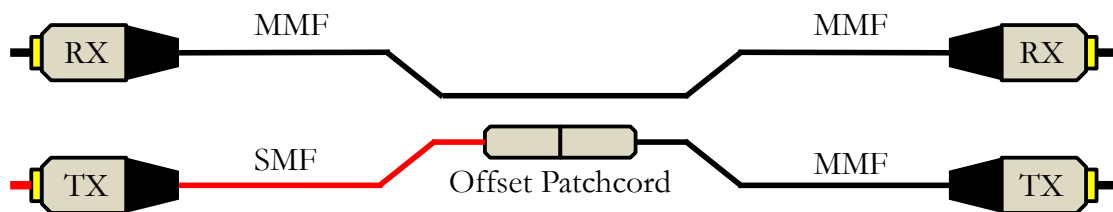


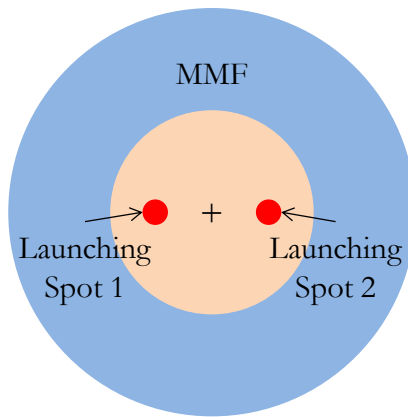
Figure 3.5 The offset launch transceiver patchcord cable for Gigabit Ethernet

#### 3.1.4. Dual Launch

Dual launch itself is not a new launch scheme. Instead, it specifies a procedure during the installation of systems based on the 10GBASE-LRM standard. In this procedure, it is required that one should test the centre launch and offset launch at both ends of the link and choose the scheme that works better. This essentially guarantees that the multimode glass fibres in a 10GBASE-LRM system are always under a preferred launching condition. However, the manual testing makes the installation more complex and costly. Therefore, it is very attractive if a single launch can be developed to achieve the same link yield as the dual launch and provide a simple and robust solution to 10GBASE-LRM systems.

### 3.1.5. Twin-spot Launch

Inspired by the offset launch, a launch scheme using two spots with symmetric radial offsets to the fibre core was developed [93]. This technique, using two anti-phase or in-phase Gaussian spots aligned symmetrically on the radial axis of the fibre with the same radial offset, excites two sets of modes with the same power distribution. Destructive interferences are formed for odd/even order modes if anti/in-phase spots are used. Therefore only those modes with constructive interferences remain. It is shown that only one mode group exists in the multimode glass fibre under the twin-spot launch condition if the offset is optimised [100]. The single mode group excitation avoids multiple peaks in received pulse caused by the large differential modal delay. Consequently, the effective modal bandwidth of a multimode glass fibre under this launch is improved.



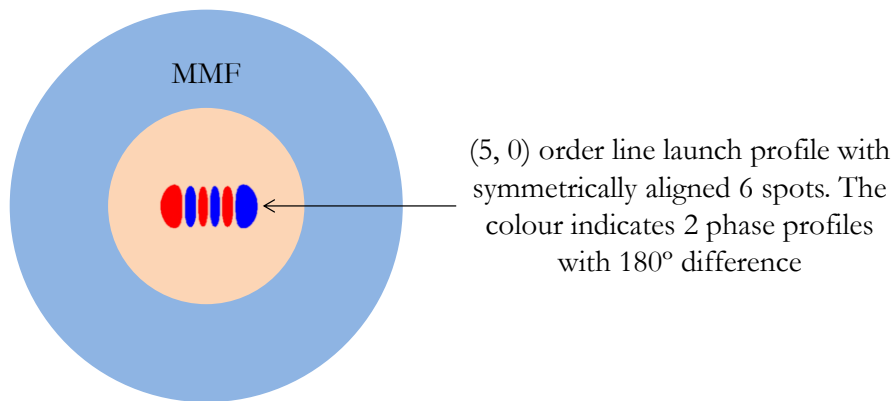
**Figure 3.6 Schematic diagram of the twin-spot launch**

Figure 3.6 shows the schematic diagram of a twin-spot launch using two in-phase spots. The spots are aligned on the radial axis of fibre core. The distance between the core centre and the launching spots is adjustable according to the overall bandwidth performance of the multimode glass fibre. An optimum offset of  $\pm 5 \mu\text{m}$  has been demonstrated to achieve near single mode group excitation and minimized dispersion penalty<sup>7</sup> [93]. The fact that two separate spots need to be aligned with exact radial offset on the same radius axis is very challenging in practice. And this also requires an additional laser source to be used in the link. Hence, the twin-spot launch scheme is rarely used in practice. However, this technique drew the attention of researchers to consider launch schemes using advanced beam profiles to achieve selective single mode group excitation for potential bandwidth improvement over multimode glass fibres.

<sup>7</sup> This represents a  $5 \mu\text{m}$  offset for both spots on either side of the core.

### 3.1.6. Line Launch

Inspired by the idea of only exciting a single mode group of a multimode glass fibre, a line launch scheme was reported in 2010 [45]. The intermodal dispersion is minimized in this technique, providing improved differential modal delay in a multimode glass fibre link. Similarly to the twin-spot launch scheme, the line launch is implemented by projecting a line of spots onto the multimode glass fibre aligned with the radial axis. These spots create a Hermite-Gaussian profile, which has an overall transverse electric field distribution that only excites one specific mode group.



**Figure 3.7 Schematic diagram of the line launch scheme with a (5, 0) order Hermite-Gaussian profile**

As shown in Figure 3.7, a (5, 0) order line launch profile is applied onto a multimode glass fibre. This profile consists of six spots symmetrically aligned along the radial axis. The spot pairs with the same radial offset from the core centre have the same intensity profile and inverted phase profiles. Unwanted mode groups are suppressed with near zero launched power so that the dispersion between mode groups is minimized. A 10 Gbit/s transmission over 220 m OM1 fibre without electrical dispersion compensation has been demonstrated using this technique [45]. The implementation of the link introduces a high coupling loss of 6.8 dB because large amount of the laser output power is blocked by the beam shaping mask used for launching beam generation [94]. Though the line launch achieves 10 Gbit/s transmission over the suggested length of 220 m OM1 fibre as specified in the 10GBASE-LRM standard, the extra power budget requirement introduced by the coupling loss dramatically challenges the reliability of the system. Therefore, the problem of finding a low-loss launch scheme with comparable bandwidth improvement as line launch remains to be investigated.

### 3.2. Theoretical Modelling of Low-loss Hermite-Gaussian Launch

This section reports two versions of the low-loss Hermite-Gaussian launch scheme which provides low coupling loss and high bandwidth improvement over multimode glass fibre links. Similar to the line launch scheme introduced in Section 3.1.6, these low-loss Hermite-Gaussian launches use phase-modulated launching patterns, which are chosen so that only one mode group of the multimode glass fibre is excited. By suppressing the unwanted neighbouring mode groups, near single mode group operation is achieved which minimizes the intermodal dispersion. Hence, an enhanced bandwidth performance is achieved. In these launches, the low-loss property is achieved by using novel implementations for the Hermite-Gaussian beam generation, which essentially reduces the coupling loss compared with the conventional line launch [45]. This is achieved using matched incident Gaussian beams and Hermite-Gaussian profiles at the beam-generation mask<sup>8</sup>. In order to fulfil this requirement, the proposed two launch versions either use an incident beam with a designed shape or novel launch profiles with preferred outlines to improve the matching between each other. In this way, high coupling efficiency is achieved whilst the bandwidth enhancement is also maintained.

In particular, one proposed scheme, namely low-loss Hermite-Gaussian line launch scheme, relies closely on the  $(5, 0)$  order line launch profile. An elliptical-shaped incident Gaussian beam is used in this scheme to match with the outline shape of the line launch profile. The other proposed scheme, namely low-loss Hermite-Gaussian square launch, extends the line launch profiles to two dimensions. Several rounded-square-shaped Hermite-Gaussian profiles are chosen so that their outlines match with circular Gaussian beams. Both schemes reduce the coupling loss at the launching beam generation stage.

The principles of the low-loss Hermite-Gaussian launches are reviewed in this section. It is demonstrated that Hermite-Gaussian beams are orthogonal to all linear polarised modes of the multimode glass fibre except for a set of modes belonging to a specific mode group. This is numerically proved and the relationship between the order of a Hermite-Gaussian launching beam and the order of an excited mode group is derived.

To evaluate the launch scheme performance, the concepts of mode group power distribution and extinction ratio are introduced. Theoretical modelling of the launches is given based on a set of worst case fibre profiles. Since the proposed launching beam

---

<sup>8</sup> The details of the beam generation mask are given in Section 3.2.3.

profiles are not able to be ideally generated in practice, simulation results are also given for launches using approximated Hermite-Gaussian beams. Approaches to the generation of these beams are discussed and the limitations of the proposed schemes are also reviewed.

### 3.2.1. Principles of the Low-loss Hermite-Gaussian Launch

The mode properties of a multimode glass fibre are defined by the core diameter and its material refractive index profile. A typical graded-index multimode glass fibre has a square-law refractive index profile introduced in Section 2.2.3. According to the scalar wave equation for a square-law radially inhomogeneous waveguide, a simplified Whittaker's equation can be written as [101]

$$\frac{d^2 f}{dx^2} + \left[ -\frac{1}{4} + \left[ \frac{a(1-\beta^2)}{k\sqrt{\Delta}} \right] \frac{1}{4x} - \frac{n^2-1}{4x^2} \right] f = 0, \quad 3-1$$

where  $f = x^{\frac{1}{4}} r^{\frac{1}{2}} \psi(r)$ . Given a finite  $\psi(0)$ , the only bounded solution to this equation can be expressed as a confluent hyper-geometric function as [85, 101]

$$f = e^{-\frac{x}{2}} x^{\frac{\nu+1}{2}} K \left( \frac{1}{2} + \frac{\nu}{2} - \frac{b}{4}, 1 + \nu, x \right), \quad 3-2$$

where  $K$  is the Kummer's function [102], which in this case fulfils the condition of

$$\frac{1}{2} + \frac{\nu}{2} - \frac{b}{4} = -\mu, \quad \mu = 0, 1, 2, \dots, \quad 3-3$$

or

$$b = 4\mu + 2\nu + 2, \quad 3-4$$

where  $b = \frac{a(1-\beta^2)}{k\sqrt{\Delta}}$ .

Hence, the exact solution to this Whittaker's equation can be written as [101]

$$\psi_{\mu\nu}(r, \theta) = r^\nu \exp \left[ -\frac{ka\sqrt{\Delta}}{2} \left( \frac{r}{a} \right)^2 \right] L_{\mu-1}^{(\nu)} \left[ ka\sqrt{\Delta} \left( \frac{r}{a} \right)^2 \right] \exp(j\nu\theta). \quad 3-5$$

The Laguerre polynomials  $L_{\mu-1}^{(\nu)}(x)$  in this expression are defined as

$$L_{\mu-1}^{(\nu)}(x) = \sum_{i=0}^{\mu-1} (-1)^i \frac{(\nu + \mu - 1)! x^i}{(\mu - i - 1)! (\nu + i)! i!}. \quad 3-6$$

For a square-law refractive index profile ( $\alpha \approx 2$ ), if the relative refractive index difference is very small ( $\Delta \ll 1$ ), the expression in the Laguerre-Gaussian product form in Equation 3-5 represents a good approximation of the available linear polarised modes.

The azimuthal order  $\nu$  and radial order  $\mu$  decide the order of a linear polarised mode. Taking account of the two polarisations ( $E_x, E_y$ ) and two orientations ( $\sin \mu\theta, \cos \nu\theta$ ), a specific order of linear polarised mode degenerates to four possible sub-modes. Given the fact that the mode power coupling is assumed independent of the polarisation and the multimode glass fibre is radially symmetric, the electric field of the linear polarised mode can be simply expressed using the real part of Equation 3-5 as

$$\psi_{\mu\nu}(r, \theta) = r^\nu \exp\left[-\frac{ka\sqrt{\Delta}}{2}\left(\frac{r}{a}\right)^2\right] L_{\mu-1}^{(\nu)}\left[ka\sqrt{\Delta}\left(\frac{r}{a}\right)^2\right] \cos(\nu\theta). \quad 3-7$$

In order to investigate the mode excitation of a multimode fibre, the power coupled into an individual mode of a given launching beam is calculated using the overlap integral [90]. This integral illustrates the overlap of the electric fields between each linear polarised mode  $E_{\mu\nu}$  and incident launching beam  $E_{launch}$  and can be written as

$$\eta_{\mu\nu} = \frac{\left|\iint E_{launch} E_{\mu\nu}^* r dr d\theta\right|^2}{\iint |E_{launch}|^2 dr d\theta \iint |E_{\mu\nu}|^2 dr d\theta} \quad 3-8$$

in polar coordinates, where \* denotes complex conjugate.

The launching beam electric field distribution  $E_{launch}$  is decided by the actual launch scheme. In centre or offset launch scenarios, this expression is simply a Gaussian beam function with a specific waist and offset. In the proposed low-loss Hermite-Gaussian beam launch scheme, the electric field distribution of the launch beam profile can be expressed in Cartesian ordinates as

$$E_{launch} = c_{mn} H_m(x) H_n(y) \exp\left(-\frac{x^2 + y^2}{2}\right), \quad 3-9$$

where  $c_{mn}$  is a constant with the expression of

$$c_{mn} = \frac{2^{\frac{m+n-2}{2}} \sqrt{\kappa}}{\sqrt{\pi} \sqrt{m! n!}}, \quad 3-10$$

and

$$\kappa = \frac{k\sqrt{\Delta}}{a} = \frac{2}{\omega_0^2}, \quad 3-11$$

where  $\omega_0$  is the waist of the fundamental mode of an ideal graded-index fibre.

As seen in Equation 3-9, the Hermite-Gaussian beam expression is in the form of a product between Gaussian function  $\exp(-\frac{\kappa r^2}{2})$  and Hermite polynomials  $H_m(x)$ ,

which is defined as

$$\begin{aligned} H_m(x) &= (-1)^m \exp(x^2) \frac{d^m}{dx^m} [\exp(-x^2)] \\ &= m! \sum_{i=0}^{m/2} (-1)^i \frac{(2x)^{m-2i}}{i!(m-2i)!} \end{aligned} \quad 3-12$$

In fact, Laguerre polynomials in Equation 3-7 can be transformed to Cartesian form Hermite polynomials using the relationship stated in [103] as

$$\begin{aligned} r^\nu L_{\mu-1}^{(\nu)}(r^2) \cos(\nu\theta) &= 2^{\frac{(-1)^{\mu-1}}{2(\mu-1)+\nu}} (\mu-1)! \sum_{q=0}^n \sum_{p=0}^{m/2} (-1)^p \binom{n}{q} \binom{m}{2p} \\ &\cdot H_{2(q-p)+\nu}(x) H_{2(\mu-1-q+p)}(y) \end{aligned} \quad 3-13$$

given the coordinates transformation of

$$x = r \cos \theta, \quad y = r \sin \theta. \quad 3-14$$

Taking a variable substitution of  $r \Leftrightarrow \sqrt{\kappa}r$ , Equation 3-13 becomes

$$\begin{aligned} \kappa^{\frac{\nu}{2}} r^\nu L_{\mu-1}^{(\nu)}(\kappa r^2) \cos(\nu\theta) &= 2^{\frac{(-1)^{\mu-1}}{2(\mu-1)+\nu}} (\mu-1)! \sum_{q=0}^n \sum_{p=0}^{m/2} (-1)^p \binom{n}{q} \binom{m}{2p} \\ &\cdot H_{2(q-p)+\nu}(\sqrt{\kappa}r \cos \theta) H_{2(\mu-1-q+p)}(\sqrt{\kappa}r \sin \theta) \end{aligned} \quad 3-15$$

Therefore, the linear polarised mode field distribution in Equation 3-7 can be written as

$$\begin{aligned} \psi(r, \theta) = E_{\mu\nu} &= 2^{\frac{(-1)^{\mu-1}}{2(\mu-1)+\nu}} (\mu-1)! \sum_{q=0}^n \sum_{p=0}^{m/2} (-1)^p \binom{n}{q} \binom{m}{2p} \\ &\cdot H_{2(q-p)+\nu}(\sqrt{\kappa}r \cos \theta) H_{2(\mu-1-q+p)}(\sqrt{\kappa}r \sin \theta) \\ &\cdot \exp\left(-\frac{\kappa r^2}{2}\right) \kappa^{-\frac{\nu}{2}} \end{aligned} \quad 3-16$$

Both Equation 3-16 and Equation 3-9 have Hermite polynomials in a product term.

Substituting them in the  $E_{launch} E_{\mu\nu}^*$  term in Equation 3-8, the result gives

$$\begin{aligned}
 E_{\text{launch}} E_{\mu\nu}^* &= c_{mn} H_m(x) H_n(y) \exp\left(-\frac{x^2 + y^2}{2}\right) \\
 &\cdot 2^{2(\mu-1)+\nu} (\mu-1)! \sum_{q=0}^n \sum_{p=0}^{m/2} (-1)^p \binom{n}{q} \binom{m}{2p} \\
 &\cdot H_{2(q-p)+\nu}(\sqrt{\kappa}r \cos \theta) H_{2(\mu-1-q+p)}(\sqrt{\kappa}r \sin \theta) \\
 &\cdot \exp\left(-\frac{\kappa r^2}{2}\right) \kappa^{-\frac{\nu}{2}} \\
 &= \frac{2^{\frac{m+n-2}{2}} \sqrt{\kappa}}{\sqrt{\pi} \sqrt{m! n!}} H_m(\sqrt{\kappa}r \cos \theta) H_n(\sqrt{\kappa}r \sin \theta) \exp\left(-\frac{\kappa r^2}{2}\right) \\
 &\cdot 2^{2(\mu-1)+\nu} (\mu-1)! \sum_{q=0}^n \sum_{p=0}^{m/2} (-1)^p \binom{n}{q} \binom{m}{2p} \\
 &\cdot H_{2(q-p)+\nu}(\sqrt{\kappa}r \cos \theta) H_{2(\mu-1-q+p)}(\sqrt{\kappa}r \sin \theta) \\
 &\cdot \exp\left(-\frac{\kappa r^2}{2}\right) \kappa^{-\frac{\nu}{2}}.
 \end{aligned} \tag{3-17}$$

Because of the orthogonal property of the Hermite polynomials, the overlap integral has to satisfy the following condition to have non-zero values

$$\begin{cases} m = 2(q-p) + \nu \\ n = 2(\mu-1-q+p) \end{cases}, \tag{3-18}$$

which requires the two Hermite polynomial terms in Equation 3-17 to have same orders. Rearranging Equation 3-18 gives

$$m + n + 1 = 2\mu + \nu - 1. \tag{3-19}$$

The mode group theory of multimode fibre states that the linear polarised mode with the azimuthal order  $\nu$  and radial order  $\mu$  should satisfy

$$M = 2\mu + \nu + 1, \tag{3-20}$$

where  $M$  is the mode group number. Rearranging Equation 3-19 and 3-20, the single mode excitation condition can be expressed as

$$m + n + 3 = 2\mu + \nu + 1 = M. \tag{3-21}$$

For a targeted mode group, the excitation solely depends on the order of the launching Hermite-Gaussian beam. It is worth noting that for a specific mode group number  $M$ , multiple combinations of  $m$  and  $n$  are available to fulfil the equality stated in Equation 3-21. In other words, different Hermite-Gaussian beams may excite the same mode group in multimode fibre as long as they have the same order ( $m + n + 3$ ). Since the launched power selectively couples into only one mode group and the linear polarised

modes in the same mode group propagate with similar velocities in the fibre, the Hermite-Gaussian launch enables single mode group operation and significantly improves the effective modal bandwidth approaching Shannon capacity [104].

The Hermite-Gaussian beam, as shown in Equation 3-9, consists of a product between the Hermite polynomials and the Gaussian terms in two dimensions. If one of them (i. e.  $y$ -axis) is set to have an order of zero (i.e.  $n = 0$ ), Equation 3-9 can be re-written as

$$E_{line-launch} = \frac{2^{\frac{m-2}{2}} \sqrt{\kappa}}{\sqrt{\pi} \sqrt{m!}} H_m(x) \exp\left(-\frac{x^2 + y^2}{2}\right). \quad 3-22$$

Here, the beam profile only extends with the order number  $m$  in the  $x$ -axis direction, whilst preserving a fundamental Gaussian distribution profile in  $y$ -axis direction. As shown in Figure 3.8, these one-direction-extended Hermite-Gaussian beams follow a line-shaped outline except for the case when  $m = 0$ , in which the profile simply exhibits a Gaussian distribution. For this reason, the launch scheme based on these profiles is named as line launch. To recognise a line launch profile with a specific order, it can be seen that the separations in the profile should equal to the order number  $m$ . The contour levels in the figure indicate the amplitudes of the electric field. For profiles with even order number, an elliptical Gaussian-shaped spot is located at the centre. On both side, pairs of spots with the same intensity profile are symmetrically aligned with respect to the  $y$ -axis. For profiles with odd order number, the symmetrically aligned spot pairs appear anti-phase. In terms of the profile complexity, a higher order line launch profile consists of more separated spots.

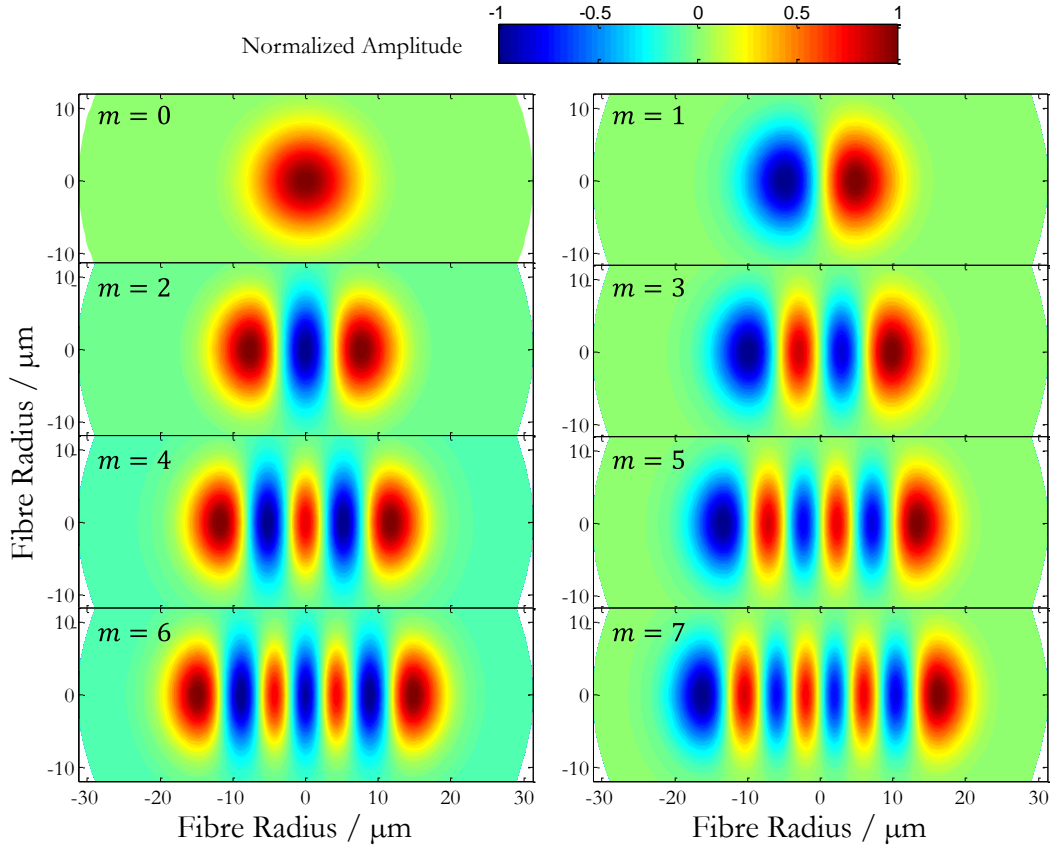


**Figure 3.8** Hermite-Gaussian beam profiles with zero vertical order ( $n = 0$ ) for a wavelength of 1310 nm

Another special case of Hermite-Gaussian beam is when the horizontal order  $m$  and the vertical order  $n$  are equal. In this case, the beam spots extend on both directions with the same number of separations. The expression for this version of Hermite-Gaussian beam therefore can be written as

$$E_{\text{square-launch}} = \frac{2^{m-1} \sqrt{\kappa}}{\sqrt{\pi} \sqrt{(m!)^2}} H_m(x) H_m(y) \exp\left(-\frac{x^2 + y^2}{2}\right), \quad 3-23$$

on which the launch scheme based is named as Hermite-Gaussian square launch, since the outline of such a launching beam tends to be a rounded square. Figure 3.9 illustrates such Hermite-Gaussian profiles for an operating wavelength of 1310 nm. Since the orders are equal on both axes, the beams are separated by crosses, forming a grid of spots in the overall profile. For the same order (i.e. same value of  $m + n + 3$ ), the profile of the square launch has more spots than that of the line launch.

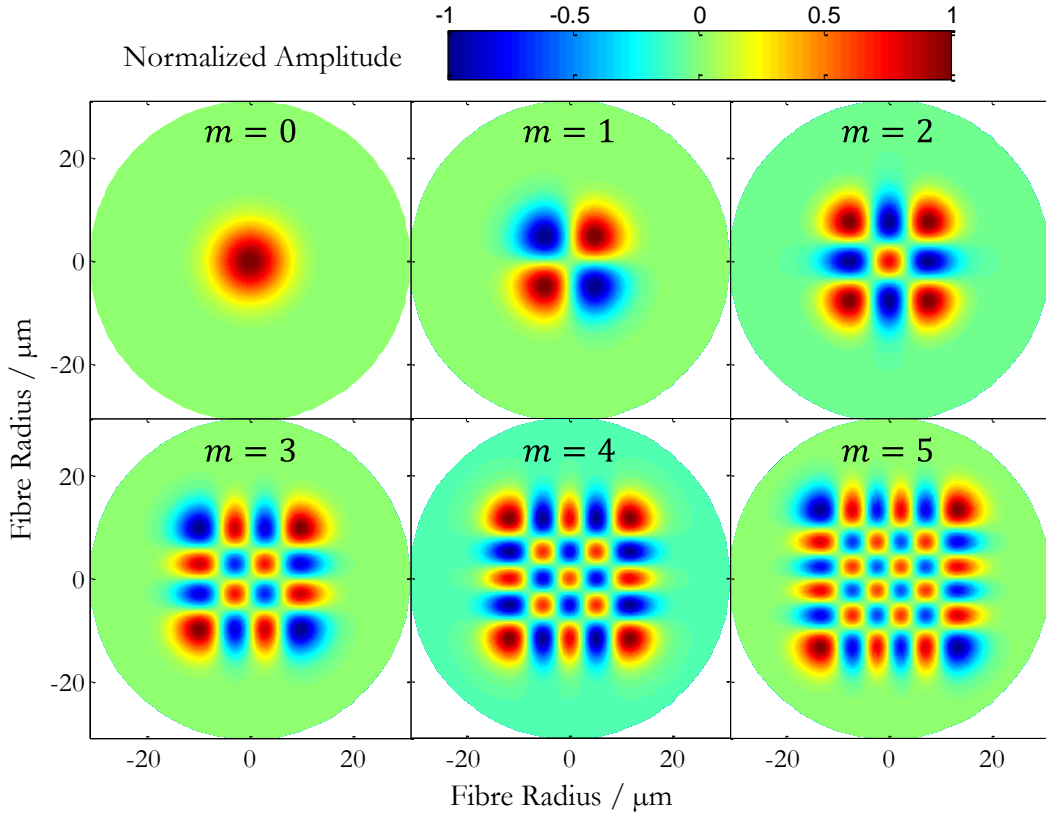


**Figure 3.9 Hermite-Gaussian beam profiles with equal order on horizontal and vertical directions for a wavelength of 1310 nm**

The light propagating through the multimode glass fibre is only allowed to be coupled into the supported electromagnetic field distributions, or in other words, modes. Hermite-Gaussian beams are such electromagnetic fields which exclusively excite a set of modes that belong to a single mode group and have zero overlap with the other modes. Hence, single mode group condition is achieved.

According to the relationship stated in Equation 3-17 to 3-21, a higher order Hermite-Gaussian beam excites a higher order mode group of a multimode glass fibre. The modes in a higher order mode group tend to travel through the fibre away from the centre as seen from the mode field profiles in Figure 2.7. This makes the higher order mode group less affected by the centre index defects and more likely to achieve higher bandwidth. However, higher order Hermite-Gaussian profiles generally have more complicated structures and are difficult to generate in practice. Thus, to have relatively high order and reasonably complex profiles, the (5, 0) order line launch profile and the (1, 1), (2, 2), (3, 3) order square launch profiles are chosen in this work for investigation. The intensity profiles of these beams are illustrated in Figure 3.10. The dark blue colour indicates zero intensity and the circle outlines the core area of the OM1 fibre.

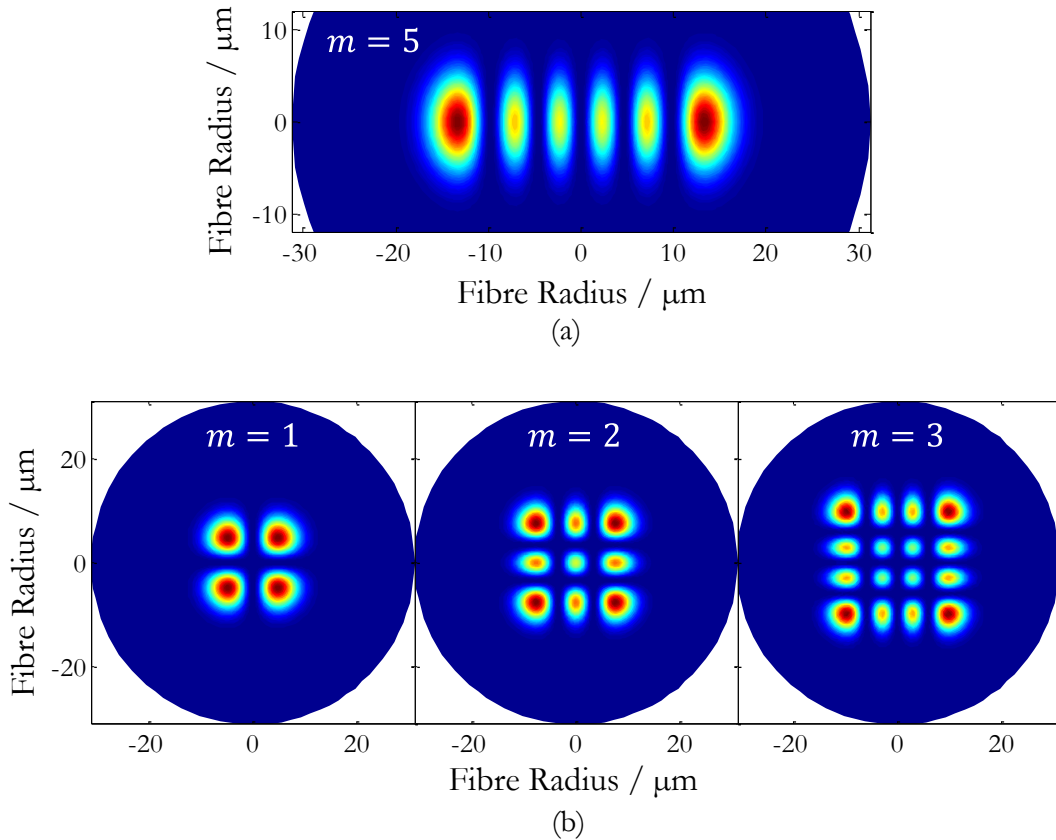


**Figure 3.10** Intensity profiles of the selected Hermite-Gaussian beams. (a) (5, 0) order line launch and (b) (1, 1), (2, 2) and (3, 3) order square launches.

### 3.2.2. Ideal Hermite-Gaussian Launch

As previously mentioned, the purpose of this work is to propose simple low-loss launch schemes that guarantee bandwidth improvements over worse case multimode glass fibres. Thus, as a proof of principle demonstration, this work mainly focuses on OM1 fibres which are specified in the ISO/IEC 11801<sup>9</sup> standard. Long wavelength of 1310 nm is considered because of its lower chromatic dispersion, which enables a bandwidth performance essentially depending on the intermodal dispersion. Consequently, the proposed launch schemes achieving single mode group operation can maximize the bandwidth and link reach enhancement. However, the proposed launches can also be applied to other fibre types at different wavelengths. The only thing that varies is the size of the launching beam profiles, which depend on the refractive index profiles and the operating wavelengths.

<sup>9</sup> This type of multimode glass fibre is categorized in BS EN 50173-1:2007 in UK with the same specifications.

The fibre model used in this work is based on a set of non-ideal OM1 fibres with defective refractive indices which consist of known imperfections from the fabrication process. This is characterized in the Cambridge-108MMF model [105, 106], in which a total number of five types of perturbation are applied to a near-ideal square-law OM1 fibre index profile. These perturbations include dip, peak or no-defect at the core centre, whether or not an exponential decay at the core/cladding boundary, whether or not a kink perturbation at a proposed position [107] and three different values of profile parameter  $\alpha$  at the inner and the outer regions of the core respectively. The combinations of these perturbations result in a total number of 108 fibre samples. Relating to the full industrial FDDI Monte Carlo model [108], the Cambridge-108MMF model is found to share the worst 5% of the differential modal delays [109].

The parameters used in the simulation work are listed in Table 3-2. First of all, a mode solver [110, 111] is used to calculate the mode profile of each supported mode of a given multimode glass fibre, whose refractive index profile is taken from the Cambridge-108MMF model. The mode solver gives asymptotic numerical solutions to the scalar wave equation, presenting the transverse electric field distribution and modal delay for each supported mode.

**Table 3-2 List of the parameters used in numerical calculations**

|   |                     |
|---|---------------------|
| <b>Fibre core radius, <math>a</math></b>                          | 31.25 $\mu\text{m}$ |
| <b>Fibre core refractive index, <math>n_{core}</math></b>         | 1.5                 |
| <b>Fibre cladding refractive index, <math>n_{cladding}</math></b> | 1.474               |
| <b>Profile parameter, <math>\alpha</math></b>                     | 1.97                |
| <b>Operating wavelength, <math>\lambda</math></b>                 | 1310 nm             |

In terms of the launching beams, a 7  $\mu\text{m}$  FWHM Gaussian beam is assumed for the centre launch and offset launch. This beam dimension refers to the FWHM of the output Gaussian beam from a single mode fibre. The radial offset for the offset launch is set to 20  $\mu\text{m}$  according to the IEEE802.3z gigabit Ethernet standard [89]. For the line launch and square launch beams, the profiles given in Equation 3-22 and Equation 3-23 are projected at the centre of the multimode glass fibre.

The coupled mode power coefficient for each mode is calculated using the overlap integral given in Equation 3-8. These correlated power coefficients are normalized and grouped into individual mode groups referring to the mode group number  $M = 2\mu + \nu + 1$ . Mode groups of order higher than 22 are ignored<sup>10</sup> since such modes are not well confined within the fibre core and the coupled powers to such modes are negligible [99]. Figure 3.11 shows the mode group power distribution for the centre launch, offset launch, proposed (5, 0) order line launch and three different orders of square launches. The colour of the bar indicates different fibres from the Cambridge-108MMF model. Each of the bars consists of 108 independent mode group powers using different fibres, which are plotted side by side for each mode group. For the centre launch, though most of the power is coupled into the fundamental mode group, a significant volume of power can be seen in mode group 5. The offset launch, on the other hand, evenly excites a wide range of mid-order mode groups. Meanwhile for the proposed Hermite-Gaussian launches, only one mid-order mode group is significantly excited for each of the cases. This figure illustrates that a targeted mode group is excited using either line launch or square launch, where single mode group operation is achieved.

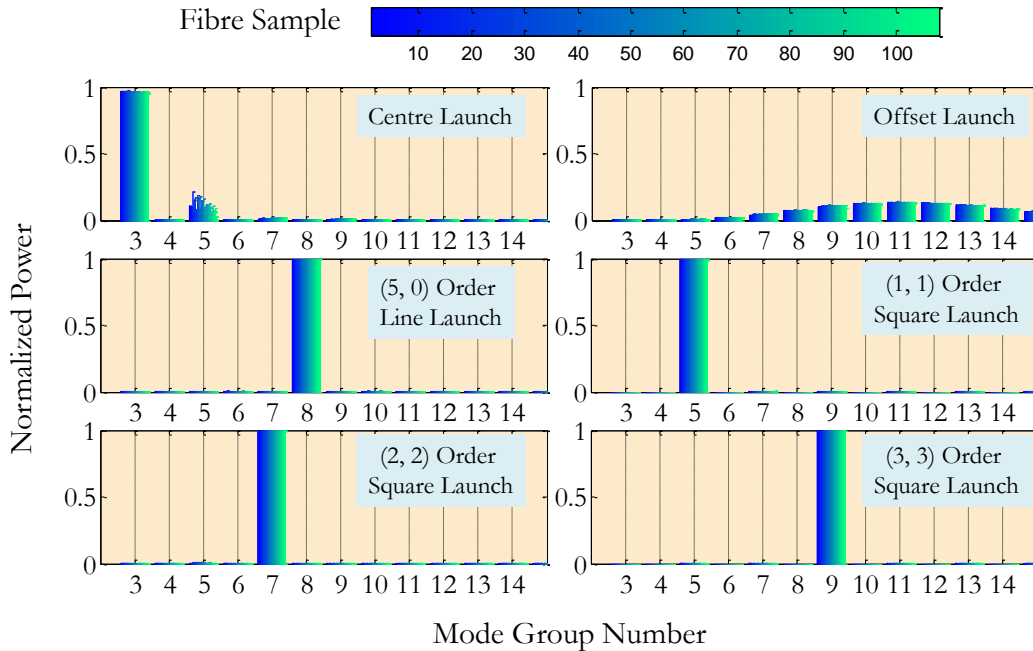


**Figure 3.11** Calculated mode power distributions for the centre launch, offset launch, and Hermite-Gaussian launches based on the Cambridge-108MMF model. The colour of the bars indicate different fibres from the model.

<sup>10</sup> Since the mode group number starts from  $2\mu + \nu + 1 = 3$ , this give a total number of 20 mode groups considered in the calculations.

The concept of mode group power extinction ratio is introduced to evaluate the performance of different launch schemes as shown in Figure 3.12.  $P_n$  is the mode group power coefficient in the order from the highest to the lowest. The extinction ratio is defined as the power ratio between the mode groups with the highest and second highest powers in decibels. A higher extinction ratio implies a stronger single mode group excitation in the multimode glass fibre, which generally gives a higher bandwidth.

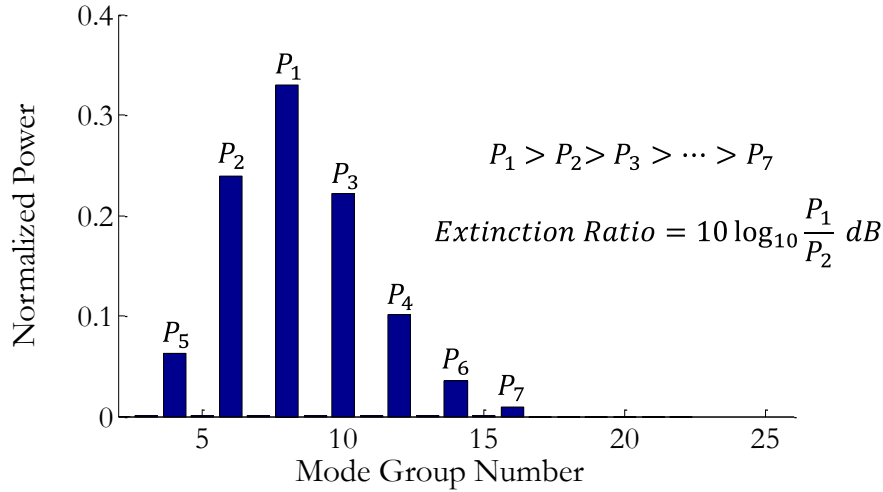


**Figure 3.12 Definition of the mode group power extinction ratio**

Figure 3.13 shows the extinction ratios of different launch schemes over OM1 fibres in the Cambridge-108MMF model. For each launch scheme, 108 extinction ratios are calculated. The symbols in each column correspond to the calculated results for 108 individual fibre profiles. It can be seen that the proposed Hermite-Gaussian launches generally have higher extinction ratios than those of the centre launch and offset launch. Since the fibre profiles used in the calculations are defective, the centre launch has low extinction ratios mainly due to the centre defects, which alter the supported mode group profiles of the multimode glass fibre. In this case, the launching beam profile is not able to perfectly match with any of the supported mode groups. Hence, the launched power is more likely to be coupled into the adjacent mode groups. The offset launch has the lowest extinction ratios near 0 dB, because it excites a wide range of mid-order mode groups. These mode groups have a Gaussian-shaped power distribution. The red dots in this figure indicate the mean values of the extinction ratios of each launch scheme. The Hermite-Gaussian launches generally have mean values that are ~25 dB and ~30 dB higher than that of the centre and offset launches respectively. The high extinction ratios of the proposed Hermite-Gaussian launches indicate near single mode group excitations.

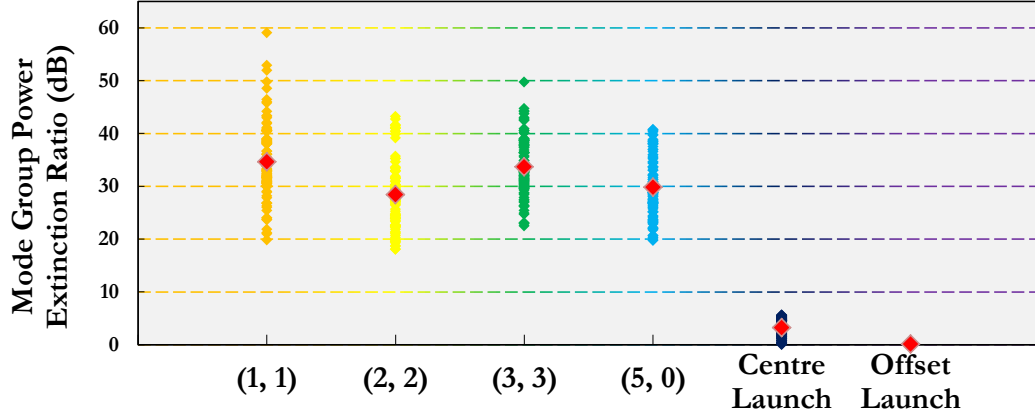


Figure 3.13 Mode group power extinction ratios based on the Cambridge-108MMF model for the centre launch, offset launch and proposed Hermite-Gaussian launches

To study the bandwidth performance of the proposed launches, the differential delay  $\tau_{\mu\nu}$  with respect to the fastest mode  $(\mu, \nu)$  can be calculated as

$$\tau_{\mu\nu} = Lc(n_{\mu\nu} - \min\{n_{eff}\}), \quad 3-24$$

where  $n_{\mu\nu}$  is the effective refractive index of a particular mode given by the mode solver,  $\min\{n_{eff}\}$  is the minimum effective refractive index of all the calculated mode,  $L$  is the fibre length and  $c$  is the speed of light. The overall impulse response can then be calculated using the mode power distribution and the modal delays as the modal dispersion effect on the impulse response can be treated as a superposed delta function weighted by the mode power distribution. Thus the frequency response of the fibre can be expressed as

$$H_{fibre}(f) = \frac{\sum P_{\mu\nu} \exp(j2\pi f \tau_{\mu\nu})}{\sum P_{\mu\nu}}, \quad 3-25$$

where  $P_{\mu\nu}$  is the power coupling coefficient of a linear polarised mode given by the mode power distribution. Since the mode power distribution calculation has normalized the power coupling coefficient, the denominator in Equation 3-25 equals 1. Meanwhile, according to the fact that the linear polarised modes in the same mode group travel with similar velocities in the multimode glass fibre, Equation 3-25 can be further simplified as

$$H_{fibre}(f) = \sum P_M \exp(j2\pi f \tau_M), \quad 3-26$$

where  $P_M$  is the normalized power coupling coefficient of the  $M^{\text{th}}$  mode group and  $\tau_M$  is the mode group delay derived by averaging the modal delays belonging to the

corresponding mode group. Consequently, the -3 dBo bandwidth of each fibre is decided from  $H_{fibre}(f)$ . The corresponding bandwidth-distance products are calculated and illustrated in Figure 3.14. The calculated products are numerically truncated at a bandwidth-distance product of 100 GHz·km, which is used to indicate a near dispersion-free circumstance where the fibre has a nearly flat frequency response. The minimum OFL bandwidth (500 MHz·km) is also labelled for comparison reasons with a horizontal dashed line. Again, the symbols in this figure correspond to calculations for individual fibre profiles taking from the Cambridge-108MMF model. And the red dots on the graph indicate the bandwidth-distance products for an 80% link yield<sup>11</sup>, which indicates the achievable bandwidth for 99% of the installed base.

It can be seen that the bandwidths of the proposed Hermite-Gaussian launches reach the numerical limit for all tested fibres. This is because the single mode operation guarantees that all of the power arrives simultaneously at the fibre output. For the centre launch however, due to low tolerance to the centre defects, several tested fibres fall under the OFL bandwidth-distance product. The offset launch provides a higher bandwidth at 80% link yield than that of the centre launch. These results confirm that the differential modal delay is greatly reduced using the proposed Hermite-Gaussian launches and the refractive index defects do not tend to severely affect this improvement.

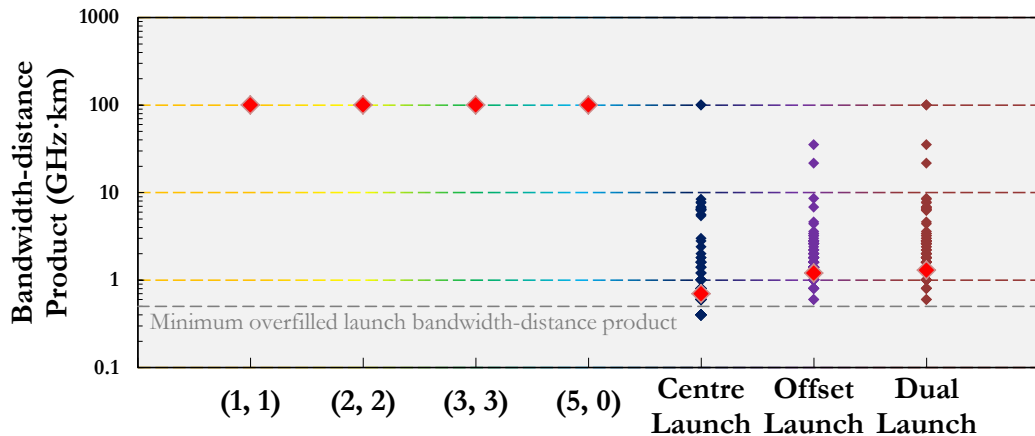


**Figure 3.14** Calculated bandwidth-distance products based on the Cambridge-108MMF model for the centre launch, offset launch, dual launch and proposed Hermite-Gaussian launches

<sup>11</sup> Since the Cambridge-108MMF model represents the worst 5% OM1 fibres, the 80% yield is chosen to indicate a total 99% yield in the installed base ( $1 - (1 - 80\%) \cdot 5\% = 99\%$ ).

### 3.2.3. Low-loss Hermite-Gaussian Launch Beam Generation

The Hermite-Gaussian beam profiles cannot be directly generated using a laser transmitter. In an optical system, these special phase and intensity correlated profiles can be generated either use far field holographic [112] or near field direct coupling [45] approaches. In the far field approach, a collimated beam spot is coupled into a hologram with a designed profile for specific Hermite-Gaussian beam generation. After the hologram, a focusing lens can be used to control the dimension of the generated beam profile for launching into the fibre. The far field approach provides precise synthesis of the desired beam profile given a digital hologram with sufficient resolution [113]. The liquid-crystal based spatial light modulator used in this approach may introduce high coupling loss and requires the incident beam to be strictly aligned. In practice, a fixed hologram implementation can provide a robust solution to this problem with high coupling efficient. Considering the system complexity and alignment tolerance issues, the holographic approach is not used in this work.

On the other hand, near field generation requires a collimating and focusing lense pair and a beam shaping mask. Figure 3.15 illustrates the near field technique that is implemented for Hermite-Gaussian beam generation in this work. The output from a single mode fibre is collimated and focused on a phase/intensity beam shaping mask, which is placed nearly touching the cleaved multimode glass fibre facet. On the mask, the Hermite-Gaussian beam profiles are presented as transparent areas with shapes of the Gaussian-like spots. The sizes of the spots are decided by the outlines representing the contour level of 5% of the maximum intensity, which means that the areas with intensity less than this level in the ideal profile are cut off. The anti-phase profile of a specific Hermite-Gaussian beam is presented as alternations of positive and negative phases between adjacent spots. This is controlled by changing the thicknesses of the transparent areas. In this way, an approximated version of Hermite-Gaussian beam can be generated. It can be seen later in the following sections that the approximated Hermite-Gaussian beams achieve comparable bandwidth improvements to the ideal cases.

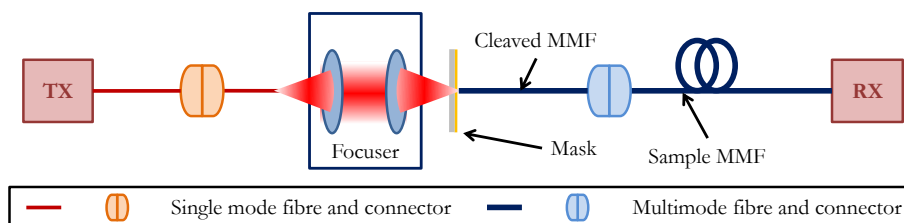
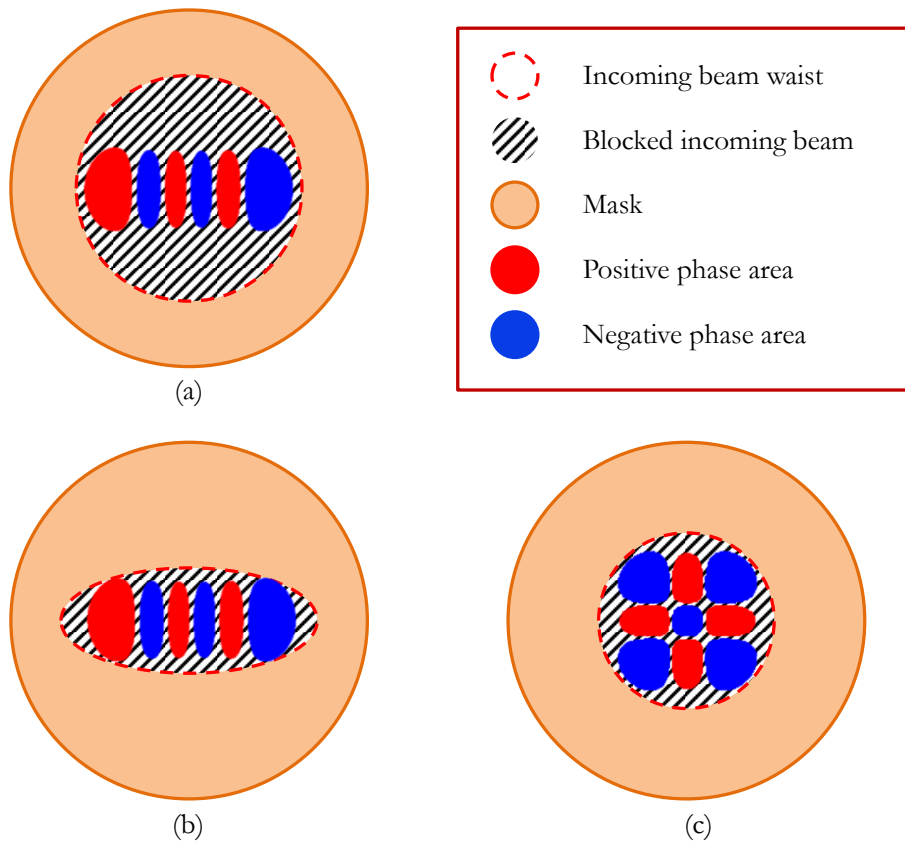


Figure 3.15 Schematic diagram of the near field Hermite-Gaussian beam generation

In the conventional line launch scheme, the incident beam at the mask is a circular Gaussian beam. As seen in Figure 3.16 (a), a great proportion of the incoming beam is blocked by the non-transparent area of the beam shaping mask. Consequently, the coupling loss of the line launch is as high as  $\sim 6.8$  dBo [94]. In this work, elliptical and circular Gaussian beams are used for line launch and square launch respectively to avoid unnecessary losses. Figure 3.16 (b) and (c) illustrate these scenarios using  $(5, 0)$  order line launch and  $(2, 2)$  order square launch by way of example. The shaded areas of both cases are much smaller than the conventional line launch approach and the coupling loss is reduced by at least 2.5 dBo as further discussed in the following section.



**Figure 3.16** Schematic diagrams of incident beams coupling at the phase/intensity shaping masks for the (a) conventional line launch, (b)  $(5, 0)$  order low-loss line launch and (c)  $(2, 2)$  order low-loss square launch

### 3.2.3.1. Coupling Efficiency of Hermite-Gaussian Launch

The idea of low-loss Hermite-Gaussian launch is based on a matched elliptical or circular incoming Gaussian beam as shown in Figure 3.16, which gives reduced coupling loss at the beam shaping mask. Generally speaking, a Gaussian beam with smaller waist is preferred to minimize the coupling loss since the centre area of the mask is mostly transparent. However, the generated beam could lose the similarity with the ideal

Hermite-Gaussian profile if the incoming beam waist is too small. As a result, the single mode excitation characteristic may no longer hold. In order to decide the suitable waists, the mode group extinction ratio performance for different incoming Gaussian beam waists is studied. These are calculated in the same way as the ideal profiles. The coupling losses are also calculated assuming all the optical power projected outside the transparent areas on the mask is completely blocked. As seen in Figure 3.17, the (1, 1) order square launch achieves optimised performance at an incoming beam waist of 12  $\mu\text{m}$ . The same calculations are carried out for all four proposed low-loss Hermite-Gaussian launches. The resulted optimal incoming Gaussian beam waists and the corresponding coupling losses are listed in Table 3-3.

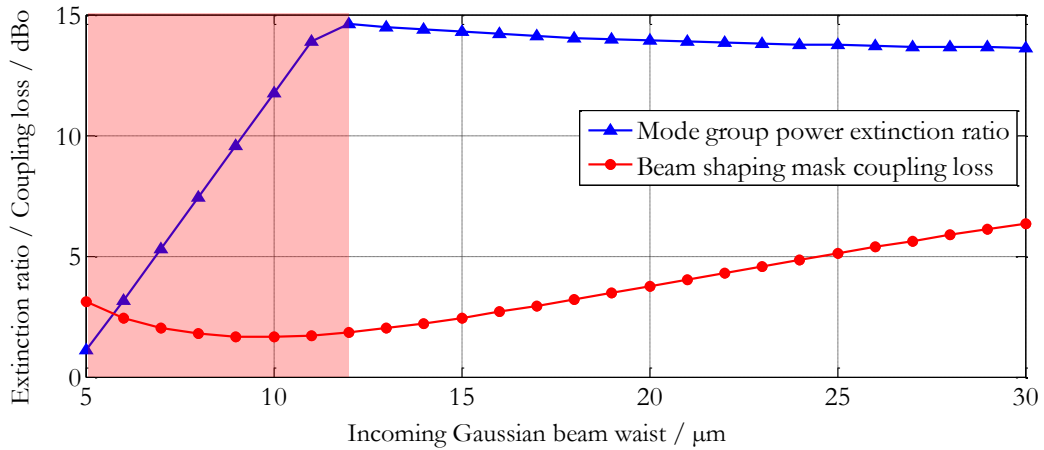


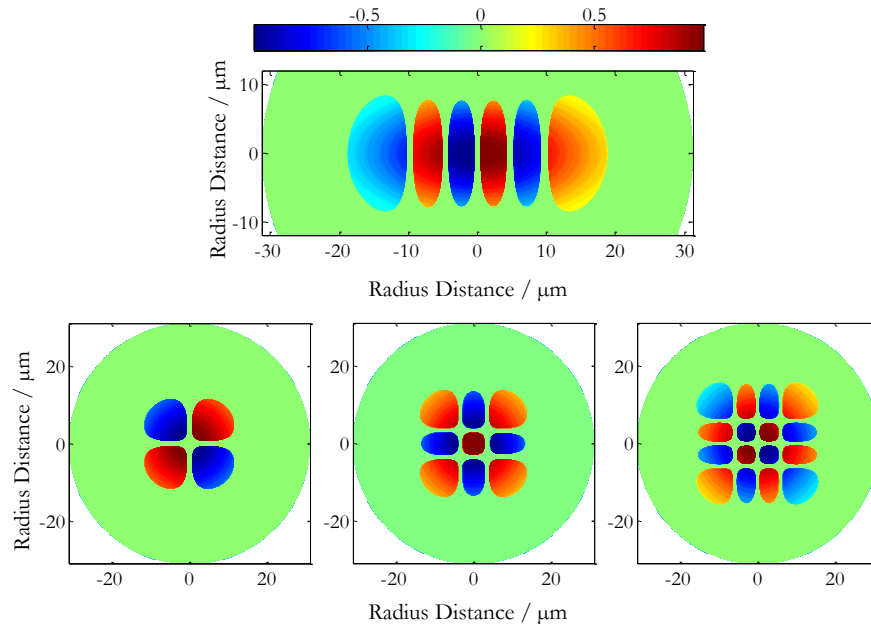
Figure 3.17 Mode group power extinction ratio against different incoming Gaussian beam waists for the (1, 1) order low-loss Hermite-Gaussian square launch

Table 3-3 List of the optimised Gaussian beam waists and corresponding coupling losses

| Low-loss Hermite Gaussian Launching Scheme | Optimised Waist / $\mu\text{m}$ | FWHM / $\mu\text{m}$ | Coupling Loss / dB |
|--|---------------------------------|----------------------|--------------------|
| (5, 0) order line launch (long axis)       | 28                              | 33                   | 3.4                |
| (5, 0) order line launch (short axis)      | 14                              | 16.5                 |                    |
| (1, 1) order square launch                 | 12                              | 14.1                 | 1.8                |
| (2, 2) order square launch                 | 18                              | 21.2                 | 2.8                |
| (3, 3) order square launch                 | 27                              | 31.8                 | 4.3                |

### 3.2.3.2. Non-ideal Hermite-Gaussian Beam

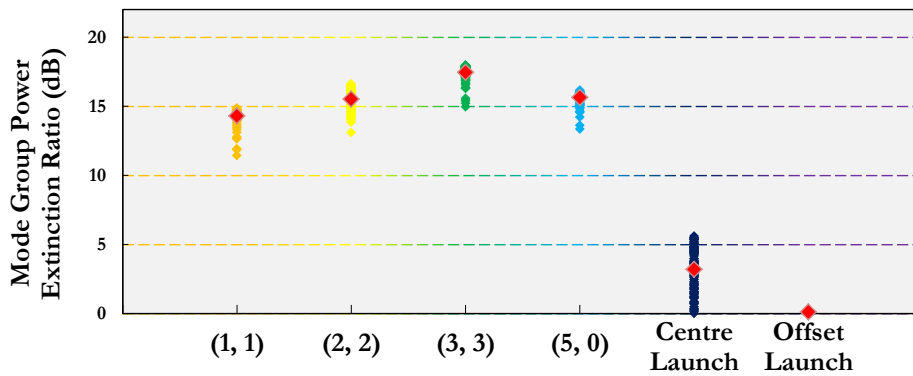
Using the beam generation approach introduced in Figure 3.15, the generated launching beam is an approximated version of the ideal Hermite-Gaussian beam. The performance of this approach is evaluated using the same numerical calculations as seen in Section 3.2.2. Figure 3.18 illustrates the beam profiles of the proposed low-loss Hermite-Gaussian launches based on the generation technique shown in Figure 3.16. An elliptical Gaussian beam with  $17\ \mu\text{m}$  FWHM on the long axis and  $8.5\ \mu\text{m}$  FWHM on the short axis is used for the low-loss line launches and a  $17\ \mu\text{m}$  FWHM circular Gaussian beam is used for the low-loss square launches. These incident beam dimensions are much smaller than the preferred dimensions listed in Table 3-3 and they are chosen for the purpose of better illustration only. It can be seen that the illuminated beams follow the corresponding Hermite-Gaussian shape outlines and appear Gaussian-like in the overall profiles. The phase profiles are precisely presented as positive and negative areas. Compared with the ideal Hermite-Gaussian beams in Figure 3.8 and Figure 3.9, these approximated profiles lose the Gaussian characteristic in individual spots whilst maintaining the overall shape and anti-phase symmetry in the profiles.



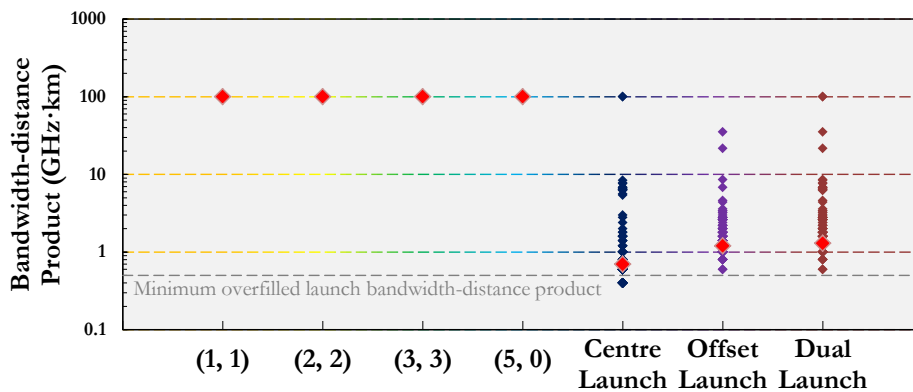
**Figure 3.18** Non-ideal Hermite-Gaussian beams generated using the beam shaping mask approach.  $17\ \mu\text{m} \times 8.5\ \mu\text{m}$  FWHM elliptical Gaussian beam and  $17\ \mu\text{m}$  FWHM circular Gaussian beam are used for the low-loss line launch and square launches respectively

The corresponding extinction ratios and bandwidth-distance products are calculated for these non-ideal Hermite-Gaussian beams as shown in Figure 3.19. Elliptical Gaussian beam of  $28\ \mu\text{m} \times 14\ \mu\text{m}$  waist and circular Gaussian beams of  $12\ \mu\text{m}$ ,  $18\ \mu\text{m}$  and  $27\ \mu\text{m}$

waist are used for the generation of the (5, 0) order low-loss line launch, (1, 1), (2, 2) and (3, 3) order low-loss square launches. As seen in Figure 3.19(a), the extinction ratios for all of the proposed low-loss Hermite-Gaussian launches generally drop from an average of  $\sim 32$  dB to  $\sim 16$  dB compared with the cases when using ideal launching beams. Profile mismatches with the supported mode groups of the multimode glass fibre are the main cause of this degradation. However, with an extinction ratio of  $\sim 16$  dB, more than 97% of the launched power is still coupled into the targeted mode group, which guarantees near single mode group operation. As seen from Figure 3.19(b), the low-loss Hermite-Gaussian launches maintain very high bandwidth-distance products, which are still all truncated at the assumed numerical limit of  $100 \text{ GHz}\cdot\text{km}$ . These results confirm that the approximated versions of Hermite-Gaussian beams generated using the beam shaping mask approach are good enough to maintain significant bandwidth improvement over multimode glass fibre links.



(a)



(b)

Figure 3.19 (a) Extinction ratio calculations for the centre launch, offset launch, and proposed low-loss Hermite-Gaussian launches. (b) Bandwidth-distance product calculations for the centre launch, offset launch, dual launch and proposed low-loss Hermite-Gaussian launches. Both calculations are based on approximate Hermite-Gaussian profiles and the Cambridge-108MMF model at a wavelength of  $1310 \text{ nm}$

### 3.2.4. Limitations of the Low-loss Hermite-Gaussian Launch

So far, the proposed low-loss Hermite-Gaussian launches are all considered under a perfect alignment and ideal phase profile condition. In a practical implementation, coupling misalignment is inevitable. The bandwidth drops dramatically with even a tiny radial misalignment at launch for some defective fibres [99]. The low-loss Hermite-Gaussian launch is useful only if it can achieve an acceptable misalignment tolerance. Furthermore, an extra concern of the proposed launches is the accuracy of the phase profile of the launching beam. It has been proved in Section 3.2.3.2 that the approximated intensity profiles do not introduce significant bandwidth degradations. In this section, the phase profile inaccuracy is further investigated. The low-loss Hermite-Gaussian launches are achieved using either elliptical Gaussian incoming beam with line launch profile or circular Gaussian incoming beams with square launch profiles. According to the nature of the incoming beams and launching profiles, the rotational misalignment issue is also discussed.

#### 3.2.4.1. Launch with Radial Misalignment

The radial misalignment is defined as the distance between the centre of launched beam and the multimode glass fibre core. As seen in Figure 3.20, a  $6 \mu\text{m} \times 6 \mu\text{m}$  area is defined as the targeted area for misalignment investigation in this work. Considering the radial symmetric characteristic of the multimode glass fibre, the area of interest can be further simplified to a quarter of the square as highlighted in red in Figure 3.20.

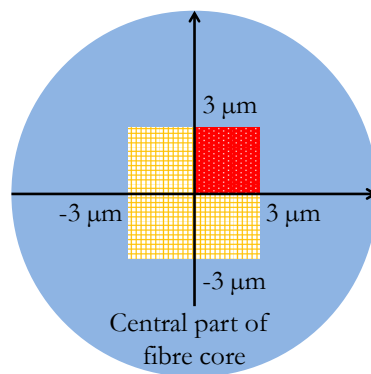


**Figure 3.20** Illustration of the area of interest for launching misalignment investigation

Based on the same numerical calculations used in the previous sections, the bandwidth-distance products are calculated for each point inside the targeted area shown in Figure 3.20. Two sets of results are shown using ideal and approximated Hermite-Gaussian beam profiles respectively. Ideal square-law index multimode glass fibre is considered in

this evaluation. The contour plots of the bandwidth-distance products at different misalignment conditions for the proposed orders of Hermite-Gaussian launches are shown in Figure 3.21. The unit of the contour levels is GHz·km.

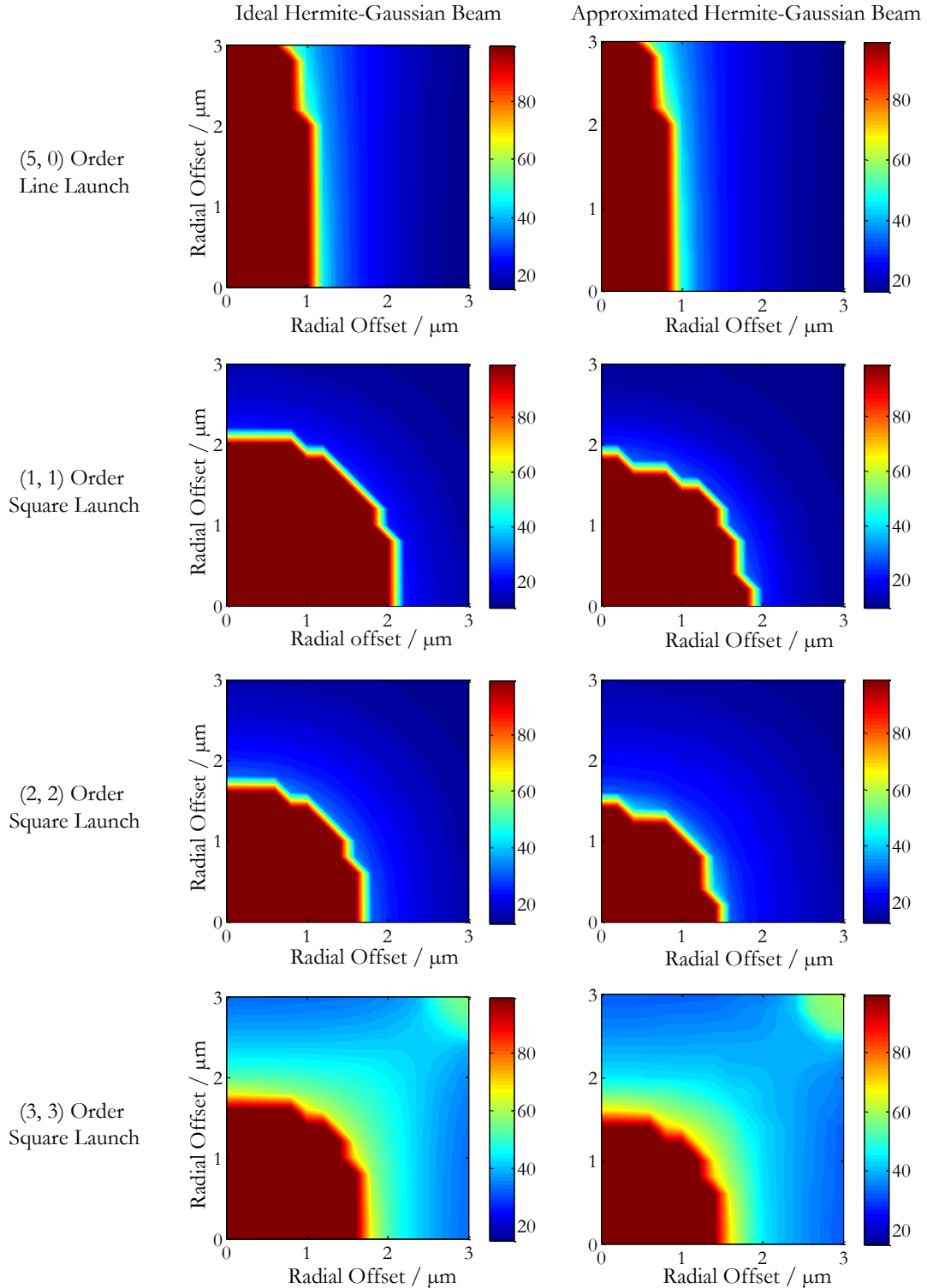


**Figure 3.21** Contour plots of the bandwidth-distance products achieved for the proposed low-loss Hermite-Gaussian launches for a misalignment region of  $3\ \mu\text{m} \times 3\ \mu\text{m}$ . The contour levels indicate bandwidth-distance products in the unit of GHz·km

For launches using ideal Hermite-Gaussian profiles, it can be seen that the numerical limit of  $100 \text{ GHz}\cdot\text{km}$  is achieved within the region of  $3 \mu\text{m}$  vertical offset and  $1 \mu\text{m}$  horizontal offset for the line launch. The higher vertical misalignment tolerance is due to the phase-invariant property on the short axis of the line launch profile, which tends to maintain the profile matching with the targeted mode group even with launching misalignment. This region is around  $2 \mu\text{m} \times 2 \mu\text{m}$  for the proposed square launches. If the beam shaping mask approach is used for launching beam generation, the areas of the regions achieving truncated bandwidth are smaller but the degradation is not significant. In the worst case scenario, a minimum bandwidth-distance product of above  $15 \text{ GHz}\cdot\text{km}$  is achieved with  $3 \mu\text{m}$  launching radial misalignment for all cases.

A further study of the radial offset is carried out using the Cambridge-108MMF model. In order to show the worst case scenario, a  $3 \mu\text{m}$  radial offset is assumed for all tested fibres and launch schemes. For the low-loss line launch, two cases are considered individually for the long and short axes, both with  $3 \mu\text{m}$  misalignments. Horizontal misalignment is assumed for the square launches. In these calculations, the beam shaping mask approach is assumed for Hermite-Gaussian beam generation where all of the launching beams are non-ideal. As shown in Figure 3.22. The bandwidth-distance products of the proposed Hermite-Gaussian launches with worst case launching radial misalignment are generally greater than  $1 \text{ GHz}\cdot\text{km}$ . The minimum bandwidth achieved at 80% yield is when using the (1, 1) order square launch, which is still at least 2x as that of the centre launch. This is also higher than the offset launch and comparable to the dual launch. If a launching beam can be generated closer to the ideal Hermite-Gaussian profile, the improvement is expected to be even higher.

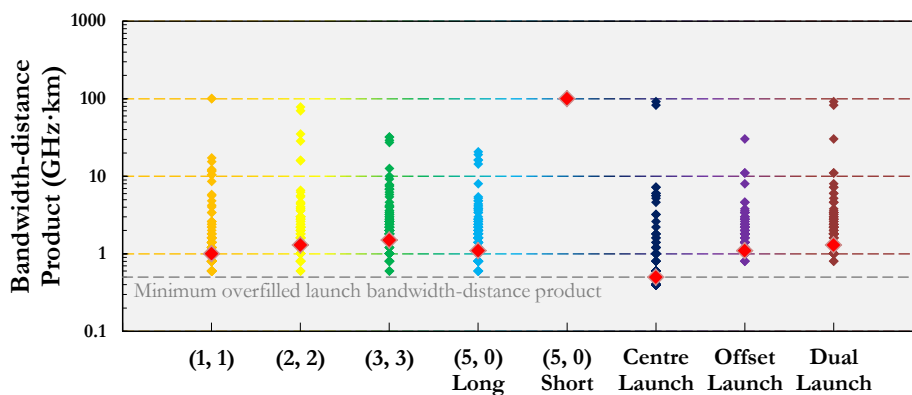


**Figure 3.22** Bandwidth-distance products based on the Cambridge-108MMF model for the centre launch, offset launch, dual launch and proposed low-loss Hermite-Gaussian launches with  $3 \mu\text{m}$  radial misalignment

As mentioned earlier, the Cambridge-108MMF modal represents the most challenging 5% of the installed OM1 fibres. An 80% link yield achieved using this model indicates an overall 99% link yield of the installed base. Taking the worst case radial offset of  $3\ \mu\text{m}$ , the link yield calculations are shown in Figure 3.23 for the conventional launches and (3, 3) order square launch. At 80% yield, the conventional centre launch, offset launch and dual launch achieve  $0.5\ \text{GHz}\cdot\text{km}$ ,  $1.1\ \text{GHz}\cdot\text{km}$  and  $1.2\ \text{GHz}\cdot\text{km}$  bandwidth-distance products respectively. In contrast, the (3, 3) order square launch achieves  $1.8\ \text{GHz}\cdot\text{km}$ , which is a 50% improvement over the dual launch under condition of  $3\ \mu\text{m}$  radial misalignment assumed for all tested fibres. Without manual testing between the centre launch and offset launch, this result proves that the low-loss Hermite-Gaussian launch provides a simple solution to bandwidth and link yield improvements over multimode glass fibre links.

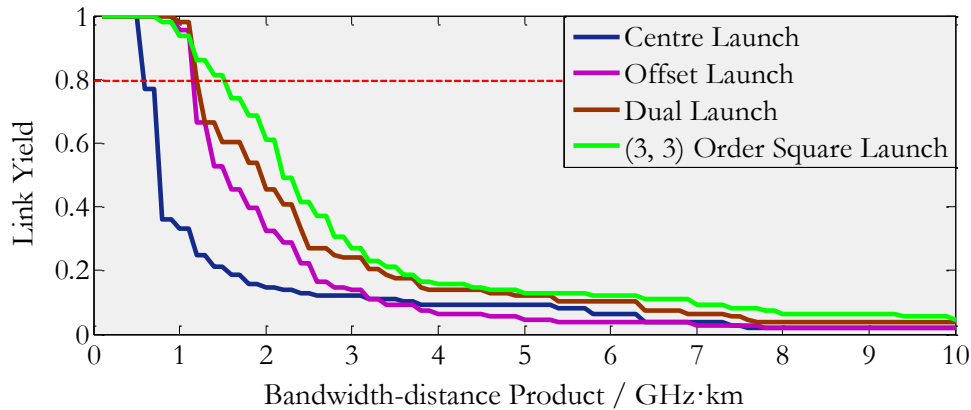


**Figure 3.23 Worst case link yields with  $3\ \mu\text{m}$  radial misalignment for the centre launch, offset launch, dual launch and (3, 3) order square launch**

### 3.2.4.2. Phase Profile Tolerance

The phase profiles of the proposed low-loss Hermite-Gaussian launching beams are controlled by the etching depths of the beam shaping mask. A further study of the system performance with respect to phase errors introduced during the mask fabrication process is carried out. A launch without radial offset is assumed in this evaluation. The result of mode group power extinction ratios are shown in Figure 3.24 based on the Cambridge-108MMF model. The phase shift is defined as the change of phase in the negative phase area on the mask with respect to a perfect anti-phase positive area. The dark blue spots indicate the average extinction ratios for each phase shift. Except for the (2, 2) order square launch, all proposed Hermite-Gaussian launches exhibit a symmetric characteristic of phase tolerance because of the same illuminating size for both negative

and positive phase areas on the beam shaping masks. The (2, 2) order square launch has a larger positive phase area so that the mode power extinction ratios are more sensitive to positive phase shifts than negative ones as shown in Figure 3.24. Taking -3 dB degradation of the extinction ratio as a reference, the illustrated results show a  $\pm 0.2\pi$  tolerance for all proposed low-loss Hermite-Gaussian launches ( $+0.1\pi$  and  $-0.3\pi$  for (2, 2) order square launch). This implies a  $\sim \pm 90$  nm etching depth tolerance<sup>12</sup> (+45 nm and -135 nm for (2, 2) order square launch). This accuracy requirement of the etching depth can be achieved using FIB [94].

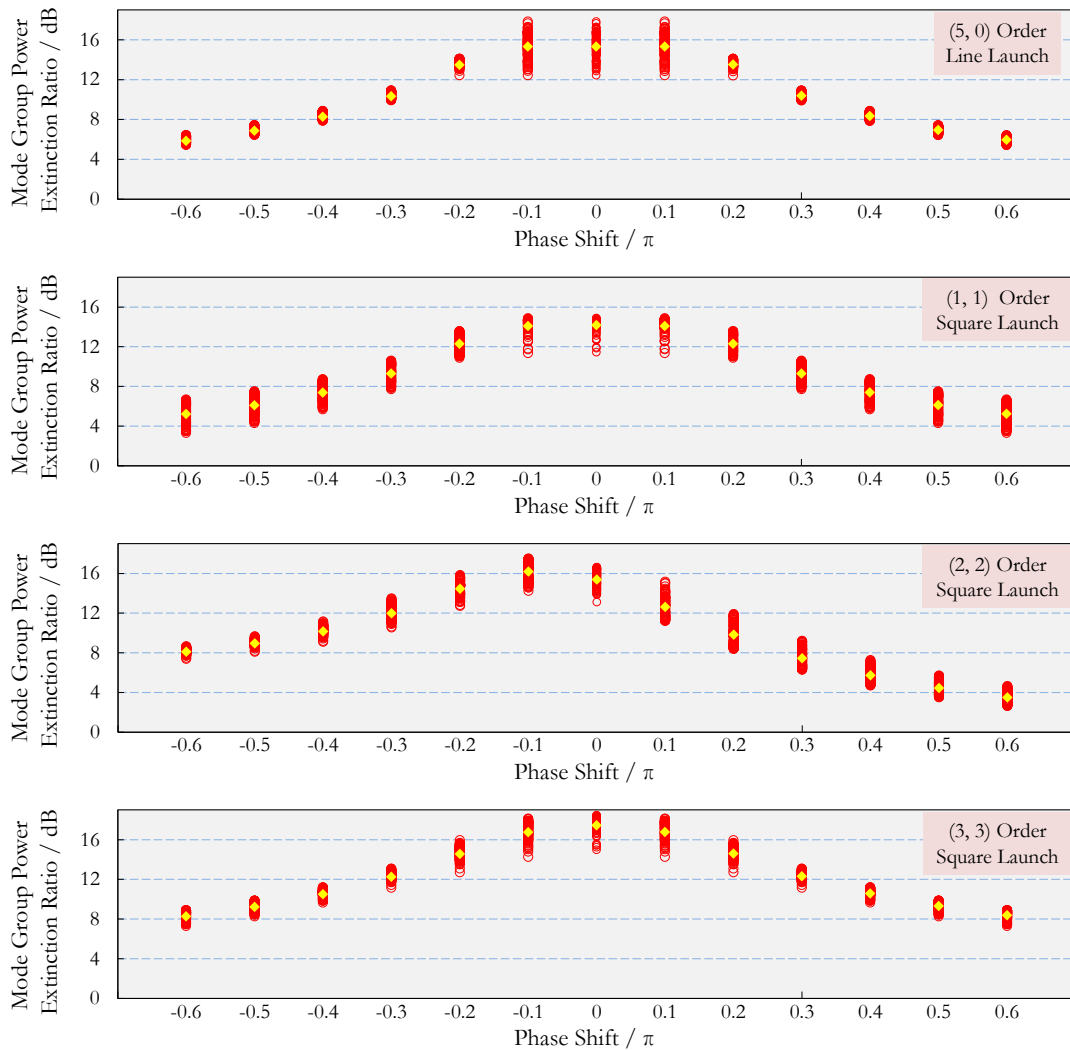


**Figure 3.24 Phase shift tolerance for different orders of low-loss Hermite-Gaussian launches. The Cambridge-108MMF model is used for all calculations**

<sup>12</sup> This corresponds to a wavelength of 1310 nm and a mask material refractive index of 1.45.

### 3.2.4.3. Rotational Misalignment

Another issue of the proposed low-loss Hermite-Gaussian launches brought by the beam generation approach is the rotational misalignment. For the low-loss line launch, the axes of the elliptical Gaussian beam need to be aligned with the profile on the beam shaping mask. As illustrated in Figure 3.25, rotational misalignment occurs when the beam shaping mask fails to be placed on the same reference axis as the elliptical Gaussian beam. In this figure, the dashed arrow indicates the reference axis and the yellow circle represents the waist of an incoming elliptical or circular Gaussian beam. For the line launch in this case, the elliptical Gaussian beam is not able to cover the line launch beam outline with a mask rotation on the transverse plane. However, the square launch is immune to the rotational misalignment because of its central symmetry. The beam shaping mask is free to rotate without any concern of mismatching.

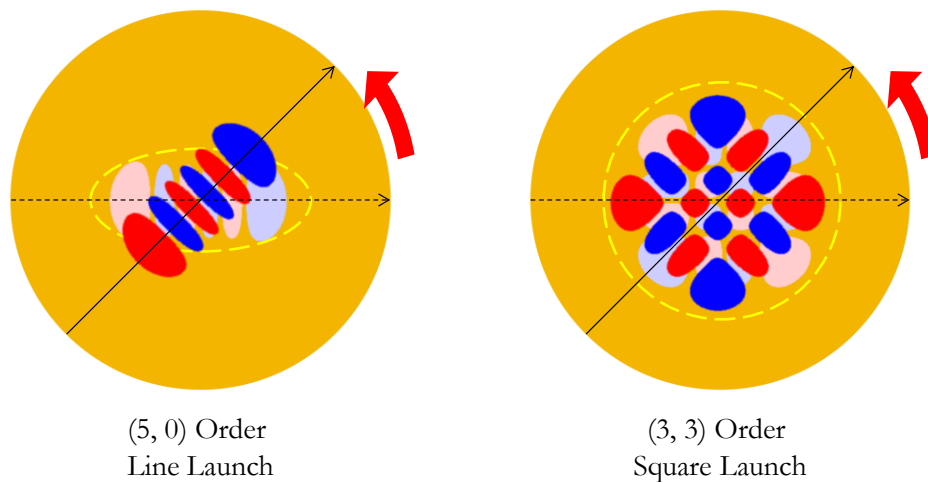


**Figure 3.25 Schematic illustrations of the rotational misalignment of the proposed low-loss Hermite-Gaussian launches**

Although the intensity and phase profile can be well maintained by the beam shaping mask, the rotational misalignment issue in low-loss line launch is still essential since it dramatically reduces the power that can pass through the beam shaping mask and may severely distort the generated beam profile. This reduction of coupling efficiency and beam profile accuracy can result in link failure caused by insufficient power budget and degraded bandwidth performance. Rotational misalignment can be removed by careful design and optimisation during the low-loss Hermite-Gaussian launch patchcord fabrication. Nevertheless, as seen in Figure 3.25, the immunity of this effect makes the low-loss square launch a simpler and more robust solution to bandwidth improvement over multimode glass fibre links compared with low-loss line launch.

### 3.3. Experimental Evaluation of Low-loss Hermite-Gaussian Launch

The performance of the low-loss Hermite-Gaussian launch scheme is experimentally evaluated in this section. For each of the examined low-loss Hermite-Gaussian launch implementations, the launching beam is generated using the beam shaping mask approach introduced in Section 3.2.3. The structure and fabrication process of the beam shaping mask are briefly discussed. Two sets of experiments are carried out for the low-loss line launch and square launches respectively. The effective modal bandwidths of these launches are measured in comparison with the conventional centre and offset launches. Misalignment tolerances are also investigated for both cases. The incident Gaussian beams are controlled by the designed optics, which gives optimised beam dimensions for low coupling losses as specified in Table 3-3. Error free 10 Gbit/s data transmissions are demonstrated for all proposed launches without equalisation.

Two worst case OM1 fibre samples, namely Fibre A and Fibre B are chosen to be used in the experiments. They are believed to present the most challenging fibres in the installed base. Test results have shown that Fibre A favours the centre launch and Fibre B favours the offset launch. The lengths of these two fibres are 250 m and 220 m respectively.

For the measurements of effective modal bandwidths, a 1310 nm direct modulated DFB laser is used at the transmitter end and a Picometrix 10 GHz multimode PIN diode is used as the receiver. The frequency response is firstly measured for a back-to-back link. This response is then used to normalize the frequency responses of the chosen fibre samples under different low-loss Hermite-Gaussian launches. Hence, the resulting responses indicate the bandwidth performance of the corresponding fibre sample. Misalignment tolerance is measured by taking a radial position scan from the core centre to 10  $\mu\text{m}$  offset with a step size of 0.5  $\mu\text{m}$ . Extra measurements are taken for low-loss line launch since the long axis (horizontal) and short (vertical) axis need to be evaluated individually. For each point, the effective modal bandwidth is taken from the measured frequency response curve. The centre launch misalignment tolerance is also measured in the same way for comparison purposes. In terms of the data transmission measurements, a 10GBASE-LRM SFP+ transceiver module is used. As proof of principle measurements, corresponding eye diagrams and BER measurements are evaluated accordingly under both the conventional and low-loss Hermite-Gaussian launches using Fibre A.

### 3.3.1. Fabrication of the Beam Shaping Mask

The beam shaping mask is used to convert the incoming Gaussian or elliptical Gaussian beam to an approximated Hermite-Gaussian beam. As shown previously in Figure 3.15, the beam shaping mask is placed between the incoming beam and the multimode glass fibre, acting as an extra optical filter in the system. The mask shapes the incoming beam by only letting through the light projected on the area where the Hermite-Gaussian beam intensity profile is above a certain amplitude threshold. The phase property is controlled by altering the thickness of the transparent layer of the mask to introduce a  $180^\circ$  phase difference between the adjacent spots in the designed intensity profile. Figure 3.26 illustrates the profile structure of a (3, 3) order square launch mask. The coloured areas are transparent and the threshold level of the shape outline is set to be 5% of the maximum intensity. The anti-phase property of the profile is illustrated in red and blue indicating the areas with a  $180^\circ$  phase difference, which is realized by the two different thicknesses of the mask material.

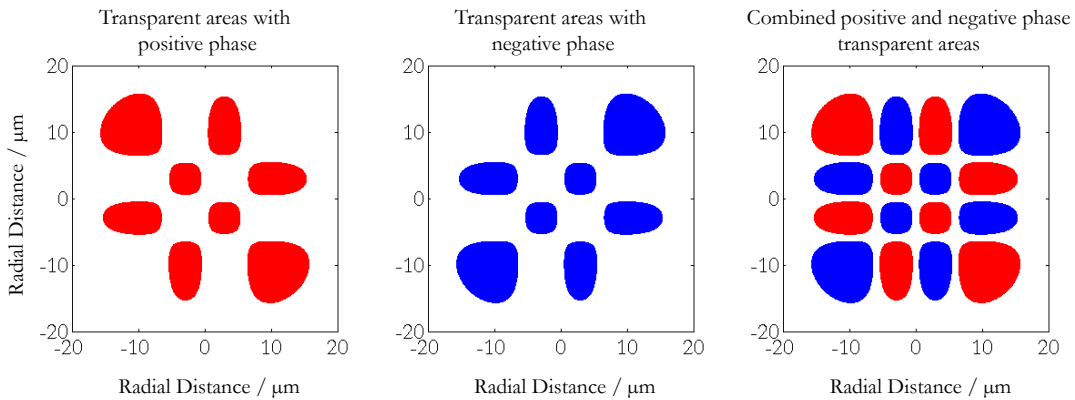


**Figure 3.26** Transparent areas on the beam shaping mask for (3, 3) order square launch at a wavelength of 1310 nm. The colour difference indicates a  $180^\circ$  phase change. The outline of the spot indicates the 5% intensity amplitude of an ideal profile

The fabrication steps of the beam shaping mask for (3, 3) order square launch are shown in Figure 3.27. A layer of 100 nm thick Au is deposited to a 5 nm Ti coated  $\text{SiO}_2$  glass surface. The 5 nm Ti coating is used for the purpose of adhesion between the gold and the glass substrate. The phase patterns of the profile are etched in two individual steps in order to perform a difference in depth. This difference, which creates a  $180^\circ$  relative phase change, can be realized using the length of half effective wavelength as

$$\text{Diff.depth} = 0.5 \times 1310 / 1.45 \approx 451.7 \text{ nm} . \quad \text{3-27}$$

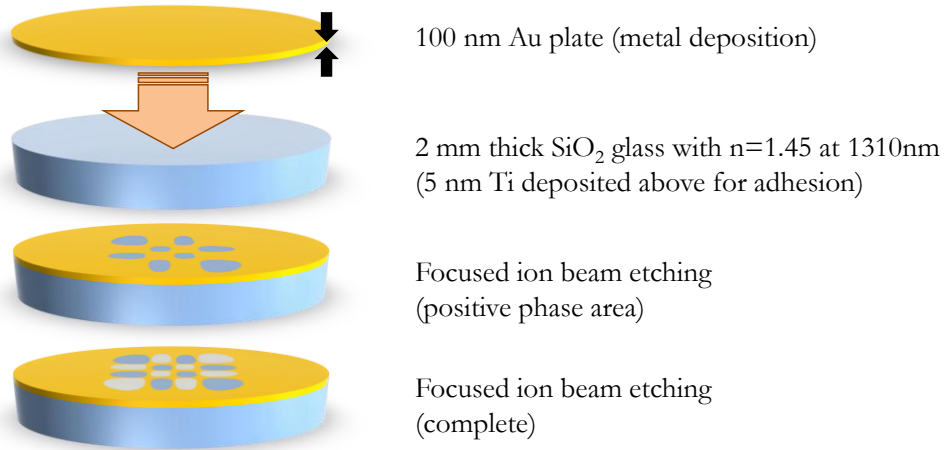


**Figure 3.27 Fabrication steps of the beam shaping mask for the (3, 3) order square launch. Dimension is not to be scaled**

Focused ion beam (FIB) is chosen to perform the etching since it avoids the process of shadow mask preparation in conventional dry/wet etching. During the etching process, several testing etches are performed first to decide the approximate time for removing the gold layer for each of the profiles. After this, further etchings are performed for the negative phase areas to generate the thickness difference stated in Equation 3-27. Since this thickness difference is the same for all the profiles, the etched volumes are solely dependent on the sizes of the transparent areas of each profile. The estimated rate of etching using the (5, 0) order line launch negative profile is around 150 nm/min [94]. Therefore, the etching times for the square launches can be decided by scaling this rate according to corresponding transparent areas sizes. The SEM images of the masks after a complete etching process for different launching profiles are shown in Figure 3.28.

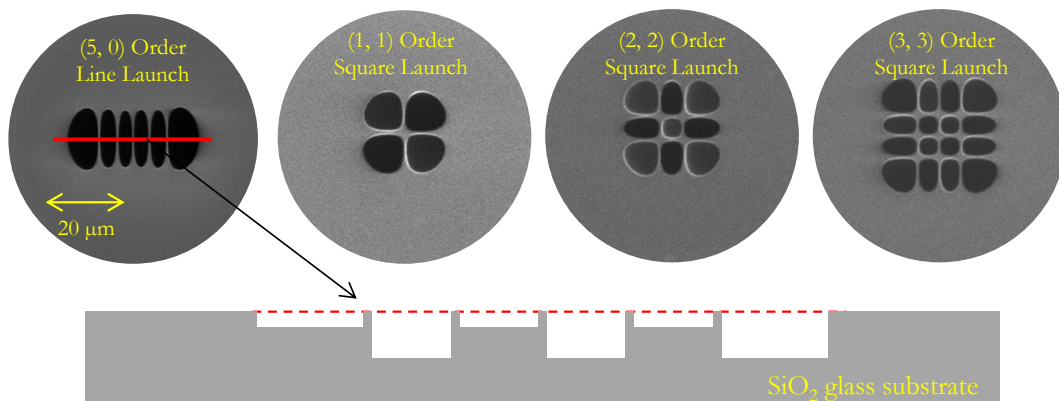


**Figure 3.28 SEM images of the masks for the (5, 0) order line launch<sup>13</sup> and (1, 1), (2, 2) and (3, 3) order square launches at a wavelength of 1310 nm and the schematic diagram of the cross section of the etched SiO<sub>2</sub> glass substrate**

<sup>13</sup> The (5, 0) order mask was fabricated by C. H. Kwok in the previous line launch work [94]

### 3.3.2. Experimental Demonstrations of the Low-loss Line Launch

Figure 3.29 illustrates the designed optical system used for the generation of the (5, 0) order low-loss Hermite-Gaussian line launch beam from an elliptical Gaussian beam. The single mode fibre provides the initial circular Gaussian beam with a 7  $\mu\text{m}$  FWHM. This Gaussian beam is collimated by two individual cylindrical lenses in two perpendicular directions independently. An aspheric lens is used to focus the collimated elliptical Gaussian beam to a pre-calculated size of 28  $\mu\text{m}$   $\times$  14  $\mu\text{m}$  in waist according to the theoretical work which provides low coupling loss and high mode group extinction ratios. The beam shaping mask is placed at the focal distance of the aspheric lens and a cleaved multimode glass fibre follows behind the mask with the facet almost touching it. The measured insertion loss of this system is 3.8 dB. This includes power loss at the beam shaping mask and the reflection of all optical parts. A 3 dB improvement in coupling efficiency is achieved compared with the previous line launch work [94].

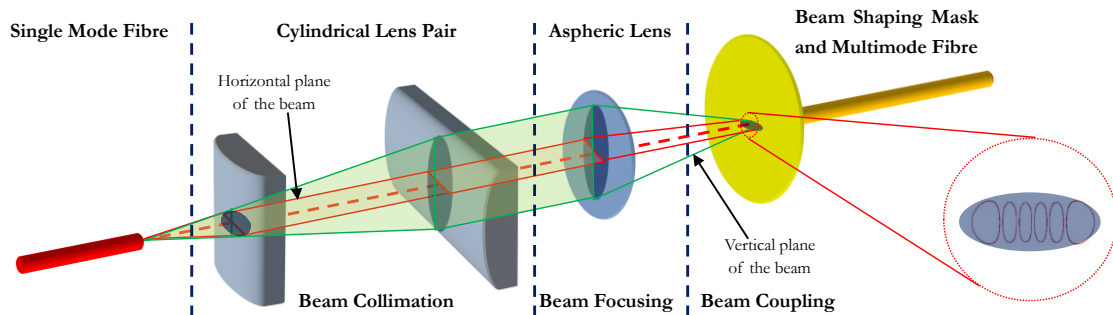
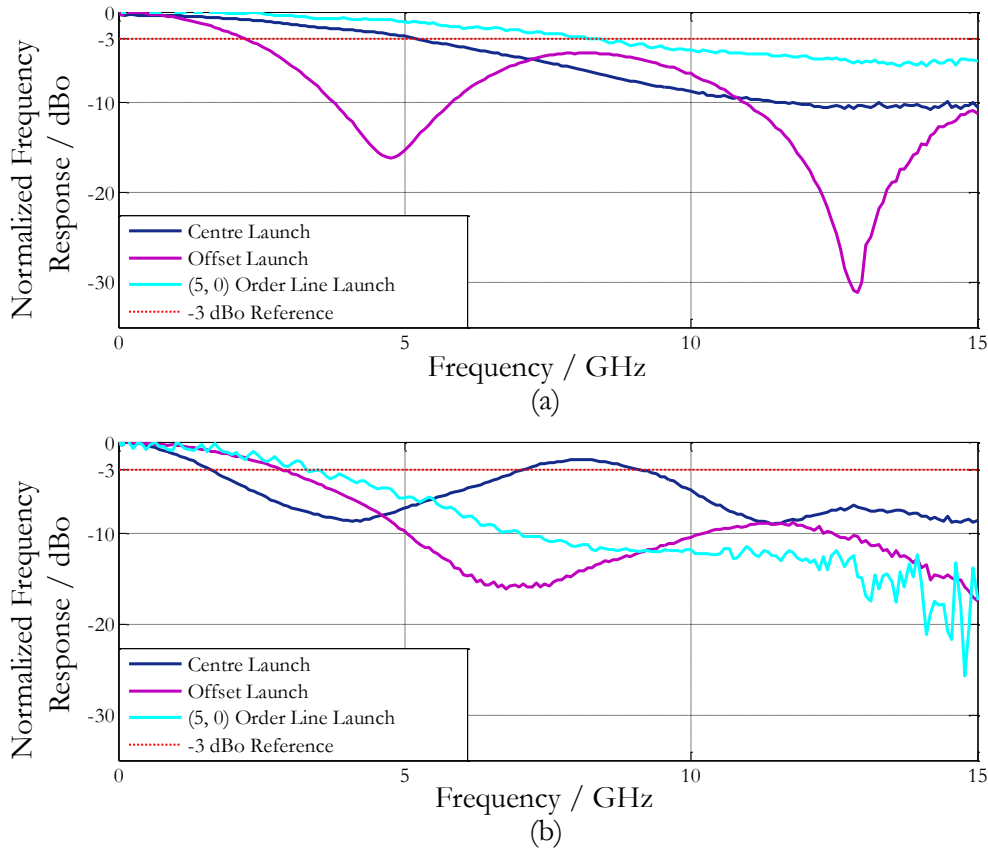


Figure 3.29 Schematic diagram of the elliptical Gaussian beam and (5, 0) order low-loss Hermite-Gaussian line launch beam generation

#### 3.3.2.1. Bandwidth Measurements

The effective modal bandwidth measurements over two multimode glass fibre samples using low-loss line launch scheme are shown in Figure 3.30. It can be seen clearly that the (5, 0) order low-loss line launch achieves higher bandwidth than the conventional centre launch and offset launch for both fibre samples. For Fibre A, which favours the centre launch in Figure 3.30 (a), a 2.05 GHz·km bandwidth-distance product is achieved using (5, 0) order line launch, whilst 1.4 GHz·km and 0.55 GHz·km are achieved by the centre launch and offset launch respectively. The bandwidth measurements for Fibre B are shown in Figure 3.30 (b), where all of the tested launches achieve relatively low bandwidths. The proposed (5, 0) order low-loss line launch outperforms both the centre launch and the offset launch with a bandwidth-distance product of 0.73 GHz·km. These

results confirm that the low-loss line launch guarantees bandwidth improvements over worst case multimode glass fibres favouring either the centre launch or the offset launch.



**Figure 3.30** Effective modal bandwidth measurements for the centre launch, offset launch and (5, 0) order low-loss line launch over (a) Fibre A and (b) Fibre B

### 3.3.2.2. Misalignment Tolerance

Launching misalignment is an important factor to evaluate the robustness of a launch scheme over a multimode glass fibre link. In Section 3.2.4.1, the numerical calculations have been given for the effect of radial offsets on the bandwidth-distance product performance of worst case multimode glass fibres. Corresponding experimental investigations are carried out over Fibre A by performing the (5, 0) order low-loss line launch with different offset positions on the directions of its long and short axes. This is done by moving the butt-coupled cleaved multimode glass fibre along both axes with a step size of  $0.5 \mu\text{m}$ . A reference peak bandwidth is measured with perfectly aligned launch condition using (5, 0) order low-loss line launch, and the bandwidths of the cases with launching offsets are then compared with this reference to show corresponding degradation. Figure 3.31 illustrates the bandwidths within an offset range of  $0\sim 10 \mu\text{m}$  for both axes of the (5, 0) order low-loss line launch profile. The centre launch bandwidths

are measured at the same misalignment positions for comparison. The results indicate that the bandwidth drops faster on the long axis (horizontal) direction than short axis (vertical) for the (5, 0) order low-loss line launch. This characteristic matches with the numerical calculations shown in Figure 3.21. The (5, 0) order low-loss line launch consistently exhibits a bandwidth improvement over the centre launch at the same offset position within the 10  $\mu\text{m}$  misalignment range. Furthermore, it has a bandwidth with radial offset higher than that of a perfectly aligned centre launch until the misalignment is greater than 8  $\mu\text{m}$ .

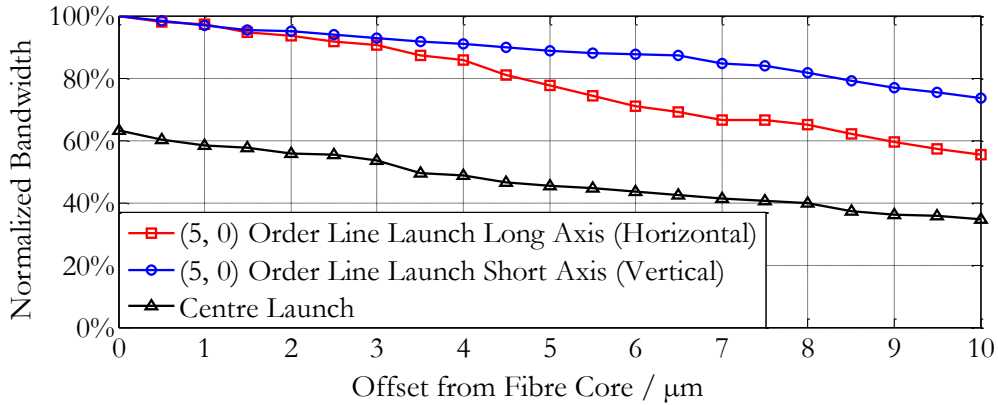


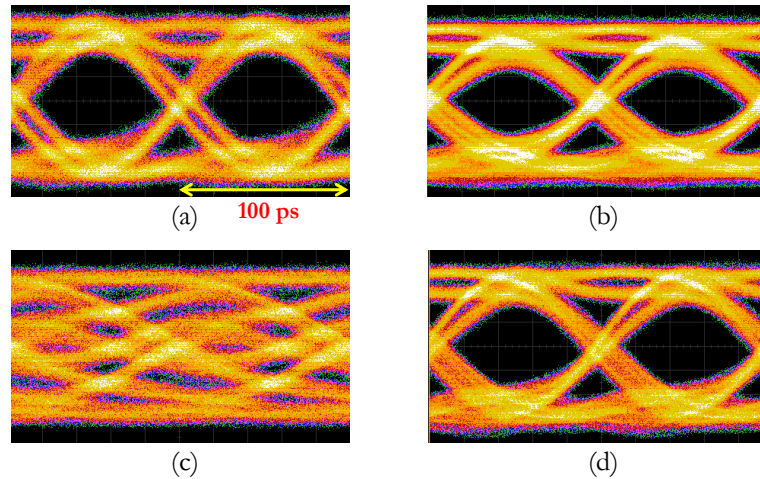
**Figure 3.31 Normalized bandwidths of the (5, 0) order low-loss line launch and centre launch with radial offsets from 0  $\mu\text{m}$  to 10  $\mu\text{m}$**

### 3.3.2.3. Data Transmission Measurements at 10 Gbit/s

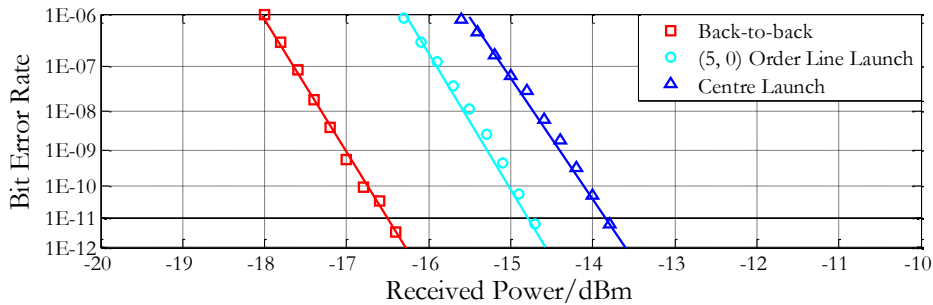
Using the same set up shown in Figure 3.29, the (5, 0) order low-loss line launch is implemented in a complete 10 Gbit/s data transmission link. A commercially available IEEE 10GBASE-LRM SFP+ transceiver is used in this experiment. This transceiver consists of a 1310 nm FP laser and a PIN diode. Fibre A is used as the worst case fibre sample in this evaluation by way of example. As specified in the IEEE 10GBASE-LRM task force, the transmitter and waveform dispersion penalty (TWDP) is evaluated using a  $2^9-1$  PRBS data sequence [114]. Hence, the PRBS with the same length is applied as the modulation signal in this experiment and the bit rate is also set according to the standard at 10.3125 Gbit/s. No equalisation is applied to the received signal in this setup.

Figure 3.32 shows the eye diagrams for the back-to-back link, centre launch, offset launch and proposed (5, 0) order low-loss line launch at a received power of -6 dBm. It is clear that the (5, 0) order low-loss line launch has a more widely open eye than that of the centre launch and offset launch. The corresponding BER measurements are shown in Figure 3.33. The offset launch cannot achieve error free ( $\text{BER} \leq 10^{-12}$ ) transmission due to

the severe ISI in an equalisation-free link as shown in Figure 3.32(c), hence is not included in the BER comparison. The (5, 0) order low-loss line launch achieves a sensitivity of -14.7 dBm. Compared with the back-to-back BER curve, which has an error free received power of -16.3 dBm, this indicates a 1.6 dB power penalty. In contrast, the centre launch achieves a sensitivity of -13.7 dBm, which gives a 2.6 dB penalty compared with the back-to-back case. Therefore, the (5, 0) order low-loss line launch achieves 1 dB sensitivity improvement over the centre launch.



**Figure 3.32** Eye diagrams of the (a) back-to-back link, (b) centre launch, (c) offset launch and (d) (5, 0) order low-loss line launch at the received power of -6 dBm



**Figure 3.33** Corresponding BER measurements for the back-to-back link, centre launch and (5, 0) order low-loss line launch

These results show that an equalisation-free 10 Gbit/s data transmission is achieved using the (5, 0) order low-loss line launch with low-loss implementation. This scheme exhibits high bandwidth performance owing to its near single mode group operation in the mid-order range, which minimizes the intermodal dispersion and has good immunity to the core centre index defects. The error free transmission over 250 m worst case fibre (Fibre A) confirms that the low-loss Hermite-Gaussian line launch, avoiding the manual testing specified in dual launch, is a robust single launch, equalisation-free solution to the IEEE 10GBASE-LRM standard with simple implementation and improved bandwidth.

### 3.3.3. Experimental Demonstrations of the Low-loss Square Launches

Figure 3.34 illustrates the schematic diagram of the (2, 2) order low-loss Hermite-Gaussian square launch beam generation in a complete multimode glass fibre link. Similarly to that for the low-loss line launch, single mode fibre is used to provide the initial circular Gaussian beam with a FWHM of  $7\ \mu\text{m}$ . An optical lens system is designed to generate a focused Gaussian beam with an  $18\ \mu\text{m}$  waist as required by the (2, 2) order low-loss square launch (see Table 3-3). This optical lens system is also used for the (1, 1) and (3, 3) order low-loss square launches for proof of principle demonstrations. Coupling losses higher and lower than the optimal calculations are expected for these two launches respectively since  $18\ \mu\text{m}$  is not the optimal configuration. The rest of the experimental setup is the same as the low-loss line launch configurations. All of the three proposed Hermite-Gaussian square launch profiles are examined using this experimental setup and the coupling losses are measured as 3.2 dB, 3.3 dB and 3.5 dB for the (1, 1), (2, 2), and (3, 3) order low-loss square launches respectively.

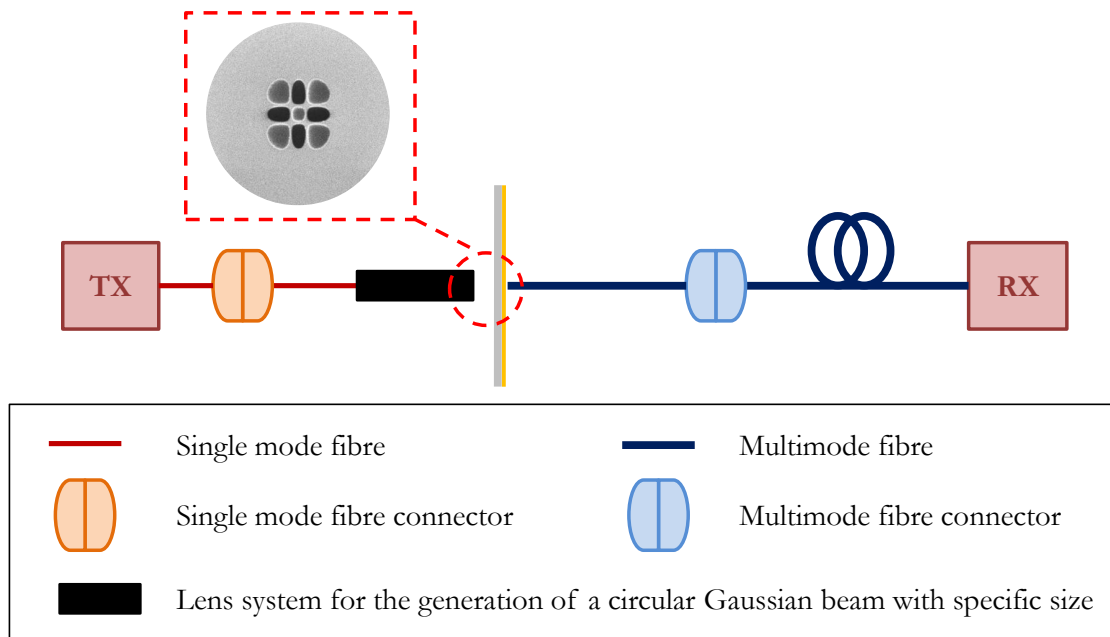
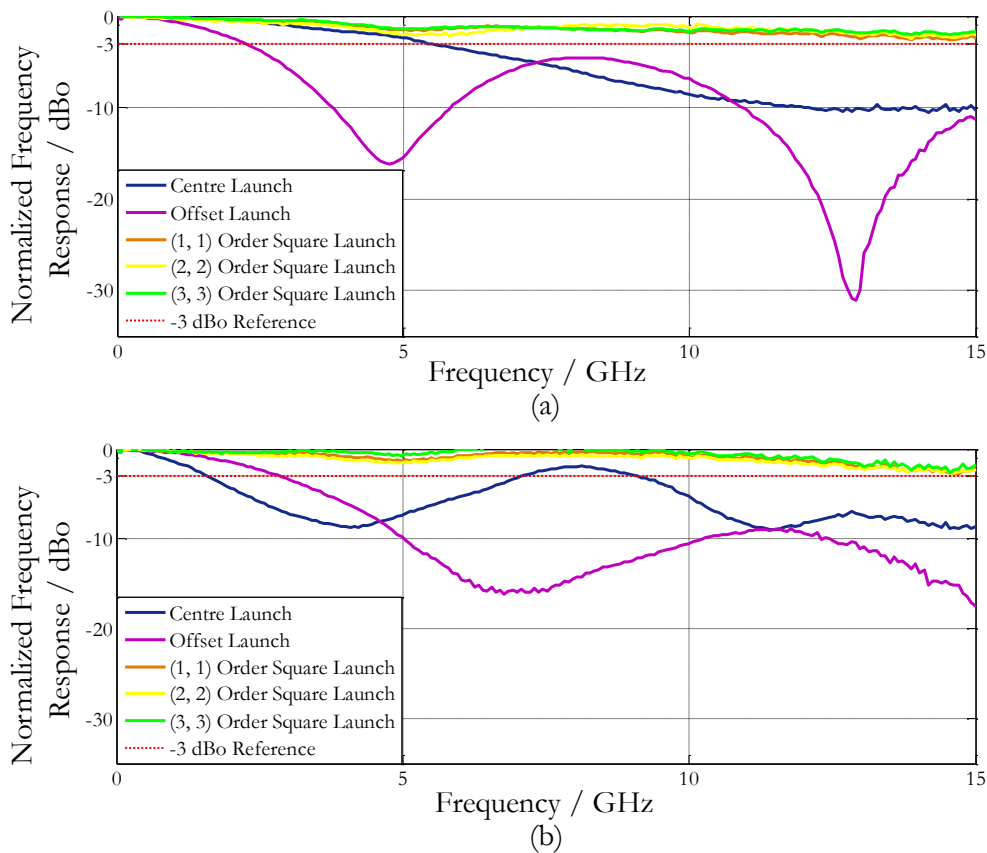


Figure 3.34 Schematic diagram of the (2, 2) order low-loss Hermite-Gaussian square launch beam generation and experimental setup

#### 3.3.3.1. Bandwidth Measurements

The effective modal bandwidth measurements using three different orders of low-loss Hermite-Gaussian square launches over two fibre samples are shown in Figure 3.35. All of the proposed low-loss square launches achieve higher bandwidths than the conventional centre launch and offset launch. As seen in Figure 3.35 (a), the frequency response curves of the low-loss square launches are above -3 dBo at over 15 GHz, which

indicates a bandwidth-distance product of greater than  $3.75 \text{ GHz}\cdot\text{km}$  for Fibre A. In contrast, the measured dual launch bandwidth-distance product for Fibre A is only  $1.4 \text{ GHz}\cdot\text{km}$ . The same measurements are taken for Fibre B as shown in Figure 3.35 (b). The low-loss square launches outperform the dual launch ( $0.7 \text{ GHz}\cdot\text{km}$ ) with an above  $3.3 \text{ GHz}\cdot\text{km}$  ( $15 \text{ GHz} \times 0.22 \text{ km}$ ) bandwidth. Near two-fold and five-fold improvements are achieved by using the low-loss square launches over Fibre A and Fibre B respectively. Furthermore, the low-loss square launches frequency responses are generally flat. This avoids the dips in the response as seen in the offset launch of Fibre A and Fibre B, which tends to ease the equalisation process if needed in an extended reach application.



**Figure 3.35 Effective modal bandwidth measurements for the (1, 1), (2, 2) and (3, 3) order low-loss square launches over (a) Fibre A and (b) Fibre B**

### 3.3.3.2. Misalignment Tolerance

The low-loss Hermite-Gaussian square launches with radial offset are evaluated in terms of normalized bandwidths with respect to a perfectly aligned launch. As seen in Figure 3.36, the misalignment tolerance performances of the low-loss square launches are similar to that of the line launch in the long axis direction. With  $10 \mu\text{m}$  radial offset, the worst case degraded bandwidth is above 60% of the case under perfect launching condition.

For the entire measured range of 0~10  $\mu\text{m}$ , the bandwidths of the low-loss square launches consistently outperform the centre launch. In general, referring to Figure 3.31 and Figure 3.36, a  $\pm 4 \mu\text{m}$  misalignment tolerance is achieved for all the proposed low-loss Hermite-Gaussian launches taking 20% degradation as a reference.

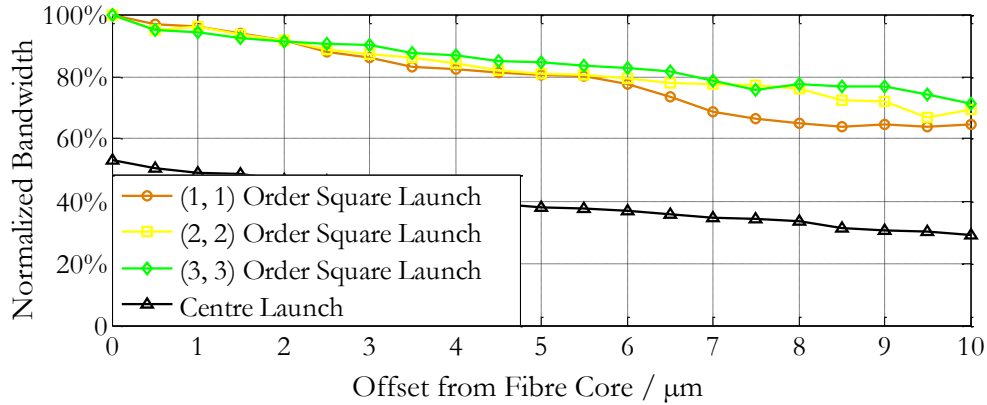


**Figure 3.36 Normalized bandwidths referring to perfectly aligned launch for the low-loss square launches and centre launch with radial offset from 0  $\mu\text{m}$  to 10  $\mu\text{m}$**

### 3.3.3.3. Data Transmission Measurements at 10 Gbit/s

The corresponding 10 Gbit/s data transmission measurements are carried out to evaluate the low-loss Hermite-Gaussian square launches. The same devices and configurations are used in this investigation as the low-loss line launch experiments. Figure 3.37 demonstrates the eye diagrams for all of the evaluated launches. It can be clearly seen that the proposed low-loss square launches generally achieve larger and wider eye openings than those of the centre launch and offset launch. The corresponding BER measurements over Fibre A for the centre launch and proposed low-loss square launches are shown in Figure 3.38. The offset launch again is not able to achieve error-free transmission, thus is not plotted in this BER graph. All of the low-loss square launches generally achieve a lower power penalty referring to the back-to-back case compared with the centre launch. The (1, 1) order low-loss square launch gives the best sensitivity performance with a back-to-back penalty of 2.2 dB, which is a 0.8 dB improvement over the centre launch. The results confirm that the low-loss Hermite-Gaussian square launches are robust solutions to bandwidth improvement over multimode glass fibre links with simple implementations.

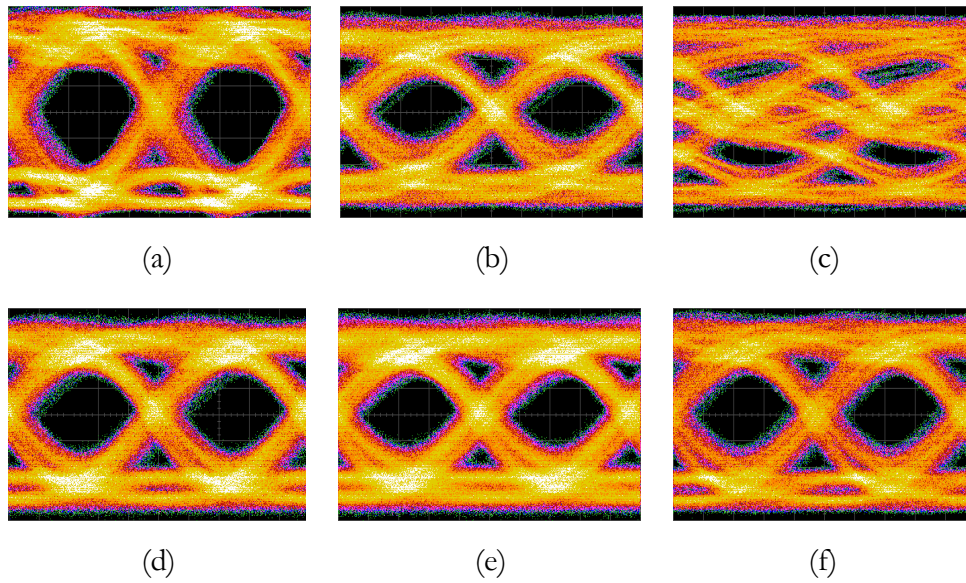


Figure 3.37 Eye diagrams of the (a) back-to-back link, (b) centre launch, (c) offset launch and (d)-(f) (1, 1), (2, 2) and (3, 3) order low-loss square launches at the received power of -6 dBm

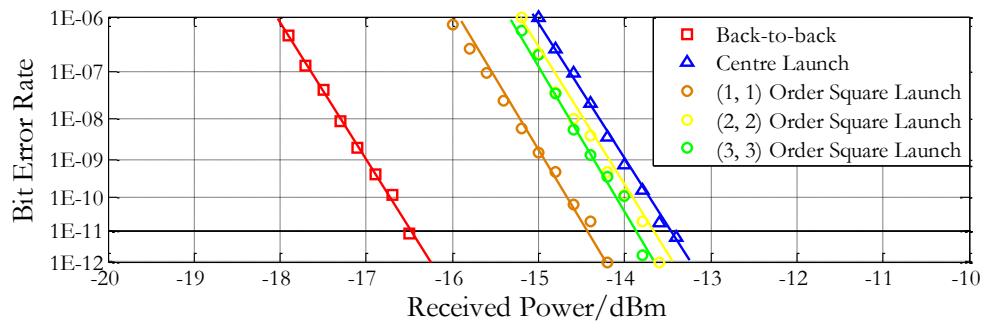


Figure 3.38 Corresponding BER measurements for the back-to-back, centre launch and proposed low-loss square launches

### 3.4. Conclusions

In this Chapter, a novel optical launch scheme, namely low-loss Hermite-Gaussian launch is proposed for bandwidth improvement for multimode glass fibre links. The principles of this launch scheme are derived and corresponding numerical calculations are demonstrated. Using the standard Cambridge-108MMF model, detailed statistical evaluation is also carried out. The low-loss approach for practical launch implementations is carefully discussed and the experimental results are given based on this approach.

Simulation has shown that the near single mode group operation can be achieved even for the worst case multimode glass fibres using the Hermite-Gaussian launches. Both the mode group extinction ratio and bandwidth-distance product results show that the Hermite-Gaussian launches outperform the conventional centre launch and offset launch with above 18 dB mode group power extinction ratios and truncated maximum bandwidths of 100 GHz·km. The improved coupling losses of the proposed Hermite-Gaussian launches are achieved using either a matched elliptical Gaussian beam with a line-shaped Hermite-Gaussian profile, or matched circular Gaussian beams with square-shaped Hermite-Gaussian profiles. Optimised beam waists are calculated to provide high mode group power extinction ratio whilst low coupling loss at the beam shaping mask. The approximately generated Hermite-Gaussian profiles are evaluated using the same worst case fibre model, which gives degraded but still high mode group power extinction ratios of above 12 dB. This maintains very high effective modal bandwidth performance which also gives the truncated numerical limit of 100 GHz·km.

Launch offset is also considered in the theoretical work to evaluate the practical implementation issues along with the proposed low-loss Hermite-Gaussian launches. With a worst case radial offset of 3  $\mu\text{m}$ , a minimum bandwidth-distance product of 15 GHz·km is achieved for all of the proposed launches for an ideal multimode glass fibre. Statistical calculations based on the Cambridge-108MMF model show that the bandwidth-distance products using the low-loss Hermite-Gaussian launches are generally higher than that of the centre launch and offset launch and comparable to the dual launch. These results are all based on the low-loss launch profile generation approach which gives approximated Hermite-Gaussian launching profile. In addition to the radial misalignment evaluation, phase profile mismatches between adjacent Gaussian-like spots in a Hermite-Gaussian profile are also studied. A  $\pm 0.2\pi$  phase tolerance for 3 dBo degradation of the mode group power extinction ratio is demonstrated. This represents a

$\sim \pm 90$  nm etching depth difference tolerance which is well within the control in the fabrication using FIB. Furthermore, in terms of the patchcord fabrication limitation, the low-loss square launch implementation exhibits a better rotational misalignment characteristic compared with the low-loss line launch implementation due to the circular-shaped incoming Gaussian beam. The overall link yield calculations using the practical low-loss launch profile generation approach and the worst case launching misalignment condition show that the (3, 3) order low-loss Hermite-Gaussian square launch, as an example, statistically gives the best performance with a 50% bandwidth improvement over the dual launch for a 99% yield of the OM1 fibre installed base.

A simple beam shaping mask is developed for practical implementations of the proposed low-loss Hermite-Gaussian launches. The mask allows through all the light with normalized intensity that is higher than 5% of the maximum and blocks the rest to create an approximated Hermite-Gaussian profile. The phase property of the profile is realized by performing an etching depth difference between adjacent spots.

Based on this beam shaping mask, significant effective modal bandwidth improvements are experimentally demonstrated under both the low-loss Hermite-Gaussian line launch and square launches for fibre samples either favours the centre launch or the offset launch. By using the optimal incident Gaussian beam for (5, 0) order line launch and (2, 2) order square launch, the measured coupling losses are 3 dB and 3.6 dB less than the previously reported conventional line launch approach. For all of the investigated low-loss Hermite-Gaussian launches, the frequency responses are smooth over a wide range. This is a strong evidence of achieving single mode group operation through the tested fibre samples. The effect of radial misalignment is evaluated by measuring the bandwidth degradation at different launching positions with respect to an ideal launch. The -3 dBo bandwidths of the proposed low-loss Hermite-Gaussian launches remain higher than that of the centre launch for offsets  $\leq 8 \mu\text{m}$  using line launch and for offsets  $\leq 10 \mu\text{m}$  using square launches. It is worth noting that the low-loss Hermite-Gaussian line launch scheme has a higher misalignment tolerance on its short axis (vertical) than long axis. This is due to the less severe phase misalignment along the vertical direction for the (5, 0) order line launch profile. In general, the measured misalignment tolerance performance in terms of bandwidth degradation rates for all of the proposed Hermite-Gaussian launches are comparable to the centre launch and remain at least 80% of the maximum bandwidth-distance product in a  $\pm 4 \mu\text{m}$  offset range.

Equalisation-free 10 Gbit/s data transmissions are demonstrated over a worst case fibre (Fibre A) favouring the centre launch, by way of example. With near single mode group operation, the proposed low-loss Hermite-Gaussian line launch and square launches exhibit excellent performance with widely opened eyes. Corresponding BER measurements indicate that the low-loss Hermite-Gaussian launches are robust solutions to the IEEE 10BASE-LRM standard with an extended reach. Without equalisation,  $\sim 1$  dB sensitivity improvement at BER of  $10^{-12}$  is demonstrated for the proposed low-loss Hermite-Gaussian launches compared with the centre launch.

Both the theoretical and experimental results shown in this Chapter confirm that the proposed low-loss Hermite-Gaussian launches are robust solutions to the bandwidth enhancement over multimode glass fibre links with improved coupling loss compared with the conventional line launch. The intensity and phase shaping mask approach is proved to be a simple and practical solution to the launch implementation and is feasible to be integrated into a patchcord similar to that for the offset launch. The studies on various aspects of misalignment issues of the launches confirm that the low-loss Hermite-Gaussian launches are reliable and feasible for practical implementations.

# CHAPTER 4

## THEORETICAL STUDY OF MULTILEVEL MODULATION SCHEMES FOR LED-BASED PLASTIC OPTICAL FIBRE LINKS

*Multilevel modulation schemes are attractive solutions to high speed SI-POF-based links because they provide high spectral efficiency. A thorough theoretical study is described in this chapter which investigates the characteristics of a baseband and a passband multilevel modulation scheme, namely pulse amplitude modulation (PAM) and carrier-less amplitude and phase modulation (CAP) respectively. It has been shown that effort needs to be given to designing a system which satisfies the Nyquist criterion to achieve an ISI-free transmission. In the simulation model, the components used in a SI-POF link are modelled as low-pass filters. Based on the bandwidth parameters of commercial devices, the modelled SI-POF system is shown to have an overall bandwidth  $< 200$  MHz for a 50 m length. Consequently, even using a modulation scheme with high spectral efficiency, the Nyquist criterion does not always hold unless strong equalisation is carried out at the receiver. In practice, feed-forward equalisers and decision feedback equalisers are commonly used in equaliser structures to compensate the channel dispersion. PAM and CAP systems with 2, 4 and 8 levels are evaluated based on the system model and various equalisation configurations.*

#### 4.1. Multilevel Modulation Schemes in Optical Communications

Since Shannon presented his original work on communication theory in 1948/1949 [115], it has always been a challenge for researchers in succeeding generations to seek technologies to approach the Shannon capacity of a linear Gaussian channel. Efforts have been made particularly on developing advanced modulation schemes [116, 117]. It is well known that by transmitting  $n$  binary bits in one symbol, one can increase the bandwidth efficiency by  $n$  times. This normally requires the symbol to have multiple levels to represent a binary sequence of a certain length. A typical multilevel modulation scheme defines  $2^r$  levels to transmit  $r$  bits in one symbol. As seen in Figure 4.1, the mappings between the original binary bit sequences and the transmitted symbols using multilevel PAM and CAP schemes are shown. Taking PAM-8 as an example, it uses only a third of the symbol rate of NRZ to achieve the same aggregate data rate. According to Ungerboeck [118], the capacities of the systems using multilevel modulation schemes asymptotically approach the Shannon capacity in an additive white Gaussian noise (AWGN) channel. This makes multilevel modulation schemes very attractive for high speed communication systems. Moreover, the multilevel regime can also be applied to quadrature modulation schemes such as CAP to further improve the spectral efficiency [119]. This will be further discussed in detail in the following sections of this chapter.

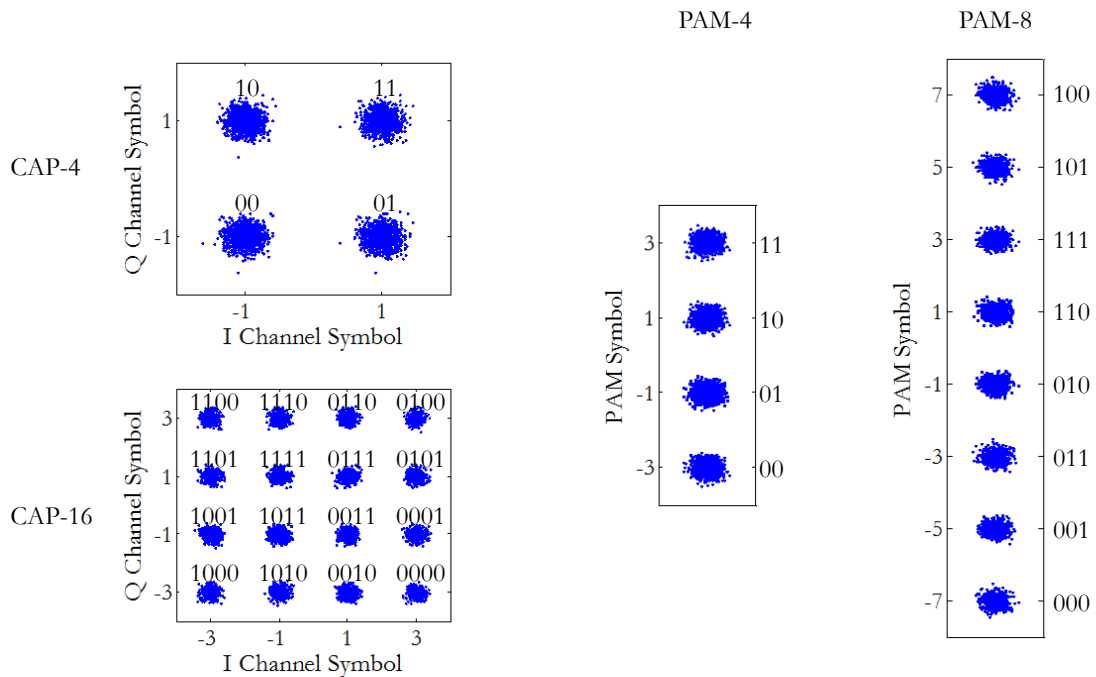


**Figure 4.1** Constellation maps of the CAP-4, CAP-16, PAM-4 and PAM-8 modulation schemes (symbols are labelled with corresponding binary sequences)

Conventionally, optical communications relied on the NRZ modulation scheme for systems with relatively low bandwidth requirements compared with the capability of available transceivers and optical fibres. The NRZ modulation also gave a simple implementation and easy clock recovery circuit design. As the data rate continued to increase in order to meet the growing traffic requirement, the electrical devices required in an optical link tended to reach their limits for bit rates above 10 Gbit/s. Multilevel modulation schemes started to be seriously considered and investigated by pioneers for their potential applications in optical communication [120-124]. Although the early stage of multilevel modulation work in the optical domain was not considered in the 10G Ethernet standard, it clearly inspired researchers to explore in this field for future optical systems. In recent decades, multilevel modulation schemes for 40G/100G optical data-communication links were intensively studied. Some exciting results were shown at a data rate of 40 Gbit/s [53, 125]. And most recently in the IEEE802.3 'Next Generation 100 Gb/s Optical Ethernet Study Group', multilevel PAM schemes were proposed by multiple active attendees and were intensively discussed [126-128].

While multilevel modulation schemes for glass fibre links have been very popular, they are also considered as strong candidates for high speed POF links. As introduced in Chapter 1, POFs exhibit lower bandwidth compared with glass fibres. Multilevel modulation schemes improve the bandwidth efficiency whilst not introducing much complexity and costs to the overall system [129]. Initially, the related research activities regarding the multilevel modulation schemes for POF were led by the POF-ALL project [130], where a 100 Mbit/s SI-POF link was extended to a length of 275 m using the PAM-8 modulation and feed-forward error correction (FEC). This fundamental work was widely recognised as the 'rebirth of the large-core POF [131]. Later, an integrated receiver was developed for the PAM-based system and a 170 Mbit/s error free transmission was demonstrated using this receiver for a SI-POF link over 115 m [132]. Furthermore, as a succeeding project of POF-ALL, the POF-PLUS set its goal to demonstrate gigabit/s POF links [133]. This not only set a technology challenge in the POF field, but also expanded the potential applications of POF links, such as in the next generation home and vehicle networks. An exciting 5.6 Gbit/s discrete multi-tone (DMT) based system was demonstrated over 50 m GI-POF [134]. Meanwhile, other advanced multilevel modulation schemes like carrier-less amplitude and phase (CAP) was also

investigated. The best performance achieved using this scheme was 300 Mbit/s over 50 m SI-POF<sup>14</sup> [57].

In Figure 4.2, some of the most recently published results of achieving high speed POF transmissions using LED-based transmitters are shown. It is believed that the next generation home networks will require a data rate higher than 1 Gbit/s and the wiring length will be  $\sim 50$  m [130]. This makes the purple region on the graph particularly interesting for this field of application. Another potential application for LED-based POF links is the future high speed media and control networks in vehicles. The bit rate and link length preferred in such networks are highlighted in green in Figure 4.2. Although the research on the conventional NRZ modulation has enabled 1.25 Gbit/s and 1 Gbit/s over 50 m and 75 m POF with forward error correction [135, 136], it will be interesting to explore potential techniques enabling even higher data rates and preferably without forward error correction for the purpose of maintaining the system cost and simplicity.

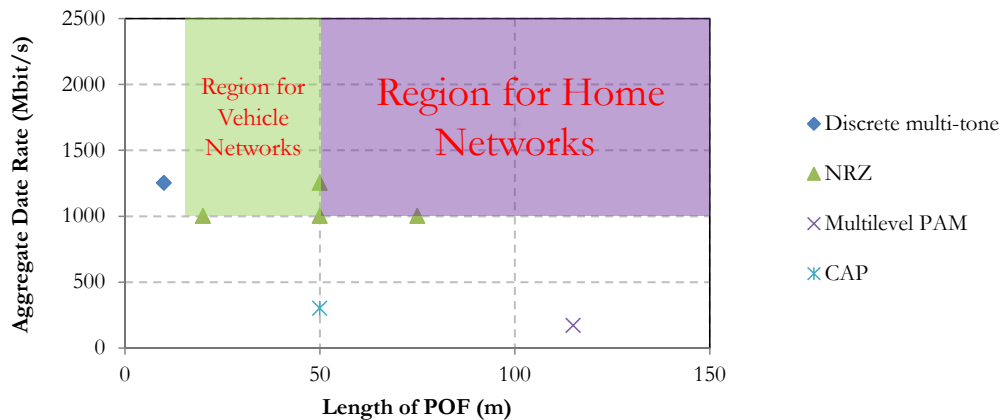


**Figure 4.2** Published data rates and reaches of LED-based POF links using different modulation schemes in recent years

<sup>14</sup> This does not include the work involved in this dissertation, where a 1.5 Gbit/s CAP-64 transmission is demonstrated over 50 m SI-POF.

## 4.2. Pulse Amplitude Modulation

Pulse amplitude modulation (PAM) is one of the most basic baseband digital modulation schemes. PAM symbols are encoded from the original binary data sequence and are represented by a finite number (usually in the order of  $2^n$ ) of evenly distributed levels. In optical communication, as the light acts as a carrier with extremely high frequency, PAM can also be regarded as amplitude shift keying (ASK) where the intensity of the light is modulated. In an incoherent optical system, the optical-to-electrical conversion at the photodiode removes the optical carrier, down-converting the received PAM signal back to a baseband signal. The original binary data sequence can then be decoded accordingly. Figure 4.3 illustrates a typical PAM transmission system.

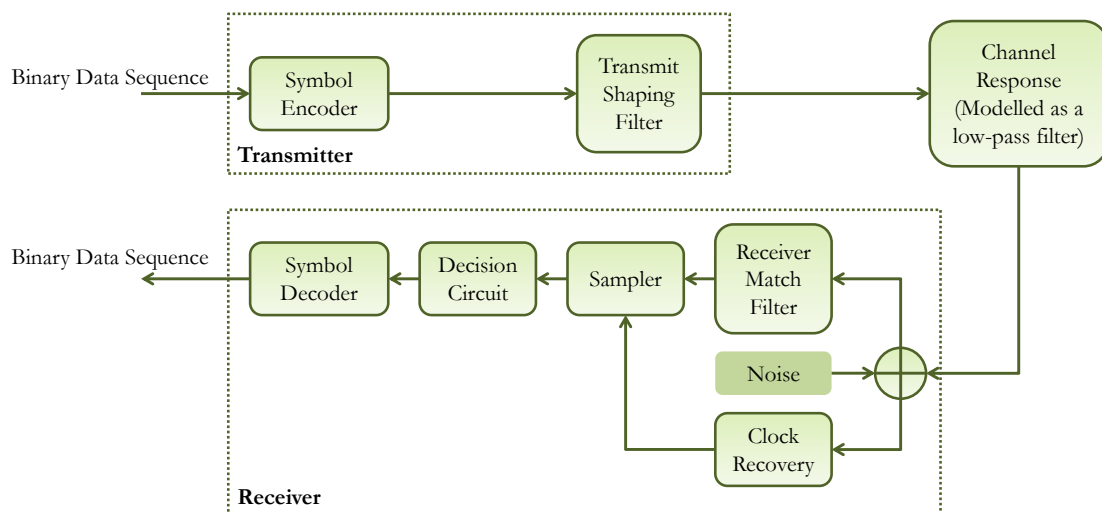


**Figure 4.3 Schematic diagram of a pulse amplitude modulation transmission system**

In the transmitter block, a binary data sequence is sent into the symbol encoder, which converts the incoming signal to PAM symbols. These symbols are applied to a transmitter shaping filter to create a continuous-time signal for transmission. The channel, for example a POF cable, can be modelled as a filter with a specific frequency response, which is normally a low pass filter that characterizes the dispersion introduced to the signal. At the receiver side, additive noise mainly comes from the thermal noise of the photodiode (i.e. PIN structure). The receiver itself also has a certain response, preferably matched to the transmitter and channel response to maximize the signal-to-noise ratio (SNR). This will be further discussed in the following sections. A clock recovery circuit is needed to recover the clock signal from incoming symbols to trigger the sampler. The samples are then processed according to a predefined threshold in the decision circuit for

the purpose of symbol recovery. Finally, a symbol decoder reverses the encoder process to recover the original binary data stream from the PAM symbols.

To better illustrate how the data is modulated in a PAM transmission, a schematic diagram of the bit-level operation in a PAM-8 transmitter is given in Figure 4.4. The PAM encoder has a code mapping table which maps the symbols to the binary sequences. In this example, the 8-level PAM encoder has a simple binary to decimal mapping and the transmitter is assumed to have an ideal rectangular response.

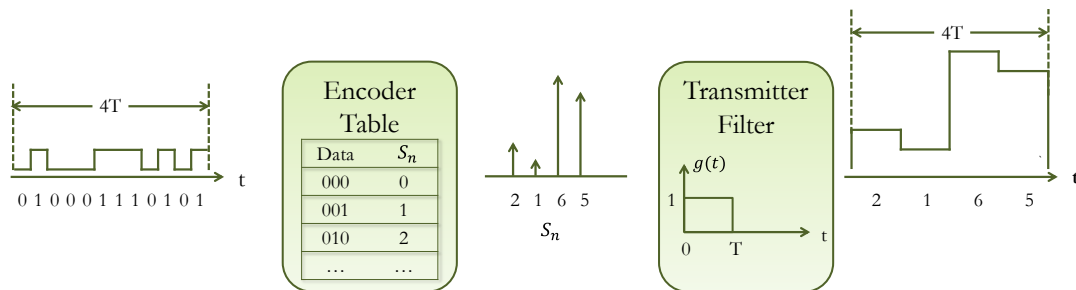


**Figure 4.4** A binary sequence is converted to PAM-8 symbols and modulated using a rectangular transmitter filter.  $T$  is the symbol period of the PAM-8 system

The output of the encoder can be seen as a train of impulses with different amplitudes representing the PAM-8 symbols. A rectangular response transmitter filter  $g(t)$  modulates the impulses to a continuous-time stair-shaped signal  $X(t)$  as

$$X(t) = \sum_{n=-\infty}^{+\infty} S_n g(t - nT). \tag{4-1}$$

After transmitting through the linear channel  $c(t)$ , the noise  $N(t)$  is added to the receiver, which results in the received signal  $Y(t)$  in the form of

$$Y(t) = \int_{-\infty}^{+\infty} c(t) \sum_{n=-\infty}^{+\infty} S_n g(t - nT - \tau) d\tau + N(t). \tag{4-2}$$

To recover the data from the received signal, a receiver needs to be designed to minimize the probability of errors. Besides eliminating any noise at frequencies higher than the PAM signal bandwidth, the pulse after the receiver should satisfy the Nyquist criterion to optimise the overall system performance [137].

### 4.2.1. The Nyquist Criterion

Ideally, the received pulse should not interfere with the adjacent pulses in digital communication systems. This can be achieved using pulses with a finite time domain response such as the rectangular pulse shown in Figure 4.4, where individual pulses have zero overlap with each other in the continuous-time signal. However, such pulses require infinite bandwidths, which cannot be achieved in a practical communication system. Therefore, other approaches are needed for the purpose of eliminating the interferences between symbols.

As demonstrated in Figure 4.3, the received signal is shaped by a filter before it is sampled. The signal just before the sampler can be written as

$$R(t) = \sum_{n=-\infty}^{+\infty} S_n q(t - nT) + M(t), \quad 4-3$$

where the received noise  $M(t)$  after the filter is

$$M(t) = N(t) * r(t), \quad 4-4$$

and the overall pulse shape  $q(t)$  at the sampler is

$$q(t) = g(t) * c(t) * r(t). \quad 4-5$$

In Equation 4-5,  $g(t)$ ,  $c(t)$  and  $r(t)$  are the responses of the transmitter filter, transmission channel and receiver filter respectively.

Sampling this signal gives the recovered symbol as

$$\begin{aligned} R(kT) &= \sum_{n=-\infty}^{+\infty} S_n q(kT - nT) + M(kT) \\ &= S_k q(0) + \sum_{n \neq k} S_n q(kT - nT) + M(kT) \end{aligned} \quad 4-6$$

Here, the second term in this equation is called inter-symbol interference (ISI) since it contains information from symbols other than  $k$  ( $n \neq k$ ). If this term is forced to zero, the ISI-free recovered symbol can be written as

$$\hat{R}(kT) = S_k q(0) + M(kT). \quad 4-7$$

Making  $\hat{R}(kT)$  and  $R(kT)$  equal, leads to the condition

$$q(kT - nT) = \begin{cases} 1, & k = n \\ 0, & k \neq n \end{cases} \Rightarrow q(kT) = \begin{cases} 1, & k = 0 \\ 0, & k \neq 0 \end{cases}, \quad 4-8$$

which makes

$$q(kT) = \delta_k, \quad \mathbf{4-9}$$

where  $\delta_k$  is the Kronecker delta function.

If we take the Fourier transform for each side of Equation 4-9, it gives [138]

$$Z(f) = \frac{1}{T} \sum_{n=-\infty}^{+\infty} Q(f + \frac{n}{T}) = 1, \quad \mathbf{4-10}$$

where  $Q(f)$  is the Fourier transform of  $q(t)$ .

It can be seen from Equation 4-8 that the received pulse  $q(t)$  must cross zero amplitude at time points of  $kT$  to get an ISI-free received signal. To interpret this in the frequency domain as shown in Equation 4-10, it requires that the sum of  $\frac{1}{T}$  shifted spectra must be equal to a constant. This condition is called the Nyquist criterion and a pulse that satisfies the Nyquist criterion is called a Nyquist pulse.

The Nyquist criterion is based on a sequence of pulses with specific shape with zero ISI between each other. As seen from Equation 4-9 and Equation 4-10, the Nyquist criterion actually concerns not only the pulse shape itself, but also the symbol rate of the corresponding system. It will be seen later that an actual Nyquist pulse always has an expression that relates to the symbol rate of the system. In other words, a pulse that satisfies the Nyquist criterion in one system is not necessarily a Nyquist pulse in other systems with different symbol rates.

To achieve the Nyquist criterion, it can be seen that given  $g(t)$  and  $c(t)$ , a specific design of  $r(t)$  can force  $R(kT)$  to have a zero ISI term. This receiver design approach is called the zero-forcing criterion. It may not be the optimal design since the change in the noise is not taken into account. As seen in Equation 4-4, the actual noise brought to the sampler also depends on  $r(t)$ . The zero-forcing criterion normally amplifies the noise quite significantly so the best adaption criterion is not always preferable.

#### 4.2.2. PAM Receiver Pulse Shape

To satisfy the Nyquist criterion, the baseband spectrum of a pulse must have a bandwidth that is larger than or equal to  $\frac{1}{2T}$ , where  $T$  is the symbol period. Figure 4.5 illustrates

the case where a pulse does not satisfy this condition. Since  $Q(f)$  has a bandwidth smaller than  $\frac{1}{2T}$ , there is a gap between each of the shifted  $Q(f)$ . Hence the equality relationship stated in Equation 4-10 cannot be satisfied.

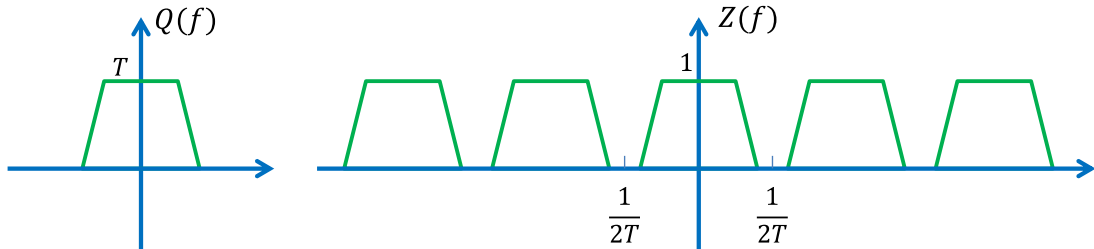


**Figure 4.5** The spectra  $Q(f)$  and  $Z(f)$  corresponding to the pulse that does not satisfy the Nyquist criterion

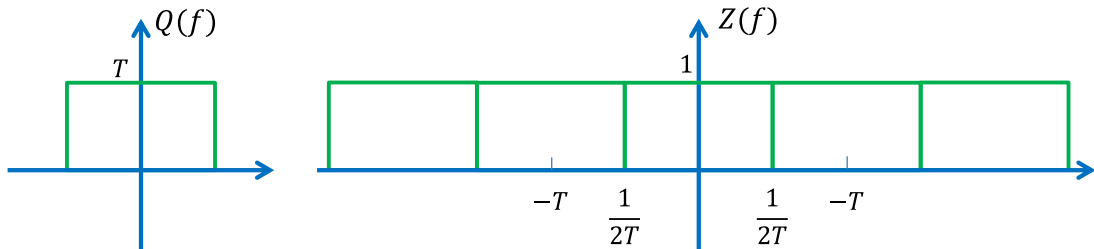


**Figure 4.6** The spectra  $Q(f)$  and  $Z(f)$  corresponding to an ideal band-limited pulse that satisfies the Nyquist criterion

The Nyquist criterion requires  $Z(f)$  in Figure 4.5 to be constantly equal to 1 for any frequency. If the minimum bandwidth  $\frac{1}{2T}$  is chosen, an ideal band-limited spectrum as shown in Figure 4.6 gives the ‘basic’ Nyquist pulse and can be expressed in the frequency domain as

$$Q(f) = \begin{cases} T, & |f| < \frac{1}{2T} \\ 0, & |f| \geq \frac{1}{2T} \end{cases}, \quad 4-11$$

and in the time domain as

$$q(t) = F^{-1}(Q(f)) = \frac{1}{T} \times T \times \frac{\sin(\pi \frac{t}{T})}{\pi \frac{t}{T}} = \text{sinc}(\frac{t}{T}). \quad 4-12$$

This is the well-known sinc function<sup>15</sup>. As seen in Figure 4.7, the pulse has zero amplitude at  $t = nT$ . Therefore, a sequence of sinc pulses with a symbol period  $T$  have no ISI at time  $t = nT$ . If a receiver is designed to sample the signal at  $t = nT$ , the samples will only contain the information from one symbol. Figure 4.8 illustrates the continuous-time waveform generated by a sinc shaping filter. It can be observed that there is no interference from either side of the transmitted pulses at  $t = nT$ .

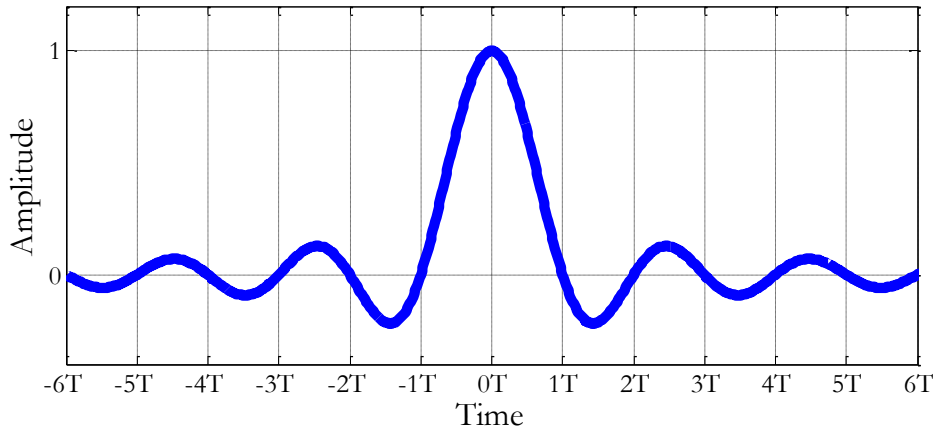


**Figure 4.7** Time domain waveform of a sinc function pulse truncated at  $\pm 6T$

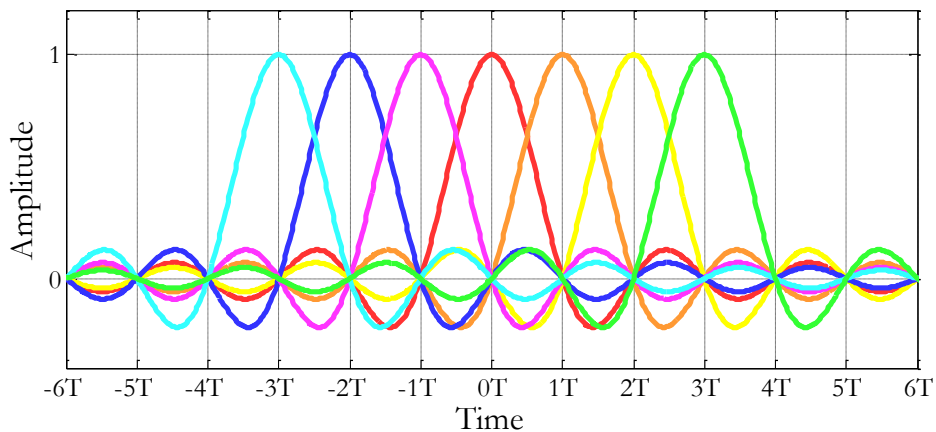


**Figure 4.8** ISI free transmission of a sinc pulse sequence with a symbol period of  $T$

In practice, a sinc pulse is not directly available due to the fact that it requires an ideal rectangular spectrum in the frequency domain, which cannot be perfectly generated by any form of electronics. Therefore, a practical Nyquist pulse normally has a bandwidth

---

<sup>15</sup> Here the sinc function is defined as  $\text{sinc}(x) = \frac{\sin(\pi x)}{\pi x}$

wider than  $\frac{1}{2T}$  with a roll-off factor in the spectrum. Typically, the raised-cosine filter satisfies these conditions and it is commonly used in communication systems.

The raised-cosine pulse can be written in the time domain as

$$p(t) = \left[ \frac{\sin(\pi t / T)}{\pi t / T} \right] \left[ \frac{\cos(\alpha \pi t / T)}{1 - (2\alpha t / T)^2} \right]. \quad 4-13$$

In the frequency domain it can be described using the following equations,

$$P(f) = \begin{cases} T, & |f| \leq \frac{1-\alpha}{2T} \\ \frac{T}{2} \{1 - \sin[\frac{T}{2\alpha} (|2\pi f| - \frac{\pi}{T})]\}, & \frac{1-\alpha}{2T} < |f| \leq \frac{1+\alpha}{2T} \\ 0, & |f| > \frac{1+\alpha}{2T} \end{cases}, \quad 4-14$$

where  $\alpha$  is the roll-off factor. Raised-cosine pulses and their Fourier transforms with several different roll-off factors are plotted in Figure 4.9. For  $\alpha = 0$ , the pulse becomes an ideal band-limited sinc pulse. For other values, the energy rolls off more gradually as  $\alpha$  increases. The roll-off factor is also known as the excess bandwidth. It indicates how much bandwidth of the pulse spectrum is above  $\frac{1}{2T}$  with respect to the -3 dB bandwidth.

For example if  $\alpha = 1$ , the excess bandwidth is 100%, where the spectrum rolls off from the peak very gradually and does not reach zero amplitude until

$$f_{zero} = \frac{1}{2T} + 100\% \times \frac{1}{2T} = \frac{1}{T}. \quad 4-15$$

As seen in Figure 4.9, the pulses extend at both ends in the time domain to infinity and the amplitudes decrease as  $\alpha$  increases. The ripples tend to have negligible amplitudes after several symbol periods. Therefore, with a reasonable large  $\alpha$ , the raised-cosine pulse can be practically approximated using a finite impulse response (FIR) filter by truncating the pulse at a certain length of integer multiples of  $T$ .

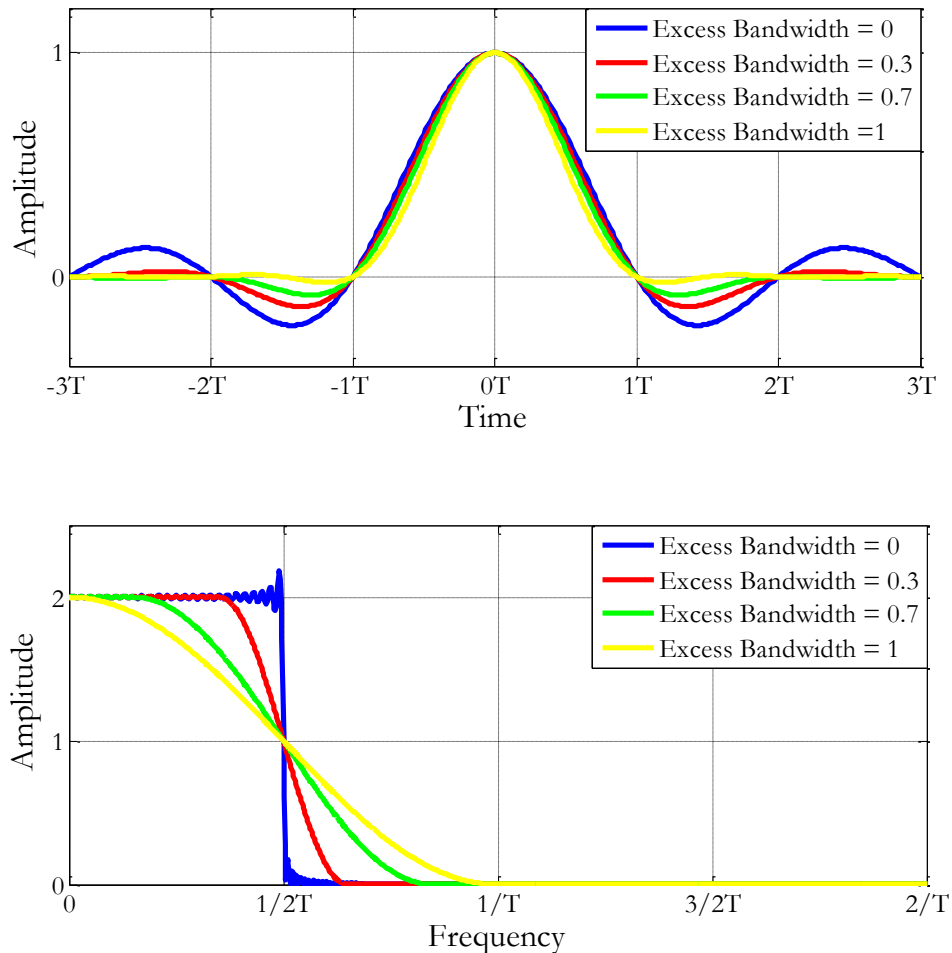


**Figure 4.9** Waveforms (top) and spectra (bottom) of a series of raised-cosine pulses with different excess bandwidths

Ideally in a PAM system, the received pulse  $q(t)$  should be designed so that it satisfies the Nyquist criterion. However, for a system where the channel bandwidth is much larger than the signal bandwidth, a simple low-pass filter receiver is sufficient to recover the data. This is normally done by choosing a filter with a bandwidth which blocks the noise components outside the signal bandwidth. The eye diagram at the receiver will still be wide open since the ISI is insignificant. For systems using a transmission signal with a bandwidth comparable to or even exceeding that of the channel, a sophisticated receiver needs to be designed to make the received pulse as close to a Nyquist pulse as possible to reduce the ISI. This normally involves the signal processing technique called equalisation, which will be further discussed in detail in Section 4.4.5.

### 4.3. Carrier-less Amplitude and Phase Modulation

Carrier-less amplitude and phase modulation (CAP) is a passband modulation scheme using two orthogonal pulses, which represent symbols in the quadrature (Q) and in-phase (I) channels respectively. CAP became popular in early copper asymmetrical digital subscriber line (ADSL) applications in the 1990s owing to its advantage of high bandwidth efficiency [139]. Recently, it has also been shown to enable high speed transmissions in both glass fibre links and plastic fibre links [53, 140].

CAP can be regarded as a variant of QAM, in which a baseband Nyquist pulse is modulated by such a carrier that is normally at a frequency comparable to the symbol rate of the system. The resulting pulses are used as the shaping filters for the I and Q channels. The amplitude of the pulse for either channel can be made to be multilevel as well. Figure 4.10 illustrates the schematic block diagram of a typical CAP modulation system. Compared with the PAM system shown in Figure 4.3, an extra channel encoder/decoder is included in the transmitter and receiver to interleave/recombine the incoming symbols to/from the I and Q channels. The symbols are modulated by the I and Q transmitter shaping filters respectively and combined simultaneously. At the receiver side, the matched filters for the I and Q channels are orthogonal, so that given an ideal Nyquist reception of the signal, the symbols can be demodulated without either ISI or cross-channel interference. Finally, the recovered symbol is decoded to the original transmitted binary data by the symbol decoder in the same way as the PAM system.

A CAP transmitter has a more complicated structure than the PAM transmitter. As shown in Figure 4.11, the encoder (the symbol encoder and channel encoder are combined in one block) maps and interleaves the incoming data to CAP-64 symbols. Unlike the transmission signal in the PAM system, the transmitted CAP signal does not have clear symbol levels interpreted by amplitudes. This is due to the fact that the symbols from two channels are combined and the levels can only be recovered by using the matched filters at the receiver end.

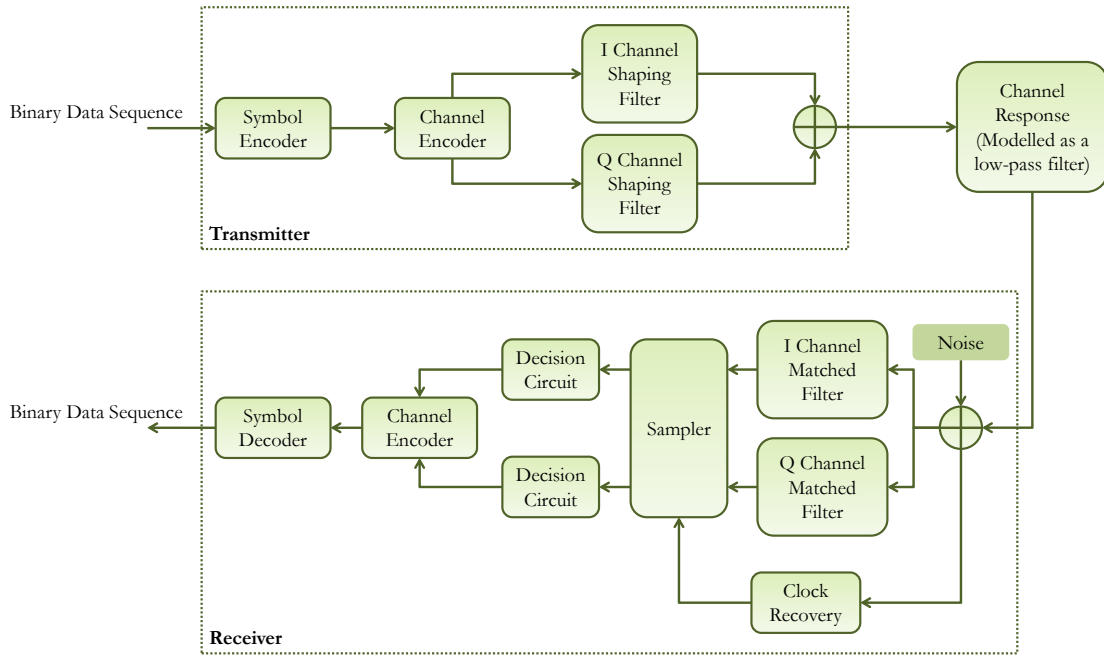


Figure 4.10 Schematic diagram of a carrier-less amplitude and phase modulation system

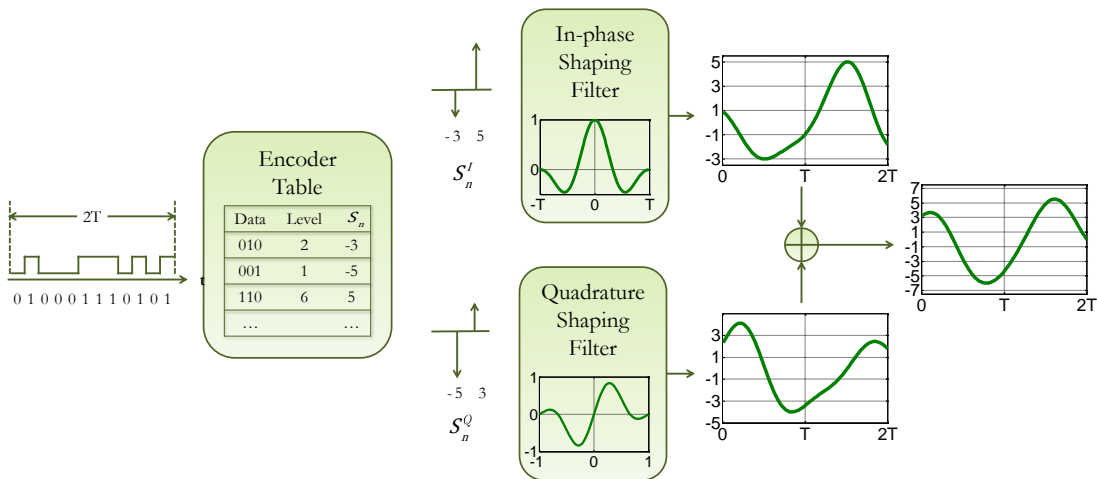


Figure 4.11 Typical transmitter for a CAP-64 system. A binary data sequence is converted to CAP symbols and modulated to the I and Q channels respectively. The symbol period is  $T$

In this example, a raised-cosine shaping filter is used for both channels. The in-phase and quadrature shaping filters are created by multiplying  $\cos$  and  $\sin$  functions respectively. Hence the pulses for both channels are shifted to the passband and have a phase difference of  $\frac{\pi}{2}$ . The continuous-time waveform after the combination of the I and Q channels is plotted for a time period of  $2T$  as an example.

### 4.3.1. Passband Nyquist Pulse

As discussed in the previous sections, the received pulse should satisfy the Nyquist criterion stated in Equation 4-10 in order to achieve an ISI-free recovery. CAP shaping filters are the shifted versions of the baseband Nyquist pulse to the passband and they maintain the Nyquist criterion as follow.

If raised-cosine filters are used for the baseband Nyquist pulse, the generated I and Q pulses can be written as

$$p_{CAPI}(t) = p(t) \cos(2\pi f_c t) = \left[ \frac{\sin(\pi t / T)}{\pi t / T} \right] \left[ \frac{\cos(\alpha \pi t / T)}{1 - (2\alpha t / T)^2} \right] \cos(2\pi f_c t), \quad 4-16$$

for the I channel, and

$$p_{CAPQ}(t) = p(t) \sin(2\pi f_c t) = \left[ \frac{\sin(\pi t / T)}{\pi t / T} \right] \left[ \frac{\cos(\alpha \pi t / T)}{1 - (2\alpha t / T)^2} \right] \sin(2\pi f_c t), \quad 4-17$$

for the Q channel, where  $f_c$  is called the centre frequency and can be regarded as the carrier frequency.

Recall that  $P(f)$  is the Fourier transform of the Nyquist pulse  $p(t)$ . According to the modulation property of the Fourier transform, we have

$$\begin{cases} P_{CAPI}(f) = \frac{1}{2}P(f + f_c) + \frac{1}{2}P(f - f_c) \\ P_{CAPQ}(f) = \frac{j}{2}P(f + f_c) - \frac{j}{2}P(f - f_c) \end{cases}. \quad 4-18$$

Since

$$\begin{cases} P(f + f_c) = 0 \text{ for } f \geq 0 \\ P(f - f_c) = 0 \text{ for } f \leq 0 \end{cases}, \text{ and } P(f) \geq 0 \text{ for all } f, \quad 4-19$$

taking the modulus of 4-18, we have

$$|P_{CAPI}(f)| = |P_{CAPQ}(f)| = \begin{cases} \frac{1}{2}P(f + f_c), f \leq 0 \\ \frac{1}{2}P(f - f_c), f > 0 \end{cases} = \frac{1}{2}P(f + f_c) + \frac{1}{2}P(f - f_c), \text{ for all } f. \quad 4-20$$

Substituting  $P_{CAPI}(f)$  in Equation 4-20 to Equation 4-10 gives

$$\begin{aligned} \frac{1}{T} \sum_{n=-\infty}^{+\infty} \left| P_{CAPI} \left( f + \frac{n}{T} \right) \right| &= \frac{1}{T} \sum_{n=-\infty}^{+\infty} \left[ \frac{1}{2} P \left( f + f_c + \frac{n}{T} \right) + \frac{1}{2} P \left( f - f_c + \frac{n}{T} \right) \right] \\ &= \frac{1}{2T} \sum_{n=-\infty}^{+\infty} P \left( f + f_c + \frac{n}{T} \right) + \frac{1}{2T} \sum_{n=-\infty}^{+\infty} P \left( f - f_c + \frac{n}{T} \right) \end{aligned} \quad 4-21$$

Equation 4-10 holds for both  $P(f + f_c + \frac{n}{T})$  and  $P(f - f_c + \frac{n}{T})$  since  $p(t)$  is a Nyquist pulse and  $f_c$  is a constant. Therefore, Equation 4-21 can be written as

$$\begin{aligned} \frac{1}{T} \sum_{n=-\infty}^{+\infty} \left| P_{CAPI} \left( f + \frac{n}{T} \right) \right| &= \frac{1}{2} \left( \frac{1}{T} \sum_{n=-\infty}^{+\infty} P \left( f + f_c + \frac{n}{T} \right) + \frac{1}{T} \sum_{n=-\infty}^{+\infty} P \left( f - f_c + \frac{n}{T} \right) \right) \\ &= \frac{1}{2} (1 + 1) = 1 \end{aligned} \quad 4-22$$

And the same holds for  $P_{CAPQ}(f)$ .

Comparing Equation 4-22 with Equation 4-10, it can be seen that  $P_{CAPI}(f)$  and  $P_{CAPQ}(f)$  satisfy the Nyquist criterion. These pulses are called passband Nyquist pulses. Figure 4.12 illustrates the comparison between the spectra of the baseband and passband Nyquist pulses. The centre frequency of the passband Nyquist pulses defines how far the spectrum is away from the DC. For a bandwidth limited channel,  $f_c = \frac{1 + \alpha}{2T}$  should be used to give the minimum centre frequency in the CAP system, which makes the spectrum closest to DC. For the minimum centre frequency, the passband Nyquist spectrum has zero DC component and has a -3 dB bandwidth of  $\frac{1}{T}$ .

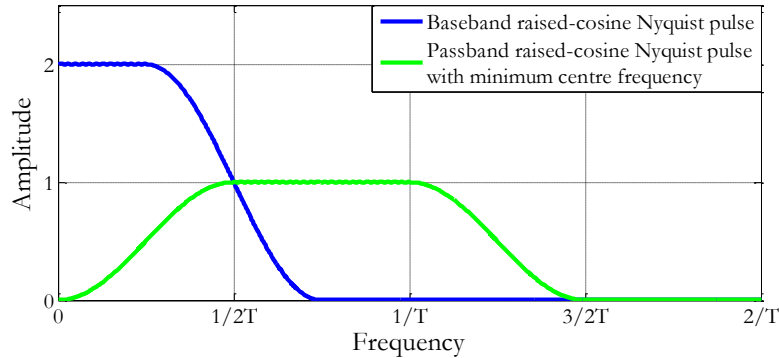


**Figure 4.12** The spectra of the baseband and passband Nyquist pulses. Raise-cosine pulse shaping filters with excess bandwidth of 0.5 are used in both cases

### 4.3.2. Orthogonal CAP Pulses

At the CAP receiver, the incoming signal contains information from both I and Q channels. The passband Nyquist criterion characteristic removes the ISI introduced by the dispersive channel but does not separate the information for each channel. In order to eliminate the cross channel interference, the CAP I and Q channel passband Nyquist pulses are designed to be orthogonal, so that matched filters can be used to demodulate the received signal for individual channels.

Given that the passband Nyquist pulses for the I and Q channels are defined using Equation 4-16 and 4-17, the Q channel matched filter can be expressed as

$$m_{CAPQ}(t) = p_{CAPQ}(-t) = p(-t)\sin(-2\pi f_c t). \quad 4-23$$

At sampling time  $t = 0$ , the I channel information remained in the filtered Q channel is

$$\begin{aligned} I_Q &= (p_{CAPI} * m_{CAPQ})(t) \Big|_{t=0} \\ &= - \int_{-\infty}^{+\infty} p(\tau) \cos(2\pi f_c \tau) p(t - \tau) \sin[2\pi f_c (t - \tau)] d\tau \\ &= - \int_{-\infty}^{+\infty} p(\tau) \cos(2\pi f_c \tau) p(-\tau) \sin[2\pi f_c (-\tau)] d\tau \\ &= \frac{1}{2} \int_{-\infty}^{+\infty} p(\tau) p(-\tau) \sin[4\pi f_c \tau] d\tau = 0 \end{aligned} \quad 4-24$$

Therefore the Q channel matched filter eliminates the information from the I channel. The same applies for the information from the Q channel in the I channel.

It can be seen that the orthogonal property of the CAP signals only holds at the optimal sampling point. Meanwhile, the Nyquist criterion also indicates that the ISI free can only be achieved at  $t = nT$ . Therefore the synchronization of the I and Q channels in a CAP-based system is essential. At the transmitter side, the in-phase and quadrature channels have to be strictly aligned with each other with a phase difference of  $\frac{\pi}{2}$ .

In practice, the orthogonal pulses chosen for the CAP system can also be designed as square root raised-cosine pulses, due to the fact that one can design such a pair of transmitter shaping filters and receiver matched filters, giving an overall Nyquist pulse shape. This design minimizes the receiver noise bandwidth and hence improves the system SNR. The square root raised-cosine pulse is defined as

$$h(t) = \begin{cases} 1 - \alpha + \frac{4\alpha}{\pi}, & t = 0 \\ \frac{\alpha}{\sqrt{2}} \left[ \left(1 + \frac{2}{\pi}\right) \sin\left(\frac{\pi}{4\alpha}\right) + \left(1 - \frac{2}{\pi}\right) \cos\left(\frac{\pi}{4\alpha}\right) \right], & t = \pm \frac{T}{4\alpha} \\ \frac{\sin\left[\frac{\pi t}{T}(1 - \alpha)\right] + \frac{4\alpha t}{T} \cos\left(\frac{\pi t}{T}(1 + \alpha)\right)}{\frac{\pi t}{T} \left[1 - \left(\frac{4\alpha t}{T}\right)^2\right]}, & \text{otherwise} \end{cases} \quad 4-25$$

The passband pulse shapes for the I and Q channels based on both the raised-cosine and square root raised-cosine shaping filters are illustrated in Figure 4.13. These pulses have an excess bandwidth of 50% and they are truncated at  $\pm 2T$  for illustration.

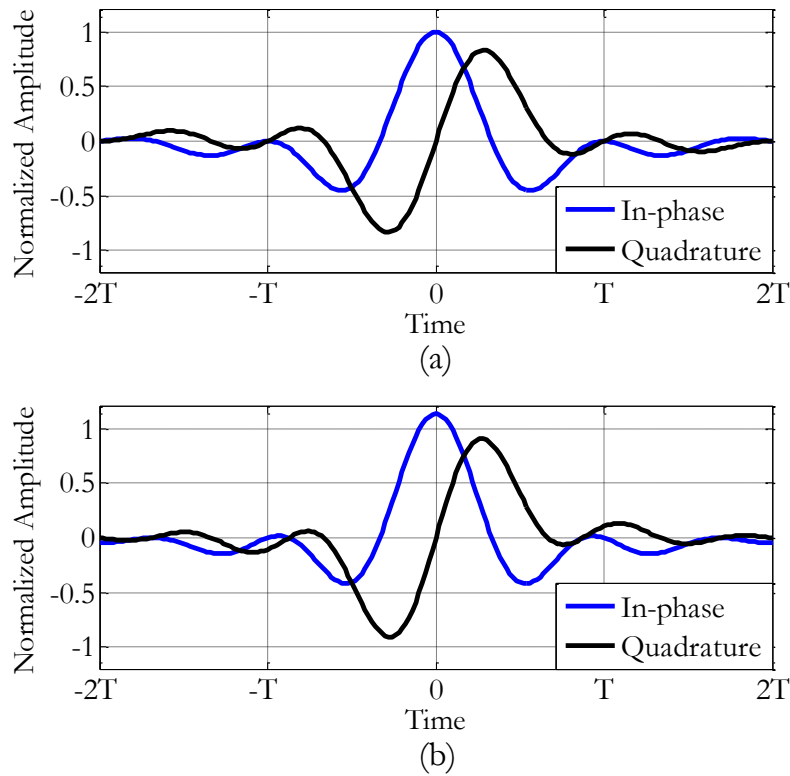


**Figure 4.13** The in-phase and quadrature pulse shapes based on (a) the raised-cosine and (b) the square root raised-cosine shaping filters. The excess bandwidth is 50% and the waveforms are truncated at  $\pm 2T$

#### 4.4. System Model for Multilevel Modulations over POF

In order to evaluate the performance of POF-based systems using different modulation schemes, each element in the system needs to be carefully modelled. The three essential elements in an optical communication system are the optical source, transmission medium (POF) and photodetector. LEDs are the most popular choice as the optical source in POF networks due to their low cost and ease of handling [86]. In this section, details are given for RC-LED in particular, which exhibits high bandwidth and is a strong potential candidate as the transmitter for high speed POF links [140]. For the transmission medium, PMMA-based step-index POFs (SI-POFs) are the most widely implemented fibres in existing POF systems. It can be seen that the SI-POF provides relaxed alignment which is essential for non-professional installations. Commonly used photodetectors are also introduced. Corresponding modelling approaches are discussed for all the system elements that are used for performance evaluations. These optical elements have various bandwidth limits, which constrain the overall system performance. As an essential signal processing technology at the receiver to compensate these limits, equalisation is also discussed. The link power budget analysis approach used to visualise the overall system feasibility with penalty bars is introduced in the last part of this section.

##### 4.4.1. Light Emitting Diode

Light-emitting diodes rely on spontaneous emission. The output from an LED is incoherent and the radiation has a broad linewidth since the energies of generated photons range over a wide distribution. The LED provides a rather large output beam size, thus it is usually used in multimode waveguide systems. The following advantages of the LED make it attractive for POF based systems.

**Cost.** The fabrication of the LEDs is much simpler than laser diodes and leads to reduced cost and high yields.

**Temperature dependence.** Since the LEDs are not threshold devices, the change of temperature tends to introduce much less fluctuation of the output power compared with laser diodes. This also leads to a simpler driving circuitry given that temperature compensation circuits are unnecessary.

**Reliability.** The LEDs are insensitive to gradual degradations. They can provide long working lifetimes with reliable performance.

#### 4.4.1.1. Resonant Cavity LEDs

Resonant cavity LEDs (RC-LED) are becoming more and more popular for optical fibre communications because they exhibit higher modulation bandwidths and radiation powers than conventional surface or edge emitters [141]. In recent years, intensive research activity has been carried out regarding such devices for applications in POF based systems [133]. The RC-LED has a Fabry-Perot resonant cavity which is constructed using the distributed Bragg reflector (DBR) at both cavity ends. The bottom DBR mirror has a very high reflectivity (higher than 95%) with a large number of high-low index layer pairs. While the top DBR is made semi-transparent using fewer pairs to allow the generated photons to exit the cavity. Such a structure is similar to that of a vertical cavity surface-emitting laser (VCSEL) except for the semi-transparent top layer which disallows the stimulated emission. This structure resonantly amplifies the spontaneous emission by the self-photon-pumping gained from the high reflectivity of the bottom DBR. Meanwhile, the DBR wavelength selectivity also makes the RC-LED a device with a narrower linewidth. The basic structure of a RC-LED is shown in Figure 4.14. In this dissertation, the RC-LED used for both simulation and experimental has a wavelength of 650 nm.

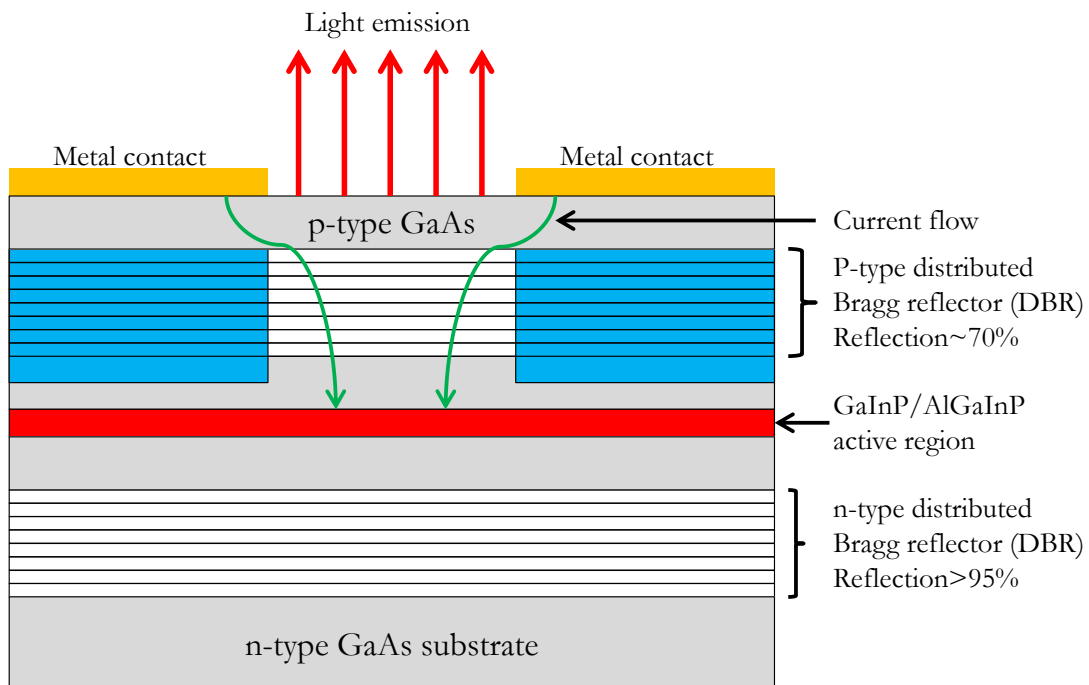


Figure 4.14 The structure of a RC-LED

#### 4.4.1.2. Modulation Bandwidth and Response Model

The modulation bandwidth of an LED may be defined either in the electrical or optical domain. In this dissertation, the bandwidth refers to the optical domain unless otherwise noted. Conventional LEDs normally have bandwidths below 100 MHz [142]. However, the RC-LED can increase this value to 200 MHz [143].

The LED optical source may be well modelled using an exponential response as [144]

$$h_s(t) = \begin{cases} 0, & t < 0 \\ \frac{1}{\tau_s} e^{-\frac{t}{\tau_s}}, & t \geq 0 \end{cases}, \quad 4-26$$

where its Fourier transform gives the normalized frequency response

$$H_s(f) = (1 + 4\pi^2 f^2 \tau_s^2)^{-0.5}. \quad 4-27$$

If the -3 dBo bandwidth is  $f_s$ , then

$$\tau_s = \frac{\sqrt{10^{0.6} - 1}}{2\pi f_s}, \quad 4-28$$

and the rise time is given by the relationship<sup>16</sup>

$$t_s = \tau_s \ln(9) \approx 2.197\tau_s. \quad 4-29$$

The frequency responses and transmitted eye diagrams of LEDs with different bandwidths modelled as low pass filters for a 100 Mbit/s PAM-2 (i.e. NRZ) signal are shown in Figure 4.15.

---

<sup>16</sup> This refers to a 10%-90% rise time based on the output optical intensity.

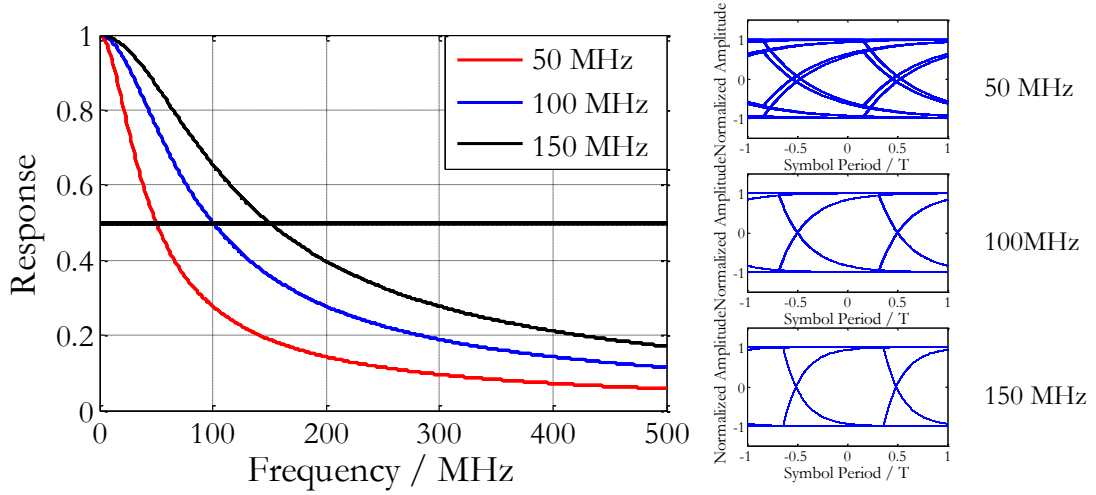


Figure 4.15 Frequency responses of LEDs with different bandwidths and corresponding transmitted eye diagrams for a 100 Mbit/s PAM-2 system

#### 4.4.2. Step-Index Plastic Optical Fibre

SI-POFs are strongly multimode waveguides and the launched power tends to spread over a wide range of modes when propagating through such fibres. Modal dispersion contributes in the most significant fashion to overall dispersion in the fibre. For a SI-POF, it is observed that the frequency response is very well modelled using a Gaussian filter [86], which is given by

$$h_c(t) = \frac{1}{\sigma\sqrt{2\pi}} e^{-\frac{t^2}{2\sigma^2}}. \quad 4-30$$

If the Fourier transform is taken then the normalized frequency response is

$$H_c(f) = e^{-\frac{4\pi^2 f^2 \sigma^2}{2}}, \quad 4-31$$

where the standard deviation  $\sigma$  can be written as

$$\sigma = \frac{\sqrt{0.6 \times \ln(10)}}{2\pi f_{channel}}, \quad 4-32$$

and  $f_{channel}$  is the -3 dB bandwidth of the SI-POF.

The frequency responses based on the Gaussian approximation for the two commercially available SI-POFs manufactured by Mitsubishi under the series brand name Eska are shown in Figure 4.16. The lengths of the fibres are 50 m.

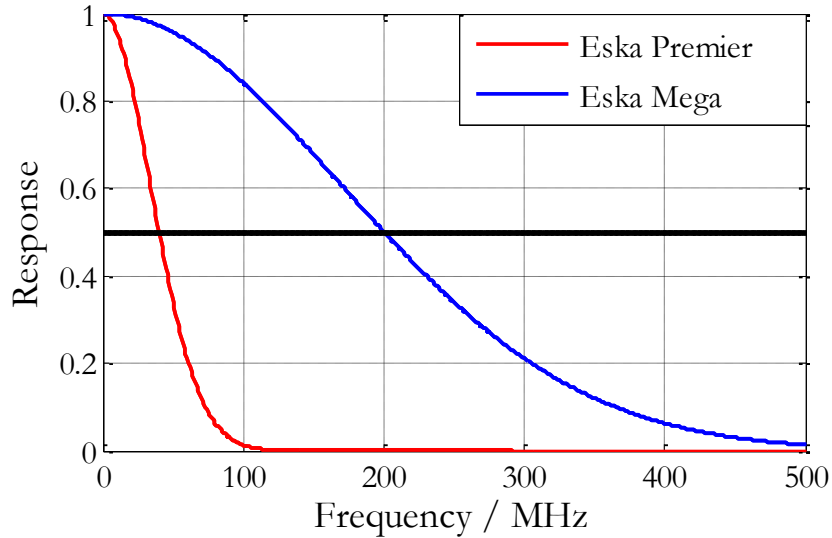


Figure 4.16 Frequency responses of Eska SI-POFs for a length of 50 m

#### 4.4.3. Receiver

A PIN structure photodetector circuit diagram is shown in Figure 4.17. The device consists of the p and n regions, which are separated by an intrinsic (i) region in the middle. The intrinsic region extends the depletion region and reduces the effective capacitance of the photodetector. A reverse bias is applied to the device, creating a depletion region which is normally designed to be exposed to the incident light for absorption. When the incident photon has energy greater or equal to the semiconductor material band-gap energy, an electron can be excited from the valence band to the conduction band. Thus, the electron flows from the p-side to n-side and the hole flows in the opposite direction due to the reverse bias. Hence the photocurrent is generated.

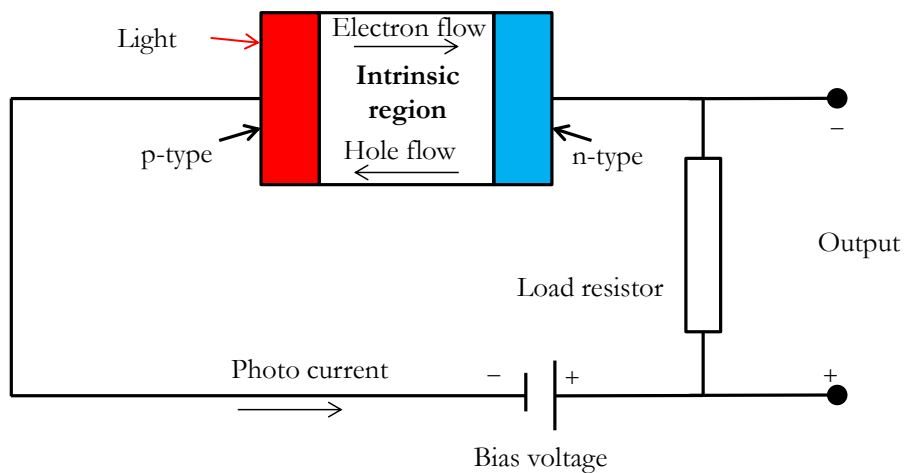


Figure 4.17 Schematic circuit diagram of a PIN photodiode with an applied reverse bias

PIN photodiodes are commonly used in POF-based links. Its frequency response can be very well modelled using a raised-cosine filter. This is given as [144]

$$h(t) \approx \frac{\sin(5.5\pi t f_r)}{2\pi t(1 - (5.5\pi t f_r)^2)}. \quad 4-33$$

The Fourier transform gives the normalized frequency response  $H(f)$  as

$$H_r(f) \approx \begin{cases} \left[ \cos\left(\frac{2\pi f}{11f_r}\right) \right]^2, & 0 \leq f \leq \frac{5.5}{2} f_r \\ 0, & f > \frac{5.5}{2} f_r \end{cases}, \quad 4-34$$

where  $f_r$  is the -3 dB electrical bandwidth of the receiver.

#### 4.4.4. Overall Response of SI-POF Links

The overall system model used in this work to evaluation POF-based transmission links is based on the component models introduced in previous sections. Each of the components is modelled as a low-pass filter, where the responses are exponential for the LED transmitter, Gaussian for the SI-POF channel and raised-cosine for the PIN photodetector. Typical examples of overall system frequency responses are illustrated in Figure 4.18, where the LED and PIN receiver have bandwidths of 150 MHz and 200 MHz respectively and the POF has a bandwidth-distance product of 10 MHz·km. It can be seen from the graph that the overall -3 dB optical bandwidths are about 150 MHz and 210 MHz for 50 m and 25 m SI-POF respectively. This certainly sets a challenge for gigabit/s transmissions over such a channel but it can be seen later in this chapter how multilevel modulation schemes tackle this challenge.

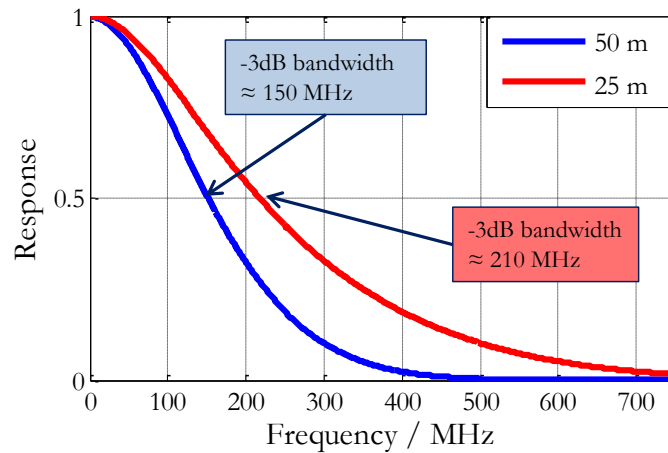
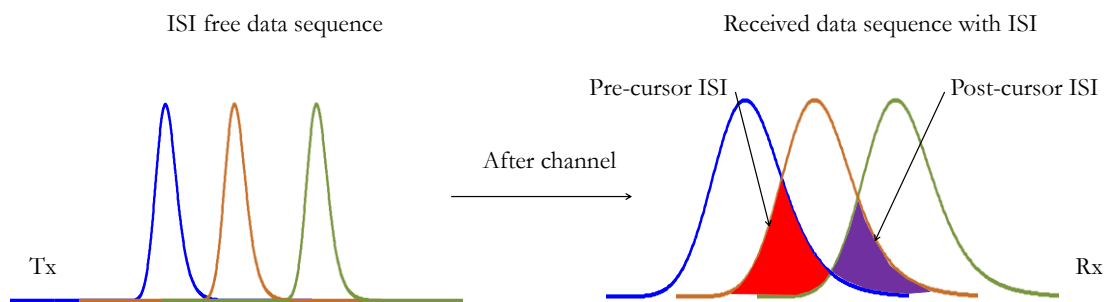


Figure 4.18 Typical overall system frequency responses for SI-POF links

#### 4.4.5. Equalisation

The Nyquist criterion specifies a condition where the original modulated data can be recovered without ISI. However as we can see from the previous sections, even if a signal is transmitted as an Nyquist pulse, the transmission channel is generally not flat, which results in breaking the Nyquist criterion. Consequently, a filter that is able to compensate for the distortion introduced by the channel is needed to reshape the signal back to Nyquist. This filter can be realized by using the equalisation techniques.

In a dispersive optical channel, ISI comes from both ends of the symbols. Figure 4.19 illustrates the interferences between symbols in a continuous time transmission. The ISI coming from the later symbols (on the left) is called pre-cursor ISI whilst the one coming from the earlier symbols (on the right) is called post-cursor ISI. The pre-cursor ISI can be recovered using a finite impulse response (FIR) filter since it extracts the ISI information from the later symbols. The post-cursor ISI on the other hand, relies on the information from the earlier symbols, which would have been already processed when the current symbol is at the receiver. Therefore a feedback is needed to gather this information to remove this ISI, which can be achieved using an infinite impulse response (IIR) filter. Later in this section we can see that the feed forward equaliser (FFE) and decision feedback equaliser (DFE) act as the implementations of the FIR and IIR filters in an overall equaliser structure.



**Figure 4.19** Pre-cursor ISI and post-cursor ISI of a symbol after a dispersive channel

The equaliser always brings noise enhancement to the system since it effectively amplifies the high frequency components to compensate the channel dispersion. This noise enhancement degrades the overall signal-to-noise ratio, which results in a power penalty. An ideal equaliser can completely remove the ISI while the noise enhancement penalty may be too large. To find an optimal equaliser tap setting configuration, the minimum-mean-square-error (MMSE) algorithm is used in this work for equaliser adaption.

#### 4.4.5.1. Feed Forward Equaliser

The feed forward equaliser (FFE) is in the same structure as an FIR filter. As illustrated in Figure 4.20, the incoming signal is sampled at the symbol rate and the delayed samples are aligned for a total length of  $N$ . These samples are multiplied by corresponding tap values, which have been pre-adapted to give the preferable equaliser response as for an FIR filter. These samples are then superposed to give the recovered symbols.

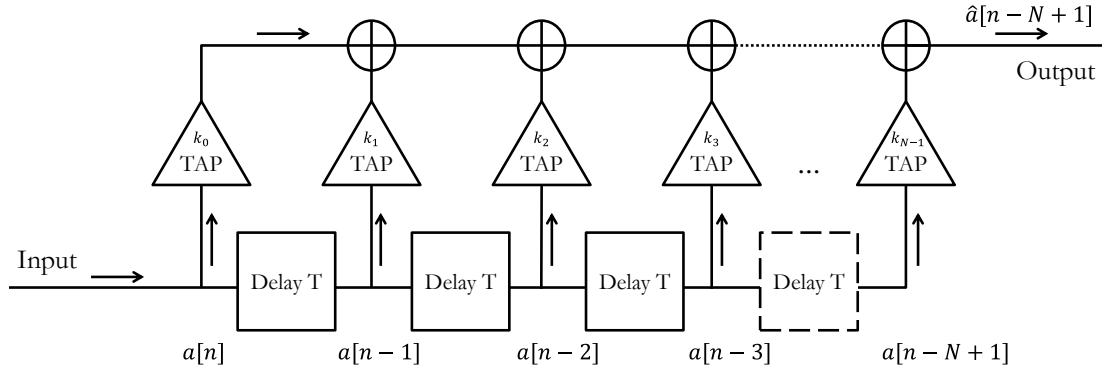


Figure 4.20 Schematic diagram of an FIR T-spaced N-tap FFE

Given an  $N$ -tap FFE, the incoming sample sequence can be written as

$$S_n = \{a[n], a[n-1], a[n-2], \dots, a[n-N+1]\}, \quad 4-35$$

where  $a[n]$  is the sample taken from the  $n^{\text{th}}$  symbol and the tap values are

$$K = \{k_0, k_1, k_2, \dots, k_{N-1}\}. \quad 4-36$$

Then we have the recovered symbol given as

$$\begin{aligned} b[n] &= a[n]k_0 + a[n-1]k_1 + a[n-2]k_2 + \dots + a[n-N+1]k_{N-1} \\ &= \sum_{m=0}^{N-1} a[n-m]k_m = \hat{a}[n-N+1] \end{aligned}, \quad 4-37$$

where  $\hat{a}[n-N+1]$  is the recovered symbol of  $a[n-N+1]$ . Since the number of the FFE taps is finite, Equation 4-37 is in the same form as a discrete convolution between  $S_n$  and  $K$  where

$$S_n * K = \sum_{m=-\infty}^{+\infty} a[n-m]k_m = \sum_{m=0}^{N-1} a[n-m]k_m = \hat{a}[n-N+1]. \quad 4-38$$

In other words,  $K$  is the sampled impulse response of the FFE, where

$$EQ(mT) = k_m, \quad 0 \leq m \leq N-1. \quad 4-39$$

#### 4.4.5.2. Decision Feedback Equaliser

The decision feedback equaliser (DFE) can be implemented as an IIR filter. The decisions made for the received symbols are sent back to the current symbol which is yet to be recovered. The decisions available for the present time must come from the time in the past, which means the feedback carries information exclusively from the earlier symbols. This also explains why the DFE recovers the post-cursor ISI. Similarly to the FFE structure, these decisions are multiplied by individual tap values and then superposed to give the recovered symbol. The basic structure of an IIR implementation of an M-tap DFE is shown in Figure 4.21.

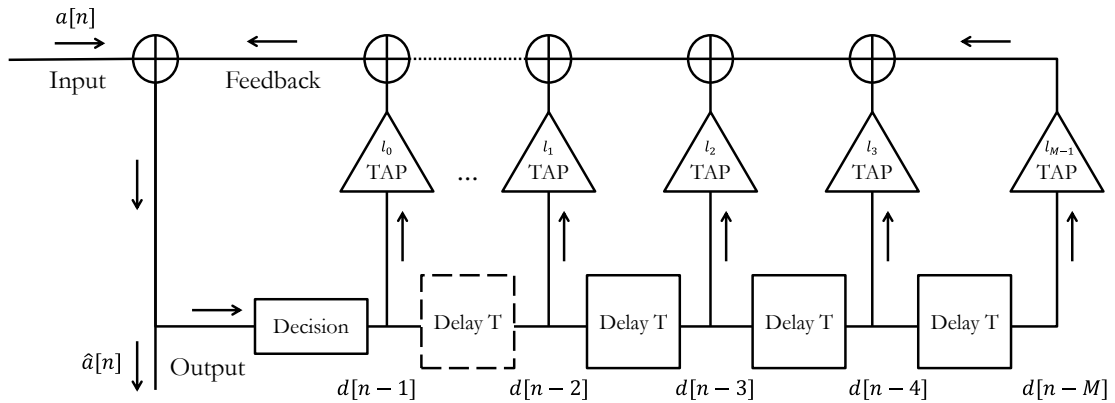


Figure 4.21 Schematic diagram of an IIR M-tap DFE

Given an M-tap DFE, the decision sequence can be written as

$$D_n = \{d[n-1], d[n-2], d[n-3], \dots, d[n-M]\}, \quad 4-40$$

where  $d(n)$  is the decision made for the  $n^{\text{th}}$  symbol of the sequence.

If the tap values are

$$L = \{l_0, l_1, l_2, \dots, l_{M-1}\}, \quad 4-41$$

then the recovered symbol is given by

$$\begin{aligned} b[n] &= a[n] + d[n-1]l_0 + d[n-2]l_1 + d[n-3]l_2 + \dots + d[n-M]l_{M-1} \\ &= a[n] + \sum_{m=0}^{M-1} d[n-m-1]l_m = \hat{a}[n] \end{aligned}, \quad 4-42$$

where  $\hat{a}[n]$  is the recovered symbol of  $a[n]$ .

This result is in the same form as Equation 4-37 as the convolution between the decision sequence and the tap values. However, it is worth noting that the example given for the DFE in Equation 4-42 is for the recovery of the symbol  $a[n]$ . An  $N - 1$  shift should be applied to this equation if  $a[n - N + 1]$  is to be recovered, which gives

$$\begin{aligned}\hat{a}[n - N + 1] &= a[n - N + 1] \\ &\quad + d[n - N]l_0 + d[n - N - 1]l_1 + d[n - N - 2]l_2 + \dots + d[n - N - M + 1]l_{M-1} \\ &= a[n - N + 1] + \sum_{m=0}^{M-1} d[n - N - m]l_m\end{aligned}\tag{4-43}$$

Therefore if we consider the equaliser with both FFE and DFE sections, the input of the DFE section is connected with the output of the FFE section. Hence, the  $a[n - N + 1]$  term in Equation 4-43 should be substituted by the summation term in Equation 4-38. In this way, the recovered symbol can be expressed as

$$\hat{a}[n - N + 1] = \sum_{m=0}^{N-1} a[n - m]k_m + \sum_{m=0}^{M-1} d[n - N - m]l_m\tag{4-44}$$

for an N-tap FFE and M-tap DFE system. The implementation is the combination of these two structures as shown in Figure 4.22. At present time,  $a[n]$  arrives at the receiver and  $a[n - N + 1]$  is the symbol to be recovered.

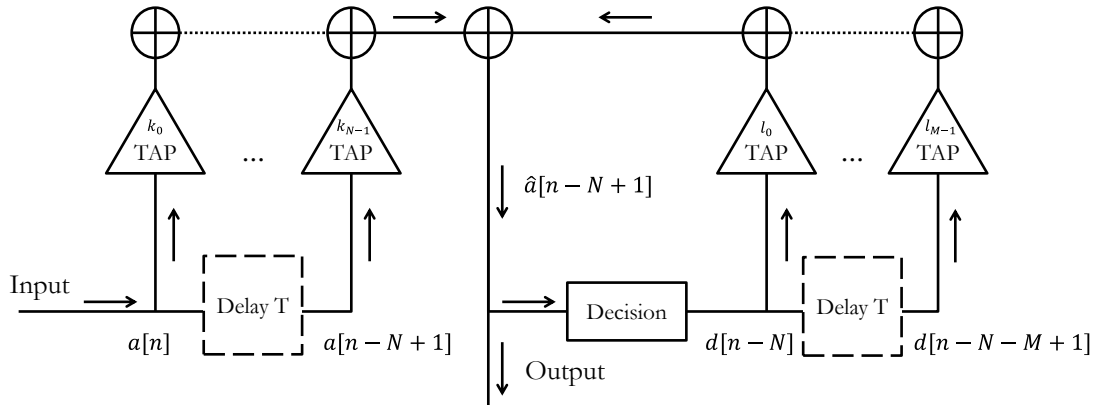
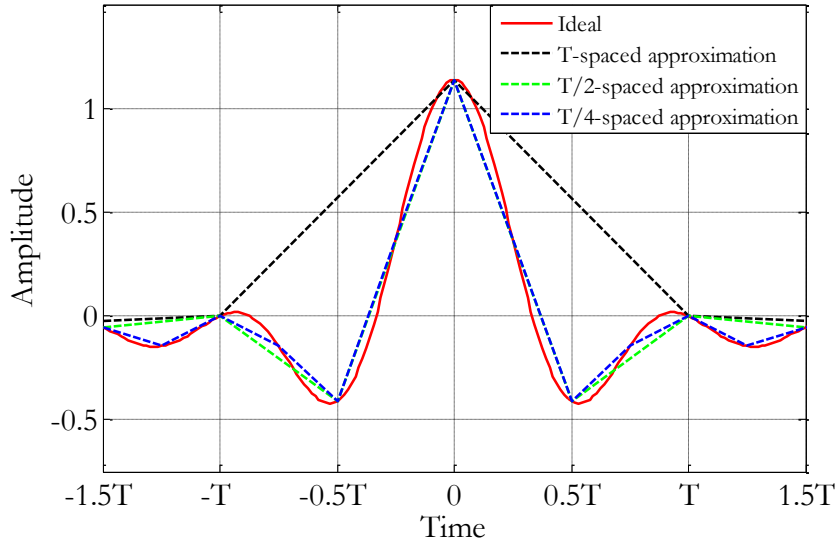


Figure 4.22 Schematic diagram of the equaliser with an N-tap FFE and an M-tap DFE

#### 4.4.5.3. Fractionally Spaced Equaliser

So far the equalisers considered are all symbol-period-spaced. For the FFE section of the equaliser, the tap spacing can also be reduced to a fraction of the symbol period for the purpose of a better approximation of the impulse response. It can be seen from Figure 4.23 that for a system requiring a receiver shaping filter in a square root raised-cosine shape, a  $T/4$  tap spacing is preferred to give a better approximation.



**Figure 4.23 Comparison between the  $T$ ,  $T/2$  and  $T/4$  spaced equalisers representing a square root raised-cosine CAP in-phase (I channel) filter**

Meanwhile, the receiver shaping filters in a CAP system need to demodulate the signal (separate I and Q channel) as well as to compensate for the channel dispersion. To establish this dual-functionality, a smaller spacing is always preferred to minimize the residual ISI and cross channel interference. However, smaller tap spacing requires a larger number of taps and faster sampling frequency, which is always a challenge in the equaliser design. In this work,  $T/2$ -spaced and  $T/4$ -spaced FFE equalisers are used for PAM and CAP systems respectively to keep low complexity whilst give relatively high performance.

#### 4.4.6. Link Power Budget

Given the transmission power and receiver sensitivity, the total system power budget is defined by the difference between these two values. The system is limited to this power budget to achieve a certain BER performance. A system is said to be feasible only if this BER can be obtained within this budget.

Link power budget analysis is a tool used in this dissertation to evaluate a system by accumulating the power penalties introduced by different elements in the system and comparing the total power penalty to the given power budget<sup>17</sup>. There are 5 main sources of power penalties considered for the POF-based systems using multilevel modulation schemes as shown in Figure 4.24.

<sup>17</sup> A reference BER of  $10^{-12}$  is assumed for all of the evaluated systems.

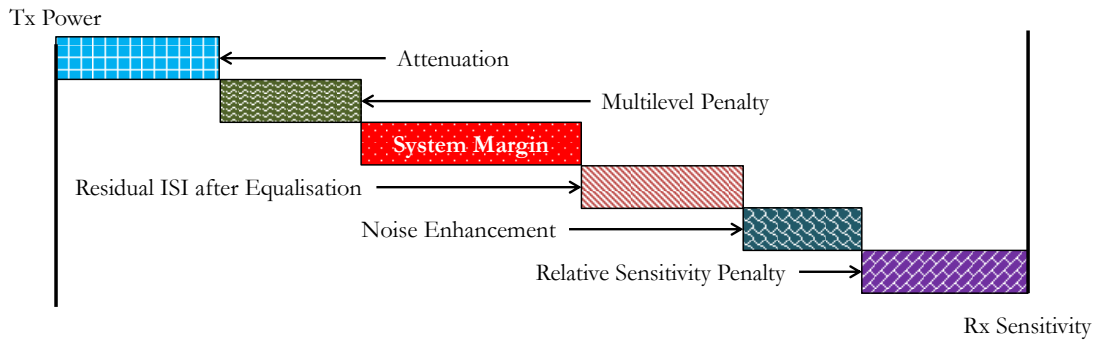


**Figure 4.24 Link power budget model for multilevel modulation schemes in SI-POF transmission systems**

**Attenuation penalty:** The light intensity attenuation introduced by the SI-POF.

**Multilevel penalty:** When a multilevel modulation is used, the modulation amplitude between the nearest two levels decreases as the number of levels increases. Therefore, given the same maximum transmission power, an eye opening penalty is introduced by multilevel modulations compared with the two-level scheme.

**Equalisation noise enhancement penalty:** An equaliser is used as a dispersion compensation filter after the photodiode receiver. It superposes the delayed replicas of the received signal to generate a recovered version of the transmitted signal. This process amplifies the receiver noise and degrades the BER as a result.

**Residual ISI penalty:** Given that a minimum-mean-square-error algorithm is used for the equaliser adaption. The equaliser tap settings are not likely to give a perfect recovery of the signal. The amount of ISI that is not able to be removed by the equaliser is referred as the residual ISI penalty.

**Relative sensitivity penalty:** The sensitivity of a receiver varies with the allowed bandwidth. Therefore, for systems with different symbol rates, the receivers have different bandwidths which increase or decrease the allowed noise bandwidth in the received signals. In the case of a system having a larger bandwidth compared with the reference system, the extra noise introduced to the system accounts for the relative sensitivity penalty.

**System margin:** Given the total system budget and taking each of the penalties out of this budget, the remained budget is the system margin. It represents the freedom of the power degradation that will still guarantee a successful link. If the margin is negative, the corresponding system is not feasible.

#### 4.5. Simulation Results

Based on the system model introduced in the previous sections, comprehensive simulations have been carried out for the PAM- and CAP-based SI-POF systems. These systems are investigated under various data rates for 25 m and 50 m reaches, which are considered as the requirement for the vehicle and home networks respectively. Using the parameters of commercially available components, this section demonstrates the transmission characteristics of the PAM and CAP modulations and investigates the overall system power budget performances. The parameters used in the simulation are listed in Table 4-1.

**Table 4-1 List of parameters used in simulations**

|                                       | PAM-2  | PAM-4 | PAM-8 | CAP-4 | CAP-16 | CAP-64 |
|---------------------------------------|--|-------|-------|-------|--------|--------|
| <b>Baud rate (at F bit/s)</b>         | F  | F/2   | F/3   | F/2   | F/4    | F/6    |
| <b>LED bandwidth</b>                  | 150 MHz  |       |       |       |        |        |
| <b>POF bandwidth</b>                  | 200 MHz·50 m                                       |       |       |       |        |        |
| <b>Photodiode bandwidth</b>           | $0.75 \times \text{symbol rate}$                   |       |       |       |        |        |
| <b>Equaliser spacing</b>              | T/2  |       |       | T/4   |        |        |
| <b>Oversampling ratio</b>             | 64   |       |       |       |        |        |
| <b>LED output power</b>               | -1.5 dBm   |       |       |       |        |        |
| <b>Reference receiver sensitivity</b> | -26 dBm at 166.7 MHz symbol rate (1 Gbit/s CAP-64) |       |       |       |        |        |
| <b>Excess bandwidth</b>               |  |       |       | 0.5   |        |        |

PAM modulation schemes with 2, 4 and 8 levels are carefully evaluated. Since the SI-POF systems are strongly bandwidth limited, intensive equalisation is applied to make such links feasible. It can be seen that the equaliser tap values are essential to achieve a successful link and corresponding optimisations have been done. These results and comprehensive comparisons are given in Section 4.5.1. The CAP modulation scheme, as another candidate for high spectral efficiency transmission over the SI-POF, is also thoroughly investigated in a similar way as the PAM scheme. In addition, the fractionally-spaced equaliser is optimised for its dual-functionality of demodulation and dispersion compensation. These results are shown in Section 4.5.2.

### 4.5.1. Evaluation of the Pulse Amplitude Modulation System

The simulation model for PAM systems is shown in Figure 4.25. A PAM-8 modulation is assumed in this diagram to give an example of the operation. A pseudorandom PAM-8 symbol sequence is constructed from a PRBS, giving the original modulation signal. The LED transmitter, POF channel and receiver are strictly defined using the parameter given in Table 4-1 respectively as exponential, Gaussian and raised-cosine low-pass filters. A  $T/2$ -spaced FFE and a  $T$ -spaced DFE are implemented at the receiver for dispersion compensation purposes.

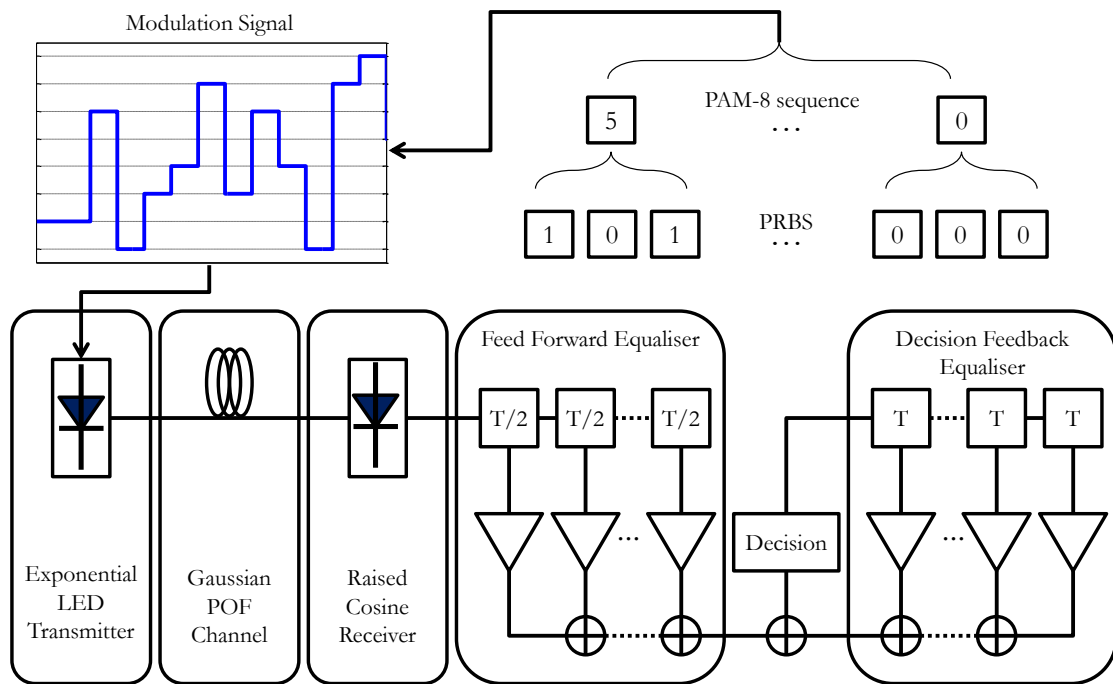
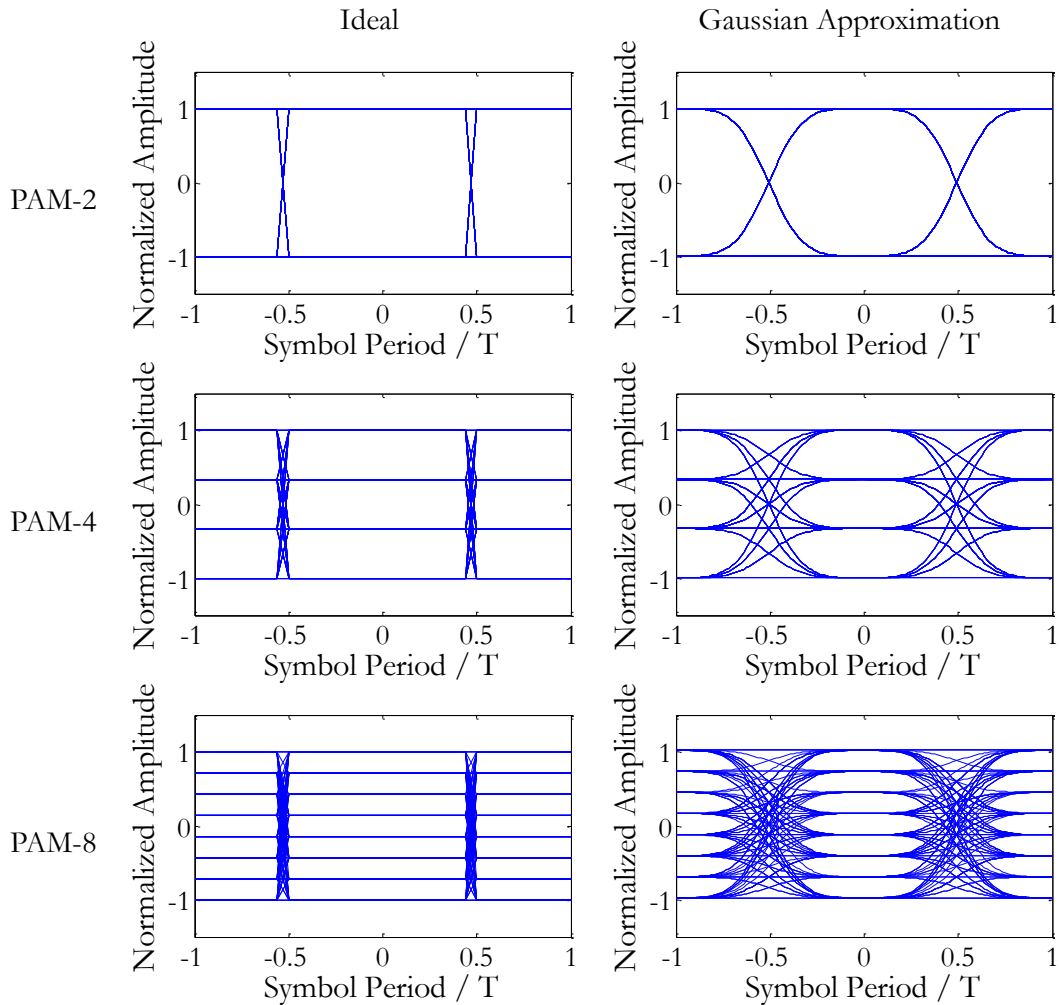


Figure 4.25 Block diagram of the simulation model for PAM system evaluations

#### 4.5.1.1. Signal Generation and Transmission

In the simulation model, a  $2^7 - 1$  pseudo-random sequence is used to emulate the practical random data stream. This length is selected because it is similar to the practical gigabit/s Ethernet data pattern. An ideal rectangular pulse shaping filter is used to create the original modulation signal with an oversampling ratio of 64, which is sufficient to create a near ideal waveform. For a real implementation, the original modulation signal cannot be in an ideal rectangular shape. This is because the devices (i.e. driving circuitry) used to generate such a signal have certain bandwidth limits. However in a practical design, this bandwidth is normally much higher than the signal bandwidth to minimize the distortion. Figure 4.26 illustrates the eye diagrams of the ideal and practical original modulation signals of PAM-2, PAM-4 and PAM-8 systems. A Gaussian filter with the

same bandwidth as the system symbol rate is assumed for the practical cases. For illustration purposes, the oversampling ratio of the ideal waveforms is reduced to 16 whilst the one for the practical waveforms is kept as 64 and no receiver noise is added. It can be seen that as the number of levels increases, the amplitude differences between the two nearest levels decrease, which introduces the multilevel penalty.



**Figure 4.26 Original modulation signals for the PAM-2, PAM-4 and PAM-8 systems. Left: With ideal rectangular pulse shaping. Right: Practical modulation signals after a Gaussian filter with the same bandwidth as the system symbol rate**

The ideal modulation signal is used to evaluate the responses of the LED, POF and receiver filters by convolving with their impulse responses defined in Section 4.4.1 to 4.4.3. The eye diagrams of the transmitted signal after the LED are shown in Figure 4.27 for the PAM-2, PAM-4 and PAM-8 systems at various data rates.

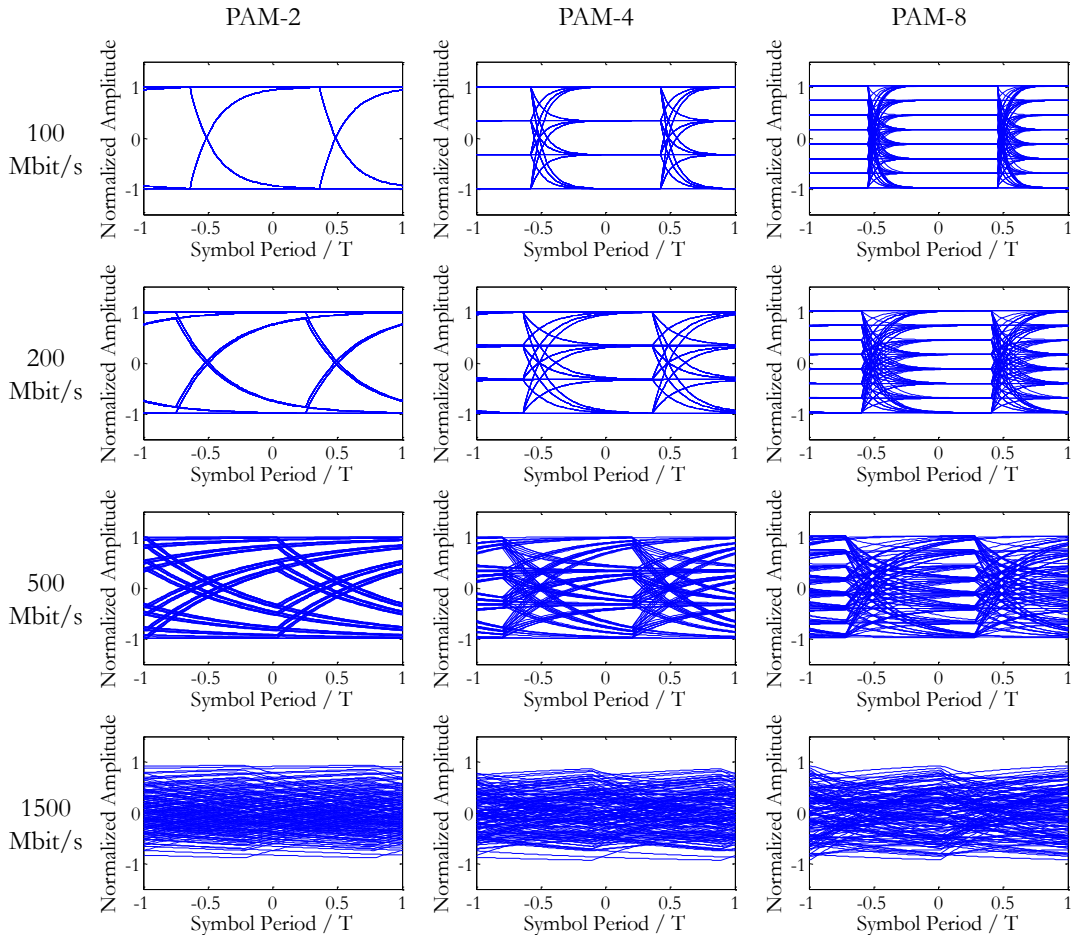


**Figure 4.27** Eye diagrams of the transmitted signals after the LED for the PAM-2, PAM-4 and PAM-8 systems at various data rates

As seen from Figure 4.27, PAM-4 and PAM-8 generally have smaller vertical eye openings between the nearest two levels in terms of the absolute amplitudes. These eye closures are caused by the multilevel penalties and ISI penalties. Since PAM-4 and PAM-8 use symbol rates a half and a third of the PAM-2 system, they have smaller ISIs and receiver noises than those of PAM-2 systems. However, they suffer from a large multilevel penalty and the overall signal-to-noise ratio performance is normally no better than the 2-level scheme. Figure 4.28 further illustrates the corresponding eye diagrams after 25 m and 50 m Eska Mega SI-POFs. Without equalisation, all three schemes can only achieve 500 Mbit/s transmissions over 25 m with rather closed eyes. The eyes for 50 m at the same data rate are completely closed.

Nevertheless, the existing ISI in the system indicates the robustness of the equalisation. As the data rate increases, the ISI of the 2-level system will quickly build up whilst the ones for multilevel systems only grow moderately due to the lower signal bandwidths. Hence the equalisation penalty is expected to be lower. When a point is reached where

the benefit of lower equalisation penalty and receiver noise is comparable to the drawback of the intrinsic higher multilevel penalty, multilevel modulation schemes will start to show the advantage in terms of overall signal-to-noise ratio performance. This will be further verified in Section 4.5.1.3 and 4.5.2.3.

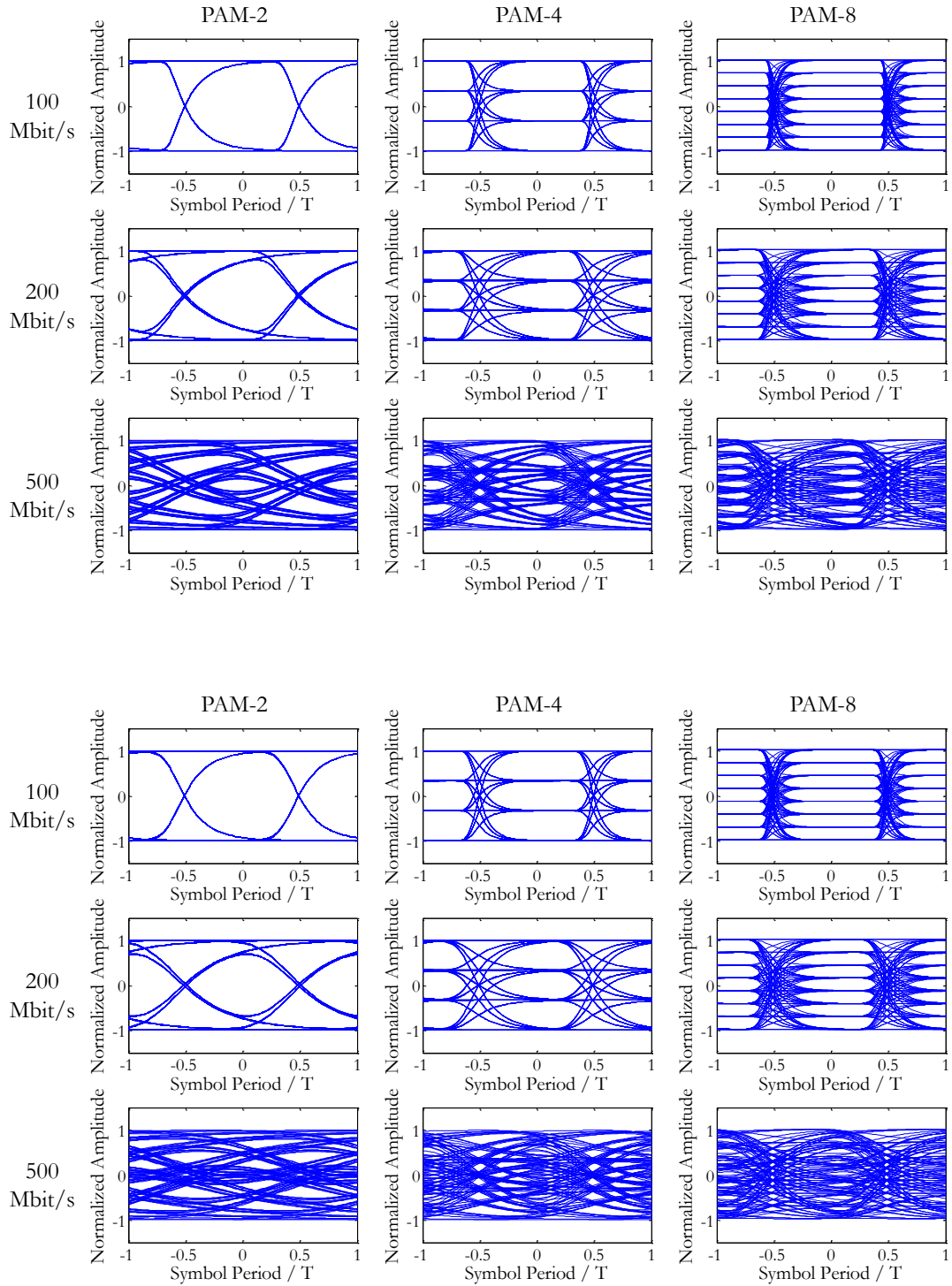


**Figure 4.28** Eye diagrams of the signal after 25 m (top) and 50 m (bottom) SI-POFs for the PAM-2, PAM-4 and PAM-8 systems at various data rates

#### 4.5.1.2. Signal Equalisation and Recovery

None of the systems considered so far can achieve gigabit/s transmission over SI-POF due to the severe distortion of the signal introduced by the limited LED bandwidth and high fibre modal dispersion. Nevertheless, the ISI can be removed if the received signal is reshaped to satisfy the Nyquist criterion. As introduced in Section 4.4.5, an equaliser can be implemented to fulfil this requirement. An example is given in Figure 4.29 to show the equalised eye diagrams of the signals at 500 Mbit/s after 50 m SI-POF. An equaliser with a  $T/2$ -spaced 16-tap FFE and a  $T$ -spaced 4-tap DFE is used in these calculations. It can be seen that the recovered eyes are wide open. Higher data rates are expected to be achievable using such equalisation at the receiver.

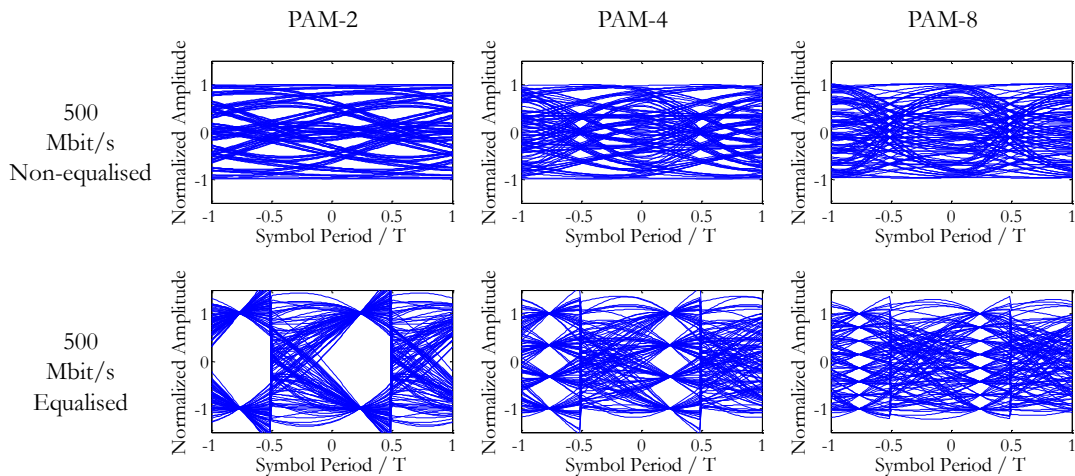


**Figure 4.29 Comparison between the non-equalised and equalised eye diagrams for the PAM-2, PAM-4 and PAM-8 systems at 500 Mbit/s over 50 m SI-POF**

The equalised eye diagrams for systems with higher data rates up to 3 Gbit/s for 25 m and 1.5 Gbit/s for 50 m SI-POFs are shown in Figure 4.30. The boxed eye diagrams imply that the systems fail with overall power penalties exceeding the allowed budgets. The main limiting factor for these non-feasible systems is the noise enhancement penalty introduced by the equaliser. As seen in this figure, PAM-2 is feasible for up to 2 Gbit/s over 25 m SI-POF, whilst PAM-4 and PAM-8 work for 3 Gbit/s at this distance. On the other hand for 50 m SI-POF, PAM-2 works for up to 1.2 Gbit/s whilst PAM-4 and PAM-8 are feasible for 1.5 Gbit/s. The optimised numbers of the equaliser taps discussed in the following paragraphs are used for each of the systems.

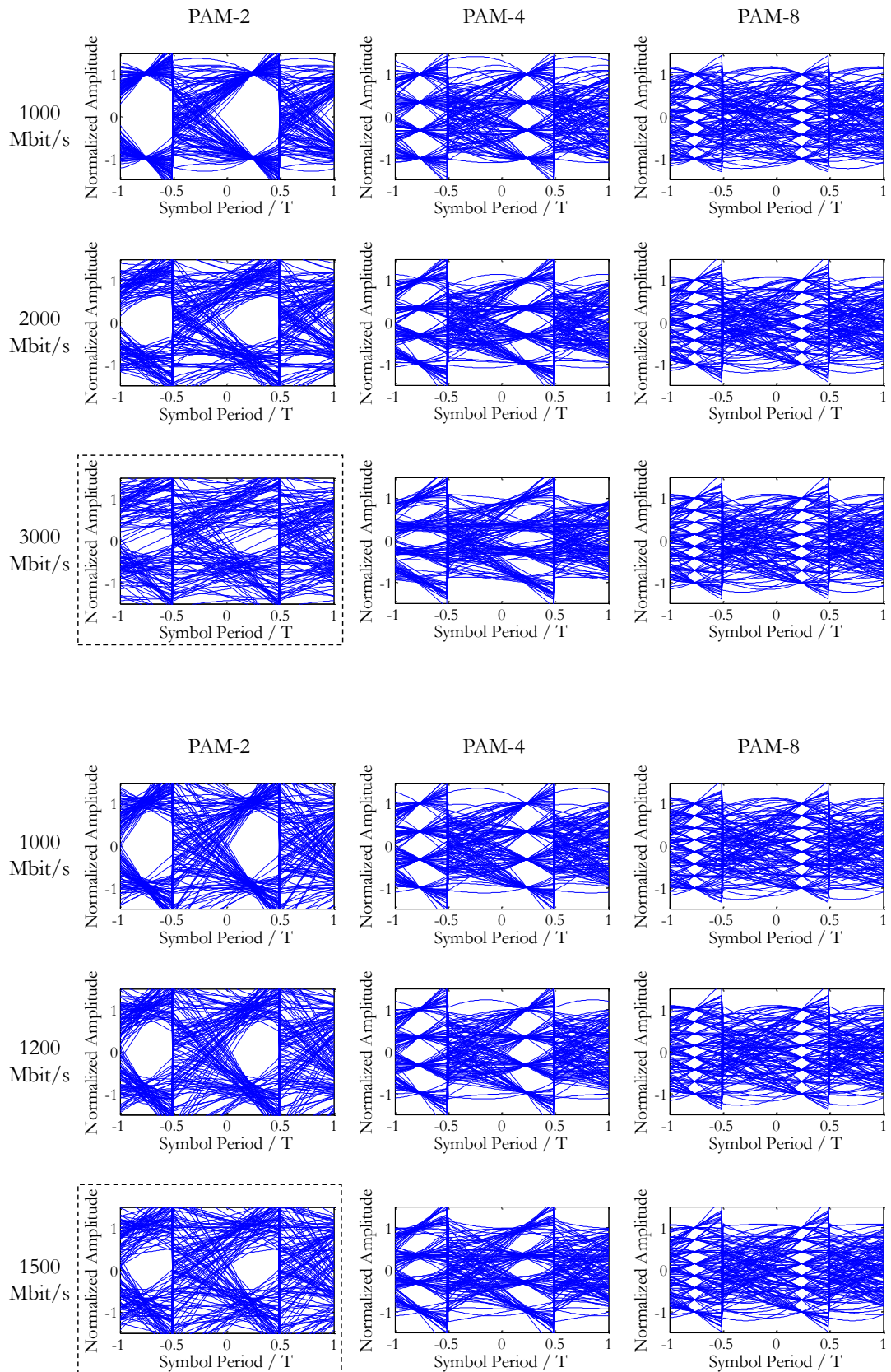
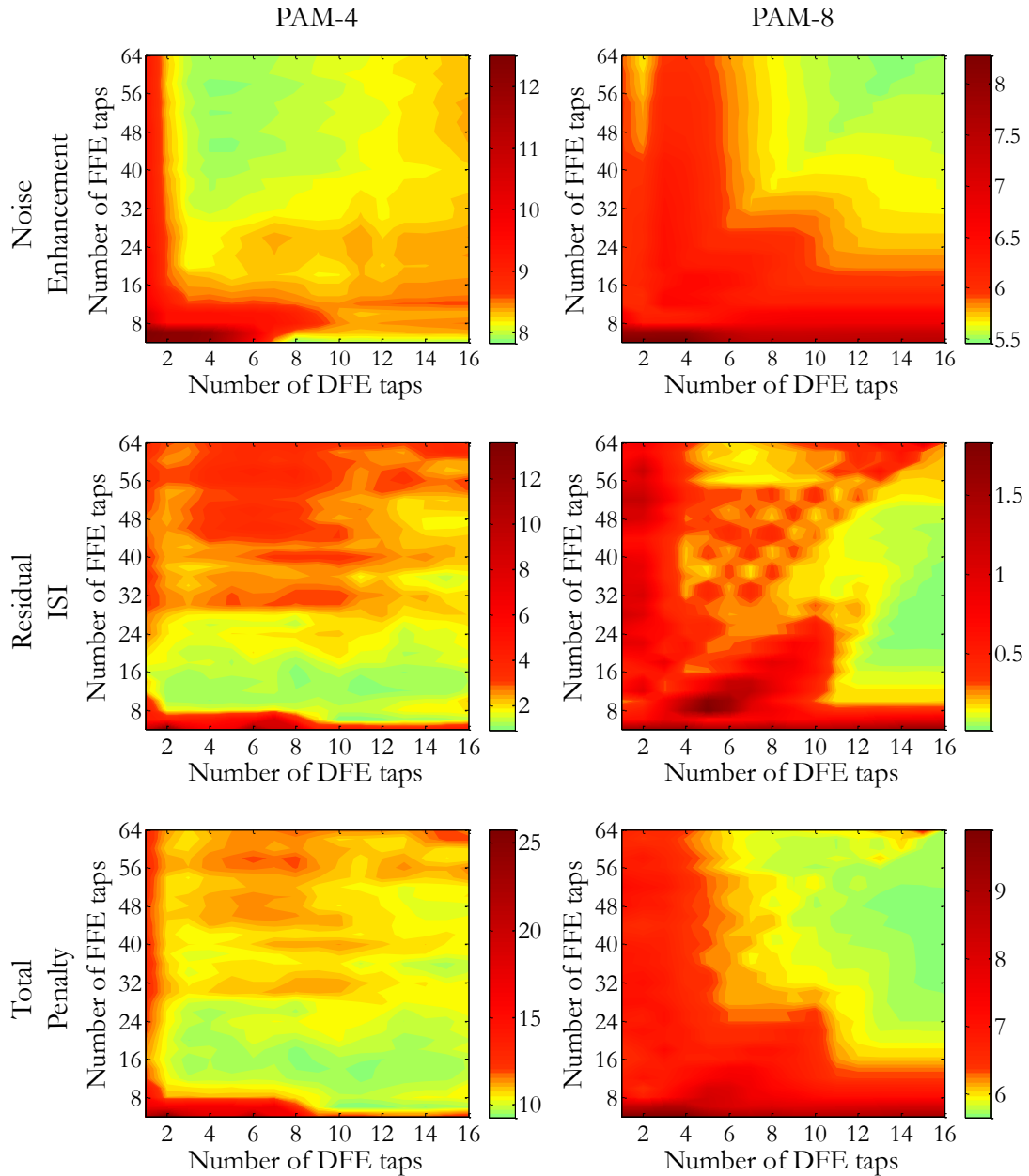
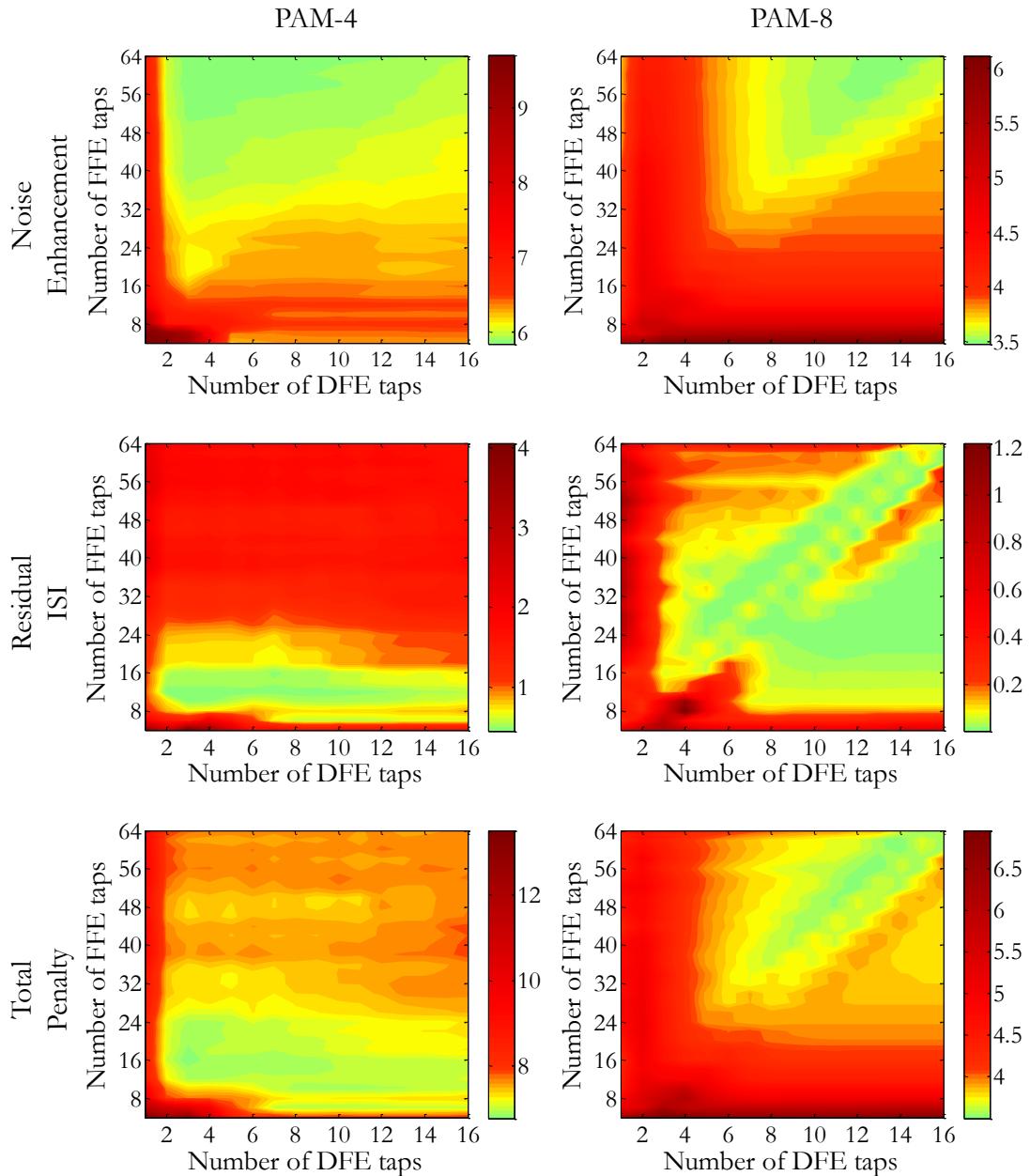


Figure 4.30 Equalised eye diagrams for the PAM-2, PAM-4 and PAM-8 systems after 25 m (top) and 50 m (bottom) SI-POFs at various data rates. The dashed boxes indicate the non-feasible systems

In order to find the balance between the noise enhancement penalty and the residual ISI penalty brought by the equaliser, the numbers of taps in the FFE and DFE sections are optimised according to the minimum combined penalty. Optimisations for the feasible systems at 3 Gbit/s over 25 m SI-POF and 1.5 Gbit/s over 50 m SI-POF are shown in Figure 4.31 and Figure 4.32 respectively.



**Figure 4.31** Optimisations of the numbers of taps in equalisers for 3 Gbit/s transmissions over 25 m SI-POF using PAM-4 and PAM-8. The contour levels indicate the power penalties in the unit of dBo



**Figure 4.32 Optimisations of the numbers of taps in equalisers for 1.5 Gbit/s transmissions over 50 m SI-POF using PAM-4 and PAM-8. The contour levels indicate the power penalties in the unit of dB0**

The light green areas imply smaller penalties. Generally speaking, a larger number of taps gives a lower noise enhancement penalty. However, if the equaliser is too long, the tail of the equaliser introduces redundant correction to the system which over-equalises the signal, resulting in a larger residual ISI penalty. In order to keep a reasonable equaliser length and complexity, the points in the total penalty graphs inside the green areas which are the closest to the origin are chosen to give the optimal equaliser configurations for each system. It can be seen that these optimal configurations are  $\sim 20$ -tap FFE and 4-tap DFE for PAM-4 systems and  $\sim 40$ -tap FFE and 12-tap DFE for PAM-8 systems.

### 4.5.1.3. Power Penalty Analysis

The overall system power penalty analysis is shown in Figure 4.33 with a total budget of 24.5 dBo with a reference symbol rate of 166.7 MHz. This symbol rate, as in the 1 Gbit/s CAP-64 system, is the lowest among all of the evaluated systems. In the 25 m links, the PAM-4 and PAM-8 systems are feasible for 3 Gbit/s transmissions with system margins of 1.2 dB and 2.2 dB whilst the PAM-2 system is not able to fulfil the link budget requirement. The 50 m links give a similar trend where the PAM-4 and PAM-8 systems both achieve 1.5 Gbit/s transmissions with 1.1 dB and 1.9 dB power margins respectively.

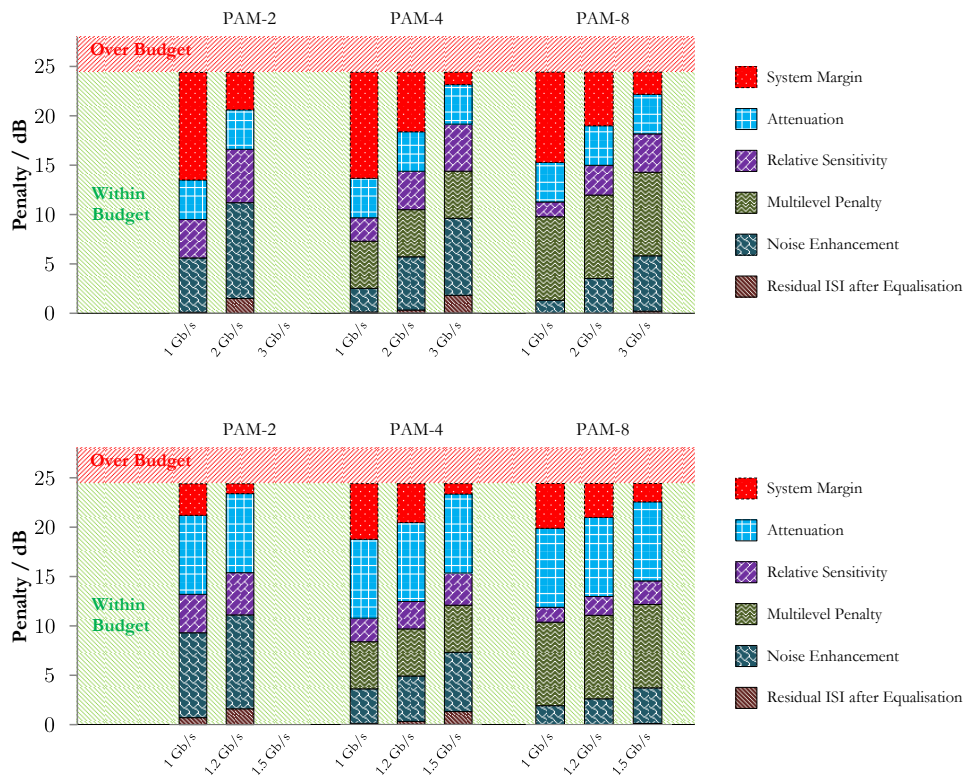


**Figure 4.33 Link power budgets comparisons between the PAM-2, PAM-4 and PAM-8 modulation schemes over 25 m (top) and 50 m (bottom) SI-POFs**

The multilevel PAM systems intrinsically introduce multilevel penalty. For a comparatively low data rate transmission, where the dispersion penalty is acceptable, multilevel PAM cannot compete with the 2-level scheme due to this high penalty. This can be seen in the 1 Gbit/s transmission over 25 m where PAM-2 gives the highest system margin. However, for higher data rates, when the dispersion tends to build up, the noise enhancement and residual ISI penalties start to dramatically increase for 2-level scheme where the multilevel schemes tend to only have moderate degradation. At a certain point, when the benefit of lower dispersion penalty outperforms the drawback of multilevel penalty, the multilevel schemes start to provide better performance.

### 4.5.2. Evaluation of the Carrier-less Amplitude and Phase Modulation System

The simulation model for CAP systems is shown in Figure 4.34. Two uncorrelated pseudo random sequences are generated and sent to the CAP I and Q channel shaping filters respectively. The pulse shapes are scaled according to the incoming symbols to generate the multilevel pulses. The modulated signals are combined before driving an LED. The transmitter, POF and receiver used in this model are the same as the ones in the PAM model introduced in previous sections. The difference is that the FFE sections in the receiver for the I and Q channels are  $T/4$ -spaced. It is also worth mentioning that the equalisers for the two channels have independent tap settings.

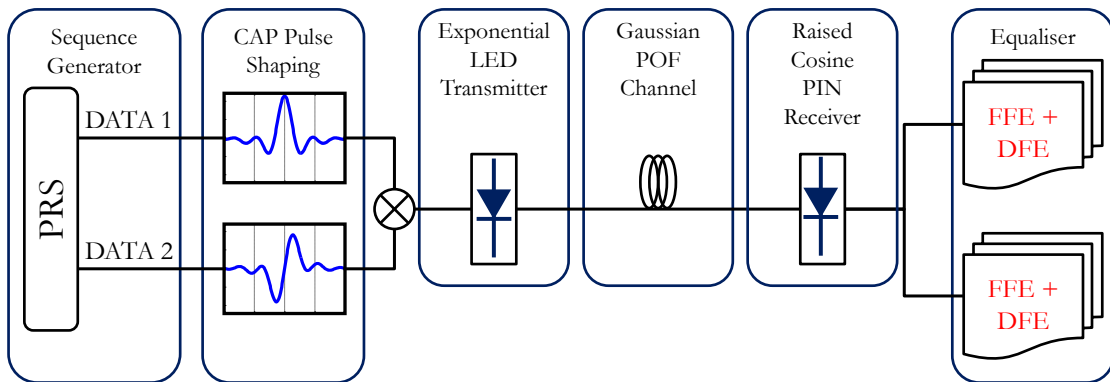
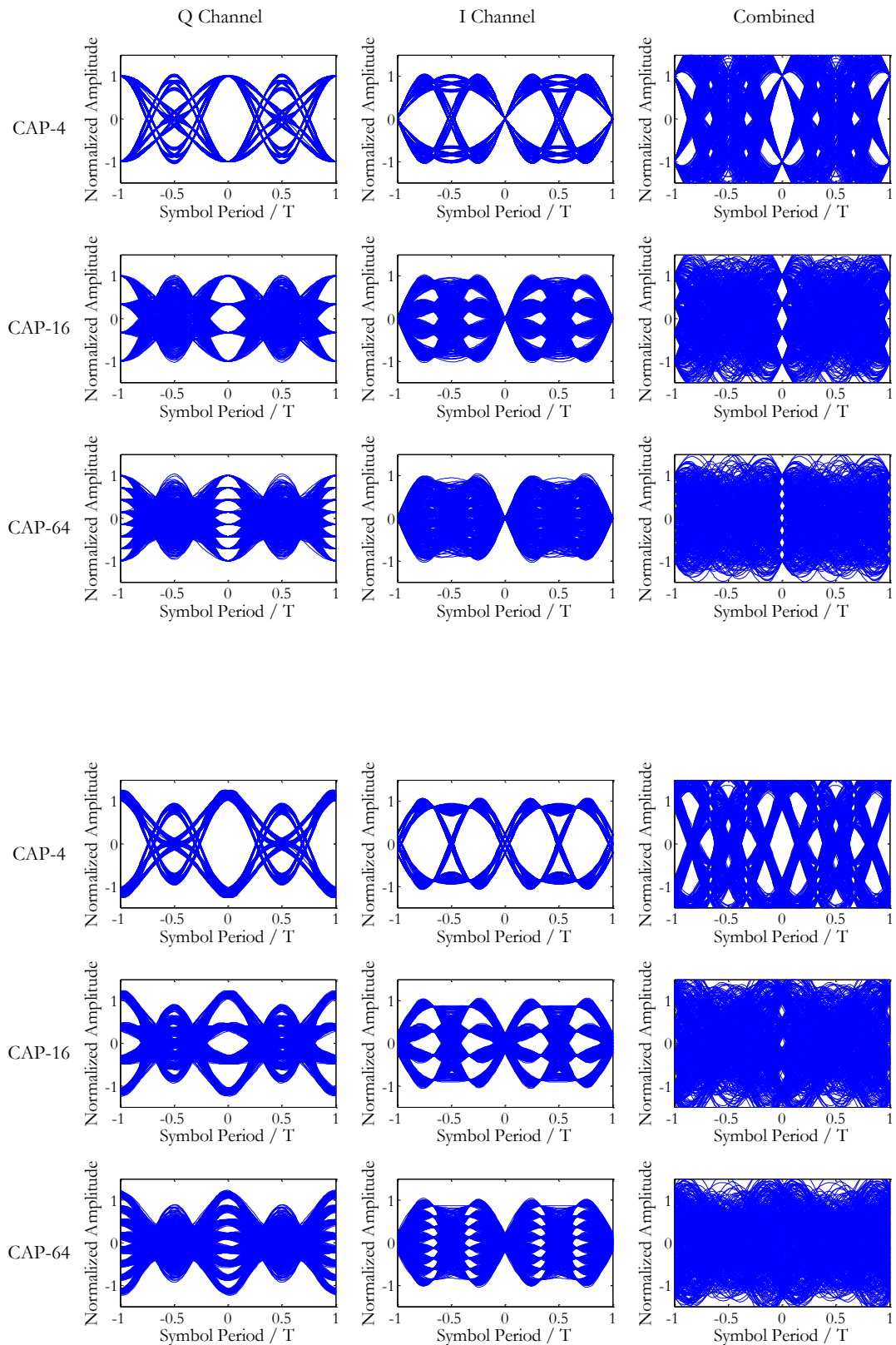


Figure 4.34 Block diagram of the simulation model for CAP system evaluations

#### 4.5.2.1. Signal Generation and Transmission

As discussed in Section 4.3, the CAP I and Q channels use passband orthogonal Nyquist pulses to achieve dual channel transmission without inter-channel interference and ISI. For illustration purposes, the eye diagrams of both the raised-cosine and square root raised-cosine transmitter CAP filters are shown in Figure 4.35. The raised-cosine CAP signals converge at symbol levels in the I channel and zeros in the Q channel. This implies that the ISIs in both channels are zero. The square root raised-cosine waveform does not converge to symbol levels or zeros since they violate the Nyquist criterion. However, with square root raised-cosine receiver filters, the overall received signal will be reshaped to Nyquist pulses for both channels in ideal cases.



**Figure 4.35** The eye diagrams of the original modulation signals using the raised-cosine (top) and square root raised-cosine (bottom) shaping filters

### 4.5.2.2. Demodulation and Equalisation

Unlike the PAM systems, the CAP systems rely on the equalisers even for low data rate transmissions because of the need for demodulation. An example is given in Figure 4.36, where 500 Mbit/s CAP signals are modulated and transmitted over 50 m SI-POF. In the calculations, the receiver noises for systems with different levels are scaled according to the actual symbol rates and the reference receiver defined in Table 4-1. The received eye diagrams are not able to show any features of the transmitted symbols for any of the three systems. Consequently, it can be seen that the pre-demodulation constellations do not appear to be in any form of clear levels. However, the constellation points after equalisation are clear. An equaliser with a  $T/4$ -spaced 16-tap FFE and a  $T$ -spaced 4-tap DFE is used in these calculations. The constellation maps given in Figure 4.36 are at the maximum transmission power with system power margins of 9.3 dB, 8.3 dB and 5.7 dB respectively for the CAP-4, CAP-16, and CAP-64 systems. In this case, CAP-4 actually gives the best performance among all three systems. This can be explained in the same way as the PAM system where the 2-level scheme is preferred for lower data rate with moderate dispersion.

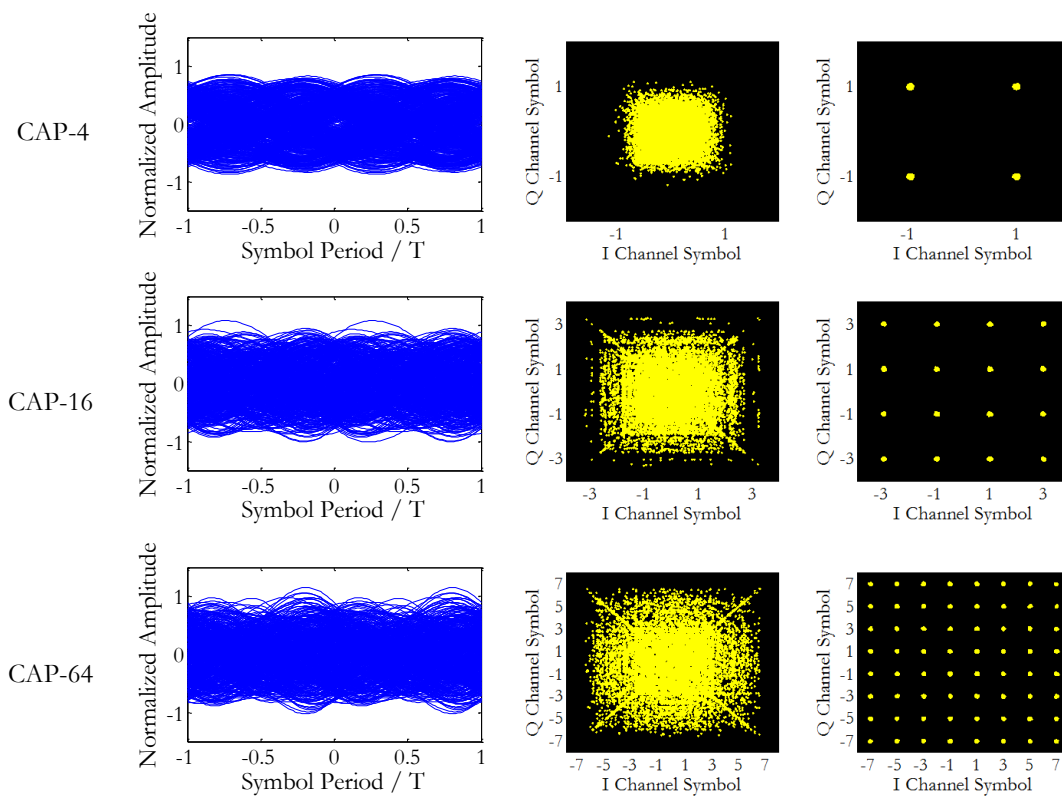


**Figure 4.36** 500 Mbit/s transmissions over 50 m SI-POF using CAP-4, CAP-16 and CAP-64. From left to right: received eye diagrams, received constellation maps, demodulated constellation maps

The constellation maps for high data rates up to 3 Gbit/s over 25 m and 1.5 Gbit/s over 50 m SI-POFs using CAP modulations are shown in Figure 4.37. Maximum transmitter power is assumed for all of the considered systems. Similarly to the previous results shown in Figure 4.36, the receiver noise levels used in these calculations are also scaled according to the symbol rate of each system and the reference receiver noise defined by the sensitivity (at 166.7 Msymbol/s) in Table 4-1. For example, 1 Gbit/s CAP-4 uses a symbol rate of 500 Msymbol/s, which gives a receiver noise 3x ( $500/166.7$ ) larger than the reference. The unsuccessful links (the total penalty is above the power budget) are boxed with dashed lines. For 25 m links, CAP-4, CAP-16 and CAP-64 achieve 1 Gbit/s, 2 Gbit/s and 3 Gbit/s respectively. And for 50 m links, only CAP-16 and CAP-64 are feasible for data rate above 1 Gbit/s with CAP-16 managing up to 1.2 Gbit/s and CAP-64 up to 1.5 Gbit/s.

Similarly, the numbers of equaliser taps are optimised to give the minimum combined power penalty of the noise enhancement and residual ISI. Since the I and Q channels are demodulated and equalised individually in the CAP systems, they tend to have slightly different power penalties. In this case, the channel with the higher penalty decides the overall system performance. As the only scheme that is feasible for 3 Gbit/s and 1.5 Gbit/s over 25 m and 50 m SI-POF, corresponding equaliser optimisation results for CAP-64 are shown in Figure 4.38. It can be observed that the tap configurations for the CAP-64 systems are more relaxed than those for PAM systems. For both data rates, the equalisation penalties are kept relatively low as long as a FFE section with more than 20 taps is used. Also, the number of DFE taps is not as decisive on the penalty performance as it is for PAM systems. As long as the FFE section is long enough, 4 taps of DFE is sufficient to keep the total penalty low. Consequently, the receiver equaliser structure for CAP systems is feasible with a simpler implementation compared with PAM systems.

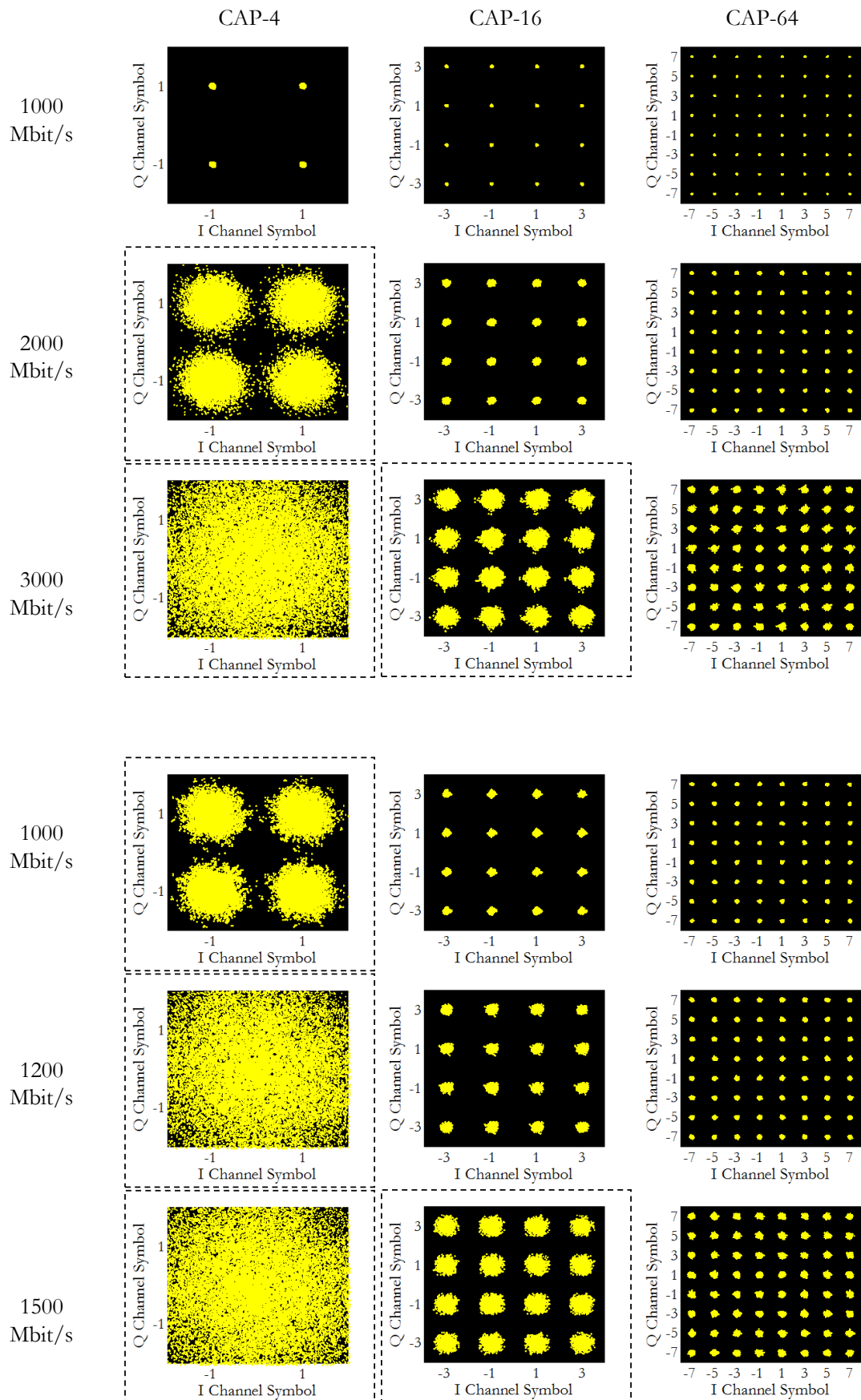
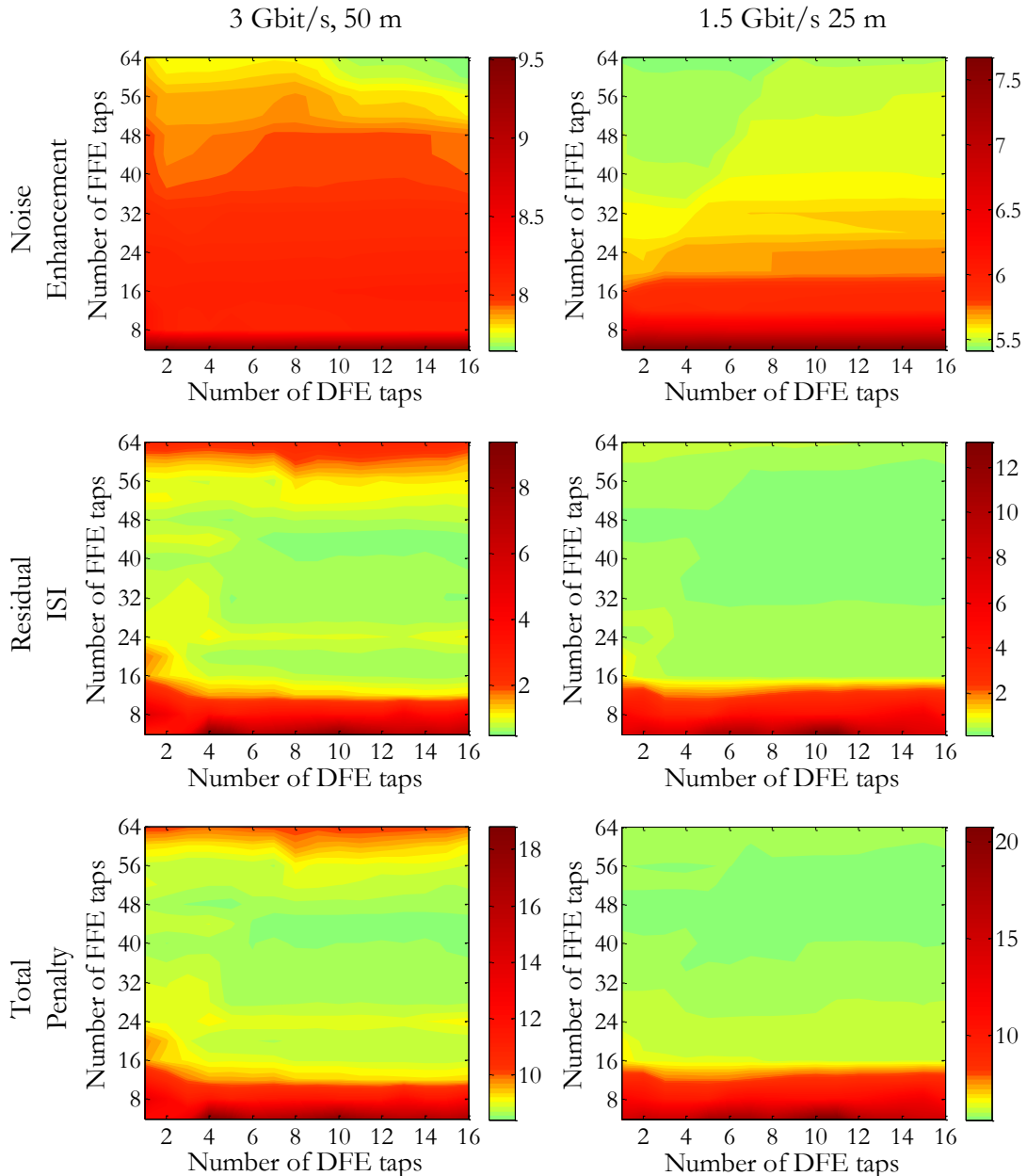


Figure 4.37 Constellation diagrams for the CAP-4, CAP-16 and CAP-64 systems at various data rates over 25 m (top) and 50 m (bottom) SI-POFs



**Figure 4.38 Optimisations of the numbers of taps in equalisers for 3 Gbit/s transmission over 25 m SI-POF (left) and 1.5 Gbit/s transmission over 50 m SI-POF (right) using CAP-64. The contour levels indicate the power penalties in the unit of dB0**

#### 4.5.2.3. Power Penalty Analysis

The system power penalties are calculated for CAP systems over 25 m and 50 m SI-POFs. In the 25 m systems, it can be observed that the lower level schemes have comparable system margin performance to the higher level schemes at 1 Gbit/s. However, when the data rate increases to 2 Gbit/s, the severe dispersion which causes significant equaliser penalties disables the CAP-4 system. CAP-64 is the only scheme feasible for 3 Gbit/s transmission with a power margin of 1.3 dB. In the 50 m systems, CAP-4 cannot even achieve 1 Gbit/s due to the extra dispersion and attenuation introduced by the extended

fibre length. CAP-16 and CAP-64 have similar performance at 1 Gbit/s with a margin of 3.5 dB. If the data rate increases to 1.5 Gbit/s, CAP-64 is the only remaining scheme that still has a system margin of 1.2 dB.

It can be seen that the CAP systems with higher levels tend to show advantages over the ones with lower levels at relatively high data rates. This is mainly due to the smaller bandwidth requirements of the higher level modulation signals, which suffer less from the ISI than the lower level systems. When equalisation is performed in the higher level modulation systems, both the noise enhancement penalty and residual ISI penalty are relatively moderate. This benefit, together with the lower receiver noise, compensates for the drawback of the multilevel penalty. Eventually, it makes the higher level modulation schemes outperform the lower level schemes as the data rate increases to a speed where the equalisation penalty is too large for the lower level schemes because of the severe ISI.

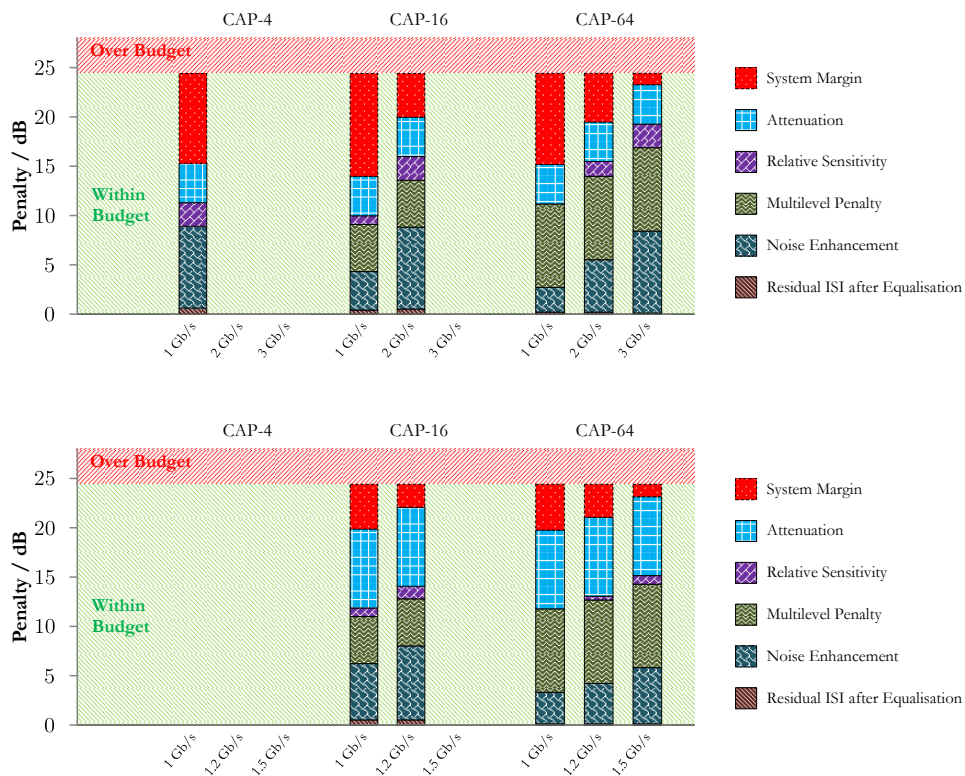


Figure 4.39 Link power budgets comparisons between the CAP-4, CAP-16 and CAP-64 modulation schemes over 25 m (top) and 50 m (bottom) SI-POFs

## 4.6. Conclusions

Multilevel modulation schemes for applications in LED-based SI-POF links are introduced in this Chapter. Both the baseband and passband modulation schemes can be scaled to multilevel to increase the overall system bandwidth efficiency. The PAM-N and CAP-N schemes are two typical multilevel schemes that have baseband and passband spectra respectively. The quadrature feature of the CAP schemes doubles the bandwidth efficiency since two orthogonal channels are transmitted simultaneously without interferences. It is shown that the Nyquist criterion is essential for both schemes in order to achieve ISI-free transmissions. Hence, receivers that can compensate for the channel dispersion and shape the received pulses back to Nyquist pulses are required. This is realized by equalisation techniques in the simulation evaluations.

A simulation model for multilevel system evaluations is developed. The LED transmitter, SI-POF and PIN photodiode are modelled as low pass filters with exponential, Gaussian and raised-cosine responses respectively. Using the parameters available from commercial devices, the -3 dB bandwidths of the LED-based SI-POF links are  $\sim 150$  MHz and 210 MHz for 50 m and 25 m respectively. This confirms that bandwidth efficient schemes such as multilevel and quadrature modulations are desired in such systems to enable gigabit/s transmissions. As an essential part of the receiver structure, equalisers are thoroughly discussed. Two popular types of equalisers, namely FFE and DFE are shown to extract the pre-cursor and post-cursor ISIs in the system. Particularly, the FFE section of the equaliser can be made with a tap spacing of fractions of the symbol rate. This configuration improves the quality of the equaliser impulse response with the expense of more taps and higher sampling rate. To keep simple equaliser structures and reasonable approximations of the ideal responses,  $T/2$  and  $T/4$ -spaced FFEs are used for the PAM and CAP systems respectively. Smaller tap spacing is used for CAP systems due to the extra demodulation process required to separate the I and Q channels, which needs relatively ideal matched filters. The link budget analysis approach is also introduced, which categorizes the penalties introduced by different elements in the system. They are the attenuation penalty, multilevel penalty, equalisation noise enhancement penalty, residual ISI penalty after equalisation and relative sensitivity penalty.

In the simulation evaluations, 2, 4 and 8 level PAM and CAP are investigated. It has been seen that none of these schemes can achieve gigabit/s transmission without using equalisation. With equalisation, the 2-level schemes outperform the multilevel schemes at

---

lower data rates (i.e. 500 Mbit/s) because of the moderate channel dispersion. However, this changes when the data rate increases to 2 Gbit/s over 25 m and 1.2 Gbit/s over 50 m SI-POFs. Obvious advantages of the multilevel schemes in both the PAM and CAP systems are shown. The numbers of taps in the equalisers are optimised to find the configurations for the minimum combined penalty (the noise enhancement and residual ISI penalties after equalisation). Results are shown for those schemes that achieve 3 Gbit/s over 25 m and 1.5 Gbit/s over 50 m SI-POFs. It is found that the PAM-8 system has an optimal configuration of  $\sim 40$ -tap FFE and 12-tap DFE whilst PAM-4 and CAP-64 have optimal configurations of  $\sim 20$ -tap FFE and 4-tap DFE. Link power budget analysis shows that PAM-8 and CAP-64 are the best schemes among the baseband and passband multilevel modulations respectively. PAM-8 achieves system margins of 2.2 dB and 1.9 dB whilst CAP-64 achieves 1.3 dB and 1.2 dB for 3 Gbit/s over 25 m and 1.5 Gbit/s over 50 m SI-POFs respectively.

# CHAPTER 5

## FPGA-BASED SYSTEM FOR PULSE AMPLITUDE MODULATION AND CARRIER-LESS AMPLITUDE/PHASE MODULATION IN PLASTIC OPTICAL FIBRE LINKS

*An FPGA evaluation platform is developed to experimentally investigate the transmission performance of multilevel modulation schemes in SI-POF links. This platform enables the generation of random bit sequences, PAM/CAP pulse shaping and has a high speed interface with a 1 Gsample/s DAC. The designs of the functional blocks within the FPGA and the interface design connecting the DAC are discussed. As a part of the system, the LED and PIN photodiode used for this experimental demonstration are also introduced. The equalisation and demodulation of the signal in the experimental work are carried out offline, where the received signal is captured using a sampling oscilloscope and then processed by Matlab programs. This approach requires extra care to be taken for the measurements of the system noises. The DAC signal generation performance is carefully compared with the theoretical results. Data transmission tests are carried out using PAM-8 and CAP-64 modulation schemes. PAM-8 is evaluated for a 3 Gbit/s transmission over 25 m SI-POF and CAP-64 for 1.5 Gbit/s over 50 m SI-POF. Both systems achieve error-free transmissions.*

## 5.1. System Architecture

The PAM and CAP multilevel modulation schemes have been shown in Chapter 4 as two feasible solutions to above 1 Gbit/s transmissions based on SI-POF. Such systems here are implemented experimentally and evaluated using commercially available components. A multilevel modulation scheme evaluation platform is developed for these purposes. In the following sections, the design of this platform is discussed in Section 5.2 to Section 5.4 and the corresponding data transmission experiments are discussed in Section 5.5.

Unlike the NRZ system, multilevel modulation schemes are yet to have any standard implementation in optical links. Owing to the fact that they require more signal processing in the electrical domain for the symbol-encoding and pulse shaping, high speed electronic components are a major challenge in such designs. It has been shown that in very high speed ( $>10$  Gbit/s) optical links that high speed power combiner can be used to generate multilevel waveforms [145] and transversal filters are capable of emulating the shaping filters at both the transmitter and receiver ends [53]. These approaches work well since no DSP is capable of such processing speed. However, POF links normally only require data rates up to few gigabit/s. If multilevel modulation is used, the symbol rate can be only few hundreds of megasymbol/s. This is well within the capabilities of the low cost and commercially available electronics such as FPGAs and DACs. Meanwhile, FPGAs enable the flexibility of implementing multiple modulation systems on a single chip and provide a multi-function system for different evaluations. Consequently, an FPGA chip is used in this work to provide a robust evaluation platform with great system flexibility.

The corresponding system architecture is shown in Figure 5.1. The FPGA is used as a combination of the pattern generator and modulator. A PRBS data stream is generated and then encoded to multilevel symbols. For a PAM system, these symbols are sent to the interface between the FPGA and DAC to generate the analogue modulation signal. For a CAP system, they are further encoded separately as the I channel and the Q channel symbols using a channel encoder. Two passband orthogonal Nyquist shaping filters are used to transform the CAP symbols to orthogonal pulses. These two pulses are aligned in time and combined to generate the actual waveform of the modulation signal. Following this, the samples are sent to the interface connecting the DAC in the same way as the PAM signal. The DAC used in this work is a 16-bit, 1 Gsample/s maximum device.

The DAC is synchronized with the FPGA at a sampling frequency the same as the interface data rate with the FPGA. Since the DAC is not capable of providing sufficient current to drive the LED, a RF amplifier is placed following the DAC to provide extra current.

At the receiver side, an ADC is needed to convert the electrical signal received by the photodiode to digital samples. In this work, this is done by using a sampling oscilloscope. A complete set of samples of the testing symbol sequence is captured and stored for further offline processing. Equalisation and demodulation are then performed offline using Matlab codes on the waveforms captured by the sampling oscilloscope.

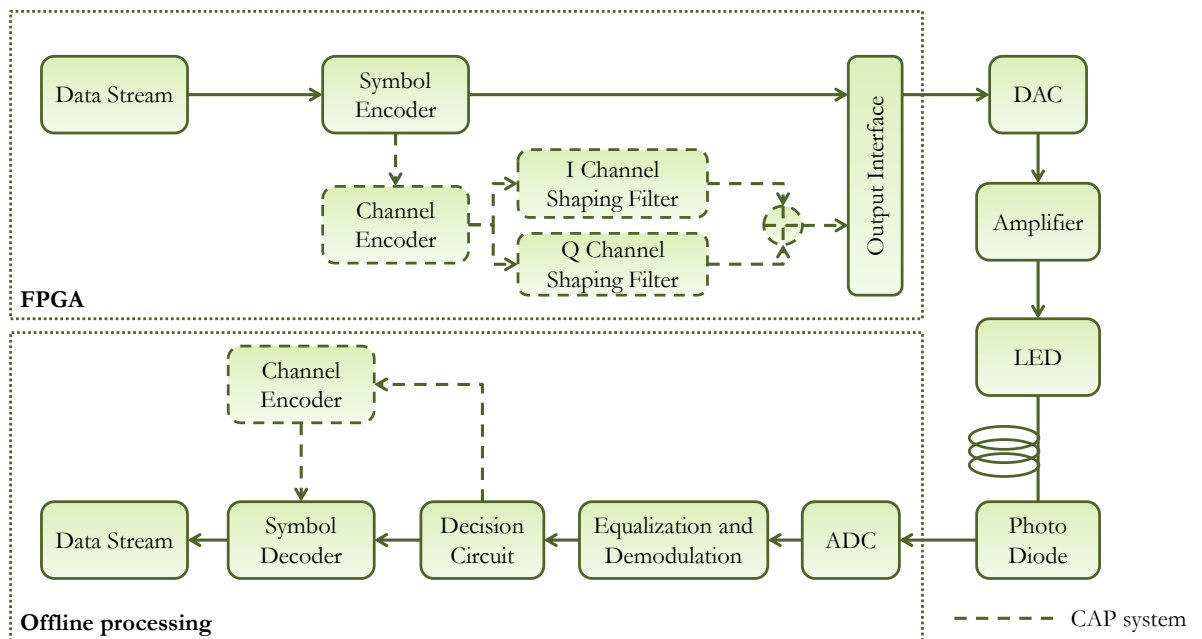


**Figure 5.1 Schematic diagram of the system for multilevel modulation scheme evaluations for LED-based SI-POF links**

## 5.2. FPGA-Based Modulation System

The FPGA platform used for this work is the Altera Stratix III development board populated with an EP3SL150F chip. This FPGA chip features 736 user I/Os, 384 multiplier blocks, 8 phase locked loops (PLL) and 132 full-duplex true low-voltage differential signalling (LVDS) channels. The high number of available I/Os makes this device very flexible to provide important system functions such as the USB programming block and parallel high speed interfaces. Meanwhile, this device can provide extra user defined I/Os, such as buttons and LED indicators to enable extra interfaces to help with system debugging. The multiplier blocks provide efficient arithmetic processing for the generation of the modulation signals. The system clock distribution is well monitored and controlled using 8 PLLs and the high speed LVDS interface provides up to 1.25 Gbit/s communication to the extension board, which is sufficient for the DAC used in this work with a sampling frequency up to 1 GHz. The 132 LVDS channels also guarantee enough pin resources for the 16-bit DAC used in this work.

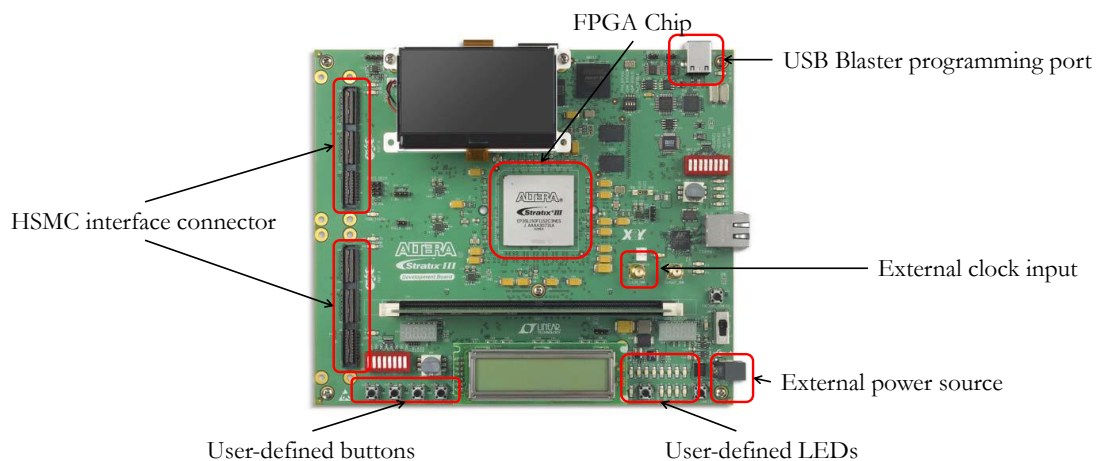


**Figure 5.2 Top view of the Altera Stratix III development board**

The Altera Stratix III development board is illustrated in Figure 5.2 with all the functional blocks used in this multilevel modulation scheme platform labelled in red boxes. The HSMC interface connectors are placed at the edge of the board to provide an easy access to the extension board (in this work, the DAC board). Four user-defined buttons are used to provide external triggers which can be used to select specific evaluation mode. User-defined LEDs are used to indicate the system status and provide visual assistance for system debugging. The board is powered using a 5 V external power source and programmed via a USB interface. An SMA connector clock input provides an external clock interface to the FPGA.

### 5.2.1. Design Overview and Clock Distribution

The clock is one of the most important issues in the design of an FPGA system, especially in the case where a DAC needs to be synchronized. The FPGA system clock has to be synchronized with the DAC sampling clock to perform stable data conversion. The system is designed with a 4x oversampling ratio to give good approximations of the CAP pulses, whilst one sample per symbol is used for PAM signal generations. Therefore, the DAC sampling frequency is 4x of the CAP system symbol rate and equal to the PAM system symbol rate.

The clock distribution network of the system is shown in Figure 5.3. A signal generator provides the reference clock for the entire system. This clock source is firstly connected to the PLL circuitry of the DAC chip, which further provides a 4x faster clock for the DAC sampling and 8x slower clock to the FPGA. The 8x divider is used to limit the external clock input through the SMA connector to the FPGA below the maximum allowed frequency of 150 MHz. The PLL network within the FPGA multiplies the clock accordingly to drive all the functional blocks. Dedicated PLL circuitry is implemented in each LVDS block to provide the clock for the data reception of the DAC in double data rate (DDR) mode where both the rising and the falling edges of this clock signal are used as the trigger.

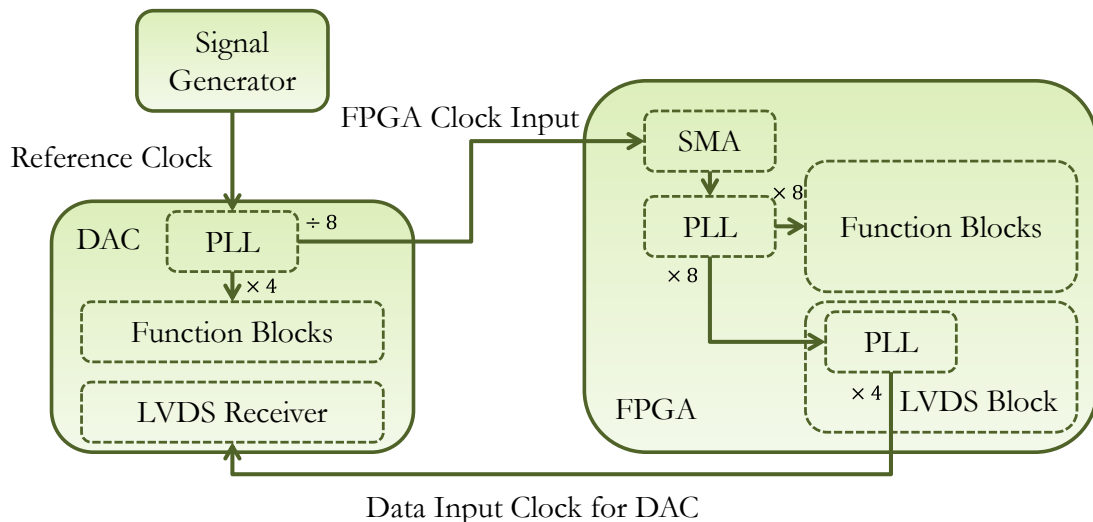


Figure 5.3 Clock distribution of the FPGA based evaluation system

Since the FPGA logic gates cannot deal with transitions at frequencies higher than  $\sim 700$  MHz within the chip, a 4x serializer is used to provide high speed LVDS interfaces with the DAC. Hence, the functional blocks within the FPGA run at a quarter of the interface output data rate to the DAC.

### 5.2.2. PRBS and PRS Generator

The Pseudorandom binary sequence (PRBS) is commonly used in data communication evaluations to emulate the data traffic in practical links. It is random since each bit in this sequence is independent from others. However it is ‘psuedo’ because it consists of repetitions of an N-bit long sequence. The most commonly used PRBS is the maximum length sequence (MLS) which can be generated using a linear feedback shift register (LFSR). For a register of length  $M$ , the corresponding MLS has a length of  $N = 2^M - 1$ .

Fibonacci LFSRs are implemented in the FPGA system to generate the PRBS. The schematic diagram of an example Fibonacci LFSR is shown in Figure 5.4. This is a 4-bit LFSR that generates an MSL with a length of 15. The sequence ‘1010’ shown in the register is the seed sequence. It can be any binary combination except for ‘0000’, which will lock the register in the ‘0000’ state. The third and fourth bit in the register is XOR’ed and fed back to the first bit. Before the result of the XOR gate is inserted, the register performs a right shift and vacates the first bit on the left for the feedback. In this example, the output of the XOR gate is ‘1’, so the next state of the register is ‘1101’. In this example, the fourth bit of the register is used as the output sequence bit.

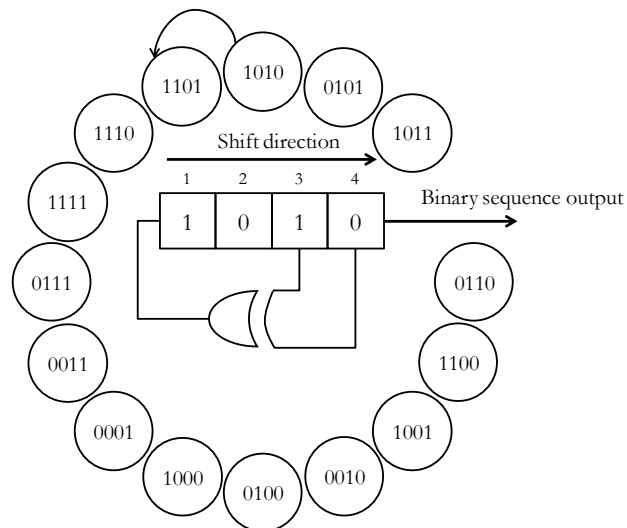


**Figure 5.4 A 4-bit Fibonacci linear feedback shift register for the MLS generation**

An additional pseudorandom sequence (PRS) generator is implemented after the LFSR to combine multiple bits in a PRBS to generate pseudorandom multilevel symbols. For all the considered systems, the length of the multilevel symbol sequence is set to 50. This number is chosen for the reason that it can be generated using a PRBS which is considered long enough for proof-of-principle system performance analysis. The FPGA achieves this by using a PRBS with length of 100 bits or 150 bits for the 4- or 8-level

scheme respectively. Every two or three bits are encoded to a multilevel symbol using simple decimal/binary mapping table. Additionally, in order to make the sequences in the I and Q channels of the CAP system completed uncorrelated, different seeds (the starting state of the register) are used in separate LFSRs.

### 5.2.3. Look-up Table for CAP System

The CAP pulses are generated using a look-up table which stores pre-defined samples of the ideal pulses. Taking the look-up table for CAP-64 as an example, it contains four linearly scaled sets of samples which can be used to represent the pulse shapes for a total number of eight levels given both positive and negative coefficients. The oversampling ratio is four and the ideal pulses are truncated at  $\pm 5$  symbol periods with 40 samples. Since the DAC has a resolution of 16 bits, the CAP pulses are limited to a peak-to-peak amplitude of 65536 ( $2^{16}$ ).

Figure 5.5 illustrates the CAP pulse shapes according to the values stored in the CAP-64 look-up table. The plotted pulses indicate the four positive levels and the negative versions are just the reverse of these cases. It is worth mentioning that for the CAP schemes with different levels, the pulse shapes with the maximum amplitudes are always used for the highest and lowest levels, which means that the pulse of level 4 and its negative inverse are used in this case. The pulse shapes with amplitudes linearly distributed between them are used for other levels.

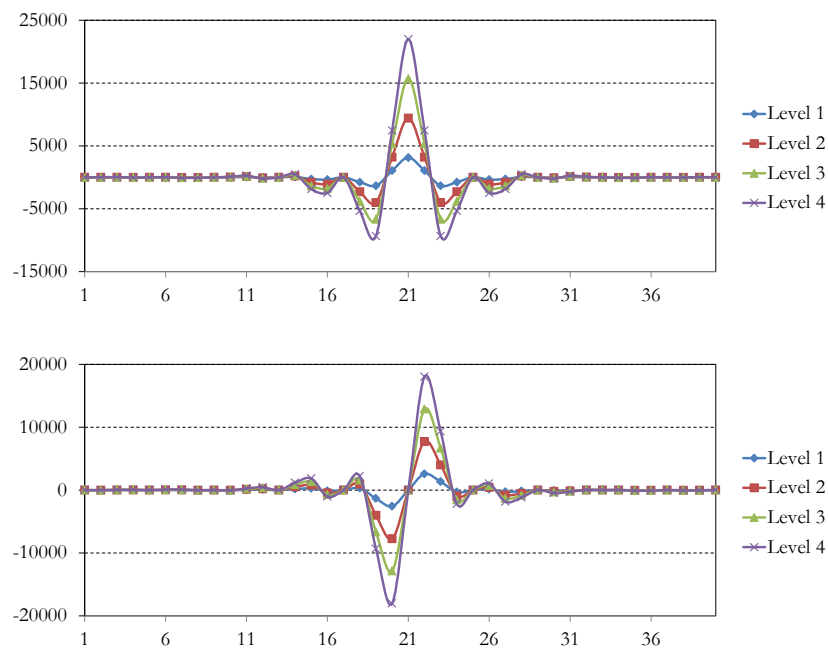


**Figure 5.5** The 40-sample look-up table for the CAP I (top) and Q (bottom) channels in the CAP-64 system. Raised-cosine shaping filters are used for both pulse shapes

The inputs to the look-up table consist of the number of levels and the I/Q channel symbols generated from the PRS generator. The look-up table block is triggered by a clock running at the symbol rate of the CAP system. The outputs of this block are the 40-sample pre-defined CAP I and Q pulses which are selected according to the input symbols. The schematic block diagram of the CAP look-up table is shown in Figure 5.6. The total length of each output is 640 bits which consists of forty 16-bit long samples with the first sample at the furthest right hand side of the register.

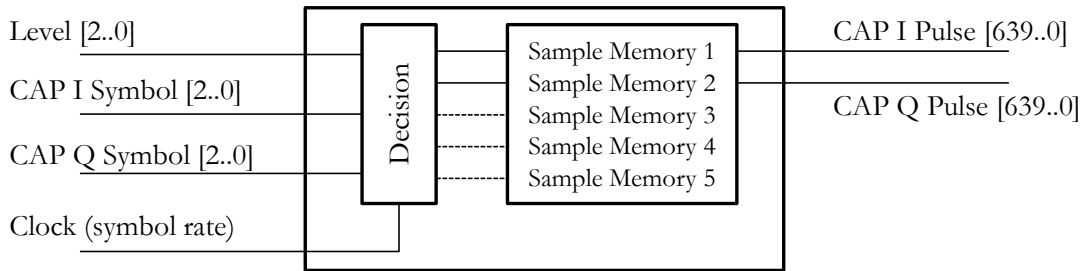


Figure 5.6 Block diagram of the CAP look-up table in the FPGA system

#### 5.2.4. CAP Sequence Buffer Block

The CAP look-up-table block generates CAP pulses according to the input symbol sequence at the symbol rate. A buffer register is needed to superpose the continuous symbols to generate the actual CAP modulation waveform for each channel. The CAP sequence buffer is 640-bits long and works like a FIFO buffer where a right shift of 64 bits (four samples) is performed at the symbol rate. The entire register values are superposed with the upcoming 640-bit output generated by the CAP look-up table after each right shift. In this way, the right most 64 bits always represent the four samples of the CAP I or Q channel modulation waveform at present time, with interferences from the earlier and later symbols been added. Each of the I and Q channels has one of this block. The schematic diagram of this block is shown in Figure 5.7. In this diagram, the FIFO-like buffer is at the state where a 64-bit right shift has just been performed and the register value is about to be updated by superposing the incoming samples (B40-B1).

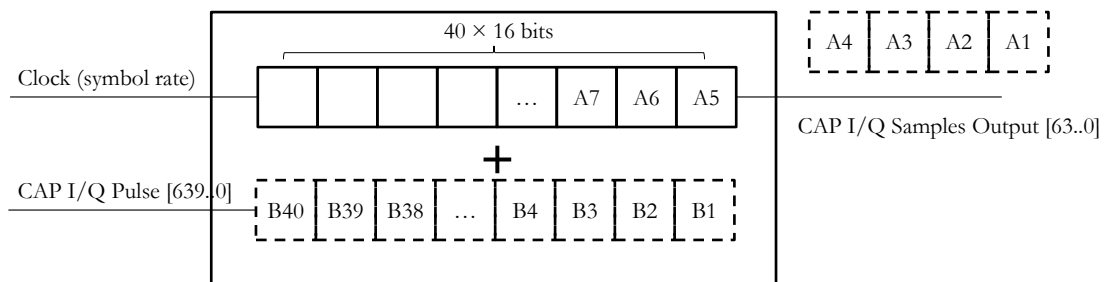


Figure 5.7 Block diagram of the CAP sequence buffer

### 5.2.5. PAM Sequence Buffer Block

Unlike in the CAP system, the pulse in a PAM system has an rectangular shape with fixed amplitude for a symbol period. There is no interference between adjacent symbols in the modulation signal. Therefore a FIFO-like buffer shown in Figure 5.7 is unnecessary. In fact, the PAM sequence buffer block has a combined functionality of the look-up table and sequence buffer. Another difference is that the output of the PAM sequence buffer is four individual PAM symbols rather than four samples from one symbol. Since four symbols are generated at each clock trigger, the input to the PAM sequence buffer requires four consistent PAM levels generated from the PRS generator. These configurations can be seen in Figure 5.8.

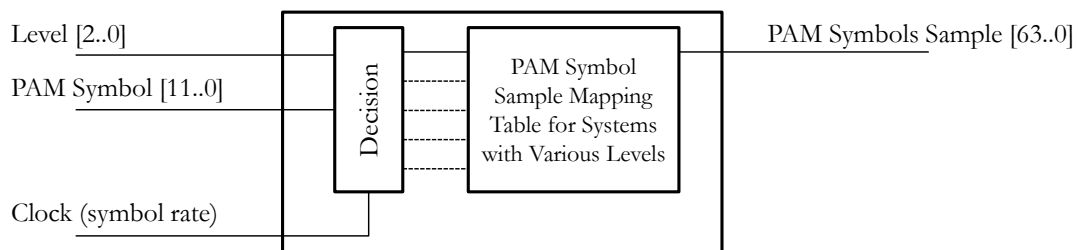


Figure 5.8 Block diagram of the PAM sequence buffer

### 5.2.6. Serializer Buffer Block

The high speed data interface between the FPGA and the DAC requires a dedicated serializer structure. Since four samples are generated per clock cycle in the FPGA system, the serializer structure has a serializing factor of four, which can sequentially transmit the samples at a clock rate 4x of the FPGA system clock. In this system, each pin of the FPGA output requires a serializer to interface with the DAC, which gives a total requirement of 16 serializers. Given the serializing factor of four, a 4-bit data sequence should be clocked into the serializer register every clock cycle. Meanwhile, for the  $m^{\text{th}}$  serializer, this 4-bit data sequence should consist of the  $m^{\text{th}}$  bit of the 4 consecutive samples. Consequently, the  $4 \times 16$ -bit samples generated from the sequence buffer have to be rearranged to a  $16 \times 4$ -bits format to fit the serializer register data format requirement.

Figure 5.9 illustrates how the serializer buffer rearranges the input four consecutive 16-bit samples generated by the sequence buffer. The 16 bits of the first sample (on the furthest right hand side of the input 64-bit data) are assigned to the MSBs of the sixteen 4-bit serializer buffers. The rest of the samples follow this process to be assigned to the second to the fourth bits. Finally, the  $16 \times 4$ -bit data is assigned to 16 serializers with the top one in Figure 5.9 configured as the MSB of the 16-bit DAC input and the bottom one as the

LSB. In this way, the four consecutive samples are serialized and transmitted at 4x the rate of the FPGA system clock.

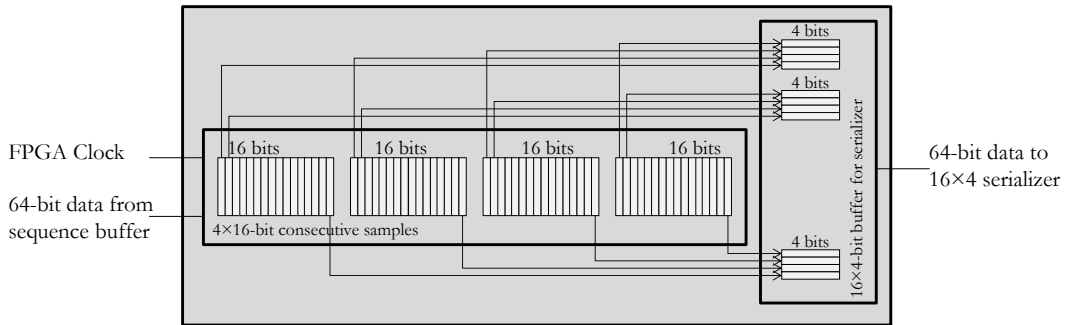


Figure 5.9 Block diagram of the serializer buffer

Figure 5.10 illustrates the interface between the serializer buffer and the dedicated serializer blocks in the FPGA for high speed LVDS outputs. A dedicated PLL is implemented to provide a DDR clock for the serial buffer inside the serializer block. The data is transferred from the self-defined serializer buffer to the parallel register in the serializer block at the FPGA system clock rate. The PLL generates a serial clock rate and a load enable signal according to the serializing factor N (which in this work is four) and clocks the parallel data into the serial shift register. After that, the shift register performs a shift triggered by the serial clock (in Figure 5.10 the shift is upward) and the MSB of the serial data is transmitted. A differential output buffer is placed at the end to provide LVDS outputs. Meanwhile, the clock generated by the dedicated PLL in the serializer block is also transmitted in LVDS format to clock the DAC reception.

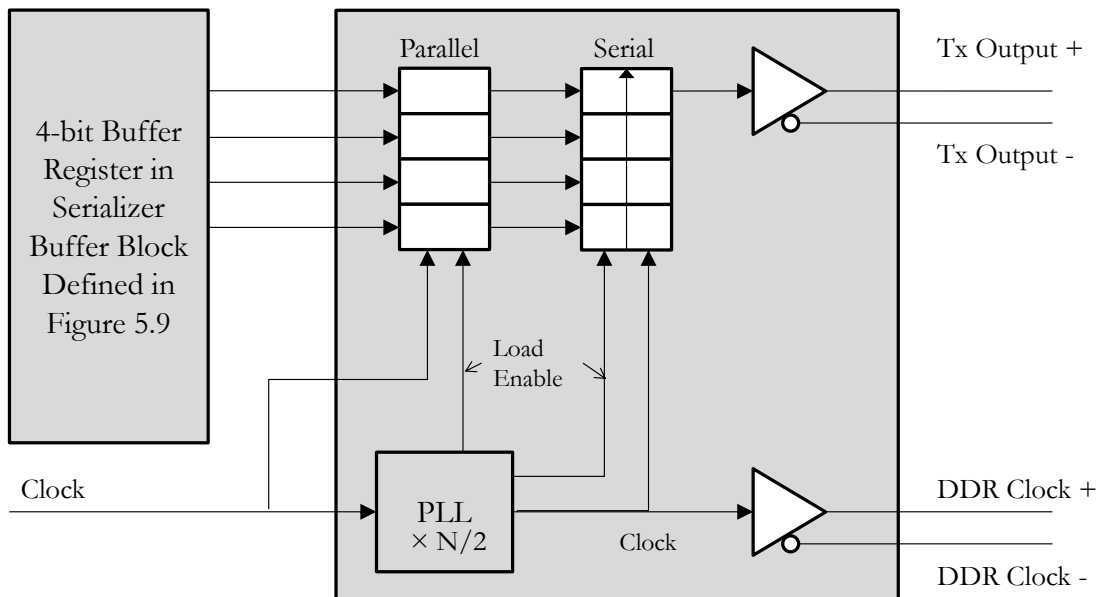


Figure 5.10 Block diagram of the dedicated serializer

### 5.2.7. Output Switch Block

Before the output of the serializer buffer is sent to the dedicated serializers, an output switch block is implemented to give user the access to the switching between operating modes of the FPGA. A total number of four individual serializer buffers are implemented as four separated channels, consisting of the CAP I channel, CAP Q channel, combined CAP I and Q channel and PAM channel. The switch is triggered by a user-defined button, which switches between these four channels. The schematic block diagram of the output switch implementation is shown in Figure 5.11.

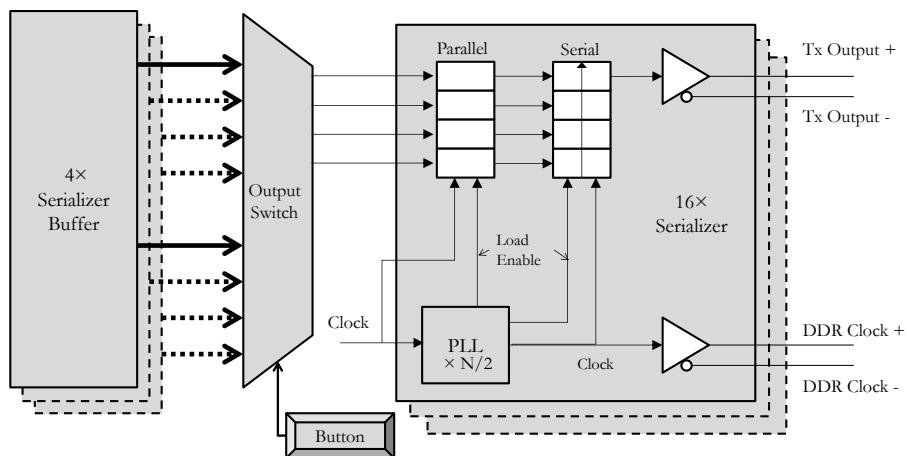


Figure 5.11 Output switch implemented between the serializer buffers and dedicated serializers in the FPGA system providing channel selectivity

### 5.2.8. The Overall FPGA System

The main functional blocks of the FPGA modulation system have been discussed. Putting all these blocks together, the overall FPGA system schematic diagram is shown in Figure 5.12. As seen in the diagram, the CLK\_Source provides the system clock for the entire FPGA system<sup>18</sup>. It can also be observed that another two user-defined buttons are connected with the PRBS\_Generator block to select the levels and sequence lengths of the evaluated modulation schemes. Meanwhile, an LED indicator is connected with one of the PRBS\_Generator block outputs to give a 1 s on/off signal to provide visual assistance for system debugging. The OUTPUT\_MUX block is the output switch block introduced in Section 5.2.7 which selects between the PAM, CAP I, CAP Q and combined CAP channels. This is also controlled by a user-defined button and a 3-bit counter. The nodes left open-circuit in this diagram are designed for programming debugging purposes and are not used when the FPGA system is running normally.

<sup>18</sup>This PLL multiplier speeds up 8x the SMA-input clock back to the frequency of the signal generator output, which is used as the FPGA system clock

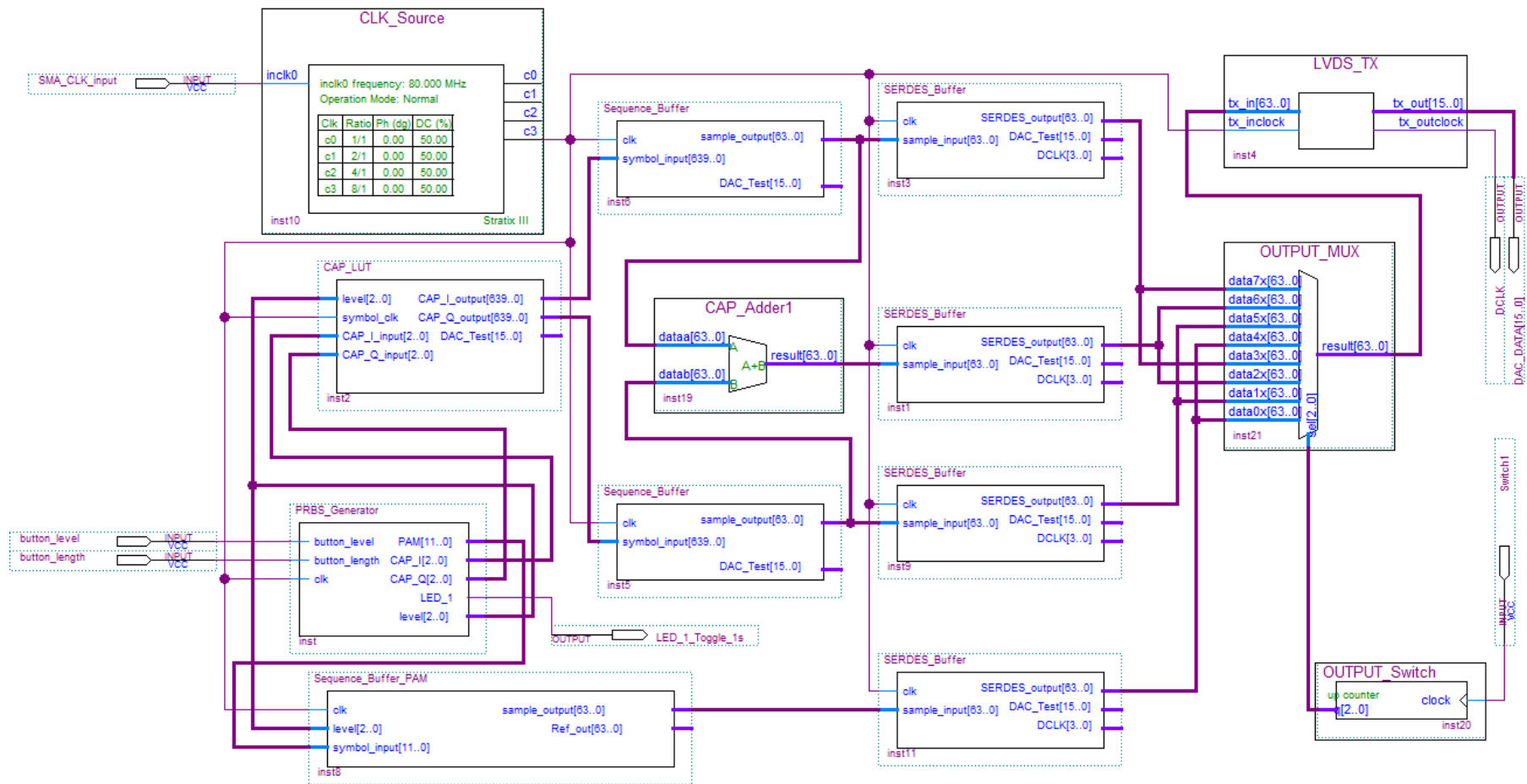


Figure 5.12 Complete schematic block diagram of the FPGA-based evaluation system

### 5.3. Digital to Analogue Converter

The DAC used in this work is the 16-bit, 1 Gsample/s DAC5682z evaluation board. The top view of this board is shown in Figure 5.13 (a). The corresponding functional block diagram is illustrated in Figure 5.13 (b). The DAC5682z chip has two DAC channels. In order to achieve the maximum sampling rate, one of them has to be disabled. The output has configured to drive a doubly terminated transformer with an impedance of  $50 \Omega$ . At the input end, data clock input is aligned with the input data using a delay loop lock (DLL). A software-controlled gain block is implemented at the output buffer to provide a 1~15x DAC amplitude control.

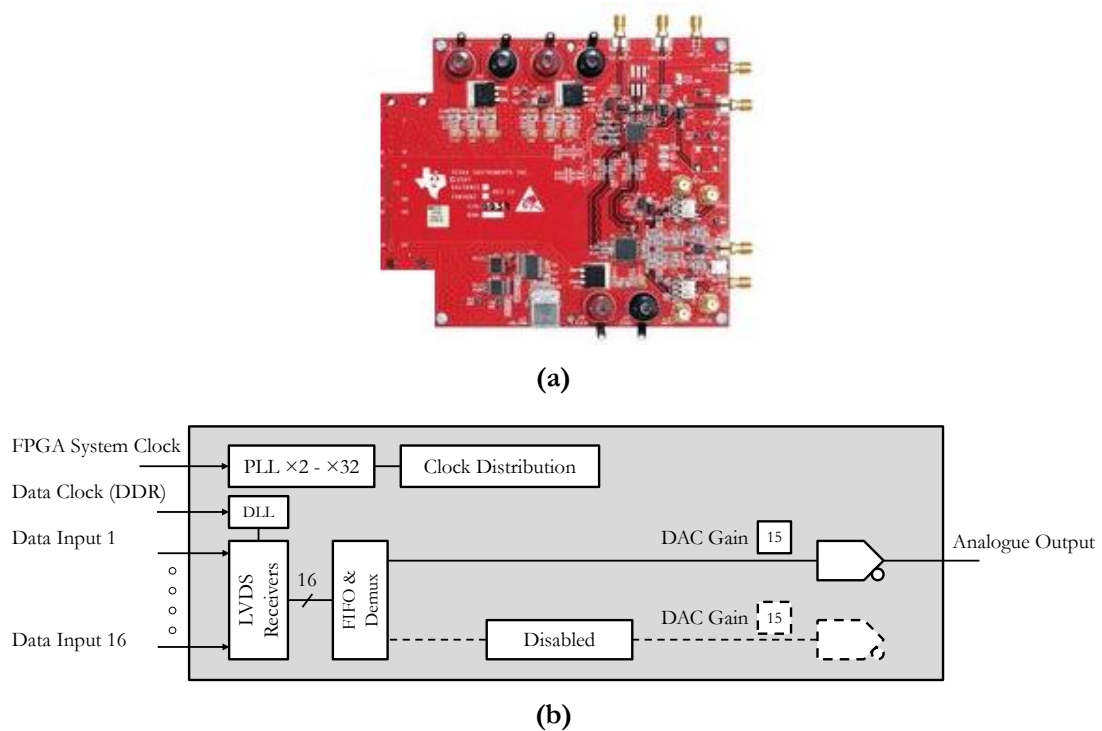


Figure 5.13 (a) Top view of the DAC5682z EVM board and (b) block diagram of the DAC5682z chip

## 5.4. Transceiver

The transceiver used in the experimental work is the FC1000T from Firecomms. It consists of an FC300R RC-LED transmitter and an FC300P photodiode. The transceiver is packaged in an Optolock connector developed by Firecomms [42], which provides butt-coupling to bare POF cables. As seen from Figure 5.14, a 3.3 V DC power supply is used to provide the bias voltage for both the RC-LED and photodiode. The amplified modulation signal from the DAC is used to drive the RC-LED via a bias-T circuitry. At the receiver end, the NT24L50 TIA from National is connected with the photodiode to generate voltage signals for the sampling oscilloscope to capture.

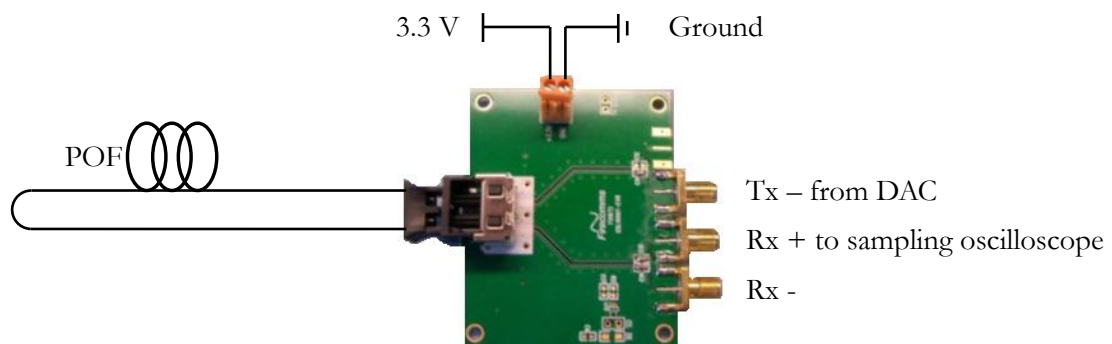


Figure 5.14 Top view of the FC1000T transceiver evaluation board

## 5.5. Experimental Results

The FPGA system described in Section 5.2 is used to generate 2-, 4- and 8-level modulation signals for the PAM and CAP systems. The DAC generated signals are carefully compared with the theoretical calculations. According to the theoretical studies in Chapter 4, the highest data rate achievable for 25 m and 50 m SI-POFs are 3 Gbit/s and 1.5 Gbit/s respectively. Since the DAC is limited to a sampling rate of 1 Gsample/s, the FPGA platform supports up to 3 Gbit/s PAM-8 and 1.5 Gbit/s CAP-64 transmissions given that one sample per symbol and four samples per symbol are used for these systems respectively. Therefore, data transmission evaluations are carried out for 3 Gbit/s PAM-8 and 1.5 Gbit/s CAP-64 in this work for 25 m and 50 m SI-POFs respectively to demonstrate the successful links using multilevel modulation schemes.

### 5.5.1. Modulation Signal Generation

For the PAM systems, the DAC generated electrical eye diagrams are shown in Figure 5.15 in comparison with the calculated results. The calculated eye diagrams are noiseless.

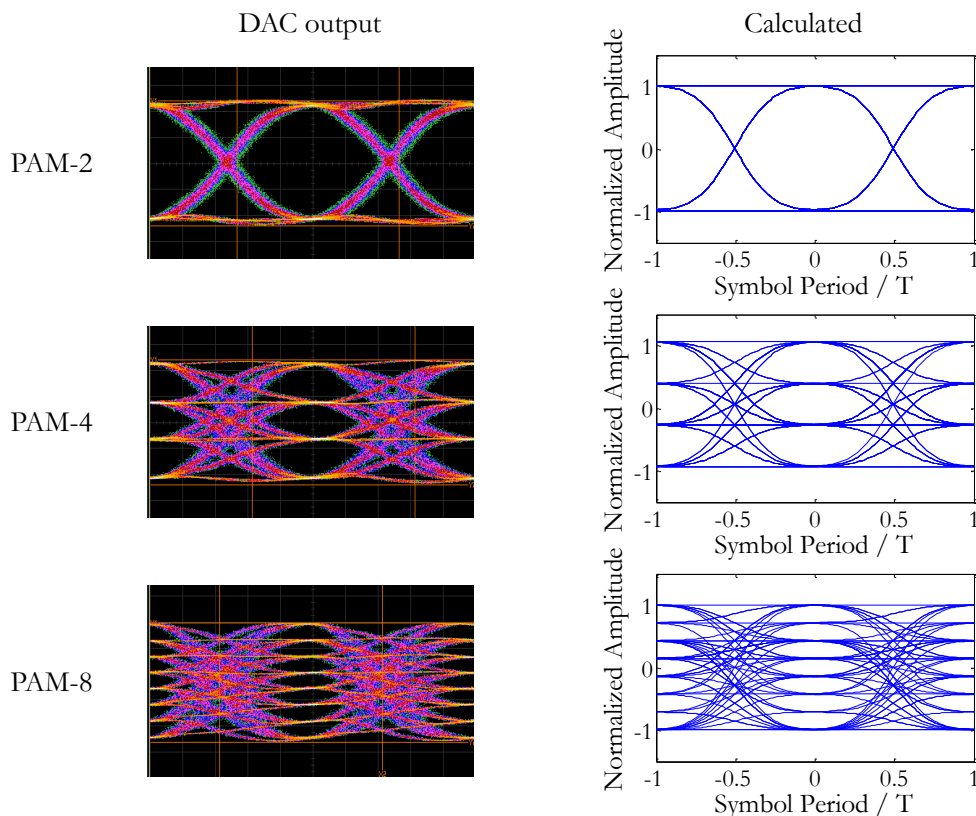


**Figure 5.15** PAM system electrical eye diagrams generated by the DAC in comparison with the calculations

Since the DAC operates at the maximum sampling rate, it can be seen from Figure 5.15 that the DAC outputs exhibit Gaussian-like responses. The eyes are wide open with some time jitter at the level transitions. The calculated results are based on an ideal PAM signal, which passes through a Gaussian filter with a -3 dB bandwidth of 1 GHz to simulate the DAC. It can be seen that the measured eyes match with calculated ones very well.

For the CAP systems, the raised-cosine-like pulses tend to be affected by the staircase effect of the DAC at low frequencies as seen in Figure 5.16. It is well known that the staircase effect introduces an extra sinc shaping filter at the DAC output. However, the device and channel bandwidths are usually much smaller than the centre lobe bandwidth of the sinc filter. Hence, the waveform will be smoothed out by the low bandwidth devices given the nearest side lobe of the DAC is at above 1 GHz (assuming the DAC operates at its maximum sampling rate), which is far beyond the bandwidths of any components used in the system.

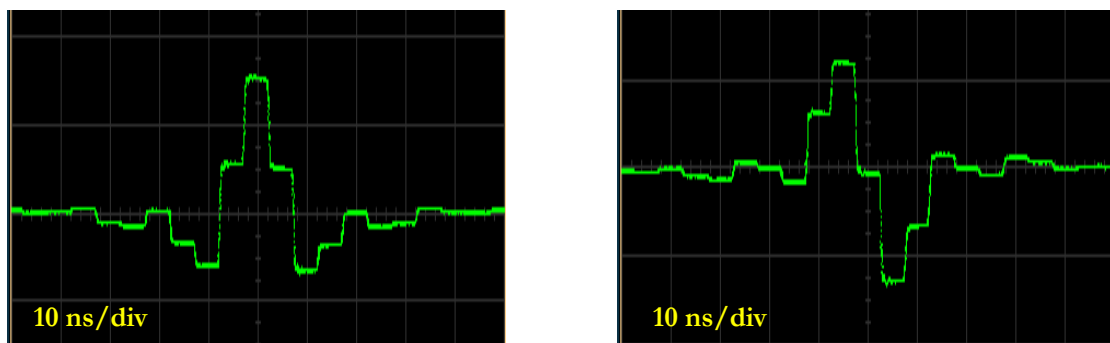


**Figure 5.16 CAP I channel (left) and Q channel (right) pulses generated by the DAC. The sampling rate is 200 MHz. Pulses are truncated at  $\pm 2.5$  symbol period**

The measured eye diagrams of the DAC outputs for the CAP systems running at 250 Msymbol/s (1 Gsample/s) with 2, 4 and 8 levels are compared with the calculated results in Figure 5.17. It can be seen that the CAP I channel eye diagrams strictly converge to the symbol levels whilst the Q channel eye diagrams converge to zero at intervals of  $nT$ . Although the staircase effect of the DAC outputs still exists, the four samples per symbol DAC outputs provide well-approximated CAP modulation signals.

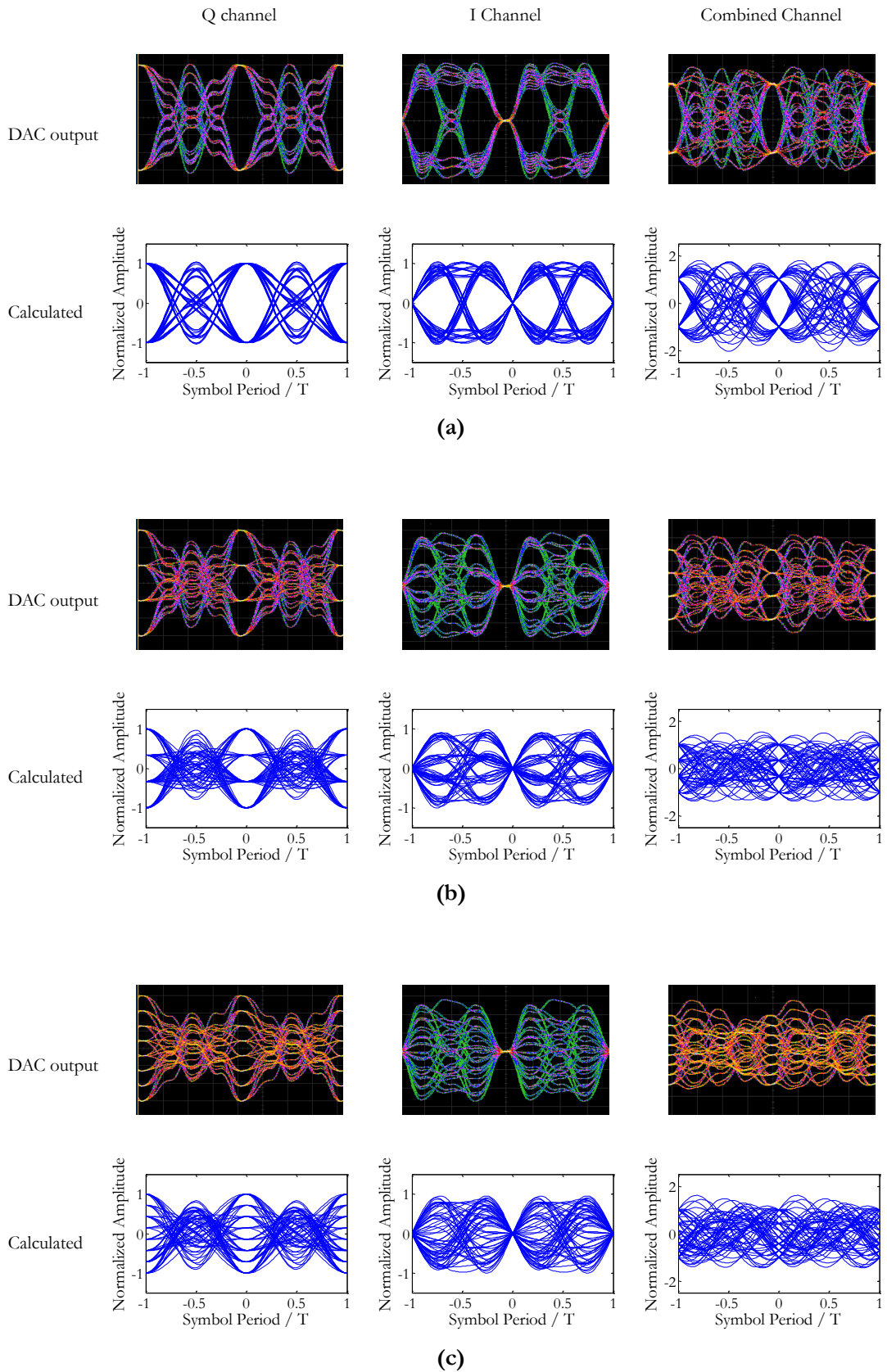


**Figure 5.17** Comparisons of the eye diagrams between the DAC outputs and calculations for the (a) CAP-4, (b) CAP-16 and (c) CAP-64 systems at a symbol rate of 250 Msymbol/s

### 5.5.2. Signal Amplification

The modulation signal generated from the DAC is not capable of driving an LED transmitter due to the limited current output. Therefore a ZHL-6A amplifier from Mini-circuit is used to provide extra current driving capability. The amplifier has an -3 dB electrical bandwidth of 500 MHz, which is sufficient for the systems evaluated in this work. It is shown in Figure 5.18 that the amplifier barely introduces any distortion to the 1 Gsymbol/s PAM-8 signal.

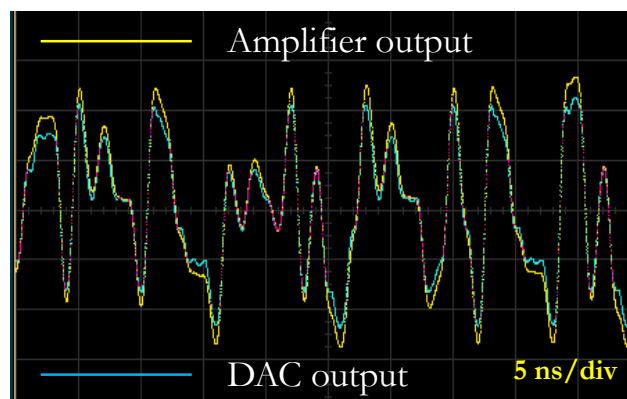


**Figure 5.18** The amplified and non-amplified PAM-8 waveforms at 1 Gsymbol/s. The amplitude of the waveforms is not to be scaled

### 5.5.3. Offline Processing Approach

To capture the received signal for offline processing, a sampling oscilloscope is triggered by the clock same as the sequence rate (symbol rate / symbol length). The oversampling ratio is 80, which gives 4000 samples for 50 received symbols. These samples are processed in Matlab offline for equalisation and demodulation purposes.

Since the noise of the system can be considered Gaussian, it can be removed by averaging the amplitudes at each sampling point during the signal capture. An averaging factor of 256 is used in this work. After averaging, the captured signals only carry the ISI information of the system. The noise is measured separately with the photodiode turned on for BER evaluation. In the offline processing, the captured signal is firstly aligned with the original modulation signal and then sent to the equaliser for tap values adaption. The noise enhancement factor is calculated using the adapted tap values and it is used to scale up the pre-measured noise to determine the post-equalisation noise amplitudes. Finally, the eye diagrams/constellation maps and BER curves can be plotted given the equalised signal and the enhanced noise.

### 5.5.4. Noise Measurements

The photodiode and the sampling oscilloscope are the two major sources of noise in this system. In order to characterize the performance of different modulation schemes, the photodiode noise has to be determined. Unfortunately, this noise cannot be measured directly since the only instrument available to quantize the noise power is the sampling oscilloscope, which is a noisy instrument as well. Since these two major noises can both be considered as additive white Gaussian noises, the following equation can be used to describe the relationship between them,

$$\sigma_{PD}^2 + \sigma_{scope}^2 = \sigma_{total}^2 \quad 5-1$$

where  $\sigma$  is the standard deviation of the Gaussian noise.

The oscilloscope noise standard deviation can be simply measured by putting the oscilloscope in free-run mode without any input signal. The signal captured in this way is the oscilloscope noise. On the other hand, the total noise standard deviation can be measured using a back to back POF link with the transceiver turned on, but not driven by any modulation signal. This will allow the pure photodiode noise to be captured by the sampling oscilloscope. Since the measured signal always combines the input noise and the oscilloscope noise, the noise standard deviation measured in this case is the  $\sigma_{total}$  term in Equation 5-1. Hence, the standard deviation of the photodiode noise can be calculated using the equation

$$\sigma_{PD} = \sqrt{\sigma_{total}^2 - \sigma_{scope}^2} \quad 5-2$$

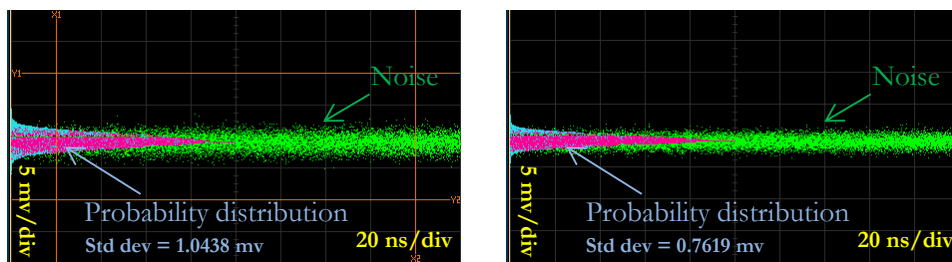


**Figure 5.19 Measured noise standard deviations with (left) and without (right) the photodiode**

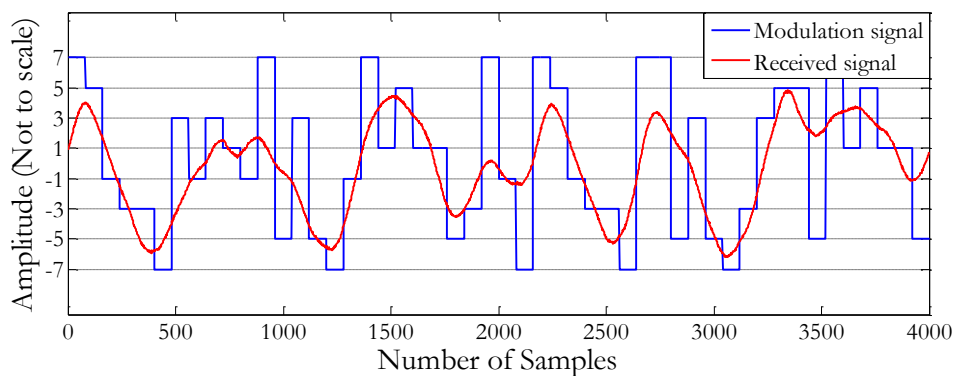
As it can be seen from Figure 5.19, the standard deviation measured with the photodiode turned on is 1.04 mV whilst the one without is 0.76 mV. This gives a pure photodiode receiver noise standard deviation of 0.71 mV calculated using Equation 5-2. This value is used to characterize the noise amplitude for all of the systems evaluated using different modulation schemes in this work.

### 5.5.5. Data Transmission Evaluations

Accordingly, data transmission evaluations are carried out based on the PAM-8 and CAP-64 systems for 25 m and 50 m SI-POFs respectively. The 50-symbol 8-level sequences are used for both systems. Particularly, three different seed registers are used to generate the original PRBS sequences for the PAM, CAP I and CAP Q channels respectively, which further gives the multilevel symbol sequences. The fibre used in the evaluation is the Eska Mega SI-POF with a bandwidth-distance product of 10 MHz·km. The software-defined DAC gain is used to change the modulation amplitude, which emulates the change of the transmission power at the transmitter side. In this way, the use of an optical attenuator is avoided during the BER measurements.

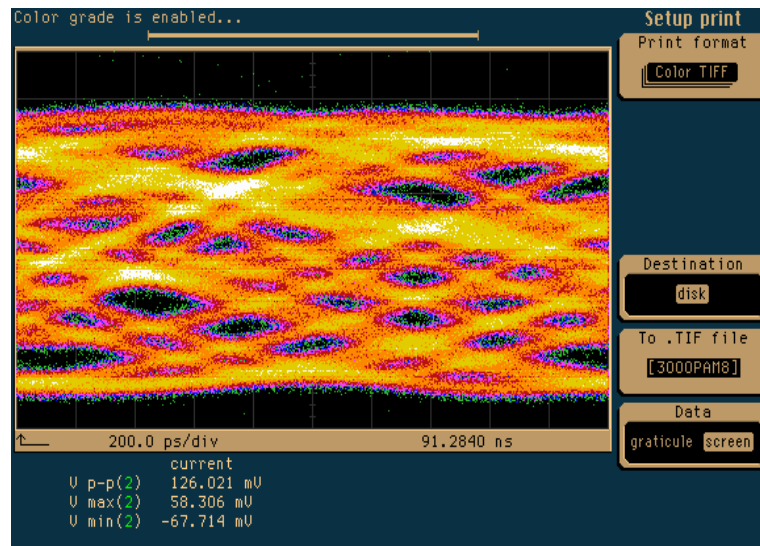
#### 5.5.5.1. 3 Gbit/s PAM-8 Transmission over 25 m SI-POF

Figure 5.20 illustrates the comparison between the modulation signal and the received signal for the PAM-8 system over 25 m SI-POF. A total number of 4000 samples are captured with an oversampling ratio of 80 samples per symbol. The received signal waveform is scaled to match the modulated signal symbol amplitude for illustration purpose. Unsurprisingly, the received signal is heavily distorted due to the limited system bandwidth. It can be seen that the signal follows the general shape of the modulation signal but the transitions between symbols are very slow.



**Figure 5.20 Comparison between the modulation and the received signals for the 3 Gbit/s PAM-8 system over 25 m SI-POF**

The corresponding received eye diagram is shown in Figure 5.21. The eye diagram hardly exhibits any clear eye structure or symbol transitions. Therefore, it is not feasible to recover any data from this waveform directly.



**Figure 5.21** Corresponding received eye diagram for the 3 Gbit/s PAM-8 system over 25 m SI-POF

The captured waveform is used for equalisation adaption in offline processing. Corresponding equalisation adaption iterations are illustrated in Figure 5.22 for two different tap lengths of 60-tap FFE/20-tap DFE and 80-tap FFE/30-tap DFE. The FFE section of the equaliser is  $T/2$ -spaced whilst the DFE section is  $T$ -spaced. It can be seen that the 60-tap FFE/20-tap DFE equaliser is not able to recover the symbols whilst the 80-tap FFE/30-tap DFE equaliser recovers the PAM-8 symbols quite well and the symbol levels can be clearly seen after  $\sim 5000$  iterations. In this evaluation, the 80-tap FFE/30-tap DFE equaliser is used to recover the eye diagram and calculate the BER.

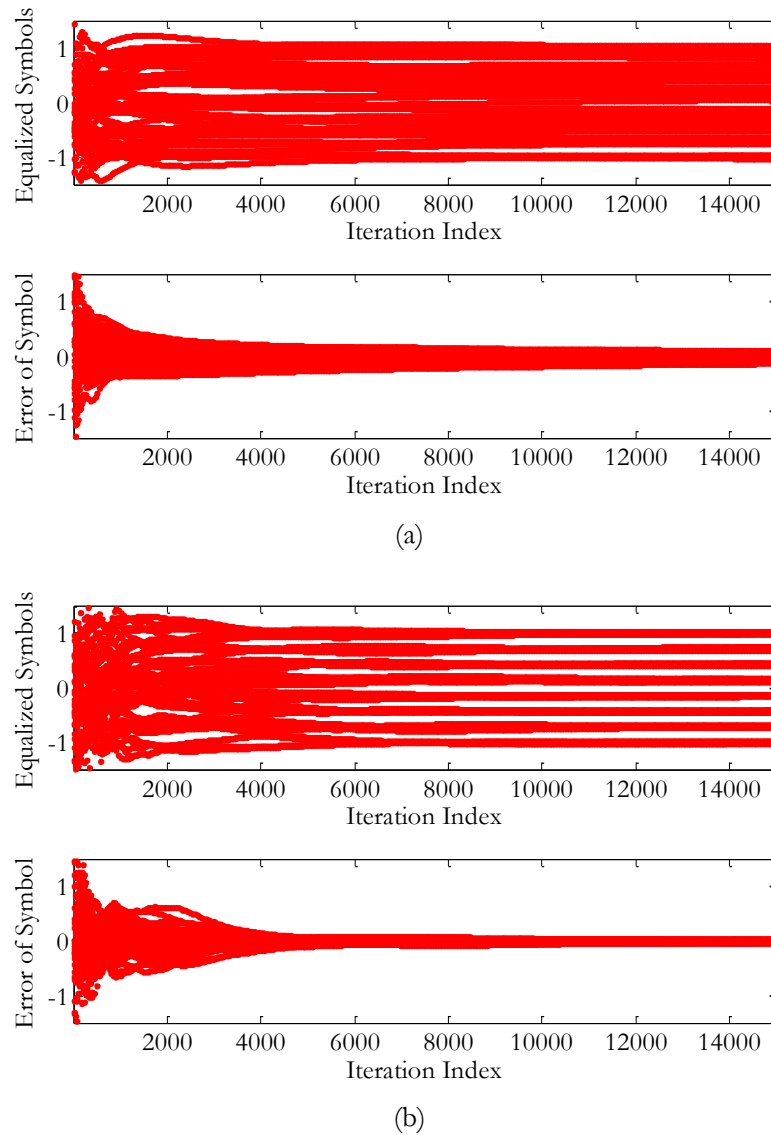


**Figure 5.22** Equalisation adaptation iterations for the 3 Gbit/s PAM-8 transmission over 25 SI-POF with (a) 60-tap FFE and 20-tap DFE and (b) 80-tap FFE and 30-tap DFE

The equalised eye diagrams for back-to-back, 10 m, 15 m and 25 m SI-POFs using the PAM-8 modulation at 3 Gbit/s are shown in Figure 5.23 (a). These eye diagrams are recovered at a received power of -12 dBm. Clear eyes are achieved between symbols. Corresponding BERs are calculated at different received powers according the measured noise. The results are shown in Figure 5.23 (b). The back-to-back link achieves a sensitivity of -11.6 dBm. Error free transmissions are achieved at received powers of -11 dBm, -9.4 dBm and -9 dBm for 10 m, 15 m and 25 m SI-POFs, which gives 0.6 dB, 2.2 dB and 2.6 dB dispersion penalties respectively. The maximum received powers at these lengths are -4.2 dBm, -6.2 dBm and -8.4 dBm, resulting in a 6.8 dB power margin for 10 m, 3.2 dB for 15 m and 0.6 dB for 25 m SI-POFs.

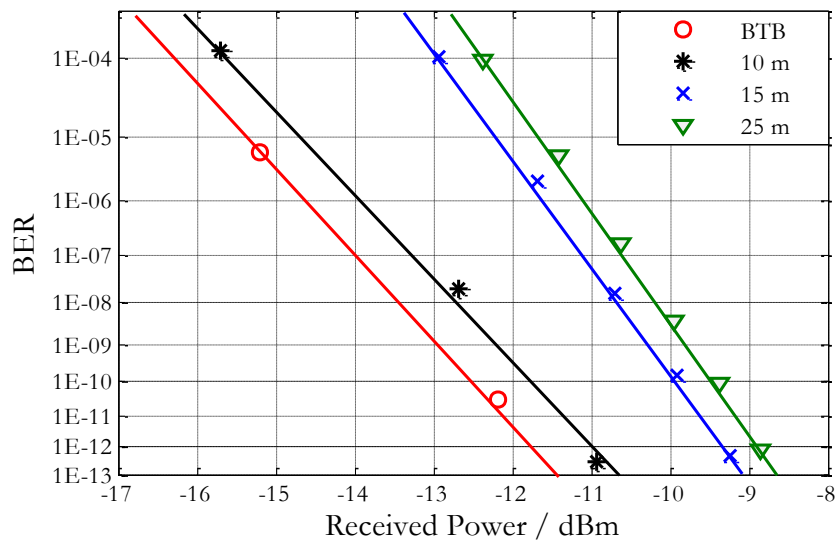
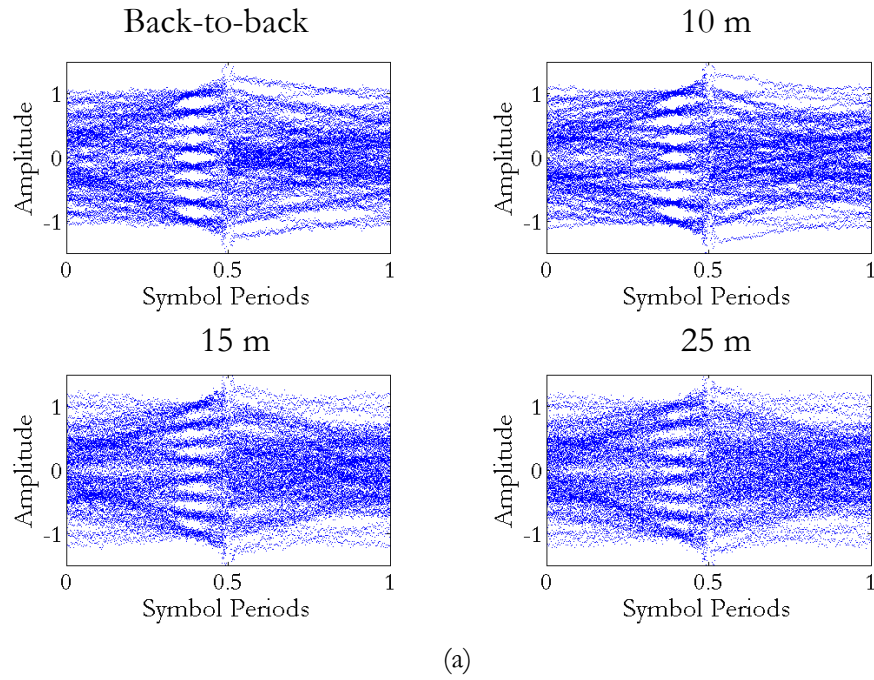
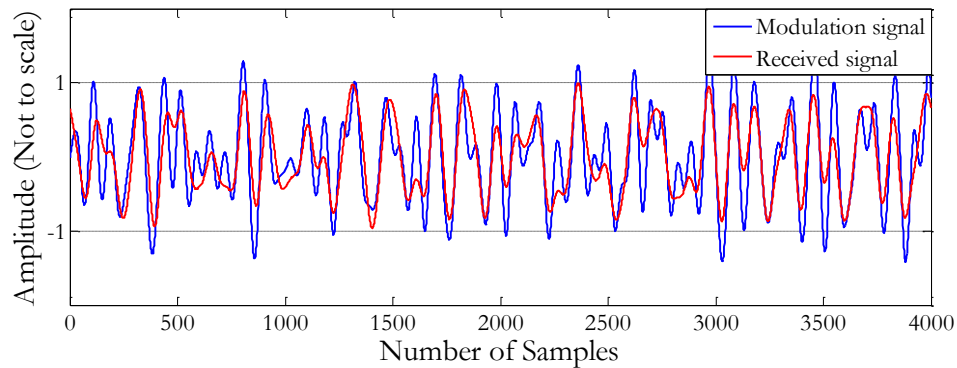


Figure 5.23 (a) Equalised eye diagrams of the 3 Gbit/s PAM-8 system at -12 dBm and (b) corresponding BER curves in comparison with back-to-back

#### 5.5.5.2. 1.5 Gbit/s CAP-64 Transmission over 50 m SI-POF

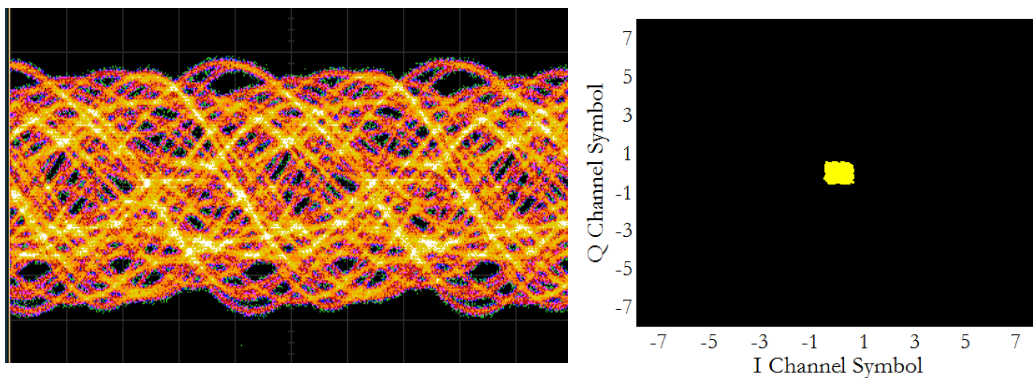
Similarly, Figure 5.24 illustrates the comparison between the modulation signal and the received signal for the 1.5 Gbit/s CAP-64 (250 Msymbol/s) transmission over 50 m SI-POF. The received signal follows the transitions of the modulation signal with some distortion. However, since the bandwidth of the CAP-64 signal at 250 Msymbol/s is mostly within the overall SI-POF system bandwidth ( $\sim 180$  MHz), the distortion

introduced to the received signal is much less than that in the PAM system as shown in Figure 5.20. It can be seen that most of the transitions in the received signal overlap with the modulation signal and only those high frequency transitions are causing insufficient rising and falling responses.



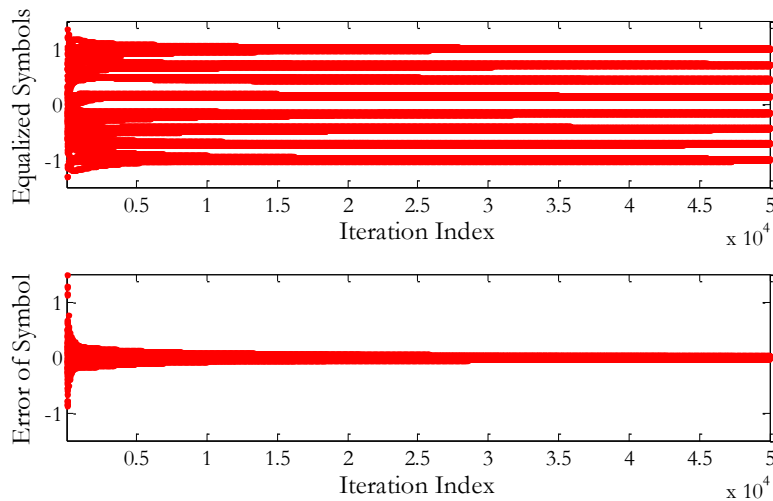
**Figure 5.24 Comparison between the modulation and received signals for the 1.5 Gbit/s CAP-64 system over 50 m SI-POF**

Figure 5.25 shows the received eye diagram and constellation map after direct demodulation without any equalisation. It can be seen that the eye diagram loses the ISI free feature of the CAP pulses and the constellation map exhibits no clear levels.

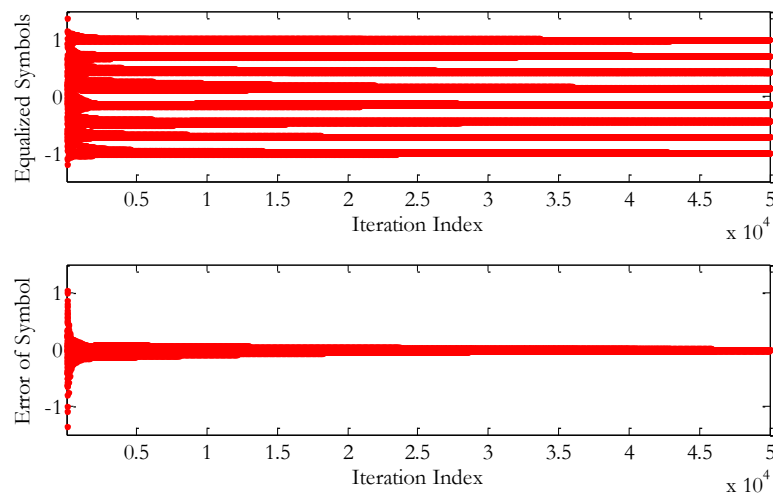


**Figure 5.25 Received eye diagram and constellation map for the 1.5 Gbit/s CAP-64 system over 50 m SI-POF**

The equaliser in the CAP-64 system functions as both the channel equaliser and the demodulator. Therefore separate equalisers are required in order to recover the data from the I and Q channels respectively. The equalisation adaption iterations for both channels are shown in Figure 5.26. Both channels are demodulated with clear symbol levels. In this evaluation, a 30-tap T/4-spaced FFE and 15-tap T-spaced DFE equaliser is used.



(a)



(b)

**Figure 5.26 Equalisation adaption iterations for the 1.5 Gbit/s CAP-64 transmission over 50 m SI-POF (a) Q channel, (b) I channel**

The constellation map and BER curve of the equalised signals are shown in Figure 5.27. A clear constellation can be seen after the equalisation. Error free transmission is achieved for 50 m SI-POF at -15.2 dBm. Compared with the back-to-back error free received power of -17.7 dBm, a 2.5 dB dispersion penalty is introduced by the SI-POF. Given that the received power after 50 m SI-POF is -11.8 dBm. The total power margin achieved is 3.4 dB.

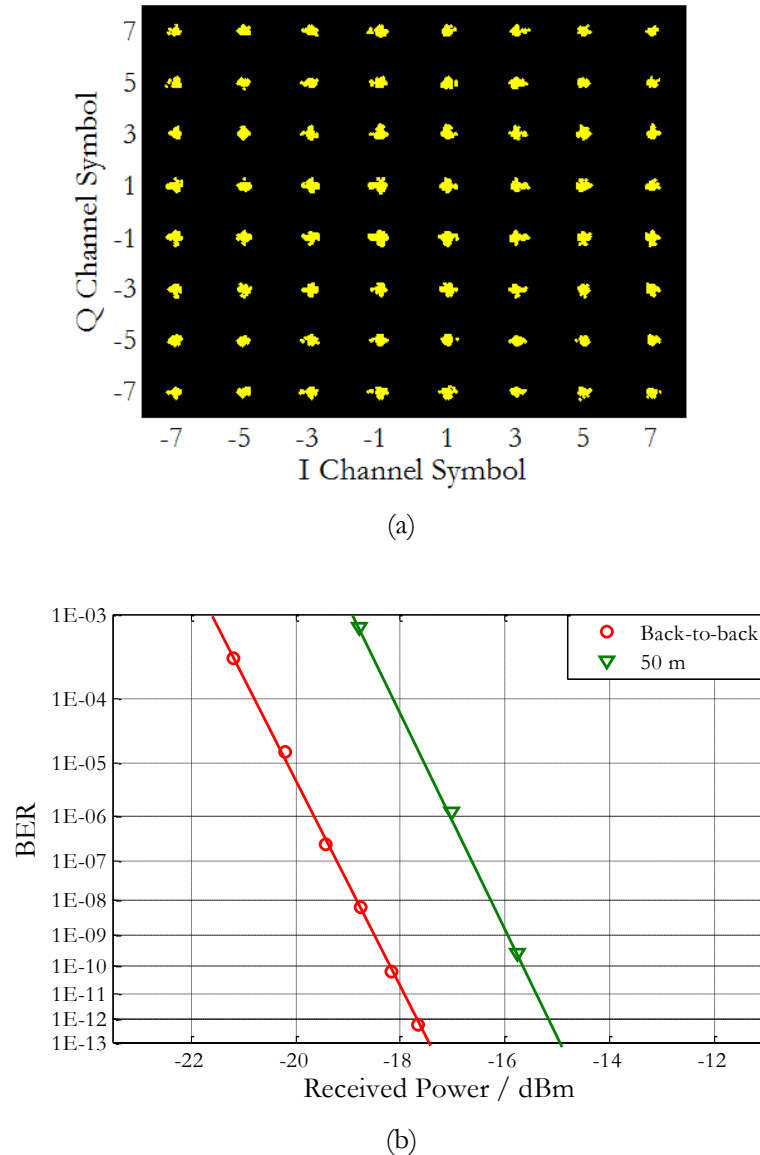


**Figure 5.27 (a) Equalised constellation map of the 1.5 Gbit/s CAP-64 transmission over 50 m SI-POF (b) Corresponding BER curve in comparison with the back-to-back case**

The 3 Gbit/s PAM-8 and 1.5 Gbit/s CAP-64 transmissions record the highest data rates achieved in LED-based SI-POF links without the use of forward error correction for 25 m and 50 m respectively. The main limiting factors in these systems are the low bandwidth and high attenuation of the SI-POF, which greatly degrades the signal-to-noise ratio performance. If forward error correction with a BER threshold of  $10^{-5}$  is implemented, a  $\sim 3$ -5 dB coding gain will be expected in the overall system, which will result in improved systems with higher margins.

## 5.6. Conclusions

An FPGA-based multilevel modulation system is realized by developing an LFSR-based multilevel symbol sequence generator, a look-up-table-based PAM/CAP shaping filter and a high speed interface connecting the DAC. This system is shown to be capable of providing 1 Gbit/s high speed interface per pin with the 16-bit DAC. This enables an overall 16 Gbit/s throughput of the FPGA chip. It has been shown that the modulation signals generated using this system match very well with the calculated results.

Using the system, a 3 Gbit/s PAM-8 transmission experiment is carried out. An offline processing algorithm is developed to perform the equalisation of the signal. By using an 80-tap T/2-spaced FFE and 30-tap T-spaced DFE, 6.8 dB, 3.2 dB and 0.6 dB power margins are achieved respectively for 10 m, 15 m, and 25 m SI-POFs. This is the highest data rate ever achieved using a 650 nm LED transmitter and a standard SI-POF<sup>19</sup> without the use of forward error correction. It also reaches the data rate goal of 3 Gbit/s for the next generation vehicle networks. In the meantime, a 50 m transmission evaluation is carried out using the CAP-64 modulation at 1.5 Gbit/s. A T/4-spaced FFE is used for this system due to the accuracy requirement by the matched filter. By using a 30-tap T/4-spaced FFE and a 15-tap T-spaced DFE, an error free transmission is achieved at a received power of -11.8 dBm, which corresponds to a system margin of 3.4 dB. This is the highest data rate achieved using LED transmitter and SI-POF over 50 m without forward error correction and is attractive for next generation gigabit/s home networks.

Multilevel modulation schemes have been experimentally evaluated in this chapter. For 8 level PAM and 64 level CAP schemes, error free transmissions at data rates over gigabit/s are both achieved. Due to the pulse shaping filter requirement, the CAP scheme requires an oversampling ratio of at least 4x the symbol rate. Limited by the DAC sampling speed, the PAM-8 scheme is chosen for the 3 Gbit/s demonstration whilst CAP-64 is chosen for 1.5 Gbit/s. It is expected that the 3 Gbit/s transmission over 25 m SI-POF is also achievable for the CAP-64 scheme given a DAC with a higher sampling speed ( $> 2$  Gsample/s). Fractionally-spaced FFEs have been shown very useful in these systems since the smaller tap spacing enables more accurate emulation of the ideal receiver shaping filters. Both schemes have provided potential low cost solutions to high speed data transmissions over SI-POF in vehicle and home networks respectively.

---

<sup>19</sup> This refers to the time when this dissertation was written.

# CHAPTER 6

## CONCLUSIONS AND FUTURE WORK

*This chapter concludes this dissertation by summarizing the major achievements. The novelty and practicality of the investigated techniques are discussed. In addition, potential future developments in the areas of both the launching schemes for multimode glass fibre and the advanced modulation schemes for plastic optical fibre are also proposed.*

## 6.1. Conclusions

Thanks to the development of high speed lasers and various electronic components in recent decades, optical communications over multimode waveguides maintain their popularity for high data rate short distance applications. In these applications, multimode glass fibres are implemented mainly for in-building networks typically with a wiring distance less than 500 m. Meanwhile, plastic optical fibres have proved to be attractive transmission media for even shorter links such as home networks and in-car networks. With the non-stop development of bandwidth-demanding services such as high-definition TV, video streaming/monitoring and cloud computing, it is predicted that the traffic requirement from the end-users will continue to increase, which will challenge the reliability of the current data-communication systems.

A restricted optical launch scheme was developed with the goal of providing a simple, low cost and low coupling loss solution to the improvement of the multimode glass fibre bandwidth. Two versions of this launch, namely low-loss Hermite-Gaussian line launch and low-loss Hermite-Gaussian square launch were investigated for the existing installed fibre base. These launches addressed the practicality issue of upgrading existing multimode systems without replacing the ‘legacy’ fibres. Theoretical analysis was firstly carried out to reveal the single mode group excitation characteristics of these launches, which allowed the minimization of the intermodal dispersion and differential modal delay. The calculations were based on the Cambridge108MMF worst case fibre model which represented the worst 5% OM1 fibres in the installed base. Results have shown that the bandwidth-distance products achieved using low-loss Hermite-Gaussian launches over these fibres were truncated at a pre-defined numerical limit of 100 GHz·km, which was at least 50x higher than those of the centre launch and offset launch.

However, ideal Hermite-Gaussian launching beams were not available to be directly generated using optical transmitters in practical implementations. To solve this problem, a beam shaping mask was introduced to realize the approximate generation of Hermite-Gaussian beams. This approach had also been used in the conventional line launch proposal [45]. In this work, it was improved to provide higher coupling efficiency by either using an elliptical Gaussian incident beam for the line launch implementation or a circular Gaussian incident beam for the square launch implementation. The incident beam for each launching profile at the mask was optimised in terms of the beam waist, which maintained the single mode group excitation characteristic whilst providing a low

coupling loss. Using the same launching profile as the conventional line launch, the coupling loss was reduced to 3.4 dB which improved the coupling efficiency by a factor of  $>2$  compared with the previous result of 6.8 dB. The proposed square launches achieved coupling losses ranging from 1.8 dB to 4.3 dB for three different orders. Even for the worst case scenario (in terms of coupling loss), the coupling loss improvement with respect to the conventional line launch was 2.5 dB. Numerical calculations have also shown that although the approximate launching profiles reduced the mode group power extinction ratios to less than 20 dB, the bandwidth-distance products were still maintained as high as the numerical limit of 100 GHz·km for all of the proposed low-loss Hermite-Gaussian launches.

As a significant factor which limited the practical performance of the multimode glass fibre links, launch misalignment analysis has shown that the proposed low-loss Hermite-Gaussian launches achieved bandwidth-distance products at least twice as high as the one for centre launch and were comparable to dual launch with a 3  $\mu\text{m}$  radial misalignment. Further studies on the phase profile mismatches introduced by the beam shaping mask revealed that less than 3 dB extinction ratio degradation could be maintained with a phase mismatch within a range of  $\pm 0.2\pi$ . This represented a  $\sim \pm 90$  nm etching depth, which required an etching time (for line launch profile) of  $\pm 35$  seconds in the case of a wavelength of 1310 nm and a mask material refractive index of 1.45. This has been shown practical for the mask fabrication process using FIB. As a comparison between the low-loss line launch and square launch implementations, the immunity of rotational misalignment made the square launch more preferable in terms of enabling simple launch patchcord fabrication for practical links. The link yield calculations using the Cambridge-108MMF model suggested that a 50 % bandwidth-distance product improvement is achieved at 99% link yield of the entire installed based using the (3, 3) order low-loss Hermite-Gaussian square launch scheme even with 3  $\mu\text{m}$  radial offset at launch.

In the experimental work, the beam shaping masks for different orders of low-loss Hermite-Gaussian launches were made from a silica chip covered with a layer of gold. Each of the masks consisted of a set of transparent areas which outlined the individual spots on a Hermite-Gaussian beam profile. The outline shape was decided by taking the contour level of 5% of the normalized maximum intensity of the launching profile. The thickness of the material in the transparent areas was designed to provide an inverse phase change between the adjacent spots.

The experimental measurement has shown that 3.8 dB coupling loss was achieved using the low-loss line launch implementation. This result matched the theoretical calculation of 3.4 dB. At the same time, 3.2 dB, 3.3 dB and 3.5 dB coupling losses were measured for the (1, 1), (2, 2) and (3, 3) order low-loss square launches using a 18  $\mu\text{m}$  waist incident Gaussian beam at the beam shaping mask. It has been shown that the low-loss Hermite-Gaussian launches outperformed dual launch in terms of measured effective modal bandwidths for both types of fibres which favoured either the centre launch or the offset launch. The square launch implementations have generally been observed with better performances over the line launch implementation with at least doubled bandwidths compared with dual launch. This was mainly due to the easier optical setups for the square launches, which guaranteed high quality launching beams and more relaxed alignment conditions (i.e. immunity to rotational misalignment). Meanwhile, the low-loss Hermite-Gaussian launches were confirmed with robust radial misalignment tolerances which maintained the bandwidths higher than that of the centre launch even with 8  $\mu\text{m}$  and 10  $\mu\text{m}$  radial offset for the line launch and square launch implementations respectively. Data transmission evaluations at 10 Gbit/s were carried out for both implementations. They achieved error free transmissions using a 250 m worst case OM1 fibre. Without the use of equalisation, the low-loss Hermite-Gaussian launches extended the link length specified in IEEE 10GBASE-LRM standard (220 m) and avoided the manual testing between the centre and offset launches at installation.

In the electrical domain for the improvement of the capacities of optical links based on multimode waveguides, multilevel modulation schemes were seen very attractive for those bandwidth-limited links, such as LED-based SI-POF links, since they provided higher bandwidth efficiency and aggregate data rate. It has been shown that multilevel modulation schemes required lower symbol rate than conventional on-off keying, which reduced the overall bandwidth requirement of the system. Two typical modulation schemes in both baseband and passband that could be made multilevel, namely PAM and CAP were studied. Theoretical calculations have shown that both modulation schemes relied on the fulfilment of the Nyquist criterion to avoid ISI. In addition, matched filters were required for CAP schemes for demodulation purpose.

To evaluate the performance of the proposed multilevel modulation schemes, a simulation model was developed for the LED-based SI-POF links. Each of the components in the system was characterized as a low-pass filter. The LED transmitter,

SI-POF and PIN photodiode were characterized as exponential, Gaussian and raised-cosine low-pass filters respectively. Using the parameters of commercially available devices, the overall -3 dB bandwidth of LED-based SI-POF links were calculated as low as 180 MHz for 25 m and 210 MHz for 50 m. For targeted data rates of over 1 Gbit/s for home networks and 3 Gbit/s for in-car networks, it was obvious that high bandwidth efficiency modulation scheme was an attractive option. For the purposes of both dispersion compensation and channel demodulation, equalisation technologies were necessary to be implemented in these links. It has been shown that the FFE and DFE extract the pre-cursor and post-cursor ISIs respectively. The FIR and IIR filters were discussed as the implementations of the FFE and DFE sections and it has been observed that the tap values represented the sampled impulse response of the equivalent equaliser filter. The fractionally-spaced FFEs with  $T/2$  and  $T/4$  tap spacings were shown to provide improved approximations of an ideal equaliser filter impulse response. Such tap spacing gave good emulation of the response whilst keeping the total number of taps in the FFE reasonable. Hence, they were chosen for the PAM and CAP modulation schemes respectively. The smaller tap spacing was used for CAP since the equalisers needed to act as matched filters in the I and Q channels for demodulation and a smaller tap spacing was preferred to avoid the cross-channel interference. The link power budget analysis approach associated with the system model was developed which defined five different types of penalties. They were attenuation, multilevel penalty, noise enhancement penalty, residual ISI penalty after equalisation and relative sensitivity penalty.

In the simulation work for multilevel PAM systems, it has been shown that gigabit/s transmission was not possible without equalisation. This was due to the severe ISI introduced by the limited system bandwidth, which made the overall received pulse violate the Nyquist criterion. With an equaliser implemented at the receiver, it was found that PAM-4 and PAM-8 could both achieve 3 Gbit/s transmissions over 25 m SI-POF and 1.5 Gbit/s over 50 m SI-POF. For the purpose of minimizing the power penalties brought by the equalisers, the numbers of taps in both FFE and DFE sections were optimised for individual systems. It has been shown that the optimal points were 40-tap FFE and 12-tap DFE for PAM-8 whilst 20-tap FFE and 4-tap DFE for PAM-4. Based on these optimal configurations, the power budget analysis suggested that the PAM-8 modulation scheme gave the best performance with system margins of 2.2 dB and 1.9 dB for 3 Gbit/s over 25 m SI-POF and 1.5 Gbit/s over 50 m SI-POF respectively.

For the CAP system, a similar simulation model was developed. Independent equaliser structures were required for the two orthogonal channels in the CAP receiver. It has been found that CAP-64 was the only feasible solution to 3 Gbit/s and 1.5 Gbit/s transmissions over 25 m and 50 m SI-POF respectively. The optimisation of the number of taps revealed that the CAP system generally had a much relaxed requirement than the PAM system. The total penalty introduced by the equaliser did not change very much as long as the numbers of taps were greater than 20 for the FFE and 4 for the DFE. This was mainly due to the lower bandwidth requirement of the CAP modulation scheme, which tended to be less distorted by the system response. The power penalty analysis has shown that CAP-64 achieved 1.3 dB and 1.2 dB system margins for 3 Gbit/s and 1.5 Gbit/s transmissions over 25 m and 50 m SI-POFs respectively.

An FPGA system was developed to experimentally investigate the multilevel modulation schemes up to 8 levels (64 levels for the CAP system) for LED-based SI-POF links. The modulation signal was generated using look-up tables defined in the FPGA system. A 1 Gbit/s DAC and a 500 MHz amplifier were used to modulate and drive the LED. The equalisation and demodulation were processed offline. As one sample per symbol and four samples per symbol were used for the PAM and CAP modulation respectively. The maximum data rates supported by the FPGA system were 3 Gbit/s using PAM-8 and 1.5 Gbit/s using CAP-64. An error free transmission at 3 Gbit/s was realized using the PAM-8 modulation over 25 m SI-POF. The measured system margin was 0.6 dB. At the same time, the CAP-64 modulation was evaluated for a 1.5 Gbit/s transmission over 50 m SI-POF with a measured system margin of 3.4 dB. Hence, the advantage of improving the aggregate transmission capacities of SI-POF links using multilevel modulation schemes has been demonstrated experimentally.

To conclude, techniques in both the optical domain and electrical domain were studied for the purpose of increasing the transmission capacity of multimode waveguide links. In the optical domain, a novel low-loss optical launch scheme was investigated to improve the capacity of the existing multimode glass fibres with reduced coupling losses of at least 2.5 dB improvement compared with the previously reported line launch approach. Among the proposed implementations, the best theoretical result indicating a 50% bandwidth enhancement at a 99% yield compared with the dual launch was achieved using the (3, 3) order square launch. Corresponding bandwidth and misalignment measurements also revealed that the low-loss Hermite-Gaussian launches were robust

solutions to enhancing the performance of multimode glass fibre links even with launching misalignment. The experimental results confirmed that the coupling loss improvement over conventional line launch and showed that 10 Gbit/s equalisation-free links over 250 m worst case OM1 fibre were achievable. In the electrical domain, multilevel modulation schemes were examined for their uses in LED-based POF links. The proposed PAM-8 and CAP-64 schemes increased the bandwidth efficiency of the system by a factor of 3 and 6 respectively compared with the NRZ scheme. Theoretical simulations have shown that the multilevel schemes were preferred options for high data rate applications over SI-POF. PAM-8 and CAP-64 were shown to be the best baseband and passband multilevel modulation schemes achieving 3 Gbit/s and 1.5 Gbit/s transmissions over 25 m and 50 m SI-POFs respectively. Using the FPGA evaluation system developed for this work, the 3 Gbit/s transmission using PAM-8 over 25 m SI-POF recorded the highest data rate achieved in a LED-based SI-POF link without forward error correction and reached the bit rate and distance requirements of the next generation in-car networks. In addition, the 1.5 Gbit/s transmission using CAP-64 over 50 m SI-POF also marked the highest data achieved without forward error correction using LED at the length of 50 m and it provided an robust solution to the next generation gigabit/s home networks.

## 6.2. Future Work

In this dissertation, new approaches have been developed for capacity improvement in multimode waveguide links. It is very attractive to investigate the combination of these approaches in one system to provide further improvement. Some possible extensions of this work including mode division multiplexing using low-loss Hermite-Gaussian launches for multimode glass fibre and multi-channel transmission utilising LED arrays over SI-POF are discussed in this section.

### 6.2.1. Mode Division Multiplexing using Hermite-Gaussian Launches

The proposed low-loss Hermite-Gaussian launches have realized selective excitations of targeted mode groups for a multimode glass fibre. To fully utilise this characteristic, these mode groups can be used as individual channels which are spatially multiplexed in a multimode glass fibre to further enhance the overall system capacity. As seen in Figure 6.1, an example setup is illustrated for a mode division multiplexing system using two different orders of the low-loss Hermite-Gaussian square launches.

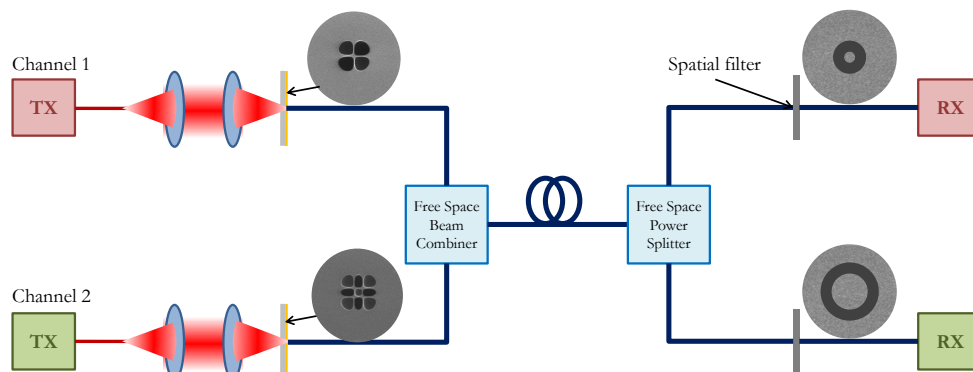


**Figure 6.1 Mode division multiplexing system using two different orders of the low-loss Hermite-Gaussian square launches**

The (1, 1) and (2, 2) order square launches are used for channel 1 and 2 in this setup respectively. The same optics and beam shaping mask introduced in Chapter 3 are used in this system. The multiplexing is achieved using a free space beam combiner. This combiner splits and directs its inputs into two orthogonal polarisation outputs. Hence each output of the combiner contains the light from both channels with the same polarisation. A 3 dB insertion loss is introduced by this device since only one of the outputs is useful. At the receiver side, the same device can be used simply as a power splitter to separate the signal to two receivers for de-multiplexing. Since the power of the higher order mode group tends to fill the fibre more widely toward the outer area of the core, free-space spatial filters can be used to de-multiplex the signal. The spatial filters

can be designed with transparent ring-shape profiles using the same beam shaping mask approach as the one used for the Hermite-Gaussian beam generation. A ring shape with larger radius should be used for the channel launched with the higher order profile. By optimising the radius and thickness of the ring profile, the crosstalk between the two channels can be minimized. Meanwhile, crosstalk cancellation technique can also be introduced to further help with the de-multiplexing process for each channel.

The link budget analysis for the two-channel mode division multiplexing system is shown in Figure 6.2. According to the transceiver parameter in 10GBASE-LRM standard, the transmitter power and receiver sensitivity are  $-6.5$  dBm and  $-21$  dBm respectively. The coupling loss at the beam shaping mask for each channel is taken from Table 3-3. The free space beam combiner introduces a 3 dB loss at multiplexing since half of the power is allocated to the unused polarisation output. It introduces another 3 dB loss at de-multiplexing since it splits the transmitted power to two channels. The fibre loss for 220 m OM1 is 0.3 dB. Another 4 dB coupling loss is estimated for both channels at the spatial filters due to the non-ideal filtering according to a similar spatial filter used in [94]. Hence, received powers of  $-18.6$  dBm and  $-19.6$  dBm are achieved for the (1, 1) order and (2, 2) order channels, which corresponds to 2.4 dB and 1.4 dB system margins respectively. These margins can be further boosted if more advanced technology such as hologram can be used to generate more sophisticated spatial masks and filters at both the transmitter and receiver ends.

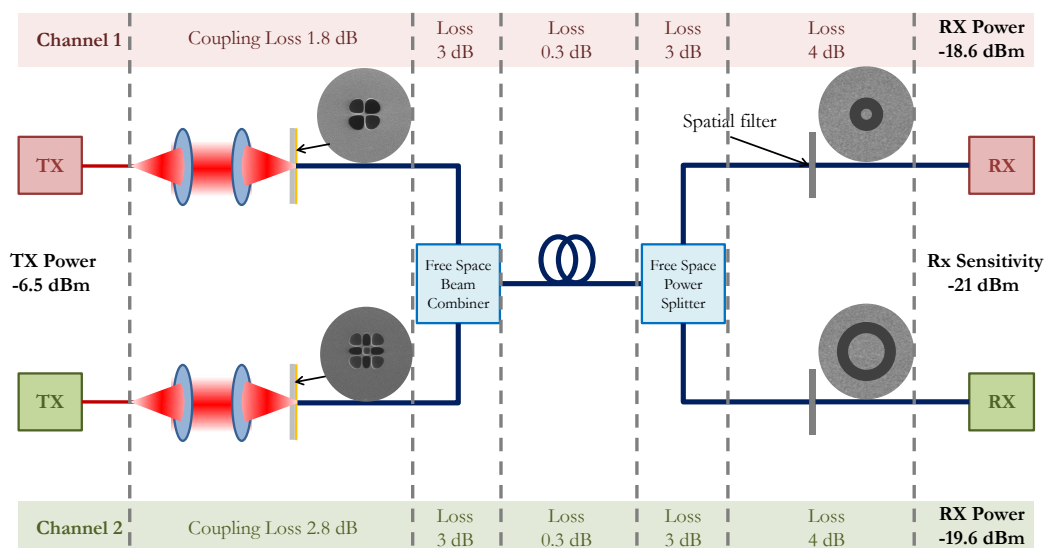
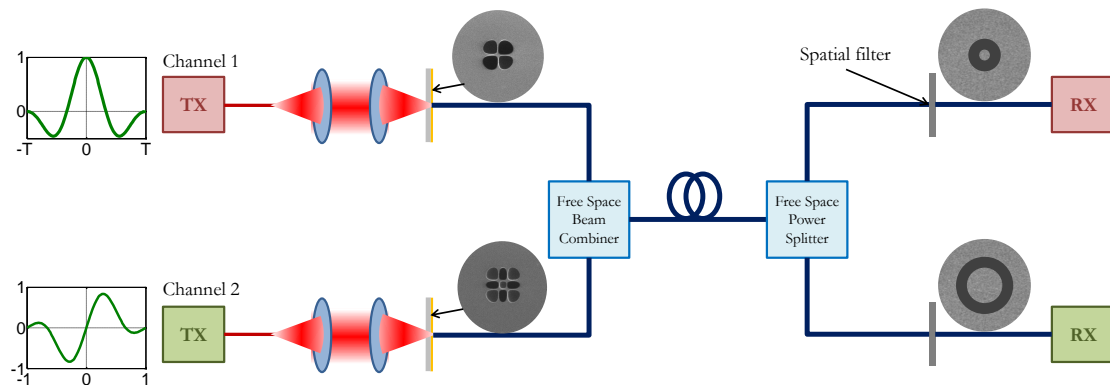


Figure 6.2 Link budget analysis of a two-channel mode division multiplexing system using the low-loss Hermite-Gaussian square launches

A further extension of this work is to use more advanced modulation schemes for each channel. The modulation schemes can be used as an approach to further increase the aggregate data rate of the system or as a technique to improve the de-multiplexing performance. The data rate improvement using this approach is rather obvious. The fundamental inspiration is that multilevel modulation schemes can provide data rate improvements without increasing the system symbol rate. On the other aspect, the two channels in the mode division multiplexing system can use quadratic pulse shapes to avoid inter-channel interference. This is realized by the orthogonal property of these pulses such as the I and Q channels in the CAP system. An example is given in Figure 6.3 where the in-phase pulse and quadrature pulse of the CAP modulation scheme are used in the (1, 1) order and (2, 2) order square launch channels respectively. Transverse filters can be used at the receiver end to demodulate the signals. In addition, CAP modulation scheme has shown great potential to provide data rate enhancement over optical links [53]. In this way, it is predicted that even higher aggregate data rates can be achieved with reduced cross-channel interferences in this system.



**Figure 6.3 Mode division multiplexing system using the optically combined CAP modulation scheme**

### 6.2.2. Multi-channel Transmission over POF

The POF links investigated in this dissertation are all based on a single commercial LED transmitter. In recent years, the development of Gallium Nitride devices has enabled the fabrication of energy efficient LEDs in array structures [147]. These devices, or MicroLEDs, normally have emitting apertures of tens of microns in diameter and the output power can be driven to few dBm [60]. As a result of the smaller aperture size, the bandwidth of each LED pixel is as high as  $> 300$  MHz [148]. The array structure provides a perfect platform for parallel optics applications. As seen in Figure 6.4, the cross section of a hexagonally arranged SI-POF bundle in a butt-coupled 7-channel

transmission system is illustrated. It can be seen that the diameter of the proposed SI-POF bundle cable is 4.2 mm. This refers to a 3 mm total fibre diameter and a 0.6 mm thick jacket cover which is also used for the standard SI-POF cables. This size is comparable to a coaxial copper cable. Hence, compact connections are achievable. The MicroLED arrays need to be designed with a pixel-to-pixel distance of 1 mm and arranged in a hexagonal shape. A photodiode array with the same structure is required at the receiver end. Hence, a 10 Gbit/s transmission can be realized if each of these channels is operating at  $\sim 1.43$  Gbit/s. According to the results shown in this dissertation, this data rate is achievable using either PAM-8 or CAP-64 modulation schemes over 50 m SI-POF. Since the MicroLED has a higher bandwidth, good system margin is expected using this seven-channel configuration for a 10 Gbit/s transmission.

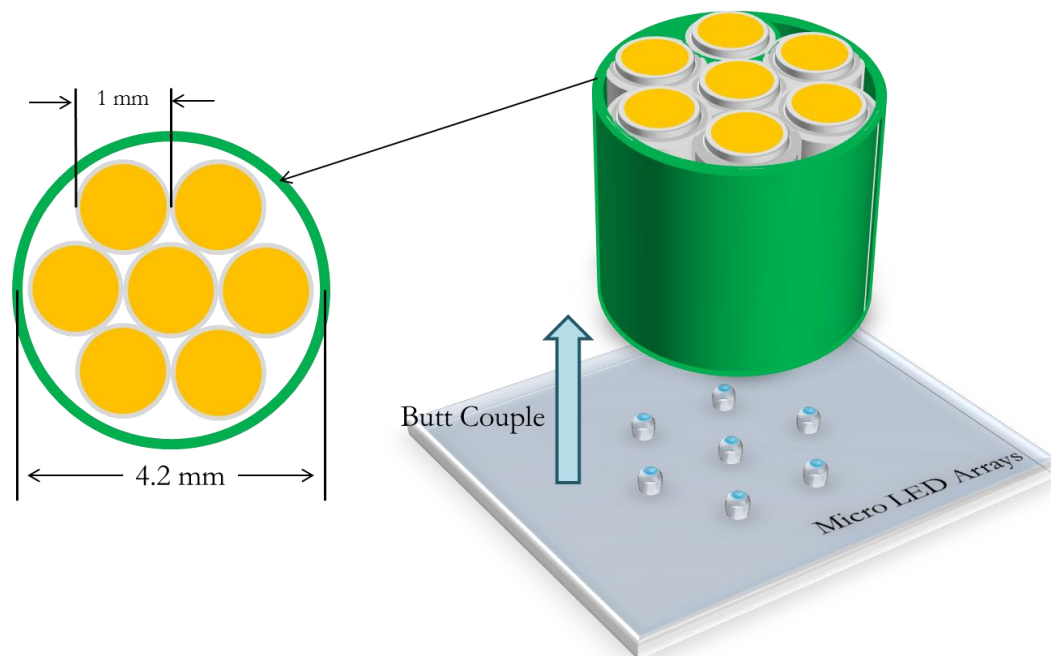


**Figure 6.4 Hexagonal SI-POF bundle for parallel transmission using an MicroLED array**

The centre-to-centre distance of the individual LEDs on the same MicroLED array can be made as small as  $\sim 100 \mu\text{m}$  [148]. Since the SI-POF has a core size of 1 mm in diameter, dozens of such MicroLED pixels can be easily fitted inside one of the core areas. Hence, the total power available for one SI-POF channel can be increased. Meanwhile, since the MicroLEDs can be individually modulated, quadratic modulation signals can be combined optically rather than electrically in such systems. This essentially reduces the number of constellations a single LED needs to deal with. Taking the CAP system as an example, the number of constellations for one LED is square-rooted since it

only needs to be modulated by the symbols on one constellation axis. In this way, the sum of the I and Q channels in the CAP system is always kept linear. This implies that the overall constellation map is always in a rectangular shape. Hence the equalisation and demodulation processes are kept simple.

The schematic diagram for the optically combined CAP system is illustrated in Figure 6.5. Two MicroLEDs are modulated using the I and Q channels of the CAP signal respectively. The outputs of the LEDs are coupled to a single SI-POF and the CAP signals are combined with each other optically. One receiver for each SI-POF is needed with the same hexagonal array structure as the transmitter array shown in Figure 6.4.

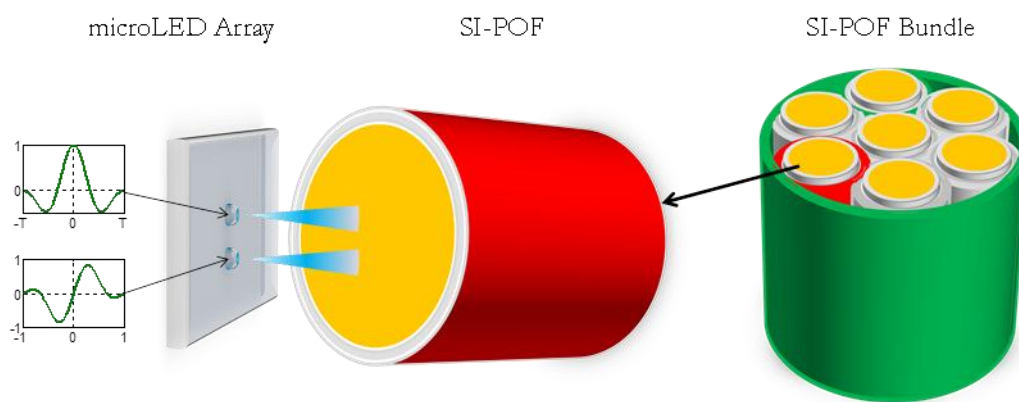


**Figure 6.5 Schematic diagram of an MicroLED pair for the optically combined CAP modulation system for a SI-POF in a hexagonal arranged bundle**

Given the maturity of the glass fibre implementations and the robustness of the plastic fibres, multimode waveguides will continue to play a significant role in optical data communications for short distance applications. This dissertation has presented some preliminary investigations to improve the transmission capacities of multimode waveguides in both the optical domain and electrical domain. As the traffic demand continues to increase, researchers will rise for the challenges and the exploration for new technologies towards more advanced communication systems will also continue.

---

# References

- [1] A. G. Bell and S. Tainter, "Photophone transmitter," USA Patent 235498, 14 Dec, 1880.
- [2] A. G. Bell, "The Photophone," *Science*, vol. 1, pp. 130-134, Sep 1880.
- [3] D. L. Hutt, K. J. Snell, and P. A. BeLanger, "Alexander Graham Bell's Photophone," *Opt. Photon. News*, vol. 4, pp. 20-25, Jun 1993.
- [4] *A Brief History of Optical Fiber*. Available: [http://www.olson-technology.com/mr\\_fiber/fiber-history.htm](http://www.olson-technology.com/mr_fiber/fiber-history.htm)
- [5] D. R. Goff, *Fiber Optic Video Transmission*. Woburn, Massachusetts: Focal Press, 2003.
- [6] N. S. Kapany, "Fiber optics. 1. Optical properties of certain dielectric cylinders," *Journal of the Optical Society of America*, vol. 47, pp. 413-422, May 1957.
- [7] N. S. Kapany, J. A. Eyer, and R. E. Keim, "Fiber optics. 2. Image transfer on static and dynamic scanning with fiber bundles," *Journal of the Optical Society of America*, vol. 47, pp. 423-425, May 1957.
- [8] J. Hecht, *City of Light: the Story of Fiber Optics*. New York: Oxford UP, 1999.
- [9] K. C. Kao and G. A. Hockham, "Dielectric-fibre surface waveguides for optical frequencies," *Proceedings of the Institution of Electrical Engineers*, vol. 113, pp. 1151-1158, Jul 1966.
- [10] F. P. Kapron, D. B. Keck, and R. D. Maurer, "Radiation losses in glass optical waveguides," *Applied Physics Letters*, vol. 17, pp. 423-425, Nov 1970.
- [11] D. B. Keck, P. C. Schultz, and F. Zimar, "Attenuation of multimode glass optical waveguides," *Applied Physics Letters*, vol. 21, pp. 215-217, Jun 1972.
- [12] B. Scott and H. Rawson, "Preparation of low loss glasses for optical fibre communication systems," *Opto-electronics*, vol. 5, pp. 285-288, Jul 1973.
- [13] "The Zettabyte Era," Cisco, USA, White Paper FLGD 10583, May 2012.

- 
- [14] Cisco. (2012). *The Zettabyte Era*. Available: [http://www.cisco.com/en/US/solutions/collateral/ns341/ns525/ns537/ns705/ns827/VNI\\_Hyperconnectivity\\_WP.html](http://www.cisco.com/en/US/solutions/collateral/ns341/ns525/ns537/ns705/ns827/VNI_Hyperconnectivity_WP.html)
- [15] C. M. Deblok and P. Matthijsse, "Core alignment procedure for single-mode-fibre jointing," *Electronics Letters*, vol. 20, pp. 109-110, Feb 1984.
- [16] A. K. Chu and S. F. Hong, "Buried sol-gel/SiON waveguide structure for passive alignment to single-mode fiber on Si substrate," *IEEE Photonics Technology Letters*, vol. 19, pp. 45-47, Jan 2007.
- [17] D. G. Cunningham and I. H. White, "Does multimode fibre have a future in data-communications?," *Electronics Letters*, vol. 43, pp. 63-65, Jan 2007.
- [18] M. Shibutani, H. Ishikawa, H. Tezuka, W. Domon, M. Soda, and K. Emura, "A gigabit-to-the-home (GTTH) system for future broadband access infrastructure," in *IEEE International Conference on Communications*, Montreal, Jun 1997, pp. 1004-1008.
- [19] F. E. Ross, "An overview of FDDI: the fiber distributed data interface," *IEEE Journal on Selected Areas in Communications*, vol. 7, pp. 1043-1051, Sep 1989.
- [20] J. McCool, "100BASE-T: an overview," in *WESCON. Conference record. 'Microelectronics Communications Technology Producing Quality Products Mobile and Portable Power Emerging Technologies'*, San Francisco, Nov 1995, p. 342.
- [21] I. H. White, J. D. Ingham, and R. V. Penty, "Multimode optical fibre links for datacommunications," in *6th International Conference on Transparent Optical Networks*, Wroclaw, Jul 2004, pp. 208-214.
- [22] R. N. Hall, R. O. Carlson, T. J. Soltys, G. E. Fenner, and J. D. Kingsley, "Coherent light emission from GaAs junctions," *Physical Review Letters*, vol. 9, pp. 366-369, Nov 1962.
- [23] B. Lax, "Semiconductor lasers," *Science*, vol. 141, pp. 1247-1255, Sep 1963.
- [24] H. Statz, J. M. Lavine, and C. L. Tang, "Spectral output of semiconductor lasers," *Journal of Applied Physics*, vol. 35, pp. 2581-2585, Mar 1964.

- 
- [25] W. A. Gambling, D. N. Payne, and Matsumur.H, "Mode excitation in a multimode optical-fiber waveguide," *Electronics Letters*, vol. 9, pp. 412-414, Sep 1973.
- [26] L. Raddatz, I. H. White, D. G. Cunningham, and M. C. Nowell, "Increasing the bandwidth-distance product of multimode fibre using offset launch," *Electronics Letters*, vol. 33, pp. 232-233, Jan 1997.
- [27] H. Frazier, "The 802.3z Gigabit Ethernet Standard," *IEEE Network*, vol. 12, pp. 6-7, May 1998.
- [28] (2006). *IEEE P802.3aq 10GBASE-LRM Task Force*. Available: <http://www.ieee802.org/3/aq/>
- [29] A. Flatman. (2007). *10GBASE-LRM and EDC: Enabling 10GB Deployment in the Enterprise*. Available: [http://www.cisco.com/en/US/prod/collateral/modules/ps5455/prod\\_white\\_p aper0900aecd806b8bcb.html](http://www.cisco.com/en/US/prod/collateral/modules/ps5455/prod_white_p aper0900aecd806b8bcb.html)
- [30] A. Carter, "Optical Components: A Customers Perspective," in *Finisar Analyst and Investor Meeting*, Oct 2008.
- [31] R. Hays and H. Frasier, "40G Ethernet Market Potential," in *IEEE 802.3 HSSG Interim Meeting*, Ottawa, Apr 2007.
- [32] F. W. Scholl, M. H. Coder, S. J. Anderson, and B. V. Dutt, "Applications of plastic optical fiber to local area networks," *Proc. SPIE 0991, Fiber Optic Datacom and Computer Networks*, pp. 190-195, Dec 1988.
- [33] J. Bliss, *Fiber optics reprint series: plastic optical fibers and applications*. USA: Information Gatekeepers Inc, 1994.
- [34] M. Kitazawa, K. Shimada, N. Saito, S. Takahashi, and K. Yagi, "Mechanical and optical performance of a new PMMA-based plastic fiber," *Proc. SPIE 1799, Specialty Fiber Optic Systems for Mobile Platforms and Plastic Optical Fibers*, pp. 30-37, Feb 1993.

- 
- [35] R. J. S. Bates, S. D. Walker, and M. Yaseen, "The Limits of Plastic Optical-Fiber for Short-Distance High-Speed Computer-Data Links," *Fiber and Integrated Optics*, vol. 12, pp. 199-208, Oct 1993.
- [36] D. A. Price and S. Ward, "High-speed plastic (PMMA) optical fiber data transmission system suitable for high-speed local-area networks and interconnects," *Proc. SPIE 1799, Specialty Fiber Optic Systems for Mobile Platforms and Plastic Optical Fibers*, pp. 2-6, Feb 1993.
- [37] W. Daum, A. Brockmeyer, and L. Goehlich, "Environmental qualification of polymer optical fibres for industrial applications," in *Plastic Optical Fibres and Applications Conference*, Paris, Jun 1992, pp. 91-95.
- [38] A. Grzemba, *The MOST System*. Germany: Franzis Verlag GmbH, 2011.
- [39] S.-J. Jang and J.-W. Jang, *A Study on Dynamic Gateway System for MOST GATEWAY Scheduling Algorithm in MOST25 and MOST150 Networks* vol. 6935. Berlin: Springer, 2011.
- [40] D. Yunzhi and K. W. Martin, "Gigabit communications over plastic optical fiber," *IEEE Solid-State Circuits Magazine*, vol. 3, pp. 60-69, Winter 2011.
- [41] T. Wipiejewski, T. Moriarty, V. Hung, P. Doyle, G. Duggan, D. Barrow, B. McGarvey, M. O'Gorman, T. Calvert, M. Maute, V. Gerhardt, and J. D. Lambkin, "Gigabits in the home with plugless plastic optical fiber (POF) interconnects," in *2nd Electronics System-Integration Technology Conference*, Sep 2008, pp. 1263-1266.
- [42] "Ethernet Optolock, EDL300T Revision R2," Firecomms Ltd.2012.
- [43] L. Raddatz, I. H. White, D. G. Cunningham, and M. C. Nowell, "Influence of restricted mode excitation on bandwidth of multimode fiber links," *IEEE Photonics Technology Letters*, vol. 10, pp. 534-536, Apr 1998.
- [44] M. Duser and P. Bayvel, "2.5Gbit/s transmission over 4.5km of 62.5  $\mu$ m multimode fibre using centre launch technique," *Electronics Letters*, vol. 36, pp. 57-58, Jan 2000.
- [45] C. H. Kwok, R. V. Penty, I. H. White, and D. G. Cunningham, "Novel passive launch scheme for ultimate bandwidth improvement of graded-index multimode

- fibers," in *Optical Fiber Communication Conference and Exposition and the National Fiber Optic Engineers Conference (OFC/NFOEC)*, San Diego, Mar 2010, p. OWA3.
- [46] H. J. Thiele, P. J. Winzer, I. H. Sinsky, L. W. Stulz, L. E. Nelson, and F. Fidler, "160-Gb/s CWDM capacity upgrade using 2.5-Gb/s rated uncooled directly modulated lasers," *IEEE Photonics Technology Letters*, vol. 16, pp. 2389-2391, Oct 2004.
- [47] "Media Access Control Parameters, Physical Layers and Management Parameters for 10 Gb/s Operation," vol. Type 10GBASE-LX4, ed: IEEE 802.3ae 10Gb/s Ethernet Task Force, The Institute of Electrical and Electronics Engineers Std. IEEE 802.3, 2002.
- [48] J. R. Edwards, "A comparison of modulation schemes for binary data transmission," *Radio and Electronic Engineer*, vol. 43, pp. 562-568, Sep 1973.
- [49] F. Breyer, S. C. J. Lee, S. Randel, N. Hanik, and Osa, "Comparison of OOK- and PAM-4 modulation for 10 Gbit/s Transmission over up to 300 m polymer optical fiber," in *Conference on Optical Fiber Communication/National Fiber Optic Engineers Conference*, San Diego, Mar 2008, p. OWB5.
- [50] F. Breyer, S. C. J. Lee, S. Randel, and N. Hanik, "PAM-4 signalling for gigabit transmission over standard step-index plastic optical fibre using light emitting diodes," in *34th European Conference on Optical Communication (ECOC)*, Brussels, Sep 2008, p. We.2.A.3.
- [51] S. C. J. Lee, S. Randel, F. Breyer, and A. M. J. Koonen, "PAM-DMT for intensity-modulated and direct-detection optical communication systems," *IEEE Photonics Technology Letters*, vol. 21, pp. 1749-1751, Dec 2009.
- [52] J. Armstrong and A. J. Lowery, "Power efficient optical OFDM," *Electronics Letters*, vol. 42, pp. 370-372, Mar 2006.
- [53] J. D. Ingham, R. V. Penty, I. H. White, and D. G. Cunningham, "40 Gb/s carrierless amplitude and phase modulation for low-cost optical datacommunication links," in *Optical Fiber Communication Conference and Exposition and the National Fiber Optic Engineers Conference (OFC/NFOEC)*, Los Angeles, Mar 2011, p. OThZ3.

- 
- [54] A. Ghiasi and B. Welch, "Investigation of 100GbE Based on PAM-4 and PAM-8," in *IEEE P802.3bm 40 Gb/s and 100 Gb/s Fiber Optic Task Force Interim Meeting*, Geneva, Sep 2012.
- [55] V. Bhatt, S. Bhoja, A. Farhood, and G. Nicholl, "PAM-N Comparison," in *IEEE P802.3bm 40 Gb/s and 100 Gb/s Fiber Optic Task Force Interim Meeting*, Geneva, Sep 2012.
- [56] J. L. Wei, J. D. Ingham, R. V. Penty, I. H. White, and D. G. Cunningham, "Update on performance studies of 100 Gigabit Ethernet enabled by advanced modulation formats," in *IEEE P802.3bm 40 Gb/s and 100 Gb/s Fiber Optic Task Force Interim Meeting*, Geneva, Sep 2012.
- [57] M. Wieckowski, J. B. Jensen, I. Tafur Monroy, J. Siuzdak, and J. P. Turkiewicz, "300 Mbps transmission with 4.6 bit/s/Hz spectral efficiency over 50 m PMMA POF link using RC-LED and multilevel Carrierless Amplitude Phase modulation," in *Optical Fiber Communication Conference and Exposition and the National Fiber Optic Engineers Conference (OFC/NFOEC)*, Los Angeles, Mar 2011, p. NTuB8.
- [58] A. Neyer, B. Wittmann, and M. Johnck, "Plastic-optical-fiber-based parallel optical interconnects," *IEEE Journal of Selected Topics in Quantum Electronics*, vol. 5, pp. 193-200, Mar 1999.
- [59] "Multi-core Optical Connector For Plastic Optical Fiber," ed. Tokyo: Honda Connectors, 2005.
- [60] H. X. Zhang, D. Massoubre, J. McKendry, Z. Gong, B. Guilhabert, C. Griffin, E. Gu, P. E. Jessop, J. M. Girkin, and M. D. Dawson, "Individually-addressable flip-chip AlInGaN micropixelated light emitting diode arrays with high continuous and nanosecond output power," *Optics Express*, vol. 16, pp. 9918-9926, Jun 2008.
- [61] D. Hondros and P. Debye, "Elektromagnetische Wellen an dielektrischen Drähten," *Annalen der Physik*, vol. 337, pp. 465-476, 1910.
- [62] O. Schriever, "Elektromagnetische Wellen an dielektrischen Drähten," *Annalen der Physik*, vol. 368, pp. 645-673, 1920.
- [63] T. Miya, Y. Terunuma, T. Hosaka, and T. Miyashita, "Ultimate low-loss single-mode fibre at 1.55  $\mu\text{m}$ ," *Electronics Letters*, vol. 15, pp. 106-108, Feb 1979.

- [64] D. Gloge, "Optical power flow in multimode fibers," *Bell System Technical Journal*, vol. 51, pp. 1767-1783, Oct 1972.
- [65] D. A. Krohn and A. R. Cooper, "Strengthening of glass fibers. 1. Cladding," *Journal of the American Ceramic Society*, vol. 52, pp. 661-664, Dec 1969.
- [66] G. Keiser, *Optical Fibre Communications*: McGraw-Hill, 1991.
- [67] I. Kaminow, D. Marcuse, and H. M. Presby, "Multimode fiber bandwidth: Theory and practice," *Proceedings of the IEEE*, vol. 68, pp. 1209-1213, Oct 1980.
- [68] S. Minami, "The development and applications of POF: Review and forecast," in *3rd International Conference on Plastic Optical Fibers*, Yokohama, Oct 1994, pp. 27-31.
- [69] N. Saitoh, "Plastic optical fibres and their application to passive components and various data links," in *1st International Conference on Plastic Optical Fibers*, Paris, Jul 1992, pp. 10-14.
- [70] M. Ishiharada, H. Kaneda, T. Chikaraishi, S. Tomita, I. Tanuma, and K. Naito, "Properties of flexible light guide made of silicone elastomer," in *1st International Conference on Plastic Optical Fibers*, Paris, Jul 1992, pp. 38-42.
- [71] E. Nihei, T. Ishigure, and Y. Koike, "High-bandwidth, graded-index polymer optical fiber for near-infrared use," *Appl. Opt.*, vol. 35, pp. 7085-7090, Dec 1996.
- [72] Y. Koike, "Status of POF in Japan," in *5th International Conference on Plastic Optical Fibers*, Paris, Oct 1996, pp. 1-8.
- [73] F. Mederer, R. Jager, P. Schnitzer, H. Unold, M. Kicherer, K. J. Ebeling, M. Naritomi, and R. Yoshida, "Multi-gigabit/s perfluorinated graded-index plastic-optical-fiber data links with butt-coupled single-mode InGaAsVCSEL," *Proc. SPIE 3896, Design, Fabrication, and Characterization of Photonic Devices*, vol. 3896, pp. 273-280, Nov 1999.
- [74] "Optical fibres - Part 2-40: Product specifications - Sectional specification for category A4 multimode fibres," ed: INTERNATIONAL ELECTROTECHNICAL COMMISSION, 2009.
- [75] (2001). *Eska Mega specification sheet*. Available: <http://i-fiberoptics.com/pdf/mh4001.pdf>

- 
- [76] S. Bottacchi, *Multi-gigabit transmission over multimode optical fibre: Theory and design methods for 10GbE systems*: John Wiley & Sons Ltd, 2002.
- [77] J. A. Buck, *Fundamentals of optical fibers*, 1st ed. New York: John Wiley & Sons, 1995.
- [78] D. N. Payne and W. A. Gambling, "Zero material dispersion in optical fibers," *Electronics Letters*, vol. 11, pp. 176-178, Mar 1975.
- [79] M. J. Adams, D. N. Payne, F. M. E. Sladen, and A. H. Hartog, "Optimum operating wavelength for chromatic equalization in multimode optical fibers," *Electronics Letters*, vol. 14, pp. 64-66, Feb 1978.
- [80] G. D. Agrawal, *Fiber-Optic Communication Systems*, 3rd ed. New York: John Wiley & Sons, Inc, 2002.
- [81] K. Okamoto, *Fundamentals of Optical Waveguides*, 2nd ed. Oxford: Elsevier Inc, 2006.
- [82] D. Gloge, "Propagation effects in optical fibers," *IEEE Transactions on Microwave Theory and Techniques*, vol. MT23, pp. 106-120, Jan 1975.
- [83] D. Gloge and E. A. J. Marcatil, "Multimode theory of graded core fibers," *Bell System Technical Journal*, vol. 52, pp. 1563-1578, Nov 1973.
- [84] C. N. Kurtz and W. Streifer, "Guided waves in inhomogeneous focusing media.1. Formulation solution for quadratic inhomogeneity," *IEEE Transactions on Microwave Theory and Techniques*, vol. MT17, pp. 11-15, Jan 1969.
- [85] C. N. Kurtz and W. Streifer, "Guided waves in inhomogeneous focusing media. 2. Asymptotic solution for general weak inhomogeneity," *IEEE Transactions on Microwave Theory and Techniques*, vol. MT17, pp. 250-253, May 1969.
- [86] O. Ziemann, *POF Handbook: Optical Short Range Transmission Systems*, 2nd ed. Berlin: Springer, 2008.
- [87] (2001). *Eska Premier specification sheet*. Available: <http://i-fiberoptics.com/pdf/gh4001.pdf>

- [88] T. Giles, J. Fox, and A. MacGregor, "Bandwidth reduction in gigabit ethernet transmission over multimode fiber and recovery through laser transmitter mode conditioning," *Optical Engineering*, vol. 37, pp. 3156-3160, Dec 1998.
- [89] (1996). *IEEE P802.3z Gigabit Task Force*. Available: <http://grouper.ieee.org/groups/802/3/z/public/presentations/>
- [90] L. Raddatz, I. H. White, D. G. Cunningham, and M. C. Nowell, "An experimental and theoretical study of the offset launch technique for the enhancement of the bandwidth of multimode fiber links," *Journal of Lightwave Technology*, vol. 16, pp. 324-331, Mar 1998.
- [91] R. A. Panicker, J. M. Kahn, and S. P. Boyd, "Compensation of multimode fiber dispersion using adaptive optics via convex optimization," *Journal of Lightwave Technology*, vol. 26, pp. 1295-1303, May-Jun 2008.
- [92] X. L. Shen, J. M. Kahn, and M. A. Horowitz, "Compensation for multimode fiber dispersion by adaptive optics," *Optics Letters*, vol. 30, pp. 2985-2987, Nov 15 2005.
- [93] Q. Sun, J. D. Ingham, R. V. Penty, I. H. White, and D. G. Cunningham, "Twin-spot launch for enhancement of multimode-fiber communication links," in *Conference on Lasers and Electro-Optics/Quantum Electronics and Laser Science Conference and Photonic Applications Systems Technologies*, Baltimore, May 2007, p. CWM6.
- [94] C. H. Kwok, "Study of advanced optical solutions for multi-gigabit data-communication links " Ph. D Dissertation, University of Cambridge, 2010.
- [95] L. Geng, C. H. Kwok, S. H. Lee, J. D. Ingham, R. V. Penty, I. H. White, and D. G. Cunningham, "Efficient line launch for bandwidth improvement of 10 Gbit/s multimode fibre links using elliptical Gaussian beam," in *36th European Conference and Exhibition on Optical Communication (ECOC)*, Torino, Sep 2010, p. We.6.B.5.
- [96] "Mode scrambler requirements for overfilled launching conditions to multimode fibers," in *FOTP-54, ANSI/TIA/EIA-455-54-2001*, ed: Global Engineering Documentation, 2001.
- [97] M. Simard, M. Carlson, F. Babin, and M. Tremblay. (2005). *Understanding launch conditions for multimode connector and cable-assembly testing*. Available: <http://documents.exfo.com/appnotes/anote092-ang.pdf>

- [98] Cisco. (2008). *Limitations of Transmission Distances over Multimode Fiber*. Available: [http://www.cisco.com/en/US/prod/collateral/modules/ps5455/white\\_paper\\_c11-463677.pdf](http://www.cisco.com/en/US/prod/collateral/modules/ps5455/white_paper_c11-463677.pdf)
- [99] M. Webster, L. Raddatz, I. H. White, and D. G. Cunningham, "A statistical analysis of conditioned launch for gigabit ethernet links using multimode fiber," *Journal of Lightwave Technology*, vol. 17, pp. 1532-1541, Sep 1999.
- [100] Q. Sun, J. D. Ingham, R. V. Penty, and I. H. White, "Statistical study of a novel launch scheme for high-performance electronic-equalized multimode-fiber links," in *Conference on Optical Fiber Communication and the National Fiber Optic Engineers Conference (OFC/NFOEC)*, Anaheim, Mar 2007, p. JWA7.
- [101] W. Streifer and C. N. Kurtz, "Scalar analysis of radially inhomogeneous guiding media," *Journal of the Optical Society of America*, vol. 57, pp. 779-786, Jun 1967.
- [102] M. Abramowitz and I. A. Stegun, *Handbook of Mathematical Functions*. Washington, D.C.: U.S. Government Printing Office, 1972.
- [103] I. Kimel and L. R. Elias, "Relations between Hermite and Laguerre Gaussian modes," *IEEE Journal of Quantum Electronics*, vol. 29, pp. 2562-2567, Sep 1993.
- [104] C. H. Kwok, D. G. Cunningham, and I. H. White, "Shannon capacity calculation on multimode fibres," *IET Optoelectronics*, vol. 3, pp. 149-157, Jun 2009.
- [105] J. D. Ingham, R. V. Penty, and I. H. White. University of Cambridge multimode fiber model results release 3.1 [Online]. Available: [www.ieee802.org/3/aq/public/tools/108\\_fiberModel/CamMMF3p1/](http://www.ieee802.org/3/aq/public/tools/108_fiberModel/CamMMF3p1/)
- [106] J. D. Ingham, R. V. Penty, and I. H. White. University of Cambridge multimode fiber model results release 2.1 [Online]. Available: [www.ieee802.org/3/aq/public/tools/108\\_fiberModel/CamMMF2p1/CamMMF2p1.xls](http://www.ieee802.org/3/aq/public/tools/108_fiberModel/CamMMF2p1/CamMMF2p1.xls)
- [107] P. Kolesar. Multimode fiber model issues [Online]. Available: [http://www.ieee802.org/3/aq/public/jul04/kolesar\\_1\\_0704.pdf](http://www.ieee802.org/3/aq/public/jul04/kolesar_1_0704.pdf)
- [108] J. Abbott. Gen67 FDDI Monte Carlo Data Set [Online]. Available: <http://www.ieee802.org/3/aq/public/tools/MonteCarlo/OM1/>

- [109] R. V. Penty. Channel Modelling Ad Hoc Task 1 – Static Channel Model [Online]. Available: [http://www.ieee802.org/3/aq/public/sep04/penty\\_1\\_0904.pdf](http://www.ieee802.org/3/aq/public/sep04/penty_1_0904.pdf)
- [110] X. Qian, P. Hartmann, J. D. Ingham, A. Diab, R. V. Penty, and I. H. White, "Modelling and simulation-based prediction of radio transmission over multimode fibre," in *IEEE International Topical Meeting on Microwave Photonics*, Ogunquit, Oct 2004, pp. 165-168.
- [111] H. S. Mackenzie, "Evanescent field devices for non-linear optical applications," Ph. D Dissertation, University of Cambridge, UK, 1987.
- [112] J. Carpenter and T. D. Wilkinson, "Holographic mode-group division multiplexing," in *Optical Fiber Communication Conference/National Fiber Optic Engineers Conference (OFC/NFCEC)*, Los Angeles, Mar 2011, p. OThN3.
- [113] J. Carpenter and T. D. Wilkinson, "Characterization of multimode fiber by selective mode excitation," *Journal of Lightwave Technology*, vol. 30, pp. 1386-1392, May 2012.
- [114] N. Swenson, P. Voois, T. Lindsay, and S. Zeng. (2005). *Proposed TP-2 test methodology*. Available: <http://www.ieee802.org/3/aq/public/tools/TWDP/v0.1/TP-2Testmethodology0.2.pdf>
- [115] C. E. Shannon, "A mathematical theory of communication," *Bell System Technical Journal*, vol. 27, pp. 623-656, Oct 1948.
- [116] Y. Daido, S. Takenaka, E. Fukuda, T. Sakane, and H. Nakamura, "Multilevel QAM modulation techniques for digital microwave radios," *IEEE Journal on Selected Areas in Communications*, vol. 5, pp. 336-341, Apr 1987.
- [117] T. V. Muoi and J. L. Hullett, "Receiver design for multilevel digital optical fiber systems," *IEEE Transactions on Communications*, vol. 23, pp. 987-994, Sep 1975.
- [118] G. D. Forney and G. Ungerboeck, "Modulation and coding for linear Gaussian channels," *IEEE Transactions on Information Theory*, vol. 44, pp. 2384-2415, Oct 1998.

- 
- [119] J. J. Werner, *Tutorial on carrierless AM/PM, Parts I and II*: ANSI X3T9.5 TP/PMD Working Group, 1992 & 1993.
- [120] D. G. Cunningham. *Multilevel Modulation for 10GbE: Link and Component Specification Issues*. Available: [http://grouper.ieee.org/groups/802/3/10G\\_study/public/july99/cunningham\\_1\\_0799.pdf](http://grouper.ieee.org/groups/802/3/10G_study/public/july99/cunningham_1_0799.pdf)
- [121] S. Walklin and J. Conradi, "Multilevel signaling for increasing the reach of 10 Gb/s lightwave systems," *Journal of Lightwave Technology*, vol. 17, pp. 2235-2248, Nov 1999.
- [122] X. Gu and L. C. Blank, "10 Gbit/s unrepeatered three-level optical transmission over 100 km of standard fibre," *Electronics Letters*, vol. 29, pp. 2209-2211, Dec 1993.
- [123] S. Walklin and J. Conradi, "A 10 Gb/s 4-ary ASK lightwave system," in *23rd European Conference on Optical Communications (ECOC)*, Edinburgh, Sep 1997, pp. 255-258.
- [124] G. May, A. Solheim, and J. Conradi, "Extended 10 Gb/s fiber transmission distance at 1538 nm using a duobinary receiver," *IEEE Photonics Technology Letters*, vol. 6, pp. 648-650, May 1994.
- [125] D. M. Gill, A. H. Gnauck, L. Xiang, W. Xing, D. S. Levy, S. Chandrasekhar, and C. R. Doerr, "42.7-Gb/s cost-effective duobinary optical transmitter using a commercial 10-Gb/s Mach-Zehnder modulator with optical filtering," *IEEE Photonics Technology Letters*, vol. 17, pp. 917-919, Apr 2005.
- [126] S. Bhoja, "Study of PAM modulation for 100GE over a single laser," in *IEEE Next Gen 100G Optical Ethernet Study Group*, Newport Beach, Jan 2012.
- [127] C. Cole and L. Lyubomirsky, "PAM-N Eye Diagrams," in *IEEE Next Generation 100Gb/s Ethernet Optics Study Group*, Newport Beach, Jan 2012.
- [128] H. Shankar, A. Szczepanek, and C. Xu, "Feasibility of transimpedance amplifiers and CDRs for PAM modulation," in *IEEE Next Gen 100G Optical Ethernet Study Group*, Newport Beach, Jan 2012.

- 
- [129] M. Atef and H. Zimmermann, *Optical Communication over Plastic Optical Fibers*: Springer, 2013.
- [130] I. Mollers, D. Jager, R. Gaudino, A. Nocivelli, H. Kragl, O. Ziemann, N. Weber, T. Koonen, C. Lezzi, A. Bluschke, and S. Randel, "Plastic Optical Fiber Technology for Reliable Home Networking: Overview and Results of the EU Project POF-ALL," *IEEE Communications Magazine*, vol. 47, pp. 58-68, Aug 2009.
- [131] D. Cardenas, A. Nespola, S. Camatel, S. Abrate, and R. Gaudino, "The rebirth of large-core plastic optical fibers: Some recent results from the EU project "POF-ALL"," in *Conference on Optical Fiber Communication/National Fiber Optic Engineers Conference (OFC/NFOEC)*, San Diego, Feb 2008, p. OWB6.
- [132] M. Atef, R. Swoboda, and H. Zimmermann, "170Mb/s multilevel transmission over 115m standard step-index plastic optical fiber using an integrated optical receiver," *Optics Communications*, vol. 284, pp. 191-194, Jan 2011.
- [133] O. Ziemann, *Handbook of the European POF-PLUS Project 2008 - 2011*: POF-AC Nürnberg, 2011.
- [134] D. Visani, C. M. Okonkwo, Y. Shi, H. J. Yang, H. P. A. van den Boom, G. Tartarini, E. Tangdionga, and A. M. J. T. Koonen, "3 x 2(N)-QAM constellation formats for DMT over 1-mm core diameter plastic optical fiber," *IEEE Photonics Technology Letters*, vol. 23, pp. 768-770, Jun 2011.
- [135] A. Antonino, S. Straullu, S. Abrate, A. Nespola, P. Savio, D. Zeolla, J. R. Molina, R. Gaudino, S. Loquai, and J. Vinogradov, "Real-time Gigabit Ethernet bidirectional transmission over a single SI-POF up to 75 meters," in *Optical Fiber Communication Conference and Exposition and the National Fiber Optic Engineers Conference (OFC/NFOEC)*, Los Angeles, Mar 2011, p. OWA2.
- [136] A. Nespola, S. Straullu, P. Savio, D. Zeolla, S. Abrate, J. Ramirez, and R. Gaudino, "Towards a new Gigabit Ethernet PHY for SI-POF," in *36th European Conference and Exhibition on Optical Communication (ECOC)*, Torino, Sep 2010, p. We.6.B.6.
- [137] H. Nyquist, "Certain topics in telegraph transmission theory," *Transactions of the American Institute of Electrical Engineers*, vol. 47, pp. 617-644, Apr 1928.

- 
- [138] F. M. J. Willems. *Pulse Amplitude Modulation*. Available: [http://www.sps.ele.tue.nl/members/F.M.J.Willems/TEACHING\\_files/TEACHING.htm](http://www.sps.ele.tue.nl/members/F.M.J.Willems/TEACHING_files/TEACHING.htm)
- [139] W. Henkel, T. Kessler, and H. Y. Chung, "Coded 64-CAP ADSL in an impulse-noise environment-modeling of impulse noise and first simulation results," *IEEE Journal on Selected Areas in Communications*, vol. 13, pp. 1611-1621, Dec 1995.
- [140] L. Geng, R. V. Penty, I. H. White, and D. G. Cunningham, "FEC-free 50 m 1.5 Gb/s plastic optical fibre link using CAP modulation for home networks," in *38th European Conference and Exhibition on Optical Communication (ECOC)*, Amsterdam, Sep 2012, p. Th.1.B.4.
- [141] E. F. Schubert, Y. H. Wang, A. Y. Cho, L. W. Tu, and G. J. Zydzik, "Resonant cavity light-emitting diode," *Applied Physics Letters*, vol. 60, pp. 921-923, Dec 1992.
- [142] J. Refi, "LED bandwidth of multimode fibers as a function of laser bandwidth and LED spectral characteristics," *Lightwave Technology, Journal of*, vol. 4, pp. 265-272, Mar 1986.
- [143] C.-L. Tsai, C.-W. Ho, C.-Y. Huang, F.-M. Lee, W. Meng-Chyi, W. Hai-Lin, S.-C. Ko, H. Wen-Jeng, J. Huang, and J. R. Deng, "Fabrication and characterization of 650 nm resonant-cavity light-emitting diodes," *Journal of Vacuum Science & Technology B: Microelectronics and Nanometer Structures*, vol. 22, pp. 2518-2521, Sep 2004.
- [144] G. D. Brown, "Bandwidth and rise time calculations for digital multimode fiber-optic data links," *Journal of Lightwave Technology*, vol. 10, pp. 672-678, May 1992.
- [145] J. D. Ingham, R. V. Penty, and I. H. White, "10 Gb/s & 20 Gb/s extended-reach multimode-fiber datacommunication links using multilevel modulation and transmitter-based equalization," in *Conference on Optical Fiber communication/National Fiber Optic Engineers Conference (OFC/NFOEC)*, San Diego, Mar 2008, p. OTuO7.
- [146] *Optical interface support for 10GBASE-LRM SFP+ transceivers*. Available: [http://www.juniper.net/techpubs/en\\_US/release-independent/junos/topics/reference/specifications/optical-interface-ex8200-support.html](http://www.juniper.net/techpubs/en_US/release-independent/junos/topics/reference/specifications/optical-interface-ex8200-support.html)

- [147] S. Zhang, S. Watson, J. J. D. McKendry, D. Massoubre, A. Cogman, E. Gu, R. K. Henderson, A. E. Kelly, and M. D. Dawson, "High-bandwidth parallel data transmission using GaN/CMOS micro-LED arrays," in *IEEE Photonics Conference*, Sep 2012, p. ME5.
- [148] J. J. D. McKendry, R. P. Green, A. E. Kelly, Z. Gong, B. Guilhabert, D. Massoubre, E. Gu, and M. D. Dawson, "High-speed visible light communications using individual pixels in a micro light-emitting diode array," *IEEE Photonics Technology Letters*, vol. 22, pp. 1346-1348, Sep 2010.